



UNIVERSITAT_{DE}
BARCELONA

Integrating nanoionics concepts in micro solid oxide fuel cells

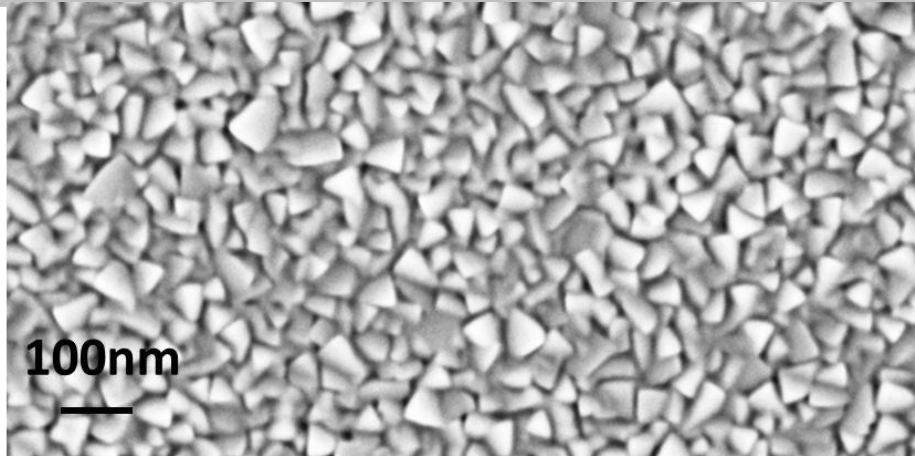
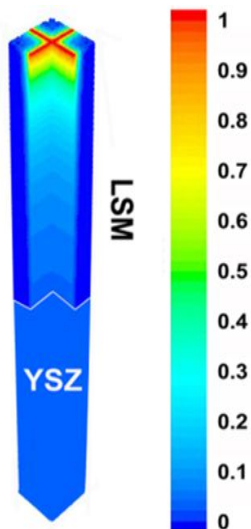
Saranya Aruppukottai Muruga Bhupathi



Aquesta tesi doctoral està subjecta a la llicència **Reconeixement 3.0. Espanya de Creative Commons.**

Esta tesis doctoral está sujeta a la licencia **Reconocimiento 3.0. España de Creative Commons.**

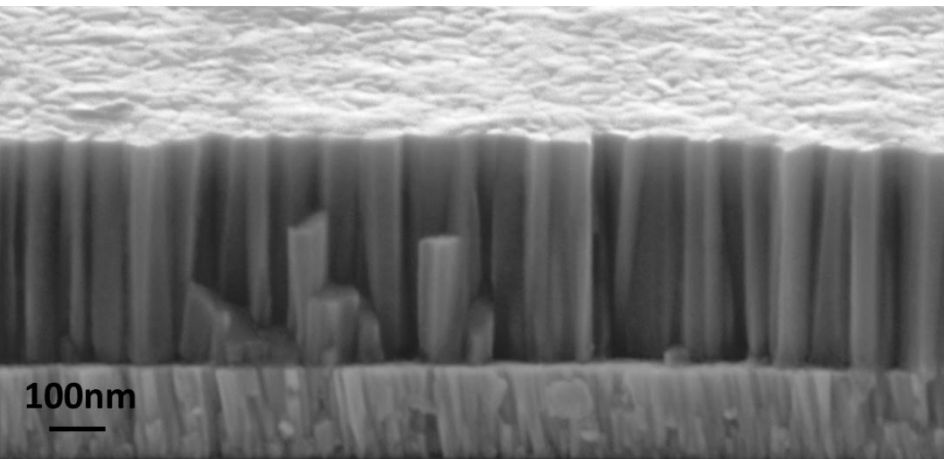
This doctoral thesis is licensed under the **Creative Commons Attribution 3.0. Spain License.**



Integrating nanoionics concepts in micro solid oxide fuel cells

PhD Thesis

- A. M. Saranya



UNIVERSITAT DE
BARCELONA

IREC^R
Institut de Recerca en Energia de Catalunya
Catalonia Institute for Energy Research



UNIVERSITAT DE
BARCELONA



Thesis submitted to apply for the degree of Doctor, in the *Nanosciences* Program of the
University of Barcelona

Departament de Electrònica, Facultat de Física

Integrating nanoionics concepts in micro solid oxide fuel cells

Saranya Aruppukottai Muruga Bhupathi

Supervisors:

Dr. Albert Tarancón Rubio

Institut de Recerca en Energia de Catalunya
Departament de Materials Avançats per a l'Energia,
Universitat de Barcelona

Dr. Alex Morata Garcia

Institut de Recerca en Energia de Catalunya
Departament de Materials Avançats per a l'Energia,
Universitat de Barcelona

Tutor: Dr. Francisca Peiro Martínez

Departament de Electrònica de la Universitat de Barcelona

October 2015

El Dr. Albert Tarancón Rubio, Group Leader de Nanoiònica i Piles de Combustible, Institut de Recerca en Energia de Catalunya (IREC), Barcelona,

El Dr. Alex Morata Garcia, investigador de Institut de Recerca en Energia de Catalunya (IREC), Departament de Materials Avançats per a l'Energia, Barcelona,

CERTIFICAN:

Que la memoria titulada **Integrating nanoionics concepts in micro solid oxide fuel cells**, presentada por Saranya Aruppukottai Muruga Bhupathi para optar al grado de Doctor en el Programa de Nanociencias de la Universidad de Barcelona ha sido realizada bajo su dirección en el Institut de Recerca en Energia de Catalunya (IREC).

Barcelona, Septiembre de 2015



Dr. Albert Tarancón Rubio



Dr. Alex Morata Garcia

El Dr. Francisca Peiro Martínez, Departament de Electrònica
de la Universitat de Barcelona,

CERTIFICA: que ha sido el tutor responsable de los estudios de
Doctorado realizados dentro del programa de Doctorado de
Nanociencias por Saranya Aruppukottai Muruga Bhupathi.

Barcelona, Septiembre de 2015.

A handwritten signature in blue ink, appearing to read 'Francisca Peiro', enclosed within a large, stylized blue oval scribble.

Dr. Francisca Peiro Martínez

Acknowledgement

The journey of my Ph.D. has been an adventurous one, and it is the support of my advisors, colleagues, family and friends. I am very thankful to my advisor Dr. Albert Tarancon for giving me the opportunity to work in his Fuel cells and Nanoionics group as a PhD student, also for his constant support and guidance throughout the PhD program. I would like to acknowledge my advisor, co-advisor Dr. Alex Morata and Dr. Monica Burriel for the valuable discussions in technical meetings related to my thesis work, which was very helpful and motivating.

During the journey of my PhD, I have made several friends and acquaintances who have contributed in ways, helped me directly and indirectly during the PhD program. Thanks to my colleagues and friends Bibiana, Dolors, Laura, Andres and Roberto Moreno. I would like to thank Erdem for introducing me to XRD fittings. A special thanks to Dr. Tariq Jawhari for the discussions on Raman results. I had wonderful time in UK where I had the opportunity to visit imperial college, London and met Dr. Andrea Cavallaro. I would like to thank Andrea for giving me a nice description about IEDP-SIMS technique. My special thanks to Dolors for making FLUENT files in the final moment which was helpful to finish the chapter on time. A special thanks to Dr. Ganapathi and Dr. Shankaran for their valuable suggestions during the PhD journey. It was a wonderful trip to India with my friends Bibiana, Laura and Dolors, where we had great time remain as nice memories forever.

I am grateful to my father R. S. M. Bhupathi for his immense support and encouragement throughout the PhD program since beginning. Thanks to my sweet heart Cendhu for his support in the recent months.

- Barcelona

29/September/2015

List of Acronyms

μ-SOFC	Micro Solid Oxide Fuel Cell
AFC	Alkaline Fuel Cell
AFM	Atomic Force Microscopy
ALD	Atomic Layer Deposition
B or b	Bulk
CCS	Continuous Composition Spread
CES	Cathode/Electrolyte/Substrate
CPLD	Combinatorial Pulsed Laser Deposition
CVD	Chemical Vapor Deposition
DCS	Discrete Combinatorial Synthesis
DMFC	Direct Methanol Fuel Cell
EDS	Energy Dispersive X-ray analysis
EIS	Electrochemical Impedance Spectroscopy
EPMA	Electron Probe Micro Analysis
FEM	Finite Element Method
FFT	Fast Fourier Transform
FTIR	Fourier Transform Infra-red Spectroscopy
GB or gb	Grain Boundary
HTS	High Temperature Superconductor
IEDP	Isotope Exchange Depth Profiling
IT-SOFC	Intermediate Temperature - Solid Oxide Fuel Cell
LAPLD	Large Area Pulsed Laser Deposition
LSC	$\text{La}_{0.8}\text{Sr}_{0.2}\text{CoO}_{3-\delta}$

LSF	$\text{La}_{0.8}\text{Sr}_{0.2}\text{FeO}_{3-\delta}$
LSM	$\text{La}_{0.8}\text{Sr}_{0.2}\text{MnO}_{3+\delta}$
LSMC	$\text{La}_{0.8}\text{Sr}_{0.2}\text{Mn}_{1-x}\text{Co}_x\text{O}_{3\pm\delta}$
MCFC	Molten Carbonate Fuel Cell
MIEC	Mixed Ionic Electronic Conductor
MOCVD	Metal Organic Chemical Vapor Deposition
OCV	Open Circuit Voltage
ORR	Oxygen Reduction Reaction
OSC	Oxygen Storage Capacity
PAFC	Phosphoric Acid Fuel Cell
PEMFC	Proton Exchange Membrane Fuel Cell
PLD	Pulsed Laser Deposition
SEM	Scanning Electron Microscopy
SIMS	Secondary Ion Mass Spectrometry
TEC	Thermal Expansion Coefficient
ToF	Time of Flight
TP	Temperature Programmed measurement
TPB	Triple Phase Boundary
WDS	Wavelength Dispersive X-ray analysis
XPS	X-ray photoelectron spectroscopy
XRD	X-Ray Diffraction
YSZ	Yttria-stabilized Zirconia

Abstract

Nanoionics has become an increasingly promising field for the future development of advanced energy conversion and storage devices, such as batteries, fuel cells and supercapacitors. Particularly, nanostructured materials offer unique properties or combinations of properties as electrodes and electrolytes in a range of energy devices. However, the enhancement of the mass transport properties at the nanoscale has often been found to be difficult to implement in nanostructures.

In this thesis oxygen ion transport is investigated in the perovskite-related Mixed Ionic and Electronic Conducting (MIEC) oxides of thin film cathodes exhibiting well-defined nanostructure with thickness <200nm, in order to correlate the oxygen ion transport with the thin film nanostructure consist of grain bulk and grain boundaries. Pulsed Laser Deposition (PLD) is used as a tool to acquire enhanced ionic transport along grain boundaries.

The work developed in this thesis is divided into six parts. The first chapter introduces the basics of solid oxide fuel cells, importance of thin film cathodes and nanoionics concept. The second chapter explains the principle and operation of all experimental techniques employed in this thesis for the microstructural and functional characterization of the thin film cathodes. The following chapters contain the main work of the thesis.

The deposition condition and microstructural optimization studies performed in PLD to fabricate thin film cathodes are compiled in chapter three. The oxygen ion transport properties of $\text{La}_{0.8}\text{Sr}_{0.2}\text{MnO}_{3+\delta}$ (LSM) thin films are studied in chapter four. Further, a novel (new) methodology for the material screening for Solid Oxide Fuel Cell (SOFC) is presented in chapter five. The methodology is based upon a combinatorial deposition of $\text{La}_{0.8}\text{Sr}_{0.2}\text{Mn}_{1-x}\text{Co}_x\text{O}_{3+\delta}$ (LSMC) thin film system by PLD on a 4-inch silicon wafer which allows generating full range binary diagram of compositions even for complex oxides. Chapter six is devoted to the functional studies of LSMC binary system.

Isotope Exchange Depth Profiling combined with Secondary Ion Mass Spectroscopy (IEDP-SIMS) is employed in the temperature range 500°C to 800°C for evaluating the oxygen mass transport properties of LSM thin film and LSMC binary system. Further, the oxygen mass transport properties of LSM thin film is studied by Electrochemical Impedance Spectroscopy (EIS).

Resumen de la tesis

Las pilas de combustible son una de las tecnologías prometedoras en la actualidad para satisfacer la creciente demanda de energía y tecnología limpia. En las pilas de combustible de óxido sólido (SOFC) la investigación está avanzando hacia la miniaturización del dispositivo (llamado "micro-SOFC" con estructuras de capas delgadas) que durante aplicación del dispositivo portátil trabajan con temperaturas alrededor de 500°C a 700°C.

En las SOFC, el cátodo es el responsable principal de la pérdida de polarización debido a la baja energía cinética de la reacción de reducción del oxígeno (ORR) a bajas temperaturas de operación que afectaría a la eficiencia del dispositivo. Para rectificar el problema, hay varios grupos que están estudiando la mejora de la funcionalidad del cátodo a bajas temperaturas. En general, su funcionalidad puede ser mejorada de dos maneras i) Mejorar las propiedades intrínsecas de los materiales de cátodo existentes modificando la microestructura del cátodo ii) Búsqueda de los nuevos materiales de cátodo.

Los cátodos de capa delgada estudiados en esta tesis son; $\text{La}_{0.8}\text{Sr}_{0.2}\text{MnO}_{3+\delta}$ (LSM), $\text{La}_{0.8}\text{Sr}_{0.2}\text{CoO}_{3-\delta}$ (LSC) y el sistema pseudo-binario $\text{La}_{0.8}\text{Sr}_{0.2}\text{Mn}_{1-x}\text{Co}_x\text{O}_{3\pm\delta}$ (LSMC; *from $x=0$ to 1*). Todos ellos son conductores mixtos iónico-electrónicos (MIEC). La investigación del LSM en capas delgadas está englobada en la primera forma propuesta para mejorar la funcionalidad del cátodo. Aunque el LSMC es un sistema de cátodo familiar en SOFC, puede ser colocado en la categoría de nuevos materiales del cátodo debido a que la fabricación del LSMC pseudo-binario mediante un método combinatorial es nueva vía para la proyección de materiales SOFC. Por lo tanto, las dos maneras mencionadas se siguen en esta tesis para mejorar la funcionalidad del cátodo mediante la implementación del concepto de la Nanoiónica.

El comportamiento de los iones conductores a nivel nano-régimen (<100nm) es totalmente diferente a nivel másico, tema que estudia la nonionica. Especialmente, las interfaces como las capas de carga espacial y los límites de grano actúan como una autopista para la rápida conducción de iones oxígeno, que puede mejorar el transporte de carga, en general, en las nanoestructuras. En esta tesis, se estudian las propiedades de transporte de masa del oxígeno en cátodos en forma de película delgada mediante modificaciones en la nanoestructura de la película fina con el fin de observar y mejorar el transporte de carga a lo largo de la interfaz de los límites de grano, así como para comprender el transporte iónico rápido de tales interfaces. La Deposición Pulsada por Laser (PLD) se utiliza como una herramienta para la fabricación de películas delgadas.

En general, las nanoestructuras de película fina obtenidas mediante el PLD presentan granos columnares que pueden actuar como una autopista para la conducción iónica y son adecuadas para el trabajo propuesto. Por lo tanto el PLD se utiliza como una herramienta para fabricar películas delgadas de cátodos densos con una elevada densidad de límites de grano para estudiar el transporte iónico en las interfaces. Además, se llevan

Resumen de la tesis

a cabo estudios de deposición de capas múltiples de LSM/LSC mediante PLD para averiguar el espesor óptimo para la fabricación de un sistema pseudo-binario de LSMC combinatorial sin ningún tipo de fases parásitas.

El LSM es un material clásico y bien estudiado dentro de los cátodos estudiados en esta tesis. Las propiedades funcionales, es decir, las propiedades de transporte masivo de oxígeno (coeficiente de auto-difusión de oxígeno y coeficiente de intercambio de superficie, D^* y k^* , respectivamente) de los cátodos de capas delgadas de LSM son analizados mediante las técnicas intercambio de isotopos en perfiles profundos utilizando iones secundarios espectroscopia de masas (IEDP -SIMS) y Espectroscopia de Impedancia Electroquímica (EIS) en el rango de temperaturas entre 500°C y 700°C. Las propiedades de transporte del oxígeno se estudian mediante la alteración de la nanoestructura de las películas delgadas de LSM. La nanoestructura se modifica mediante la fabricación de películas de LSM con una elevada densidad de límites de grano mediante el control de las condiciones de deposición en el PLD.

A continuación, se observa una mejora en el transporte de iones oxígeno a lo largo de los bordes de grano de la capa delgada del LSM con nanoestructuras modificadas. La nanoestructura del LSM se investigó adicionalmente por Microscopía Electrónica de Transmisión de alta resolución (HRTEM) y se encontró que las deformación inducidas por la alta densidad de dislocación son las responsables de la mejora en 6 a 7 órdenes del transporte de iones oxígeno a lo largo de las regiones del límite del grano del LSM.

La proyección de nuevos materiales y propiedades de las composiciones de ajuste fino es una tarea esencial pero compleja que requiere mucho tiempo. Por desgracia, sólo se puede obtener información discreta sobre las composiciones sintetizadas y en general las optimizaciones primarias originales se han mantenido durante años. Recientemente, un enfoque combinatorial para la síntesis y caracterización de materiales está abriendo una nueva vía en la generación de la totalidad de los diagramas de composición en un solo experimento. En el estudio del LSMC pseudo-binario, se presenta a una nueva metodología para la selección de materiales aplicables en las pilas de combustible. La metodología se basa en una deposición combinatorial de películas delgadas por PLD en obleas de silicio de 4 pulgadas, además es posible predecir el espesor y el mapa de composición del LSMC binario utilizando esta metodología. La metodología propuesta se puede ampliar para generar diagramas binarios y ternarios de composiciones completas, incluso para óxidos muy complejos (debido a una excelente transferencia de la estequiometría).

Con el fin de ser capaz de mapear las propiedades estructurales y funcionales de los diagramas sintetizados, se han empleado técnicas de caracterización puntual y no destructiva. La Espectroscopia de Micro- Raman se emplea para evaluar la composición y estructura local, mientras que IEDP-SIMS se lleva a cabo para evaluar las propiedades de transporte de masa del oxígeno del sistema LSMC en las composiciones con un contenido

Resumen de la tesis

en cobalto de $x \approx 0.04$ a 0.85 en el rango de temperatura de 600°C a 800°C . Los valores obtenidos para D^* y k^* a través del interior de grano siguieron la misma tendencia que los reportados previamente por *De Souza et al.* para composiciones discretas en forma másica [1, 2]. Por otra parte, se han encontrado de 6 a 7 órdenes de magnitud de mejora a lo largo de los límites de grano en el sistema LSMC.

Dado que no existe una solución analítica disponible para un sistema de película delgada heterogénea bicapa con valores distintos de D^* y k^* , los perfiles de difusión del isótopo de oxígeno de las capas delgadas de LSM y el sistema de pseudo-binario LSMC/8YSZ son estudiados utilizando el Método de Elementos Finitos (FEM) para extraer los parámetros de transporte de oxígeno a lo largo de los límites de grano y interior del grano (D_b^* , D_{gb}^* and k_b^* , k_{gb}^*). También hay otro modelo llamado "Two-slab" que se utiliza en ciertas condiciones para encontrar los valores medios de D^* y k^* en el LSMC.

Esta tesis se estructura en seis capítulos con un breve resumen en cada capítulo y dos apéndices.

Capítulo 1: Introducción al alcance de la tesis.

Capítulo 2: Introducción al método experimental empleado en esta tesis.

Capítulo 3: LSM y LSC; optimización microestructural mediante PLD.

Capítulo 4: Estudio de transporte de iones de oxígeno en cátodos de LSM de película delgada.

Capítulo 5: Fabricación y caracterización microestructural de sistemas pseudo-binarios de película delgada de LSMC.

Capítulo 6: Estudio de transporte de iones de oxígeno en sistema de película delgada de LSMC.

Apéndice 1: Introducción al método "Two-slab".

Apéndice 2: La fabricación de sistema de pseudo-ternario LSM-LSC-LSF.

References

- [1] R. A. De Souza, J. A. Kilner, *Solid State Ionics*, 1998, 106, 175.
- [2] R. A. De Souza, J. A. Kilner, *Solid State Ionics*, 1999, 126, 153.

Table of contents

Chapter I

1.1 Fuel cells	1
1.1.1 Solid Oxide Fuel cells (SOFCs)	3
1.1.2 Disadvantages of high-temperature SOFC operation (800-1000°C)	4
1.1.3 Miniaturization of SOFC	5
1.2 Perovskite-type oxides as cathodes in SOFC	6
1.2.1 $\text{La}_{0.8}\text{Sr}_{0.2}\text{MnO}_{3+\delta}$: Structural, defect chemistry and electrical properties ..	7
1.2.2 $\text{La}_{0.8}\text{Sr}_{0.2}\text{CoO}_{3-\delta}$: Structural, defect chemistry and electrical properties	9
1.2.3 Oxygen transport properties of LSM and LSC	10
1.3 Enhancing oxygen ion transport in thin film cathodes using nanostructured films	12
1.3.1 Thin film cathodes Vs thicker cathodes	12
1.3.2 Nanoionics effect in thin film cathodes	14
1.3.3 LSM and LSC thin film cathodes	16
1.4 Scope of the thesis	17
References	19

Chapter II

2.1 Chapter outline	21
2.2 Thin film fabrication techniques	21
2.2.1 Pulsed laser deposition	22
2.2.1.1 Laser-Target interaction	23
2.2.1.2 Plume expansion dynamics	24
2.2.1.3 Thin film deposition	25
2.2.2 Large Area Pulsed laser deposition (LAPLD)	26
2.2.3 Combinatorial Pulsed laser deposition (CPLD)	27
2.3 Microstructural characterization techniques	29
2.3.1 X-Ray diffraction (XRD)	29
2.3.2 Scanning electron microscopy (SEM)	30
2.3.3 Energy dispersive X-ray analysis (EDS)	31
2.3.4 Wavelength-dispersive X-ray analysis (WDS)	31
2.3.5 Transmission electron microscopy (TEM)	32

2.3.6	Atomic force microscopy (AFM)	33
2.3.7	Raman spectroscopy	34
2.4	<i>Functional characterization techniques</i>	34
2.4.1	Electrical measurements	34
2.4.1.1	Cell measurement setup	35
2.4.1.2	Electrochemical impedance spectroscopy (EIS)	36
2.4.2	IEDP-SIMS measurement	38
2.4.2.1	Oxygen isotope exchange	38
2.4.2.2	Time of flight - Secondary ion mass spectrometry (ToF-SIMS)	39
2.5	<i>Conclusion</i>	42
	<i>References</i>	42

Chapter III

3.1	<i>Chapter outline</i>	45
3.2	<i>LSM, LSC and LSF parent layer PLD deposition optimization</i>	47
3.2.1	Effect of substrate temperature on phase formation	47
3.2.2	Effect of pressure on thin film microstructure	53
3.3	<i>Interdiffusion mechanism</i>	54
3.3.1	What is interdiffusion/intermixing process?	54
3.3.2	Rate-limiting factors of intermixing mechanism	55
3.3.3	Methodology to fabricate new composition in thin film form by intermixing process	56
3.3.4	Mn, Co and Fe diffusivity in perovskite-related structures	58
3.3.5	Influence of thickness on effective diffusion time (t_{eff}) of Mn, Co and Fe cations	60
3.4	<i>Validation of interdiffusion mechanism</i>	61
3.4.1	LSF/LSC multilayer deposition	61
3.4.2	LSM/LSC multilayer deposition	64
3.5	<i>Conclusion</i>	65
	<i>References</i>	65

Chapter IV

4.1	<i>Chapter outline</i>	68
4.2	<i>Microstructural Characterization of LSM films</i>	69

4.3 Oxygen mass transport study in LSM dense thin films by IEDP-SIMS and EIS techniques	72
4.3.1 IEDP-SIMS technique	72
4.3.2 Finite Element Analysis (FEM) of oxygen diffusion profiles to determine oxygen transport parameters	74
4.3.3 EIS technique	78
4.4 Conclusion	82
References	82

Chapter V

5.1 Chapter outline	84
5.2 LSM and LSC thickness map	86
5.2.1 Large-area LSM and LSC deposition and sample preparation.....	86
5.2.2 Thickness determination by SEM and micro-Raman analysis.....	87
5.2.3 LSM and LSC thickness map	90
5.3 Optimization of plume center position from superposition of LSM and LSC layers	94
5.3.1 Effect of plume center position on thickness and Co concentration distribution	97
5.4 LSMC combinatorial sample preparation in PLD	100
5.5 Microstructural characterization of combinatorial sample	102
5.5.1 Structural investigation by X-Ray diffraction (XRD)	102
5.5.2 Structural investigation by Raman analysis	107
5.5.2.1 Phonon modes of LSMC Rhombohedral crystal system	108
5.5.2.2 Effect of Co content on Raman mode peak wavenumber	109
5.5.2.3 Effect of Co content on Raman mode peak intensity	110
5.5.3 Morphology study by Atomic Force Microscopy (AFM)	111
5.5.4 Thickness mapping by Scanning Electron Microscopy (SEM) and comparison with parent layers superposition results	113
5.5.5 Composition mapping by Energy Dispersive Spectroscopy (EDS), Wavelength Dispersive Spectroscopy (WDS) and comparison with superposition results	114
5.6 Validation of plume superposition results with experimental results	116
5.7 Conclusion	117
References	118

Chapter VI

6.1	<i>Chapter outline</i>	120
6.2	<i>IEDP-SIMS measurements in combinatorial sample</i>	121
6.2.1	IEDP-SIMS measurement sample details	121
6.2.2	^{18}O concentration profile in LSMC combinatorial system	123
6.3	<i>Determination of oxygen transport parameters of LSMC system by FEM simulation</i>	127
6.3.1	Oxygen self-diffusion coefficients D_b^*, D_{gb}^* Vs Co content	131
6.3.2	Oxygen self-exchange coefficients k_b^*, k_{gb}^* Vs Co content	134
6.4	<i>Conclusion</i>	137
	<i>References</i>	138
7	Conclusion	140
Appendix A		
A.1	<i>Outline</i>	142
A.2	<i>Classical models and its validity</i>	142
A.2.1	Solution to semi-infinite medium	142
A.2.2	Solution to Plane-sheet model	143
A.3	<i>Two-Slab model</i>	145
A.3.1	Plane sheet model Vs Two-slab model	145
A.3.2	Solution to Two-slab model	145
A.3.3	Special case 1: D_1^*, D_2^* are finite	147
A.3.4	Special case 2: D_1^* is finite and D_2^* is ∞	148
A.3.5	Validation of Two-Slab model by manual fitting and MATLAB fitting routine.	149
A.3.6	Two-slab model - Place of validity	151
	<i>References</i>	152
Appendix B		
B.1	<i>LSM-LSC-LSF multilayer test deposition</i>	153
B.2	<i>LSM-LSC-LSF Ternary sample preparation</i>	153
	Scientific contribution	155

Chapter I

Introduction

Chapter I

1.1 Fuel cells

Science and technological growth in the last centuries have improved the standard of living of world population in an exceptional way. Energy is the driving force of all such accelerated growth and is the lifeblood of the world economy. Therefore, energy growth is directly linked to comfort-living and prosperity across the world.

At present, the world's major energy requirement and daily energy needs are fulfilled by the usage of fossil fuels such as petroleum, coal and natural gas which are the primary sources of CO₂ emission [1]. As a consequence of the vast consumption of fossil fuels, the global temperature is rising accompanied by changes in the global weather and climate. In the last century earth's average temperature has risen by 0.7°C due to industrialization [2]. According to the recent statistics of *United States environmental protection agency* it is believed that global temperature will rise to another ~ 1 to 5°C in the next hundred years [2]. Even a small increase in the global temperature can cause huge impact on climate, weather and eco-system. Therefore, scientists are looking for alternatives as a challenge a) to reduce the global warming b) scarcity of fossil fuels and c) to meet the growing demand for energy due to increasing population. The alternative energy should be safer for environment.

Fuel cells, an alternative energy source, is currently attracting interest for power-generation with wide range of applications including stationary power generation, portable power generation and transportation. Fuel cells are electrochemical energy conversion devices that convert chemical energy into electrical energy with water and heat as by-products [1, 3]. The advantages of fuel cells are high efficiency, lower emission of sulfur, nitrogen oxide and hydrocarbon pollutants and significantly lower amount of CO₂ emission making them a non-polluting and renewable way of electricity generation [1, 3].

Up to now, there are six varieties of fuel cells each differ in terms of operating temperature and the type of electrolyte material used [4]. However, the basic principle of operation is the same. The different varieties of fuel cells are Proton Exchange Membrane (Polymer Electrolyte) Fuel Cell (PEMFC), Alkaline Fuel Cell (AFC), Phosphoric Acid fuel Cell (PAFC), Molten Carbonate Fuel cell (MCFC) Solid oxide Fuel Cell (SOFC) and Direct Methanol Fuel Cell (DMFC).

Table 1.1. Comparison of six fuel cells on the axis of operating temperature and electrolyte type. η represents efficiency.

Fuel cell type	T (°C)	Electrolyte	Charge carrier	Electrochemical reaction (i) Anode (ii) Cathode	η (real) %
PEMFC	50-100	Hydrated Polymeric Ion Membrane Exchange	H^+	i) $H_2 \rightarrow 2H^+ + 2e^-$ ii) $\frac{1}{2}O_2 + 2H^+ + 2e^- \rightarrow H_2O$	40-50%
AFC	50-200	Liquid solution of KOH	OH^-	i) $H_2 + 2(OH^-) \rightarrow 2H_2O + 2e^-$ ii) $\frac{1}{2}O_2 + H_2O + 2e^- \rightarrow 2(OH)^-$	~50%
PAFC	~200	Phosphoric acid(H_3PO_4)	H^+	i) $H_2 \rightarrow 2H^+ + 2e^-$ ii) $\frac{1}{2}O_2 + 2H^+ + 2e^- \rightarrow H_2O$	40%
MCFC	~650	Li_2CO_3 , KCO_3 in $LiAlO_2$	CO_3^{2-}	i) $H_2O + CO_3^{2-} \rightarrow H_2O + CO_2 + 2e^-$ ii) $\frac{1}{2}O_2 + CO_2 + 2e^- \rightarrow CO_3^{2-}$	>50%
SOFC	800-1000	Ceramic ionic conductor	O^{2-}	i) $H_2 + O^2 \rightarrow H_2O + 2e^-$ ii) $\frac{1}{2}O_2 + 2e^- \rightarrow O^{2-}$	>50%
DMFC	60-200	Solid polymer membrane	H^+	i) $CH_3OH + H_2O \rightarrow CO_2 + 6H^+ + 6H^-$ ii) $3O_2 + 12H^+ + 12H^- \rightarrow 6H_2O$	40%

The low temperature fuel cell technologies such as PEMFC, AFC and PAFC require relatively pure hydrogen for stable performance to ensure the adequate reaction kinetics in electro-catalysts (eg. expensive Platinum-based catalyts) [5]. They are highly sensitive to impurities such as CO, CO₂ and H₂S. The necessity of pure hydrogen to avoid electrode deactivation raises efficiency of fuel cells [4]. DMFC offers lower efficiency due to low-operation temperature and the usage of methanol is toxic and flammable [4]. MCFC can reach higher efficiency due to high-operation temperature and it does not need expensive precious-metal catalyts. The main drawback of MCFC is corrosive-nature of electrolyte moreover molten electrolyte resulting in corrosion and degradation issues [4, 5].

Among these six fuel cell technologies, SOFC presents various advantages. The high-temperature operation (800-1000°C) removes the usage of expensive noble-metals as electrodes, thereby reducing cost [4, 5]. The main advantages of SOFCs compared to other types are higher efficiency, in the range 60 to 85% and mechanical stability of the solid electrolyte. High-temperature operation offers the possibility of reforming the fuel by an internal reformer, which is a cost-effective solution compared to adding a separate external reformer. Further, SOFC has higher tolerance to the impurities such

as carbon monoxide than other fuel cell types which gives fuel flexibility (hydrogen and hydrocarbon) [3-7].

1.1.1 Solid Oxide Fuel cells (SOFCs)

A single SOFC unit consists of two electrodes (a cathode and an anode) separated by an electrolyte as shown in Fig.1.1. Generally, the electrolytes are gas-tight pure oxide-ion conducting oxides [1, 3]. On the cathode side of the fuel cell, O₂ is reduced to oxide ion (O²⁻) that is transported through the electrolyte to the anode, where it reacts with the gaseous fuel (H₂, CH₄ etc.) releasing electrons and yielding heat and water as by-products. The electrolyte conducts these oxide ions between electrodes, maintaining overall electrical charge balance. The flow of electrons in the external circuit gives useful power (Fig.1.1).

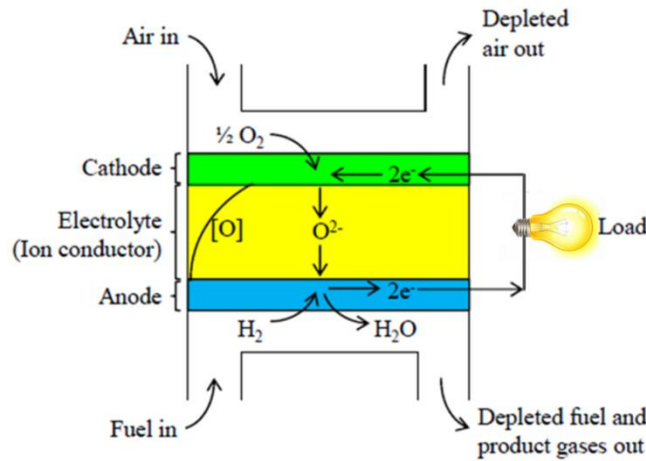


Figure 1.1. Schematic diagram of Solid Oxide fuel cell (SOFC).

Since oxide ion is transported from higher oxygen concentration side ($P_{O_2}^{high}$) i.e. cathode to lower oxygen concentration side ($P_{O_2}^{low}$) i.e. anode, SOFC can be considered as an oxygen concentration cell that generates an electromotive force (emf) given by Nernst equation,

$$E_{emf} = \frac{RT}{4F} \ln \left[\frac{P_{O_2}^{high}}{P_{O_2}^{low}} \right] \quad (1.1)$$

where E_{emf} is the reversible voltage that can be achieved by an SOFC under open circuit voltage (OCV) condition. OCV defines the voltage obtained in open circuit condition or without current flow. R is gas constant (8.314 J/mol.K), T is temperature and F is Faraday constant (9.65×10^4 C/mol).

The measured voltage E of an operating cell is always lower than E_{emf} . This is due to as the current is drawn from the cell (**Fig.1.2**), the cell voltage falls due to internal resistance and various polarisation losses. The voltage of an operating cell can approximately be expressed as,

$$E = E_{emf} - IR_i - \eta_{act} - \eta_{conc} \quad (1.2)$$

where IR_i is the ohmic loss, I is cell current, R_i is internal resistance. η_{act} and η_{conc} are the activation and concentration losses of anode and cathode.

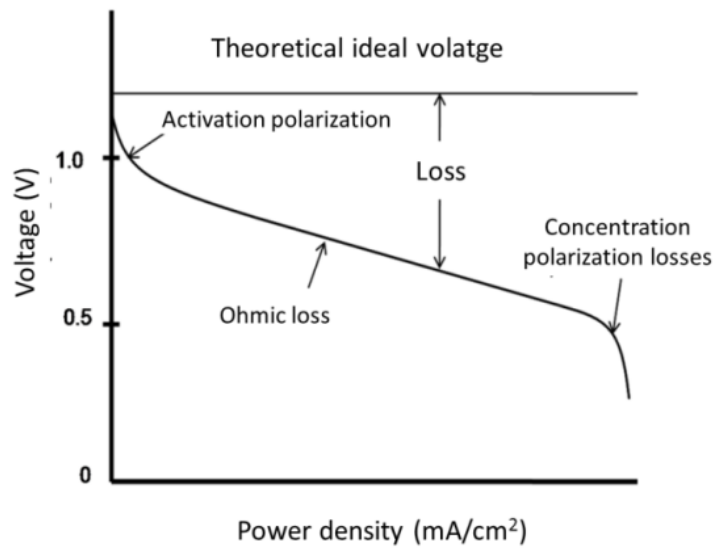


Figure 1.2. Ideal and measured current –voltage (IR) curve for an SOFC with corresponding polarization losses dominant in each region (activation polarization (η_{act}), ohmic polarization (IR_i) and concentration polarization (η_{conc})).

Fig.1.2 shows the measured voltage in SOFC is not same as the theoretical voltage due to various polarization losses associated with different components of fuel cell. Ohmic loss is associated with the resistance of electrolyte and other cell components. Activation loss is mainly caused by the slowness of the reaction on the electrode surface. Concentration loss mainly comes from the change in the concentration of reactant as the fuel is used.

1.1.2 Disadvantages of high-temperature SOFC operation (800-1000°C)

The major technical issue behind the development and commercialization of SOFC technology is its high-operation temperature (800-1000°C). It consists of various drawbacks like thermal stresses between SOFC components, longer start-up times, degradation problems and chemical instability between electrode and electrolytes

which affect the life-time and efficiency of SOFC [6, 7]. Therefore, significant effort has been put in the last decades to lower the operation temperature of these devices giving rise to the intermediate-temperature SOFC (IT-SOFC) which operate at 500-750°C.

However, decreasing the operation-temperature of SOFC is not an easy task as it consists of lot of challenges embedded in SOFC components and electrochemical activity that have to be resolved. Mainly, the ionic-conductivity of electrolyte and the electrode activity decrease rapidly with decreasing the operation temperature. In particular, reducing the temperature increases ohmic losses resulting from the ionic transport of the electrolyte.

The possible solutions for SOFC temperature reduction are **a)** reducing electrolyte thickness **b)** using (exploring) electrolyte materials with excellent ionic-conductivity in the intermediate-temperature of operation **c)** exploring new active electrode materials or improving the existing ones [6, 7].

1.1.3 Miniaturization of SOFC

In the past decades, the majority of the SOFC research and applications has been conducted in the form of bulk ceramics for large amount of power generation. Conventional SOFCs are used for stationary power generation in kilowatt to megawatt range due to high-temperature operation 800-1000°C [1].

In recent years, there is an increasing interest towards the miniaturization of SOFC by implementing thin film components. There are some technological objectives behind the increasing trend towards the scaling-down of SOFC. One of the objectives is the temperature reduction of SOFCs from high-temperature to intermediate-temperature [8] already discussed in the last **section 1.1.2**. The second driving force is the development of micro-SOFC (μ -SOFC) with thin film SOFC components for the power generation in portable electronic devices such as laptop, mobile phones, digital cameras etc., in the range of milliwatt to several watts [8, 9].

Today's increasing demand on modern portable consumer electronics and integration of various features (MEMS - Micro Electro Mechanical Systems) into a single device will increase the energy requirements to a level that cannot be sustained by current Li-ion batteries [9]. On this scenario, SOFCs can fulfil the energy demand for portable electronics as it is expected to produce energy densities per volume three to four times larger than Li-ion, Ni metal hydride batteries and PEMFC [8-10]. Therefore, fuel cell miniaturization will lead to the commercialization of SOFC.

The SOFC component studied in this thesis are cathodes in thin film form for intermediate-temperature SOFCs, operating in the temperature range from 500°C to 750°C. The oxygen reduction reaction (ORR) mechanism taking place in the cathodes are studied in thin films and new strategies to obtain enhanced performance at intermediate-temperature is given in this thesis. The cathodes materials studied in this thesis are well-known compounds which are perovskite-related oxides explained in the following sections.

1.2 Perovskite-type oxides as cathodes in SOFC

Perovskite is a general term used to define certain structural family of compounds which have the same type of crystal structure as CaTiO_3 . The general formula of a perovskite is ABO_3 and its ideal cubic structure is given in **Fig.1.3**.

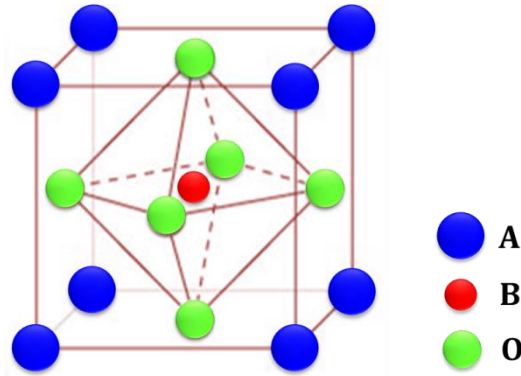


Figure 1.3. Structure of ideal cubic perovskite ABO_3 .

In ABO_3 cubic structure (**Fig.1.3**) A-cations are located in the corner of the unit cell. O^{2-} ions are located in the face-centered positions and B-cation occupies the center of the cube. Besides, B-site cations are surrounded by six oxygen ions forming BO_6 octahedral structure [7, 11].

The stability of perovskite structure depends on the radii of constituent ions in the perovskite structure. Goldschmidt [7, 11] defined the tolerance limit for perovskite structure which can be given as,

$$t = \frac{r_A + r_O}{\sqrt{2}(r_B + r_O)} \quad (1.3)$$

Where t is tolerance factor. r_A , r_B and r_O are ionic radii of A, B and oxygen ions respectively. The perovskite structure is preserved if t is in between 0.8 and 1. The

value of t is 1 for an ideal perovskite structure. As t decreases from 1, the cubic structure deforms to lower symmetry orthorhombic and rhombohedral structures, which are commonly found distortions in perovskites. If $t > 1$ calcite and aragonite structures are preserved while if $t < 0.8$ ilmenite structure is stabilized. A perovskite structure can accommodate number of different cations with +1 to +5 valence states and ionic sizes of 0.45 to 0.75 Å [7, 11].

Most cathode materials used in SOFC are perovskite oxides that exhibit significant oxygen ionic and electronic conductivity (MIEC – Mixed Ionic Electronic conductors) at elevated temperatures, which is suitable for oxygen reduction. The electrical conductivity is desirable for the extraction of current. The functional properties of such MIEC cathodes can be tuned by aliovalent substitution in A and B-sites. The doping can alter the ionic and electronic conductivities of MIEC by formation of oxygen vacancies (\dot{V}_o) and electronic defects such as holes and electrons that can influence the electrochemical activity of the cathode [7, 11].

In this thesis, the perovskite-type oxides $\text{La}_{0.8}\text{Sr}_{0.2}\text{MnO}_{3+\delta}$ (LSM), $\text{La}_{0.8}\text{Sr}_{0.2}\text{CoO}_{3-\delta}$ (LSC) and $\text{La}_{0.8}\text{Sr}_{0.2}\text{Mn}_{1-x}\text{Co}_x\text{O}_{3+\delta}$ (LSMC) are studied in thin film form. In LSMC, the intermediate compositions of a solid solution system attained from LSM and LSC are studied. In which pure LSM and LSC are well-studied and traditional cathode materials with unique electrochemical properties. In the following sections, some general properties of LSM and LSC such as structural, defect chemistry, electrical and oxygen ion transport properties are explained.

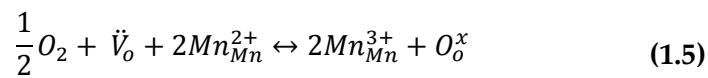
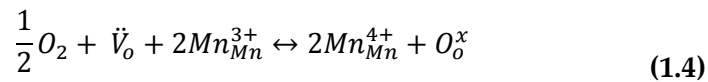
1.2.1 $\text{La}_{0.8}\text{Sr}_{0.2}\text{MnO}_{3+\delta}$: Structural, defect chemistry and electrical properties

LSM are oxygen-excess perovskites which are commonly used as cathodes for high-temperature operating SOFC (800°C-1000°C). LSM presents high chemical compatibility with electrolytes like Ytria-stabilized Zirconia (YSZ) at its operating conditions. But LSM react with YSZ at high-temperature forming secondary phases such as $\text{La}_2\text{Zr}_2\text{O}_7$ and SrZrO_3 [1]. Another advantage for the traditional choice of LSM is its mechanical compatibility with the typically used electrolyte Ytria-stabilized Zirconia (YSZ). The Thermal expansion coefficient (TEC) of LSM is $\sim 10.08 \times 10^{-6} \text{K}^{-1}$ [12] while 8YSZ is $\sim 10.05 \times 10^{-6} \text{K}^{-1}$ at 900°C [13].

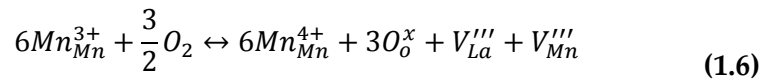
Basically, LaMnO_3 without Sr exist in orthorhombic structure at room temperature. It shows an orthorhombic to rhombohedral transition at $\sim 600^\circ\text{C}$. LaMnO_3 with Sr exist in three different phases depending upon Sr content. $\text{La}_{1-x}\text{Sr}_x\text{MnO}_{3+\delta}$ exists in

rhombohedral structure when $0 \leq x \leq 0.5$, tetragonal at $x = 0.5$ and cubic at $x \leq 0.7$ [14].

Regarding oxygen non-stoichiometry (δ) of LSM, δ is zero under intermediate partial pressure of oxygen (P_{O_2}) ranging between 10^{-5} and 1 Pa. On the other hand, LSM is oxygen-deficient at very low $P_{O_2} < 10^{-5}$ Pa, where oxygen vacancies \check{V}_o are compensated by reduction of Mn^{4+} ions to Mn^{3+} and Mn^{2+} [14] which can be expressed with the following equation,



At high oxygen partial pressure, LSM shows oxygen-excess stoichiometry (≥ 1 Pa) which is compensated by oxidation of Mn and formation of cation vacancies which can be given as,



Hence, oxygen vacancies are the major defects at low P_{O_2} while holes and cation vacancies are major defects at high P_{O_2} . Fig.1.4 depicts oxygen non-stoichiometry trend in LSM under different ranges of P_{O_2} at different temperature in which the maximum oxygen content in LSM at 873K is ~ 3.06 .

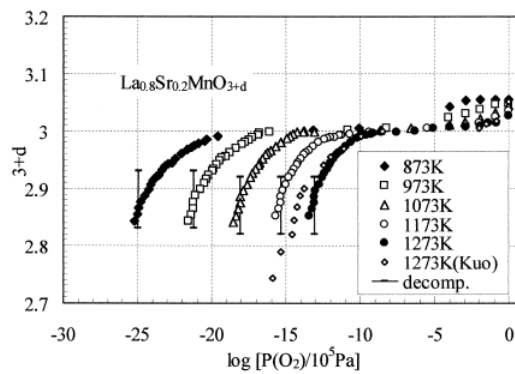
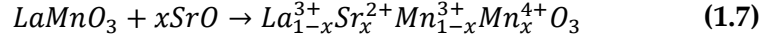


Figure 1.4. Oxygen non-stoichiometry of $La_{0.8}Sr_{0.2}MnO_{3+\delta}$ perovskite is plotted against P_{O_2} [15].

Regarding electrical properties, LSM is a p-type conductor [12] and the conductivity is proportional to Sr concentration. When trivalent La^{3+} ions are replaced by divalent

Sr²⁺ ions, holes are created in the B-site by oxidation of Mn ions to compensate the charge neutrality leading to increased conductivity [14, 16] which can be given as,



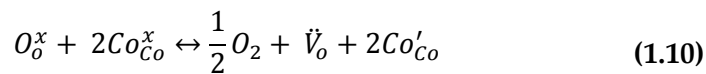
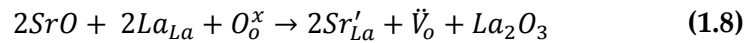
The electrical conductivity of LSM also depends upon PO₂. Generally, the conductivity of LSM decreases under reducing condition (PO₂ < 1 to 10⁻⁵ Pa) due to the formation of \dot{V}_o and reduction of Mn ion that will reduce the hole concentration. In the oxygen excess region PO₂ > 1 Pa it shows a constant conductivity [15].

1.2.2 La_{0.8}Sr_{0.2}CoO_{3-δ}: Structural, defect chemistry and electrical properties

LSC are oxygen-deficient perovskites, it has high catalytic activity towards ORR at intermediate-temperature itself, due to the large concentration of oxygen vacancies. It is a good mixed ionic and electronic conductor, but the chemical and thermal compatibility of LSC with YSZ is lesser than LSM. For example LSC reacts with YSZ at ~900°C forming Co₃O₄, SrZrO₃, La₂Zr₂O₇ [17, 18]. The TEC of LSC is ~21.54 × 10⁻⁶ K⁻¹ [12] and 8YSZ is ~10.05 × 10⁻⁶ K⁻¹ at 900°C shows high thermal mismatch between LSC and YSZ.

La_{1-x}Sr_xCoO_{3-δ} (x ≤ 0.5) exists in rhombohedral structure when 0 ≤ x ≤ 0.5, orthorhombic when x > 0.5.

In LSC, when a higher-valence La³⁺ ion is substituted by lower-valence Sr²⁺ ion electroneutrality will be attained in two ways, either by the formation of oxygen vacancies (\dot{V}_o) or holes [12, 19]. In general both processes occur and compete each other depending upon composition, T and PO₂. The defect chemistry of LSC can be given as following equations,



The above **equation 1.8** represents aliovalent doping of La³⁺ by Sr²⁺ and the formation of oxygen vacancies. **Equation 1.9** is charge the disproportionation of Co ions in

LSC which lead to p and n-type carriers. In **equation 1.10** the oxygen vacancy formation in LSC is compensated by n-type charge carriers [19].

Regarding oxygen non-stoichiometry, at high PO_2 , oxidation of LSC is compensated by holes. At low PO_2 ($< 10^2$ Pa) oxygen vacancies become predominant defects attained by the reduction of Co ions **Fig.1.5**.

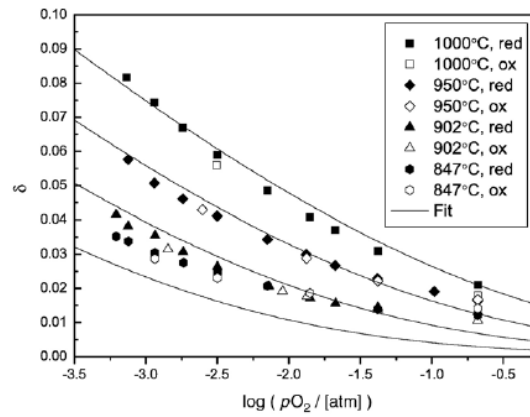


Figure 1.5. Non-stoichiometry in $La_{0.8}Sr_{0.2}CoO_{3-\delta}$ perovskite over PO_2 under different temperature [20].

LSC is a p-type electrical conductor in which conductivity occurs by thermally activated hopping of p-type charge carriers and the conductivity increases over Sr content [19, 20].

1.2.3 Oxygen transport properties of LSM and LSC

The incorporation of oxygen on the cathode/gas surface and oxygen ion conduction in cathode bulk are the rate-limiting factors of oxygen reduction reaction (ORR) in cathode. These factors are defined by D^* and k^* which are the decisive parameters of the performance of mixed conducting cathode materials. where D^* is oxygen self-diffusion coefficient, k^* is oxygen self-exchange coefficient can be determined from oxygen tracer measurement (for a description of this technique, see **chapter 2 section 2.5.2**).

In **Fig1.6a** and **1.6b**, the D^* and k^* values of pure LSM and LSC are compared with similar materials found in the literature [21, 22] exhibiting different amount of Sr content in the A-site, Co and Mn content in the B-site.

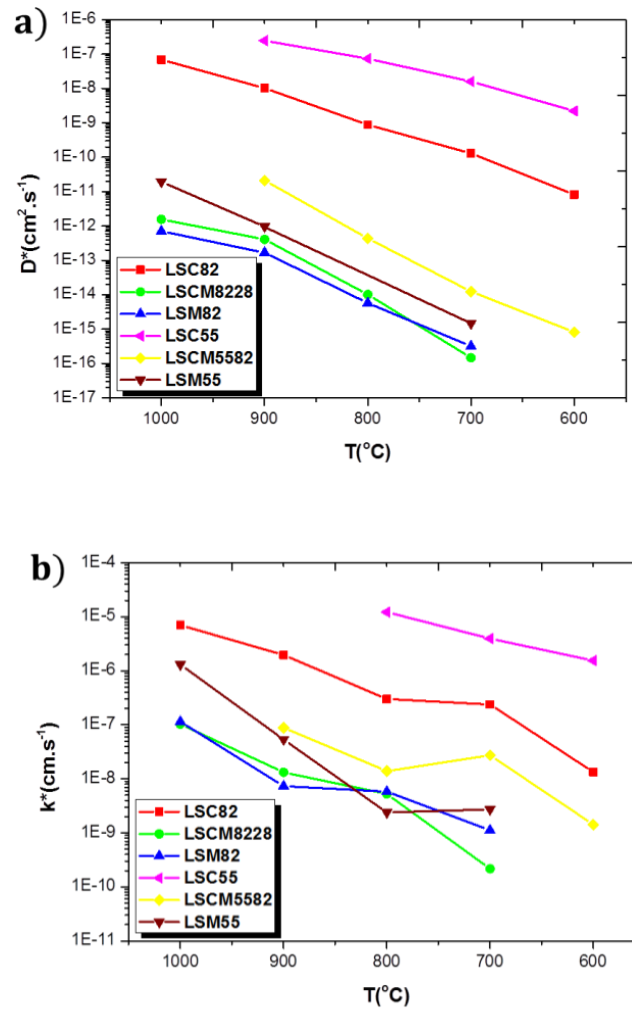


Figure 1.6. a) Oxygen self-diffusion coefficient D^* and b) Oxygen self-exchange coefficient k^* of LSM82 and LSC82 is plotted against temperature. They are compared with similar materials given in the literature [21, 22]. LSC82- $\text{La}_{0.8}\text{Sr}_{0.2}\text{CoO}_3$, LSCM8228- $\text{La}_{0.8}\text{Sr}_{0.2}\text{Co}_{0.2}\text{Mn}_{0.8}\text{O}_3$, LSM82- $\text{La}_{0.8}\text{Sr}_{0.2}\text{MnO}_3$, LSC55- $\text{La}_{0.5}\text{Sr}_{0.5}\text{CoO}_3$, LSCM5582- $\text{La}_{0.5}\text{Sr}_{0.5}\text{Co}_{0.8}\text{Mn}_{0.2}\text{O}_3$, LSM55- $\text{La}_{0.5}\text{Sr}_{0.5}\text{MnO}_3$.

Fig.1.6 a and b illustrates that there is a dramatic difference between D^* and k^* values of Mn and Co rich materials. This difference is highly pronounced in oxygen-diffusion coefficients than in oxygen-exchange coefficients. The D^* values of LSM-82 and Mn rich compositions such as LSCM-8228, LSM-55 and LSCM-5582 are ~4 to 5 times lower than pure Co materials LSC-82 and LSC-55 with different amount of Sr concentration. Similarly, k^* values of Mn rich compounds are ~1 to 2 orders of magnitude lower than the corresponding to pure Co compounds.

This is due to LSM oxygen-excess stoichiometry and has poor oxygen vacancy concentration (**section 1.2.1**), which is responsible for the lower oxygen-diffusivity and

exchange coefficients of Mn rich materials. On the other hand, pure LSC has oxygen-deficient stoichiometry and the presence of high concentration of oxygen vacancies (section 1.2.2) enhances the oxygen transport properties of pure Co materials.

1.3 Enhancing oxygen ion transport in thin film cathodes using nanostructured films

While the ohmic losses in electrolytes are largely understood today, the physics governing overpotential losses of cathodes is not yet clearly understood due to the geometrical constraints offered by porous electrodes. Further, cathode causes major polarization losses in IT-SOFC which affect the fuel cell performance [23]. Therefore, understanding ORR kinetics is crucial to enhance/tune the functionality of cathodes to improve the device performance. ORR kinetics can be understood well in dense thin film cathodes and its functionality can be enhanced by implementing nanoionics concepts [8, 24, 25, 26]. Further, thin film technology can offer a useful tool for the study of oxygen transport in cathodes.

1.3.1 Thin film cathodes Vs thicker cathodes

ORR reaction in a MIEC cathode takes place by several steps such as oxygen gas diffusion ($\text{O}_{2(\text{g})}$), adsorption (O_2^{ad}), dissociation and ionization ($\text{O}_{\text{ad}}^{2-}$) on the electrode surface and oxygen ion incorporation ($\text{O}_{2(\text{g})} + 2V_o + 4e^- \leftrightarrow 2\text{O}_o^{2-}$) into cathode as a final step. These steps are collectively called as oxygen exchange process [27, 28]. After incorporation, oxygen ion diffusion occurs in the cathode bulk. If the cathode is a pure electronic conductor ORR is confined in Triple-phase boundary (TPB).

ORR steps in porous and dense cathodes are depicted in the following figure (Fig.1.8).

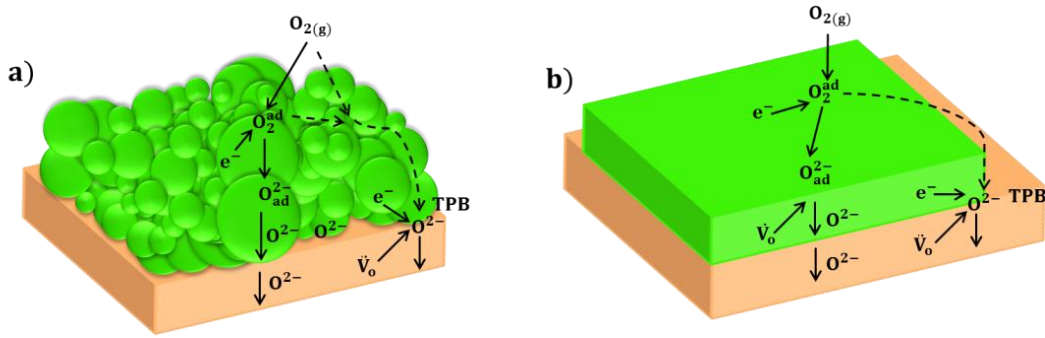


Figure 1.7. Illustration of oxygen reduction reaction (ORR) steps in **a)** porous electrode **b)** thin film dense electrode. TPB is Triple-phase boundary. If the electrode is a pure electronic conductor ORR takes place in TPB. If the electrode is made by MIEC, then ORR will be extended into cathodes.

In the last decades cathode materials were prepared by conventional ceramic processing routes (eg. tape casting, screen printing) resulting in 20 to 100 μ m thickness with porous microstructure. Even after spending a couple of decades in understanding ORR mechanism in porous cathodes, still a general conclusion is not yet attained on which of the possible kinetic steps limits the cathode performance. This is due to ill-defined, complex morphology and microstructure (**Fig.1.7**) offered by porous microstructures that cannot be measured and reproduced [29]. It makes difficult to relate intrinsic properties of cathode with the electrode geometry and microstructure.

Hence, dense thin film cathodes can be the best alternative to overcome the complexities emerging from porous cathodes. Typically, the geometry and morphology offered by thin film cathodes are simple (**Fig.1.7**), providing simple architectures where intrinsic properties can be directly correlated to the electrode geometrical parameters and microstructure [19]. Further, the geometry and microstructure of thin films can be precisely controlled and reproduced by controlling the deposition conditions by means of thin film vacuum deposition techniques [27].

Oxygen surface exchange process and oxygen bulk diffusion are the two main rate-limiting steps in ORR (**Fig.1.7**). These rate-limiting steps can be controlled by the thin film thickness. The so-called “critical thickness” (L_c) indicates whether oxygen exchange or diffusion to be rate-limiting [19, 28]. It can be given as,

$$L_c = \frac{D}{k} \quad (1.11)$$

Where D is oxygen diffusion coefficient and k is oxygen surface exchange coefficients.

If the electrode thickness is below the critical thickness ($L < L_c$) ORR will be limited by the oxygen exchange process. If it is above the critical thickness ($L > L_c$) it will be limited by the oxygen diffusion in the cathode bulk. The typical value of L_c for most perovskite materials presents values in between 1 nm to 150 μ m which depends on temperature and PO₂ [30].

1.3.2 Nanoionics effect in thin film cathodes

Nanoionics is the study of ionic charge transport in ion-conducting solids in nano-regime (less than 100nm) [27]. Nanoionics effect in which the behavior of electronic and ionic transport in nanoscale is totally different than bulk, which is highly pronounced in hetero-interface and grain boundaries. when study the conductivity in the nanoscale, the influence of defects, space charge layers at grain boundaries and its surface etc. is more visible than when studying the systems at the macro-scale.

It has been reported that in most cases, hetero-interfaces and space-charge layers are responsible for fast ionic transport [31-34]. Usually ionic transport parallel to the interface is enhanced compared to the transport perpendicular to the interface. The typical grain size of thin film cathodes processed at low temperature is in the nanometer scale at which nanoionics effects are dominant and can be examined [31-34]. Unlike charge transport in bulk, the charge and mass transport in ionic materials along interfaces and its dependency on interfacial structure are less understood [33, 35]. The interface modification in favour of ionic conduction is one of the main challenge in nanoionics [33]. Measuring, understanding and predicting ionic behavior over size variation is technically challenging [33]. Hence, research on nanoionics is a relatively new field of study.

A short introduction to such space-charge zone and grain boundary is given below.

Space charge layer is the region adjacent to the boundaries where charged species and defects tend to accumulate/segregate to lower the strain and electrostatic energies of the system which are compensated by the formation of opposite charges in the boundary of adjacent grain. The graphical representation of space-charge region is given in **Fig.1.8**. This region acts as a transition zone for two grains with different orientation or interface of two solid phases, therefore it has its own chemistry and defect chemistry [31-34].

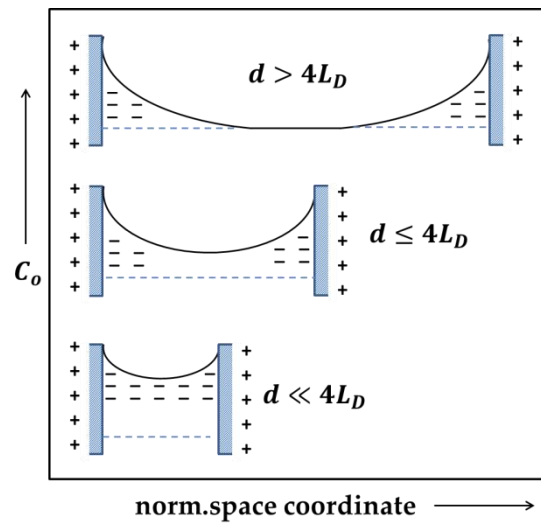


Figure 1.8. A qualitative description of space-charge zone. Defect profile C_o in space charge layer and grain bulk with different size which is plotted against space coordinate. The space charge layer has positive and negative charge carrier which is in interfacial core. Blue line (dotted) is background defect concentration. d is average grain size, L_D is space charge width [34].

Fig.1.8 shows the influence of grain size (average) d on the majority carrier concentration C_o in space charge layer and grain bulk. As grain size is reduced to equal to space charge width ($d \leq 4L_D$) the concentration of majority carrier in the grain center does not return to background value. If the grain size is further reduced, the overall conductivity can be enhanced due to high density of space charge layers. The space charge effect can be observed in single heterostructure (thin film/substrate) and multilayer heterostructures. As an example, *N. Sata et al.* [35] found a great enhancement in F^- ion conductivity of CaF_2/BaF_2 thin film heterostructures, showing that the conductivity increased with increasing periodicity. This is due to the fact that F^- ions in BaF_2 is transferred to neighboring CaF_2 layer, leaving F^- in BaF_2 and increasing charge carrier concentration in space charge layer.

Apart from space charge zone, sometimes grain boundary itself acts as fast conduction pathways for ionic transport **Fig1.9**. Space-charge do not exist when the charge carriers are highly mobile [36].

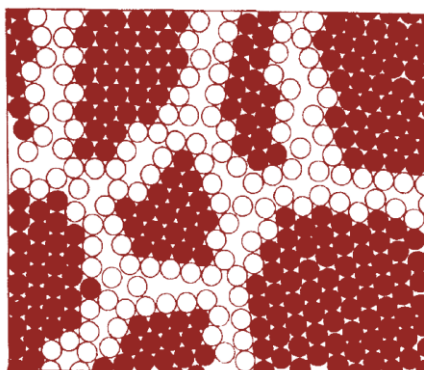


Figure 1.9. Illustration of Grains (dark-red circles) separated by grain boundary region (Open circles) taken from reference [33].

The presence of high defect densities and excess volume in the interface of adjacent grains can enhance ionic diffusion along grain boundaries. [34, 37].

1.3.3 LSM and LSC thin film cathodes

Some interesting works on LSM and LSC thin films found in the literature are organized in this section to emphasize the importance of thin film electrodes and the influence of nanoionics effect in ORR.

La O' et al. [38] studied oxygen exchange in 65nm thickness LSM electrodes in the temperature range 660-790°C, showing that k^q values are 1 to 2 orders of magnitude higher than LSM bulk. k^q is oxygen exchange coefficient obtained from electrical measurements.

The same authors further reported oriented epitaxial LSC thin film (20nm) exhibit 1-2 orders of magnitude higher k^* than bulk through EIS measurement [39]. *Kubicek et al.* [40] and *Ji et al.* [41] studied oxygen transport properties in LSC epitaxial thin films of 20nm, 60nm and 243nm thickness in the temperature range 280-475°C [40] and 550-650°C [41]. They reported an enhancement in D^* and k^* values due to lattice strain in the epitaxial film.

The surface decoration of LSC thin film is an emerging topic of research in recent days, in order to improve the surface exchange properties of LSC thin film. In most of the work, ((La, Sr)CoO_{3-δ})₁₁₃ perovskite thin films are decorated with islands of ((La, Sr)₂CoO_{4+δ})₂₁₄ layers a Ruddlesden-Popper phase (RP phase) [42-46], sometimes decorated with perovskite structures [47].

Epitaxial LSC thin films (~85nm) with partial LSM coverage (0.1 to 0.9nm) displayed an enhancement in k^q values 2 to 3 times higher than undecorated LSC film [47]. LSC film (~85nm) with partial $(\text{La}_{0.5}\text{Sr}_{0.5})_2\text{CoO}_{4\pm\delta}$ decoration (0.1 to 15nm) exhibited k^q values 3-4 orders of magnitude higher than LSC bulk [42]. Similarly, LSC film (~140nm) partial decoration of Sr (4 to 7.5nm) displayed 1-2 orders of magnitude of enhancement in k^q value due to the formation of $(\text{La, Sr})_2\text{CoO}_{4\pm\delta}$, an RP phase between LSC/Sr interface [43].

Lattice strain, increase in oxygen vacancy concentration, interfacial properties such as strain and space-charge effects are considered as responsible for an enhancement in ORR. In particular, a great enhancement in k^q obtained in the above works confirm that in the surface decorated LSC films, interface (LSC film/decorated layer) acts as active sites for fast oxygen exchange rate an impact of nanoionics effect.

1.4 Scope of the thesis

This thesis is devoted to investigate the oxygen ion transport in perovskite-related MIEC thin film cathodes (< 200nm thickness) exhibit well-defined nanostructure in order to correlate the nanostructure with oxygen transport properties.

Pulsed Laser Deposition (PLD) is intentionally used to fabricate thin films with high density of grain boundaries displaying vertically aligned grains with columnar microstructure and nanocrystalline grain size to observe fast ionic transport along grain boundaries.

This thesis is organized in the following way,

- **Chapter 2** compiles and briefly describes the experimental techniques used in the thesis. A detailed explanation of principles and operation of PLD is also included.
- **Chapter 3** is devoted to optimize the depositions conditions of thin film perovskite LSM, LSC and LSF in PLD. The deposition conditions optimized in chapter-3 is the basis for sample fabrication in the following chapters. Moreover, the possibility of attaining a new composition in thin film form from ultra-thin film multilayer deposition is presented.
- **Chapter 4** describes the oxygen ion transport studies carried out in LSM thin films.

The next following chapters are about the fabrication of a combinatorial pseudo-binary system and its functional studies.

- **Chapter 5** describes the fabrication of LSMC thin film pseudo-binary system and its microstructural characterizations. Further, a new methodology is introduced in this chapter to generate layers with a determinate composition and thickness distribution in the binary system.
- **Chapter 6** describes the oxygen transport studies carried out in the LSMC binary system.

Chapters 3 to 6 including appendixes is given as flowchart which is as follows,

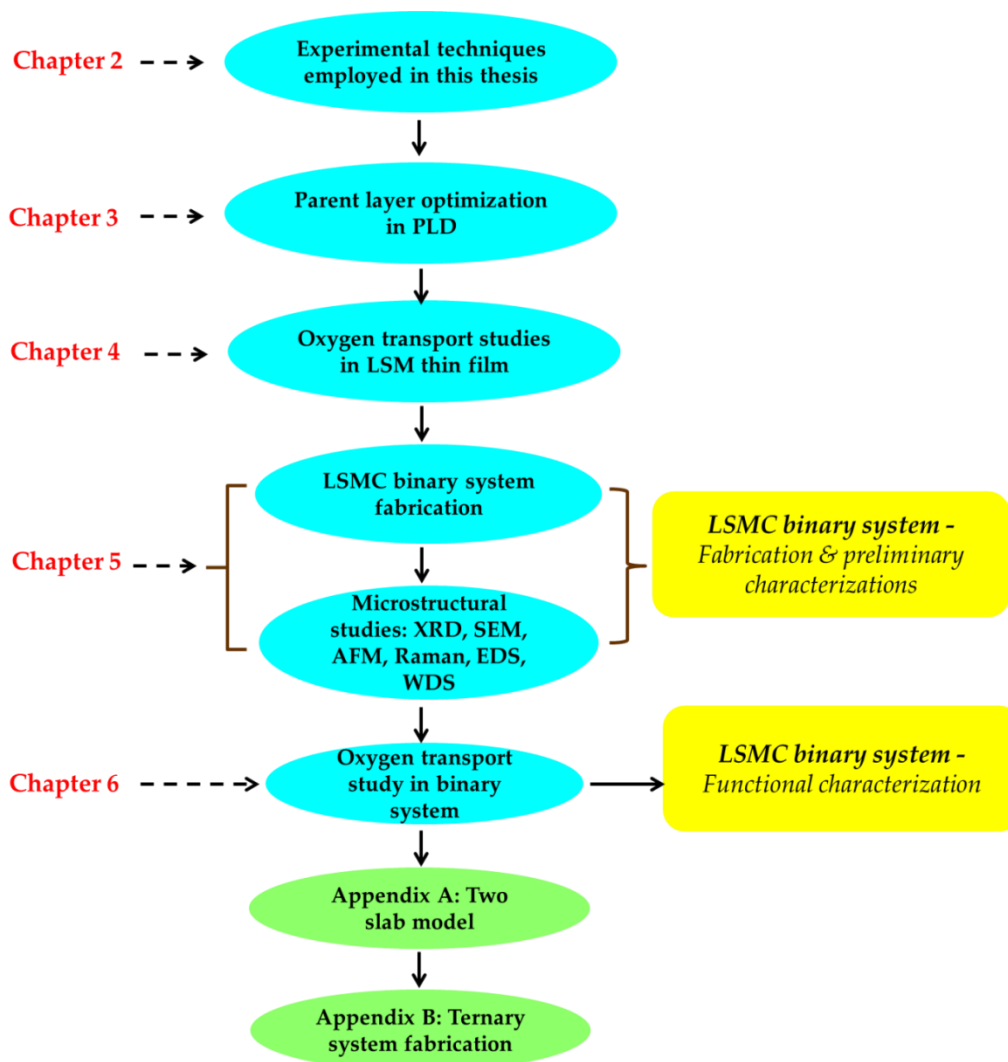


Figure 1.10. Flow-chart of the thesis chapters and Appendixes.

References

- [1] B. Viswanathan, M. A. Scibioh, *Fuel Cells: Principles and Applications*, Universities Press, India, 2006.
- [2] www.epa.gov/climatechange/basics/
- [3] R. M. Ormerod, *Chem. Soc. Rev.*, 2003, **32**, 17. Fuel cell review
- [4] A. Kirubakaran, R. Nema, *Renew. Sustainable Energy Rev.*, 2009, **13**, 2430. Types of fuel cells
- [5] D. J. L. Brett, A. Atkinson, N. P. Brandon, S. J. Skinner, *Chem. Soc. Rev.*, 2008, **37**, 1568.
- [6] A. T. Rubio, *Ph.D. Thesis*, University of Barcelona, July, 2007.
- [7] T. Ishihara, *Perovskite oxide for Solid Oxide Fuel Cells*, Springer, 2009.
- [8] E. Trvaersa, *The ECS Interface*, **18**, 2009, 49.
- [9] H. L. Tuller, S. J. Litzelman, W. Jung, *Phys. Chem. Chem. Phys.*, **11**, 2009, 3023.
- [10] A. Evans, A. B. Hutter, J. L. M. Rupp, L. J. Gauckler, *J. Power Sources.*, 2009, **194**, 119.
- [11] J. Sunarso, S. Baumann, J. M. Serra, W. A. Meulenber, S. Liu, Y. S. Lin, J. C. Diniz da Costa, *J. memb. Sci. Technol.*, 2008, **320**, 13.
- [12] R. V. Wandekar, B. N. Wani, S. R. Bharadwaj, *Solid State Sci.*, 2009, **11**, 240.
- [13] H. Hayashi, T. Saitou, N. Maruyama, H. Inaba, K. Kawamura, M. Mori, *Solid State Ionics*, 2005, **176**, 613.
- [14] S. P. Jiang, *J. Mater. Sci.*, 2008, **43**, 6799. Singapore
- [15] J. Mizusaki, N. Mori, H. Takai, Y. Yonemura, H. Minamiue, H. Tagawa, M. Dokiya, H. Inaba, K. Naraya, T. Sasamoto, T. Hashimoto, *Solid State Ionics*, 2000, **129**, 163.
- [16] E. O. Ahlgren, F. W. Poulsen, *Solid State Ionics*, 1996, **86**, 1173.
- [17] H. He, Y. Huang, J. Regal, M. Boaro, J. M. Vohs, R. J. Gorte, *J. Am. Ceram. Soc.*, 2004, **87**, 331.
- [18] S. P. Simner, J. P. Shelton, M. D. Anderson, J. W. Stevenson, *Solid State Ionics*, 2003, **161**, 11.
- [19] F. S. Baumann, *Ph.D. Thesis*, Max Planck Institute for Solid state Research, June, 2006.
- [20] M. Sogaard, P. V. Hendriksen, M. Mogensen, F. W. Poulsen, E. Skou, *Solid State Ionics*, 2006, **177**, 3285.
- [21] R. A. De Souza, J. A. Kilner, *Solid State Ionics*, 1998, **106**, 175.
- [22] R. A. De Souza, J. A. Kilner, *Solid State Ionics*, 1999, **126**, 153.
- [23] S. B. Adler, *Chem. Rev.*, 2004, **104**, 4791.
- [24] J. Maier, *Nat. Mater.*, 2005, **4**, 805.

-
- [25] J. Maier, *Solid State Ionics*, 2002, 154, 291.
- [26] J. Maier, *Solid State Ionics*, 2003, 157, 327.
- [27] S. J. Litzelman, J. L. Hertz, W. Jung, H. L. Tuller, *Fuel cells*, 8, 2008, 294.
- [28] R. A. De Souza, *Phys. Chem. Chem. Phys.*, 2006, 8, 890.
- [29] S. B. Adler, J. A. Lane, B. C. H. Steele, *J. Electrochem. Soc.*, 1996, 143, 3554.
- [30] L. M. Van der Haar, M. W. den Otter, M. Morskate, H. J. M. Bouwmeester, H. Verweij, *J. Electrochem. Soc.*, 2002, 149, J41.
- [31] J. Maier, *Phys. Chem. Chem. Phys.*, 2009, 11, 3011.
- [32] X. Guo, J. Maier, *Adv. Mater.*, 2009, 21, 2619.
- [33] S. Kim, *The ECS Interface*, 2006, 15(3), 28.
- [34] H. L. Tuller, *Solid State Ionics*, 2000, 131, 143.
- [35] N. Sata, K. Eberman, K. Eberl, J. Maier, *Nature*, 2000, **408**, 946.
- [36] C. Korte, N. Schichtel, D. Hesse, J. Janek, *Monatsh Chem.*, 2009, 140, 1069.
- [37] J. H. Shim, J. S. Park, T. P. Holme, K. Crabb, W. Lee, Y. B. Kim, X. Tian, T. M. Gur, F. B. Prinz, *Acta Materialia.*, 2012, 60, 1.
- [38] G. J. la O, Y. S. Horn, *J. Electrochem. Soc.*, 2009, 156(7), B816.
- [39] G. J. la O, S. J. Ahn, E. Crumlin, Y. Orikasa, M. D. Biegalski, H. M. Christen, Y. S. Horn, *Angew. Chem. Int. Ed.*, 2010, 49, 5344.
- [40] M. Kubicek, Z. Cai, W. Ma, B. Yildiz, H. Hutter, J. Fleig, *ACS Nano*, 2013, 74, 3276.
- [41] H. Ji, J. Hwang, K. J. Yoon, J. W. Son, B. K. Kim, H. W. Lee, J. H. Lee, *Energy Environ. Sci.*, 2013, 6, 116.
- [42] E. J. Crumlin, E. Mutoro, S. J. Ahn, G. J. la O', D. N. Leonard, A. Borisevich, M. D. Biegalski, H. M. Christen, Y. S. Horn, *J. Phys. Chem. Lett.*, 2010, 1, 3149.
- [43] E. Mutoro, E. J. Crumlin, M. D. Biegalski, H. M. Christen, Y. S. Horn, *Energy Environ. Sci.*, 2011, 4, 3689.
- [44] D. Lee, Y. L. Lee, W. T. Hong, M. D. Biegalski, D. Morgan, Y. S. Horn, *J. Mater. Chem. A*, 2015, 3, 2144.
- [45] M. Sase, K. Yashiro, K. Sato, J. Mizusaki, T. Kawada, N. Sakai, K. Yamaji, T. Horita, H. Yokokawa, *Solid State Ionics*, 2008, 178, 1843.
- [46] E. J. Crumlin, S. J. Ahn, D. Lee, E. Mutoro, M. D. Biegalski, H. M. Christen, Y. S. Horn, *J. Electrochem. Soc.*, 2012, 159, F219.
- [47] D. Lee, Y. L. Lee, A. Grimaud, W. T. Hong, M. D. Biegalski, D. Morgan, Y. S. Horn, *J. Phys. Chem. C*, 2014, 118, 14326.

Chapter 2

Experimental methods

Chapter II

2.1 Chapter outline

The **aim of this chapter** is to give a general overview of the experimental methods and tools employed in this thesis to carry out experiments, emphasizing its place of application in the following chapters. The work developed in this thesis can be simply divided into two categories: (i) Thin film fabrication techniques (ii) characterization techniques. The sample fabrication methods adopted in this thesis is explained in **section 2.2**. The equipments used for the thin film microstructural studies are presented in **section 2.3** and the techniques used to study the sample functionality are described in **section 2.4**.

2.2 Thin film fabrication techniques

The whole thesis is based upon the samples in thin film form, thickness within the 250nm to 40nm range. There are various deposition techniques are available to fabricate oxide thin films. Existing physical and chemical deposition techniques such as thermal evaporation, sputtering, PLD, spray pyrolysis, Atomic layer deposition (ALD), Chemical vapor deposition (CVD) or metal organic chemical vapor deposition (MOCVD) are commonly used for thin film technology [1-5]. Preserving stoichiometry in thin films is one of the main challenges in these deposition techniques [1-5].

In this thesis, Pulsed laser deposition (PLD) is used as a tool to fabricate MIEC thin film cathodes and electrolytes. PLD is a physical vapor deposition (PVD) technique where a high power laser pulses are focused on a target to melt, vaporize and ionize the material from the target surface. The ablated material from the target generates a highly energetic plasma that will be collected on a substrate upon which it condenses form a thin film (**Figure 2.1**).

The advantage of PLD is its stoichiometric material transfer which preserves the thin film composition [6]. Inside the PLD chamber, only the target material is ablated that avoids contamination issues. Congruent evaporation with excellent stoichiometry control, microstructure control, low thin film processing temperature and the possibility of attaining high quality films with high dense layers are the most attractive features underneath the employment of this technique in this thesis. The disadvantages of PLD are particulate ejection, small area deposition that lead to a thin film with

inhomogeneous thickness and substrate surface modification due to ion impingement and implantation on the substrate.

The basic principle and the different versions of PLD equipment available are compiled in **section 2.2.1, 2.2.2 and 2.2.3.**

2.2.1 Pulsed laser deposition

Pulsed laser Deposition (PLD) is a material processing technique for growing thin films of wide variety of materials. The usage of lasers to deposit thin films by laser ablation was started in the 1960s, after the invention of the Ruby laser. However, this technique did not draw much attention for two decades, until it was applied for growing high temperature superconducting (HTS) thin films.

When most of the conventional growth techniques like sputtering, e-beam evaporation failed for this application, PLD was invented by Dr. Venkatesan in 1987, leader of Surface group at Bell labs, USA [7, 8]. They had successfully grown first $\text{YBa}_2\text{Cu}_3\text{O}_{7-x}$ (YBCO) thin film, a High Temperature T_c Superconductor (HTS) on carbon foil using pulsed Nd-YAG laser [7, 8].

After his discovery, the importance of the PLD was realized worldwide, followed by subsequent development in laser technology that led PLD technique to attain a rapid growth in thin film technology. In material science the application of PLD is nowadays frequent. It is applied to make ceramic films, hard coatings with diamond based films, exotic alloys, multi-component films, multilayer films like superlattice structures or heterostructure (p-n junctions) [1-5]. The schematic diagram of PLD deposition is given in **Figure 2.1.**

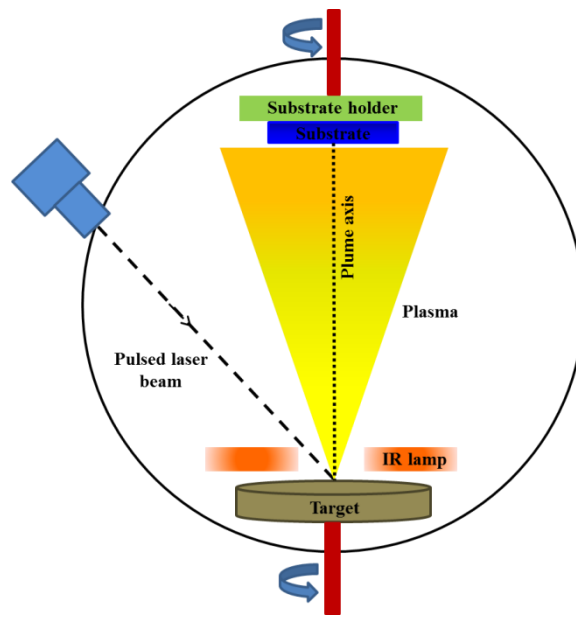


Figure 2.1. illustration of laser ablation of a target inside PLD chamber.

The principle of PLD is simple. When a laser pulse is irradiated onto the surface of a solid target in a vacuum chamber, a small amount of material is ionized from the surface and ejected away from the target. The laser-induced plasma expands adiabatically making it highly-forward directional. The plasma goes toward the substrate, where it is cooled down to form a thin film.

Basically, in PLD the deposition of a thin film is taken place by three steps which are a) Laser-target interaction b) Plume expansion dynamics c) Thin film deposition [3-6]. Each step depends on the type of material, the deposition condition used to control the film growth.

2.2.1.1 Laser-Target interaction

During laser-target interaction the material is removed from the target surface by several processes. There are thermal, electronic contributions involved during laser-target interaction and their relative importance depends on the target material type, laser excitation wavelength and pulse width.

When the laser is irradiated on a target, the photon absorption by target surface causes surface heating. The surface temperature of the target can easily exceed the melting point of ceramics ($\sim 1500^{\circ}\text{C}$) that can evaporate the molten surface. Normally, target surface temperature depends on optical absorption property and thermal conductivity of the material as well as the repetition rate of laser [4, 5].

Electronic contributions generally dominate when a material is irradiated with ultrashort-laser pulses like femtosecond (fs) laser. Continuous irradiation using ultrashort laser pulse can rapidly excite electron that can rise the electron temperature through electron-electron coupling. Consequently, target lattice is heated up with a rate proportional to electron-phonon coupling strength, eventually target is vaporized [4, 5].

Thermal contributions generally dominate when a material is irradiated with long-laser pulses like nanosecond (ns), picosecond (ps) lasers. This long duration laser pulse has enough time that allows a photon to propagate into target material, thereby interacts with electrons and vibrational modes of lattice simultaneously, make the melting and evaporation of the target material.

During congruent evaporation all chemical species are detached away from the target at the same time, which ensures stoichiometric material transfer from the target [4, 5].

Laser ablation of the material is only possible if the laser energy density is above a certain threshold energy density. The threshold energy density is required to create the plasma, which mainly depends on the optical absorption property of the target material and the laser excitation wavelength [3, 9].

2.2.1.2 Plume expansion dynamics

Continuous exposure to laser lead to plasma expansion. In the early stages of expansion, the plasma close to the target surface possesses anisotropic expansion of velocity distribution, directed away from the target surface. Later, collision among the ablated species changes anisotropic to isotropic expansion of velocities. Therefore the region close to the target surface is called as the Knudsen layer where the laser energy is absorbed by plasma [5, 9, 10].

In the first few mm of expansion, Bremsstrahlung emission from atoms, ions and emission from multiple charged ions are normally observed. The above emissions are no longer observed after certain mm of expansion.

Under the background gas, plasma pushes the gas ahead which gives a sharp shape to the plume front. The collision of particles with background gas can alter the original trajectory of plasma and widen the angular distribution. The expanding plasma is highly-forward directional, in which direction the density is distributed exponentially and velocity is maximum (10^6 cm/s) [5].

The angular distribution of plasma consists of two distinct cosine components **Figure 2.2a**. One of the components is a stoichiometric highly forward-directed component, with $\cos^n\theta$ dependence ($9 < n < 12$) and θ is measured with respect to the target normal (**Figure 2.2a**). The other component is a non-stoichiometric and arises due to the thermal evaporation of the target, located $\geq 20^\circ$ (**Figure 2.2b**) on either side of the plume front [7, 10]. Thermal component is considered to evolve from the deeper part of the target, where the energy density is below the threshold value lead to a non-stoichiometric thermal evaporation of materials [7, 10].

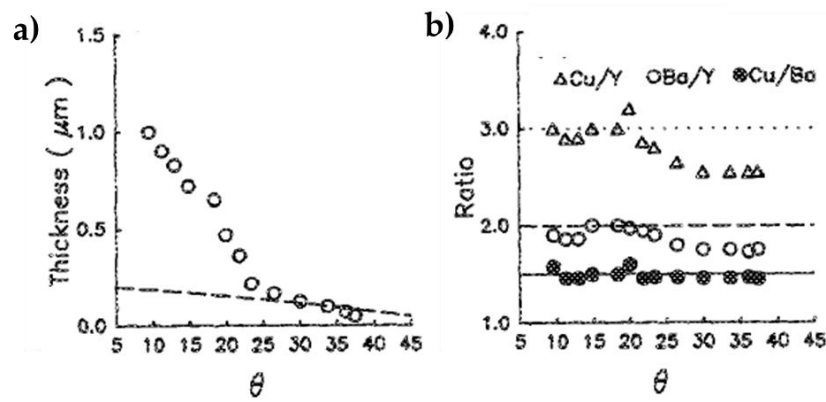


Figure 2.2. Angular distribution of YBCO film a) Thickness (dashed line is $\cos\theta$ fit) b) Composition. The diagram is taken from ref [10].

2.2.1.3 Thin film deposition

In thin film deposition, the way of nucleation determines the structure and morphology of the films. Under certain circumstances, deposition conditions such as substrate temperature, pressure can affect the thin film microstructure, composition and properties. Typically, the thin film growth process can be explained by any one of the following three conventional growth modes (**Figure 2.3**) [3, 11, 12].

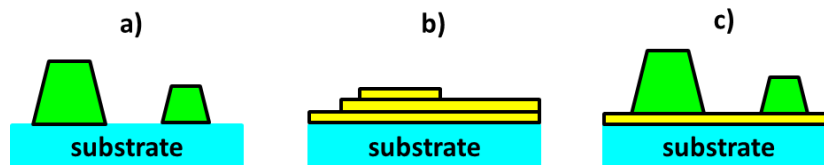


Figure 2.3. Illustration of three basic growth modes of thin film growth. a) Volmer-Weber mode b) Frank-van der Merwe mode c) Stranski-Krastanov mode.

i) Volmer-Weber mode is a three-dimensional island growth mode. It dominates when both the thin film and substrate are dissimilar materials with different crystal structure. During this growth mode the surface adatoms are strongly coupled to each other and more than with the substrate leading to polycrystalline thin films (**Figure 2.3a**).

ii) Frank-van der Merwe involves layer-by-layer 2-dimensional growth mode, where film growth is promoted by strong film-substrate bonding leading to the highest crystalline quality epitaxial films (**Figure 2.3b**).

iii) Stranski-Krastanov is a mixed growth mode in which initially the film growth is promoted by layer-by-layer growth for one to five monolayers then the growth way turn to three-dimensional island growth due to a change in the energetics of the underneath monolayers (**Figure 2.3c**).

The selection of growth modes by a substrate-thin film system depends on the thermodynamics of film-substrate surface energies and film-substrate interface energy.

2.2.2 Large Area Pulsed laser deposition (LAPLD)

Although PLD has several advantages in material processing, the deposition on small substrate area of size $1 \times 1\text{cm}^2$ restricts the implementation of PLD at the industrial level. After the first successful growth of YBCO thin film in 1986, the scale-up in PLD technology was accelerated leading to a large area pulsed laser deposition (LAPLD) tool.

The world's first LAPLD was designed and developed at Research Division of Raytheon (USA) to deposit thin films on ≈ 3 -inch diameter wafers [13]. The advancement in laser beam scanning techniques in conjunction with large-diameter target allows one to fabricate high quality film with homogeneity in thickness and composition on large area substrates for the application in Research and Development as well as commercial productions [3, 13, 14].

Figure 2.4 depicts the multi-functional PLD employed in this thesis for a small area chip level deposition to a large area 4-inch wafer deposition. Large area deposition is possible in this PLD with the help of laser beam rastering or mirror rastering where the target is ablated by moving the laser beam across it. It will provide an excellent target utilization leading to uniformity in thickness. In order to keep the spot size constant

during mirror rastering, a motor driven linear translation stage is provided to move the focus lens with the mirror [3].

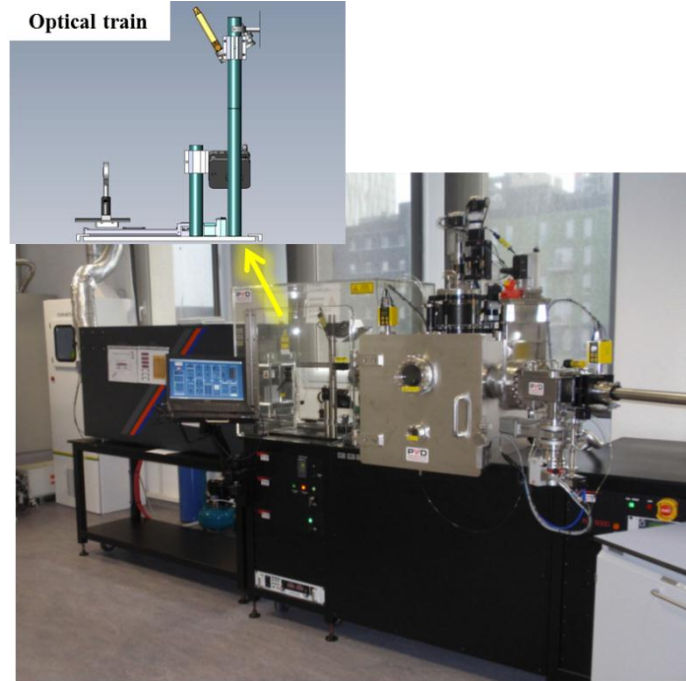


Figure 2.4. The main picture represents PLD-5000 system from PVD products a multi-functional PLD. It can perform small area to large area deposition including combinatorial deposition. The optical train setup is used for directing and focusing the excimer laser beam into the PLD chamber.

The place of application of LAPLD deposition mode in this thesis is given in the following section.

2.2.3 Combinatorial Pulsed laser deposition (CPLD)

CPLD is a recent advancement in PLD technology facilitated for fabricating a novel continuous compositional-spread (CCS) [15, 16] thin film systems on a large area through multilayer deposition. The CCS based combinatorial sample can be achieved in different ways of depositions depending on the equipment adapted in the CPLD system. In most cases, CCS based combinatorial samples are prepared by simultaneous ablation from multiple targets or sequential deposition technique where a single material is ablated at one time forming multilayers [15, 16].

The CCS based combinatorial thin film system can be fabricated in a special PLD utilizing combinatorial layer growing package with computer controlled automated program. With this package it is possible to fabricate binary, ternary, and quaternary

continuous compositional spreads by indexing both the target and substrate in appropriate fashion as well as programming the important deposition conditions such as temperature T , pressure P , laser fluence F , laser frequency f and number of cycles n to repeat the sequential deposition etc. Further, the possibility of fabricating a multi-component combinatorial system depends on the number of target holders available in PLD.

In this thesis PLD-5000 system from PVD products (Figure 2.4) has been used for small area, large area and combinatorial depositions. It has Lambda Physik COMPEX PRO 205 KrF excimer Laser (wavelength $\lambda = 248\text{nm}$, pulse duration 20ns , max Power $P = 30\text{W}$, max repetition rate $f = 50\text{Hz}$). Further, it has four target holders in the target carousel which facilitates to perform binary to ternary depositions (Figure 2.5).

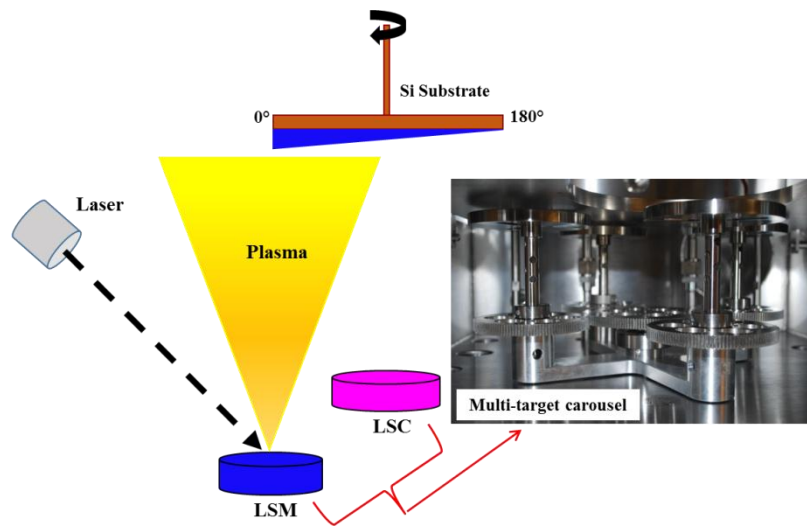


Figure 2.5. Graphical representation of multi-target carousel in PLD-5000 system to perform multilayer and combinatorial depositions.

PLD-5000 system is used for typical chip level depositions ($1 \times 1\text{cm}^2$) in the **chapter 3 and 4** to grow LSM, LSC and LSF thin films. LAPLD mode is applied in **chapter 5** to deposit 8YSZ layer on a 4-inch silicon wafer by using mirror rastering facility in PLD-5000 system. CPLD is applied in **chapter 5** to fabricate a CCS combinatorial LSMC thin film system.

Commercial targets with nominal compositions $\text{La}_{0.8}\text{Sr}_{0.2}\text{MnO}_3$ (LSM), $\text{La}_{0.8}\text{Sr}_{0.2}\text{CoO}_3$ (LSC), $\text{La}_{0.8}\text{Sr}_{0.2}\text{FeO}_3$ (LSF) ($\approx 99.95\%$ purity, 99.99% density, 2-inch diameter, 4mm thickness) from SurfaceNet, and home-made target 8 mol-% Y_2O_3 (8YSZ) (99.99% density, 4-inch diameter, 5mm thickness) are used as targets in PLD. It was found that the

LSM and LSC targets are under-stoichiometry in the B-site and the average value of A/B ratio is ≈ 1.2 , estimated by EDS measurement (section 2.3.3) due to the frequent laser ablation of PLD targets. The same targets are used throughout the whole thesis for PLD depositions.

2.3 Microstructural characterization techniques

After thin film fabrication, preliminary studies such as phase, microstructure and composition analysis are performed by various measurement techniques such as XRD, SEM, TEM, AFM, Raman spectrometry, EDS and WDS. A short introduction to each technique is given in the upcoming sections. (section 2.3.1. to 2.3.7).

2.3.1 X-Ray diffraction (XRD)

X-ray diffraction is a non-destructive structural characterization technique in which the diffraction pattern of a material is obtained by exposition of that material to X-rays. When a beam of X-rays interact with the target material, the X-rays are scattered by the atoms present in the target material. The scattered X-ray beam will undergo constructive and destructive interference produce diffraction [18, 19].

The generated diffraction pattern acquire various information about the crystallinity of the material under study. A qualitative and quantitative analysis of the pattern allows to identify the crystalline phase and determining the lattice parameter. The diffraction of X-rays can be described by Bragg's law (Figure 2.6) which is,

$$2d\sin\theta = n\lambda \quad (2.1)$$

Where d is inter-planar distance, θ is angle of incidence, n is integer, λ is wavelength of incident X-rays.

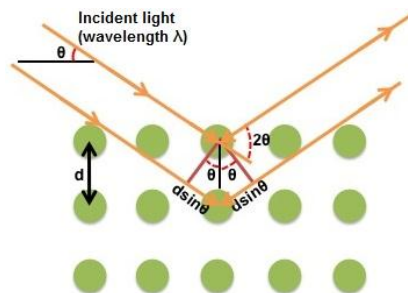


Figure 2.6. Illustration of Bragg's law of diffraction.

The XRD measurements in thin films are mainly performed at low incident angles to maximize the signal from the thin layers as well as to avoid signal from the substrate.

XRD technique is frequently used **in this thesis** to check the phase and purity of LSM, LSC, LSF thin films and LSMC combinatorial thin film system in **chapters 3, 4 and 5** including **Appendix B**. Most of the XRD patterns are acquired using Bruker D8 diffractometer (**Figure 2.7**) equipped with CuK α radiation ($\lambda = 1.54184\text{\AA}$) in the offset scanning mode. It has a nickel filter and Lynx Eye detector. FullProf software was employed to perform the Le Bail fitting on XRD spectra to determine the lattice parameters.



Figure 2.7. Bruker D8 diffractometer.

2.3.2 Scanning electron microscopy (SEM)

Scanning electron microscopy (SEM) utilizes a focused beam of electrons to generate image by scanning the sample surface. The interaction of electron beam with the sample surface generates various signals that contain information about the sample topography and composition.

When the electron beam knocks out an inner-shell electron of an atom, the electrons from higher orbital (outer-shell) will jump to the empty lower orbital (inner-shell) by emitting an electromagnetic radiation in the energy range of X-rays. These characteristic X-rays are used to identify the composition and abundance of the elements of the sample [20, 21].

The beam of accelerated electrons which typically have energy in the range \sim eV to keV is focused by a series of electromagnetic lenses on the sample surface with a spot size up to 1 nm. The interaction of accelerated electrons with the specimen makes the

electron to be scattered in different directions by elastic and inelastic scattering. It has secondary, back-scattered, Auger electrons and X-rays that can be collected by various detectors for different applications [20, 21]. The following different modes are commonly used to study the microstructure of solid materials.

The electrons resulting from inelastic scattering possess low energy electrons called **secondary electrons** which is the most common imaging mode. Due to their low energy (< 50 eV) these electrons are generated few nanometers from the surface. It contains information about the sample topography and morphology.

Backscattered electrons (BSE) are higher energy electrons produced by elastic scattering. Since the elements with different atomic number backscatter different, BSE provide compositional information of the sample.

The electrons emitted from the atomic layers very close to the sample surface are called **Auger electrons** containing valuable information about the sample surface chemistry.

In this thesis SEM is often used in **chapter 3, 4 and 5** to perform topography, morphology, thickness, grain size studies in LSM, LSC, LSF thin films and LSMC combinatorial thin film system. SEM images are obtained using *ZEISS AURIGA SEM*.

2.3.3 Energy dispersive X-ray analysis (EDS)

Energy dispersive X-ray spectroscopy (EDS) is an electron probe X-ray microanalysis technique (EPMA). It is also a non-destructive qualitative and quantitative analytical technique to study the chemical composition of a sample for elements with atomic number, $Z > 3$ [20, 21].

X-rays emitted from the sample are characteristic in energy. Each element has its own characteristic X-ray lines that allow a sample's elemental composition to be identified [20, 21].

The Zeiss Auriga SEM is also equipped with EDS which is often used in **chapter 3, 4 and 5** to estimate the atomic percentage of constituent elements in LSM, LSC, LSF thin films and LSMC combinatorial sample.

2.3.4 Wavelength-dispersive X-ray analysis (WDS)

Wavelength dispersive X-ray spectroscopy (WDS) is also an electron probe X-ray microanalysis technique. It is also similar to EDS but more powerful than EDS in terms of peak resolution.

This technique is also based on the measurement of characteristic X-ray intensities emitted by the constituent elements in the sample when it is bombarded by a focused electron beam. The ratio of the characteristic X-ray intensities emitted from the sample to that emitted from a standard of known composition called as k-ratio. Then the composition is obtained by fitting the predictions of a thin film software program in order to the measured k-ratio [28, 29].

In EDS, X-rays are distinguished based on energy whereas in WDS it is distinguished by wavelength. In ED spectrometer the overlapping between adjacent X-ray lines makes it difficult to find accurate X-ray intensities. But in WD spectrometer the peaks are well resolved between each other so that the detection limit of WD spectrometer is 10 times higher than ED spectrometer. In WDS detection limit for most elements is down to 100ppm or even less [30].

WDS is suitable for the analysis of thickness of bulk layers in micrometer scale. It can also be used for the analysis of thin films and multilayers with thicknesses in the sub-micron range.

Both EDS and WDS can be coupled with Scanning Electron Microscopy (SEM) or Transmission Electron Microscopy (TEM) for several applications.

In this thesis WDS facility (model- Jeol JXA-8230) in university of Barcelona has been used to check the composition of LSM thin film (**chapter 4**) and LSMC combinatorial system (**chapter 5**). The data obtained from WDS analysis is processed using Stratagem Surface Layers Analysis software (SAMx).

2.3.5 *Transmission electron microscopy (TEM)*

Transmission electron microscopy (TEM) is a powerful technique for microstructural and crystallographic characterization in material science. When a high energy focused electron beam from electron gun is illuminated through an ultra-thin specimen, the interaction between electrons and atoms creates the image of the sample.

The transmission of electron beam through the sample depends upon the thickness and electron transparency of the specimen. The transmitted electrons can suffer diffraction, due to the interaction of electrons with the crystalline material being observed. The diffracted beam can be used to study the crystal structure of atoms [26, 27]. Once the transmitted electrons are collected by an objective lens and the image will be projected onto a phosphor screen or CCD camera where the image can be observed.

High-resolution TEM (HRTEM) can capture image in atomic scale resolution which is used to study the sample crystal structure, lattice imperfections, point defects, stacking fault, dislocations, defects in grain bulk and grain boundary etc [26, 27].

There are two types of imaging in TEM, depending on the type of electrons used which can be scattered (diffracted) or unscattered (direct) electrons. The scattered electrons can be blocked by deflecting them away from the optical axis of the microscope, in order to obtain high contrast images. An aperture is used to perform the type of electron selection and inserted into the back focal plane of the objective lens. Normally, an aperture allows the direct beam by blocking the diffracted beam except that which is visible to the aperture.

The apertures can be moved using external drives to make either direct or scattered electrons go through it. If the direct beam is selected the resultant image is called as bright-field image. If we select scattered electrons of any form, we call it a dark-field image [26, 27].

In this thesis Jeol JEM-2100 Transmission electron microscope at the University of Castilla La Mancha (UCL) operated at 200kV was used to study the defects in LSM/YSZ heterostructures in **chapter 4**.

2.3.6 Atomic force microscopy (AFM)

Atomic force microscopy is a non-destructive technique used to study the sample surface. It works by scanning a probe over the sample surface mapping the height or topography of the sample surface.

The instrumentation of an AFM consist of piezoelectric transducers (or piezoelectric scanners), force transducers (force sensors), and feedback control. Generally, the piezoelectric transducer moves the tip over the sample surface, the force transducer measures the force between the tip and the surface, and the feedback control feeds the signal from the force transducer back in to the piezoelectric, to maintain a fixed force between the tip and the sample. AFM stage is the heart of the instrument. The major components of AFM stage are Z motor, which can move the AFM scanner towards the sample. There is an X-Y stage useful for positioning the feature for imaging under the probe. There is an optical microscope for viewing the probe and surface.

Maintaining the tip-sample force at a set value effectively maintains the tip-sample distance fixed. To scan the probe across the surface in a raster-like pattern, the X-Y

piezoelectric elements are used. In this way, by monitoring the voltage applied to the Z-piezo, a map of the surface shape (a height image) is measured.

In this thesis the surface morphology and roughness of samples such as LSM thin film in **chapter 4** and LSMC combinatorial system in **chapter 5** are studied by AFM. XE15-AFM from Park systems was used in contact and non-contact modes [24, 25].

2.3.7 Raman spectroscopy

Raman spectroscopy is a spectroscopic technique that provides information about molecular vibration that can be used for sample identification. It is based on the inelastic scattering of a monochromatic radiation.

During the sample-photon interaction the energy is exchanged such that the energy of scattered photon can be higher or lower than the incident photon. If the energy of scattered photon is less than the incident radiation form Stokes line. If the energy is greater than the incident radiation form anti-stokes lines. The shift in the wavelength of inelastically scattered photon provides the vibrational modes of the sample which is useful to study the sample structural information [22, 23]. Raman spectroscopy is also used for the sample quantification where scattered intensity is proportional to the quantity or thickness (concentration in liquid) of the material [22, 23].

The Raman measurements were carried out using micro-Raman facility in University of Barcelona. It has T-64000 Jobin Yvon/Atago Bussan triple spectrometer equipped with liquid nitrogen cooled CCD detector. Green laser light of wavelength $\lambda = 514.5nm$, spot size $0.5 \mu m$ was used to excite the samples.

In this thesis micro-Raman spectroscopy is mainly applied in **chapter 5** to study the spatial thickness distribution of LSM and LSC parent depositions. It is also used in the **same chapter** to study the local structure of LSMC combinatorial thin film system.

2.4 Functional characterization techniques

2.4.1 Electrical measurements

The electrochemical properties of thin film cathodes are studied by impedance spectroscopy in symmetrical cell configuration in order to understand the ORR mechanism over thickness and microstructure. The symmetrical cell measurement setup is detailed in **section 2.4.1.1**. The basic principle of impedance spectroscopy is explained in **section 2.4.1.2**.

The experimental setup to electrochemically characterize a symmetrical cell is composed of the following elements such as a) Cell sample holder b) Furnace and temperature control system c) Gas flow and humidifier d) Impedance analyzer e) Potentiostat/galvanostat. Different programs developed in Matlab at IREC are used to fully automate and control the measurements of the cells (Figure 2.8).

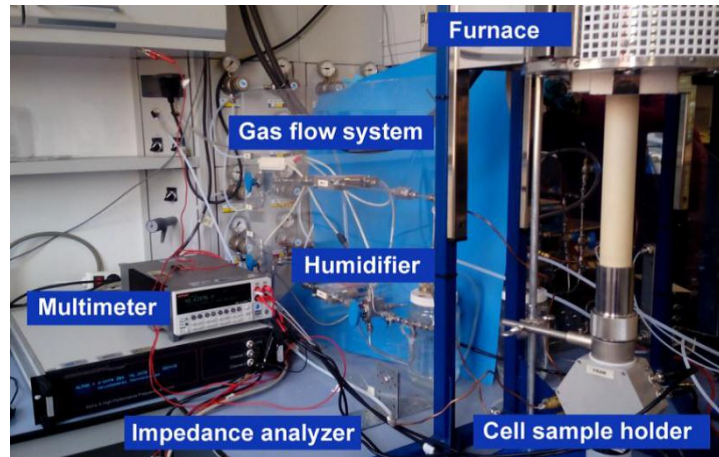


Figure 2.8. Image of one experimental setup used in this work to electrochemical characterize the Solid Oxide Fuel Cells (located in IREC).

2.4.1.1 Cell measurement setup

The graphical representation of LSM/YSZ/LSM symmetrical cell arrangement setup is given in Figure 2.9. The Au (gold) painted symmetrical cell is sandwiched between Pt meshes. Both Au layer and Pt mesh acts as current collectors.

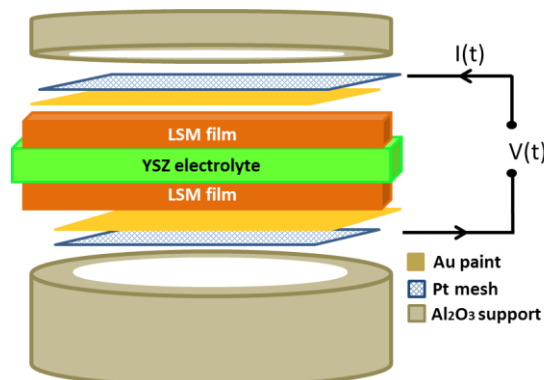


Figure 2.9. Schematic diagram of LSM/YSZ/LSM symmetrical measurement configuration.

This setup is placed in between alumina supports. The alumina support holding the symmetrical cell (facing downward) is a long tube around 1 meter length that acts as a

support. The other side of the cell (facing upward) is pressed by another small alumina support which is connected to a metal hook through a thin-long alumina rod. The metal hook is connected back to the bottom part of one meter alumina tube that makes a good contact between current collector and LSC electrode by pulling them tightly. Both alumina supports has a hole in the middle through which air reaches the active part of the cathode.

In this thesis LSM/YSZ/LSM symmetrical cells are measured based on the depicted configuration in **Figure 2.9** and the results are discussed in **chapter 4**.

2.4.1.2 *Electrochemical impedance spectroscopy (EIS)*

The electrochemical impedance spectroscopy (EIS) is a powerful tool to study the electrochemical properties of solid state ionic devices such as solid oxide cells (SOC), batteries and gas sensors. EIS has the capability to separate the different impedance contributions ranging a frequency domain [31].

In impedance spectroscopy a small, alternating perturbation voltage (signal) is applied to the sample and the resulting voltage/ current response is measured. The measurement is performed in a frequency range from several orders of magnitude to few Hz in a way that, one can distinguish the impedance contribution from different electrochemical processes according to their relaxation times. The time required for a polarized region to come to equilibrium after a perturbation signal is the relaxation time (τ) which is the characteristic time of the each electrochemical process involved in the electrochemical system. Therefore, the relaxation time of two different processes (e.g. relaxation time of ionic transport in the electrolyte faster than electrode) should be different that can be distinguished from impedance spectroscopy [31].

The impedance data are commonly represented as Nyquist plot (**Figure 2.10**) a polar plot where impedance response is plotted in a complex plane ($Z'(\omega)$ vs $Z''(\omega)$). Where Z' , Z'' represents the real and imaginary values of impedance as a function of angular frequency ω .

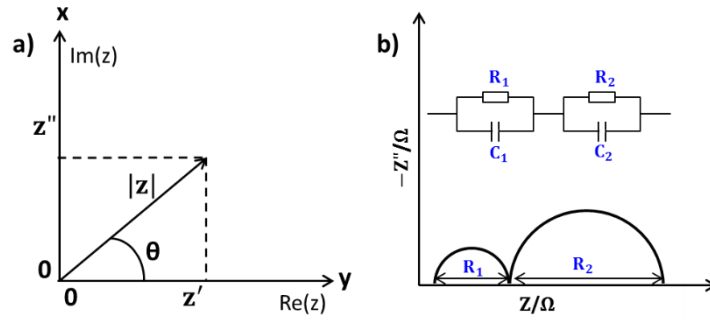


Figure 2.10. a) Impedance Z is plotted in a complex plane with polar coordinate $Z(\omega) = Z' + jZ''$. b) Appropriate RC equivalent circuit to fit the impedance spectra with two semicircles associated with two electrochemical processes with different time constants.

The interpretation of impedance data is sometimes simple or difficult which depends on the complexity of the electrochemical system under investigation. The most common approach is constructing an equivalent circuit with resistance (R) and capacitive (C) elements [32]. The simplest equivalent circuit is a single RC-element with R and C connected parallel to each other. The resultant impedance is,

$$Z(\omega) = \frac{R}{1 + i\omega RC} \quad (2.2)$$

where

$$\omega = \frac{1}{RC} = \frac{1}{\tau} \quad (2.3)$$

Where ω relaxation frequency equivalent to time constant $\tau = RC$.

Bauerle [33] proposed a model based on the linear combination of RC circuits to fit a more complex system (*i.e.* electrode/electrolyte/electrode) in order to extract the separate values of R, C and the time constant (τ) characteristic of each individual process. For example a circuit with two RC elements is suitable to apply in an impedance data with two well-separated semicircles with different time constants (Figure 2.10b).

However, this kind of circuits do not fit well the impedance spectra due to the appearance of a depressed (imperfect) semicircle in the complex plane which is related to non-ideal capacitance, therefore, the use of constant-phase elements (CPEs (Q,n)) is

often required. A number of equivalent circuits based on different models can be used to fit the same impedance spectra apart from a conventional RC equivalent circuits offer less-accurate fitting and fitting parameters. Moreover, all the elements chosen in the fitting must have a physical meaning in terms of resistive processes in the material, charge transfer or mass transfer processes.

In this thesis impedance spectroscopy is applied to study the electrochemical properties of LSM/YSZ/LSM symmetrical cells in **chapter 4**. All the generated impedance spectra were analyzed by *ZView* software.

2.4.2 IEDP-SIMS measurement

2.4.2.1 Oxygen isotope exchange

Isotope Exchange Depth Profiling using Secondary Ion Mass Spectrometry (IEDP-SIMS) is a powerful technique to determine oxygen diffusion coefficient D^* and oxygen exchange coefficient k^* in oxides in thin film or bulk form [35]. Before doing SIMS, oxygen isotope exchange annealing process has to be performed to allow the diffusion of ^{18}O isotope inside the sample. There are some important steps that have to be followed during ^{18}O isotope exchange process which is explained below in detail. The experimental setup used for the isotope exchange annealing process is given in the following figure (Figure 2.11).

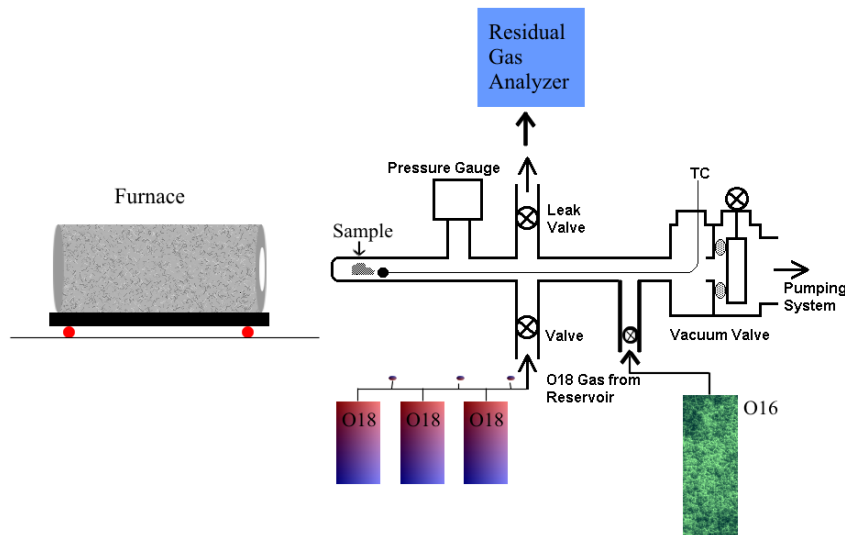


Figure 2.11. isotope exchange experimental setup. The diagram is taken from the reference [36].

The first step in the isotope exchange process consists of a proper sample selection with suitable geometry and long-time annealing for time t , temperature T and oxygen pressure P in pure oxygen. For that, the sample is mounted on a silica crucible placed inside a silica tube. Initially, the chamber is evacuated to the base pressure $< 5 \times 10^{-7}$ mbar using a pumping system consisting of a rotary and a turbo molecular pump. Then the chamber is filled with pure dry oxygen (research grade oxygen $\approx 99.9996\%$ purity) with natural ^{18}O isotopic abundance (^{18}O molar fraction 0.002). The sample is heated in a furnace which can function as roll-on, roll-off type where the temperature, ramping and dwelling can be controlled. The sample is annealed for a period of time 10 to 30 times higher than the isotope exchange annealing time, in order to equilibrate the sample with oxygen.

After the first step, the sample is cooled down and the pure oxygen is replaced by ^{18}O enriched atmosphere (55.3% to 93.9%) and then heated to a temperature at which the annealing under pure oxygen is performed as a first step. The sample is annealed under ^{18}O enriched atmosphere for a time t (≈ 20 min to 3 hours). During this annealing ^{18}O will be introduced into the sample to create oxygen diffusion profile over sample depth which is called diffusion-annealing step. Once the diffusion-annealing is finished, the sample is quenched down by rolling the furnace off in order to quench the oxygen diffusion profile.

The annealing temperature is the temperature of interest where ^{18}O diffusion wanted to be studied. The sample temperature and ambient pressure is being continuously monitored during different annealing steps. Oxygen composition in the sample ambient is continuously monitored by residual gas analyzer (RGA) gating through a leak valve which confirms that the applied oxygen concentration is constant throughout the exchange. A correction is made for the heating and quenching time period, temperature using Killoran method [36, 38].

2.4.2.2 Time of flight - Secondary ion mass spectrometry (ToF-SIMS)

ToF-SIMS (**Figure 2.12**) is a very sensitive surface analytical technique to study the chemical composition on the surface and near-surface region of a solid sample. ToF-SIMS combined with IEDP is used to acquire the oxygen isotope concentration profile over sample depth [38-40].

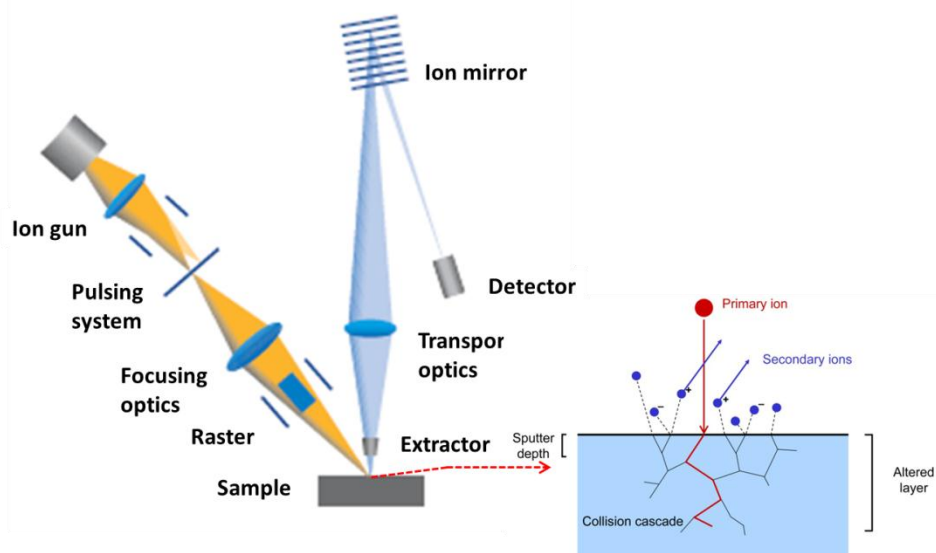


Figure 2.12. Schematic diagram of TOF-SIMS⁵ system from ION TOF website [41] sputters the sample surface with primary ions ejecting secondary ions.

The principle of ToF-SIMS is when the sample surface is bombarded by pulsed energetic primary ion beam in keV, the primary ions transfer their energy to target atoms by cascade collisions of atoms. The interaction of primary ions with the target surface led to the ejection of secondary ions. The ejected species may include atoms, clusters of atoms, and molecular fragments. After sputtering process the secondary ions are accelerated towards the detector where the ions are collected based on the time of arrival of ions to the detector.

The main role of the detector is to count the secondary ions with positive or negative polarity and recording the arrival time of various ions in order to perform quantitative analysis such as composition study on the surface or isotopic concentration in the sample. To fulfil them, the SIMS detector is equipped with microchannel plate, scintillator, and photomultiplier [39].

The type of analysis depends on the geometry of the sample. The sample with short diffusion profile $<10\mu\text{m}$ can be analyzed by conventional depth-profiling method [35]. It involves the sputtering of sample over depth with simultaneous collection of secondary ion oxygen isotopes (**Figure 2.13**).

The line-scan analysis is used when the profiles extend to hundreds of micron [35]. In line-scan analysis a portion perpendicular to sample surface is sliced out from the whole sample and analyzed over depth with a very fine primary ion beam.

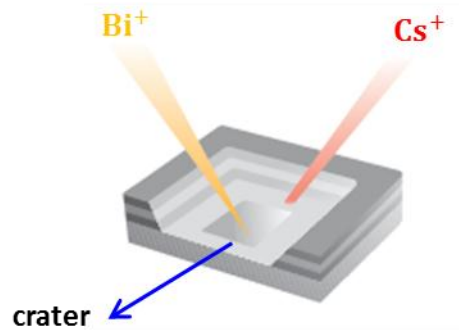


Figure 2.13. Depth profiling by dual beam mode. First beam is sputtering crater. The second beam analyzing the crater bottom.

The main challenge in SIMS measurement is achieving sufficient intensity for minor isotopes and the signal saturation of major isotope. Consequently, the secondary ions with enhanced intensity can cause collision-induced ion interactions and the detector dead time effects. Both effects lead to an underestimation of major isotope intensities which in turn create systematic errors in the concentration of secondary ion intensities.

In order to avoid such error, ToF-SIMS was operated in burst mode [39, 40] in which the primary ions with long pulse 100ns is chopped into short pulses (bursts) with 1ns out of a larger pulse (**Figure 2.14**).

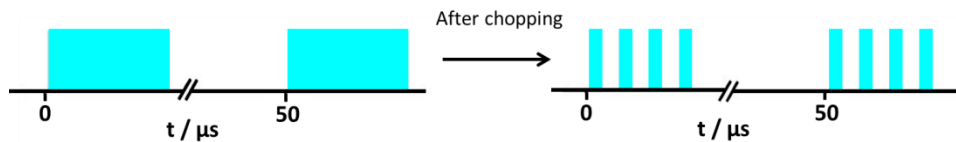


Figure 2.14. illustration of burst-mode operation.

In this thesis TOF.SIMS⁵ machine from ION-TOF (GmbH, Munster, Germany) is used to determine the oxygen diffusion coefficient D^* and oxygen exchange coefficient k^* in LSM thin film (**chapter 4**) and LSMC combinatorial system (**chapter 6**). The detection limit of TOF.SIMS⁵ is 10^{15} atoms/cm³ and the sensitivity to secondary ions is

in ppm/ppb range. The depth resolution is $\approx 1\text{nm}$ and the lateral resolution is $<60\text{nm}$ [41].

Some common experimental conditions used in the IEDP-SIMS measurements on LSMC combinatorial system and LSM thin films are: in both studies a 25kV Bi^+ ion beam that was used as primary ions and the primary beam was alternated with 2kV Cs^+ ion beam for sputtering based on dual-beam mode. The charge compensation during the analysis was solved by flooding 21eV low energy electrons from the electron gun.

2.5 Conclusion

The principle of various experimental techniques employed in this thesis for performing sample fabrication and characterization studies has been described in this chapter. In addition the specification and the place of application of each measurement in this thesis have been given. The experimental conditions and the results produced from those experimental techniques are given in the following chapters.

References

- [1] D. G. Schlom, L. Q. Chen, X. Pan, A. Schmehl, M. A. Zurbuchen, *J. Am. Ceram. Soc.*, 2008, 91, 2429.
- [2] L. W. Martin, Y. H. Chu, R. Ramesh, *Mater. Sci. Eng.*, 2010, 68, 89.
- [3] R. Eason, *Pulsed laser deposition of thin films*, John Wiley and sons, New Jersey, USA, 2006.
- [4] P. Schaaf, *Laser processing of materials: Fundamentals, applications and developments*, Springer, 2010.
- [5] M. N. R. Ashfold, F. Claeysens, G. M. Fuge, S. J. Henley, *Chem. Soc. Rev.*, 2004, 33, 23.
- [6] B. Dam, J. H. Rector, J. Johansson, S. Kars, R. Griessen, *Appl. Surf. Sci.*, 1996, 96, 679.
- [7] T. Venkatesan, *J. Phys. D: Appl. Phys.*, 2014, 47, 034001.
- [8] M. Lorenz, M. S. R. Rao, *J. Phys. D: Appl. Phys.*, 2014, 47, 030301.
- [9] S. S. Harilal, C. V. Bindhu, M. S. Tillack, F. Najmabadi, A. C. Gaeris, *J. Appl. Phys.*, 2003, 93, 2380.
- [10] T. Venkatesan, X. D. Wu, A. Inam, J. B. Wachtman, *Appl. Phys. Lett.*, 1988, 52, 1193.
- [11] N. Kaiser, *Appl. Optics*, 2002, 41, 3053.

- [12] I. Petrov, P. B. Barna, L. Hultman, J. E. Greene, *J. Vac. Sci. Technol.*, 2003, A21, S117.
- [13] J. A. Greer, *J. Phys. D: Appl. Phys.*, 2014, 47, 034005.
- [14] B. Schey, T. Bollmeier, M. Kuhn, W. Biegel, B. Stritzker, *Rev. Sci. Instrum.*, 1998, 69, 474.
- [15] X. D. Xiang, I. Takeuchi, *Combinatorial Materials Synthesis*, CRC Press, Florida, USA, 2003.
- [16] H. M. Christen, I. Ohkubo, C. M. Rouleau, G. E. Jellison, A. A. Puretzky, D. B. Geohegan, D. H. Lowndes, *Meas. Sci. Technol.*, 2005, 16, 21.
- [17] C. Duran, G. L. Messing, S. T. McKinstry, *J. Mat. Sci.*, 2002, 37, 5041.
- [18] B. B. He, *Two-dimensional X-Ray diffraction*, John Wiley and Sons, New Jersey, USA, 2009.
- [19] B. B. He, U. Preckwinkler, K. L. Smith, *International centre for diffraction data, Advances in X-ray analysis*, 2000, 43, 273.
- [20] J. I. Goldstein, D. E. Newbury, P. Echlin, D. C. Joy, C. E. Lyman, E. Lifshin, L. Sawyer, J. R. Michael, *Scanning electron microscopy and X-Ray microanalysis (3rd ed)*, Springer, 2003.
- [21] A. Bogner, P. H. Jouneau, G. Thollet, D. Basset, C. Gauthier, *micron*, 2007, 38, 390.
- [22] S. S. R. kumar, *Raman spectroscopy for Nanomaterials characterization*, Springer, 2012.
- [23] M. Moskovits, *J. Raman. Spec.*, 2005, 36, 485.
- [24] P. Eaton, P. West, *Atomic Force Microscopy*, Oxford University Press, Oxford, UK, 2010.
- [25] N. Jalili, K. Laxminarayana, *Mechatron.*, 2004, 14, 907.
- [26] D. B. Williams, C. B. Carter, *Transmission Electron Microscopy*, Springer, 2009.
- [27] K. D. V. Parry, A. C. Wright, *III-Vs review.*, 2001, 14, 48.
- [28] X. Llovet, C. Merlet, *Microsc. Microanal.*, 2010, 16, 21.
- [29] C. Merlet, X. Llovet, *IOP Conf. Ser.: Mater. Sci. Eng.*, 2012, 32, 012016.
- [30] X. Llovet, *Electron probe microanalysis: principles and applications*, 2012, UB.
- [31] J. Ross Macdonald, *Impedance Spectroscopy: Theory, Experiment, and applications*, John Wiley and Sons, New Jersey, USA, 2005.
- [32] D. Andre, M. Meiler, K. Steiner, H. Walz, T. S. Guth, D.U. Sauer, *J. Power Sources*, 2011, 196, 5349.
- [33] J. E. Bauerle, *J. Phys. Chem. Solids*, 1969, 30, 2657.
- [34] T. Matsumura, Y. Sato, *J. Mod. Phys.*, 2010, 1, 340.
- [35] R. A. De Souza, M. Martin, *MRS Bulletin*, 2009, 34, 907.
- [36] R. J. Chater, *Ph.D. Thesis*, University of London, June, 2014.
- [37] M. B. Lopez, *Ph.D. Thesis*, Autonomous University of Barcelona, March, 2007.

- [38] D. R. Killoran, *J. Electrochem. Soc.*, 1962, 109, 1215.
- [39] R. A. De Souza, J. Zehnpfenning, M. Martin, J. Maier, *Solid State Ionics*, 2005, 176, 1465.
- [40] G. Holzlechner, M. Kubicek, H. Hutter, J. Fleig, *J. Anal. At. Spectrom.*, 2013, 28, 1080.
- [41] TOF.SIMS⁵ manual from www.iontof.com website.

Chapter 3

***Interdiffusion mechanism and optimization of LSM,
LSC and LSF deposition by PLD***

Chapter III

3.1 Chapter outline

Advances in thin film processing methods have provided the ability to grow thin film heterostructures, which were previously inaccessible by traditional material processing means. Heterostructures are artificially processed materials which are composed of multiple layers of different phases, and these are stacked in periodic manner.

These multilayers (multiple layers) have sharp boundary in the interface of successive layers and stacked with a highly ordered average spacing between each layers. However, the individual layer may be amorphous or polycrystalline with low degree of structural coherence in the interface (**Figure 3.1**). Multilayers composed of single-crystal layers that possess same crystal structures, in which the interfaces are in perfect atomic registry, are called super lattice structures [1, 2].

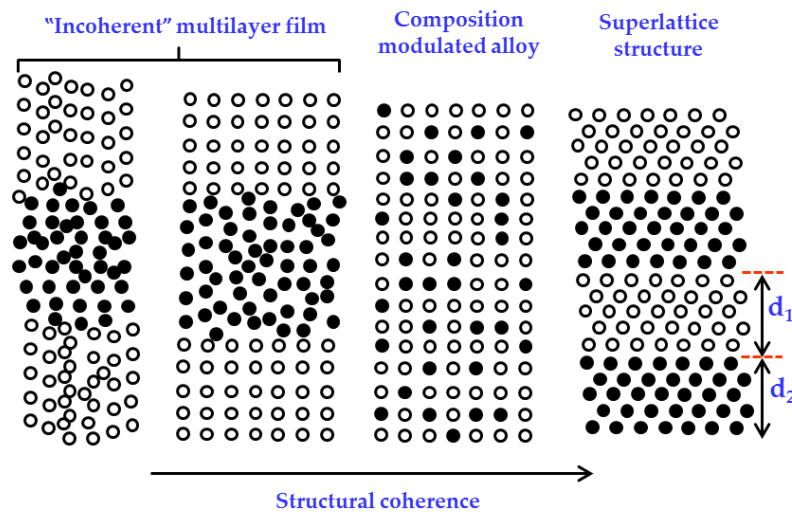


Figure 3.1. illustration of structural coherence in different multilayer systems taken from reference [1].

Although several multilayer deposition trials ended up in failure in early 1940's, the first stable thin film metallic multilayer system Ag-Au, Cu-Pd was successfully grown by Hillard et al. in 1969 [3]. Later, investigations on multilayered structure attained tremendous growth after observing the possibility of tuning a multilayer system properties by reducing the successive layer thickness below electron mean free path in the year 1968 [4].

With the latest thin-film processing techniques, it is possible to fabricate high quality heterostructural oxide thin films with multi-functional properties by precisely controlling the thickness and composition of each layer. Functional properties can be tuned by engineering lattice, strain, and interfaces [5] in these nanostructures under nanometer to atomic length scale, for a wide range of applications in different fields. Some exciting technological development has been obtained from high quality thin film heterostructures with well-defined composition, nanoscale in dimension. Applications include: band gap engineering of materials for optoelectronic devices [6], high speed computer processor and memories [7, 8], thin-film micro batteries, electro chemical capacitors [9] for portable electronic device applications, etc.

Artificially tailored, a thin film multilayer system can be fabricated by using various thin film processing techniques which are typically based upon layer by layer epitaxial or poly crystalline growth [1, 2]. Apart from fabricating heterostructural thin film with different crystal structures, a new composition with single phase is possible to be achieved from such multilayer system by taking advantageous of short diffusion length existing in the successive thin layers. This can be done by precisely controlling the thickness of every adjacent layer. The current chapter is about the possibility of achieving a homogeneous layer composition by means of subsequent depositions of ultra-thin films. The current chapter is organized in following way.

Section 3.2 is devoted to optimize the deposition conditions of LSM, LSC and LSF layers in PLD. The influence of deposition condition on the thin film microstructure is discussed in **section 3.2.1** and **3.2.2**.

A general outline about interdiffusion mechanism in thin films and the rate-limiting factors of diffusion processes is given in **section 3.3.1** and **3.3.2**. There are two methodologies introduced in **section 3.3.3** to fabricate a new composition from ultra-thin film multilayer deposition technique.

Fabricating $\text{La}_{0.8}\text{Sr}_{0.2}\text{Mn}_{1-x}\text{Co}_x\text{O}_{3\pm\delta}$ ($x \approx 0$ to 1) a pseudo-binary system from $\text{La}_{0.8}\text{Sr}_{0.2}\text{MnO}_{3+\delta}$ (LSM), $\text{La}_{0.8}\text{Sr}_{0.2}\text{CoO}_{3-\delta}$ (LSC) multilayers is the objective of chapter-5. The multiple layers involved in the new product formation are called “**precursor or parent layers**” [10, 11]. LSM and LSC are parent layers here, in which B-site atomic diffusion (B = Mn, Co) play a significant role during interdiffusion between parent layers. It is necessary to acquire primary knowledge in the diffusion of atomic species involved in interdiffusion mechanism in order to achieve the desired composition.

Therefore, Mn, Co and Fe atomic diffusion in perovskite-related structure and its effective diffusion time are studied in **section 3.3.4** and **3.3.5**.

After optimizing the deposition conditions in PLD, a few number of LSC/LSF, LSM/LSC thin film multilayer depositions are performed by using the optimum parent layer thickness estimated from Co and Fe atomic diffusion coefficients. The Influence of parent layer thickness on the quality of desired new composition is discussed in **section 3.4.1** and **3.4.2**.

3.2 LSM, LSC and LSF parent layer PLD deposition optimization

An important advantage of PLD technique is the stoichiometric material transfer in thin film. In PLD chamber, only the target material is ablated which avoids contamination issues. Congruent evaporation with excellent stoichiometry control, microstructure control, low thin film processing temperature, possibility of attaining high quality films with highly dense layers [10, 12, 13] are the most attractive and required features underneath the employment of this technique in this thesis for thin film fabrication. Readers are asked to refer **section 2.2 in chapter 2** for the detailed description about principle and function of PLD.

The deposition conditions such as Temperature (**T**), pressure (**P**), laser fluency (**F**), frequency (**f**), target-substrate distance (**d**) have to be optimized in PLD to fabricate a dense LSM, LSC and LSF thin films. Apart from dense layers, deposition conditions have to be also optimized to obtain porous layers for performing electrochemical measurements on thin film with dense and porous microstructures. These optimizations can also be considered as preliminary step for performing LSM/LSC, LSC/LSF multilayer depositions. All preliminary optimization depositions are performed in Si substrate with 8 mol-% Y₂O₃ (8YSZ) layer on top of it. The depositions are performed in the temperature range from 500°C to 800°C and different pressure of oxygen of 20mT, 70mT and 200mT to optimize the dense and porous microstructures.

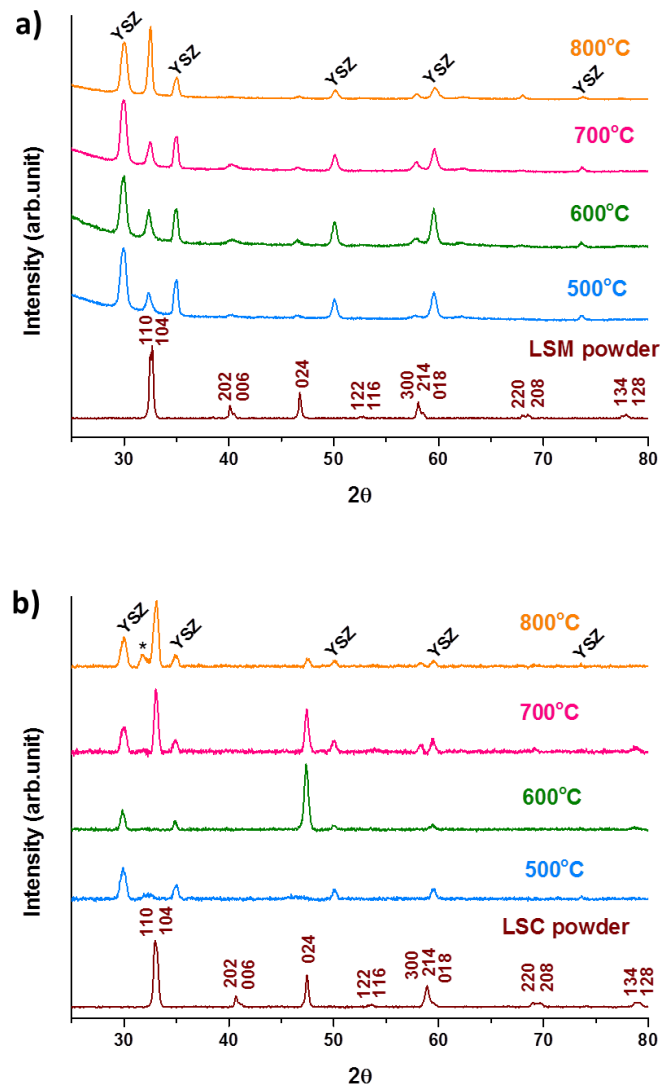
3.2.1 Effect of substrate temperature on phase formation

Initially, LSM, LSC and LSF films are grown at different temperatures such as 500°C, 600°C, 700°C and 800°C under 70mT of oxygen pressure to optimize the LSM, LSC and LSF phases in PLD.

In **Figure 3.2 a) b) c)** XRD pattern represents the phase evolution of LSM, LSC and LSF thin films over different substrate temperatures such as 500°C, 600°C, 700°C and

III - Interdiffusion mechanism and optimization of LSM, LSC and LSF deposition by PLD

800°C. In that, LSM layer attained crystallinity at low temperature 500°C itself, however LSC and LSF peaks do not appear at that temperature, indicating the generation of amorphous layers. Hence deposition temperature is increased to achieve the polycrystalline LSC and LSF layers.



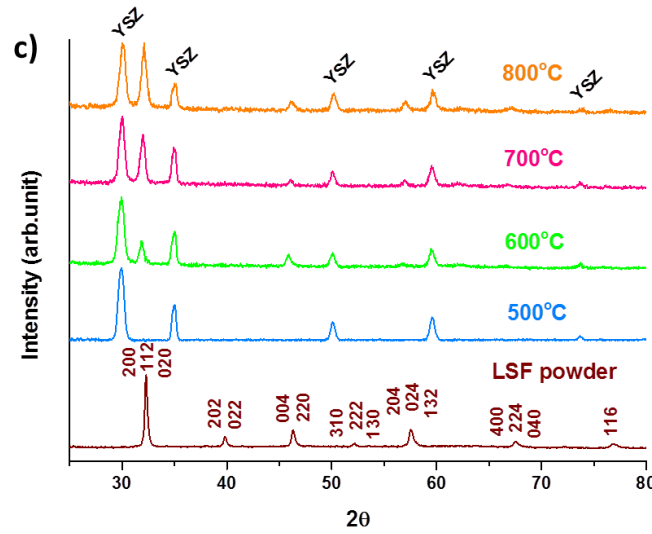


Figure 3.2. XRD pattern of *a)* LSM *b)* LSC *c)* LSF thin film phase evolution over substrate temperature is compared with its powder pattern.

At 600°C, 700°C and 800°C all these three layers look polycrystalline with different levels of preferential orientation. Although LSC is polycrystalline at 800°C, a parasitic phase is observed at 31.6° which is indexed as SrCoLaO₄ (indicated by star). There are other parasitic phases such as Co₃O₄, SrZrO₃, La₂Zr₂O₇ reported in the literature at high temperature 900°C when LSC reacts with YSZ [14, 15]. Here SrCoLaO₄ might be formed due to instability of LSC at 800°C.

Regarding crystal structure, LSM and LSC thin films are crystallized in Rhombohedral symmetry with $R\bar{3}c$ space group. LSF is crystallized in orthorhombic symmetry with $Pbnm$ space group. Generally LSF is crystallized in rhombohedral structure when Sr is ≤ 0.2 [16, 17].

Thin film phase evolution over substrate temperature confirms the influence of deposition temperature on the film crystallinity and preferential orientation (for a fixed thickness of ≈ 150 nm) which can be seen in XRD pattern. The morphology of LSM, LSC and LSF layers are observed by SEM. **Figure 3.3, 3.4 and 3.5** shows the microstructural evolution of LSM, LSC and LSF layers at different substrate temperatures such as 500°C, 600°C, 700°C, 800°C.

**III - Interdiffusion mechanism and optimization of LSM,
LSC and LSF deposition by PLD**

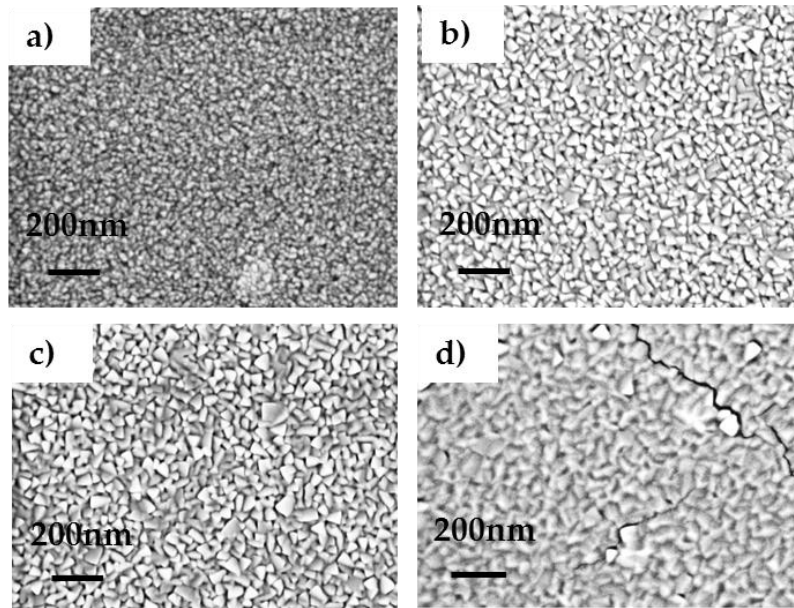


Figure 3.3. Evolution of LSM microstructure deposited at P=70mT with respect to substrate temperature a) 500°C b) 600°C c) 700°C d) 800°C.

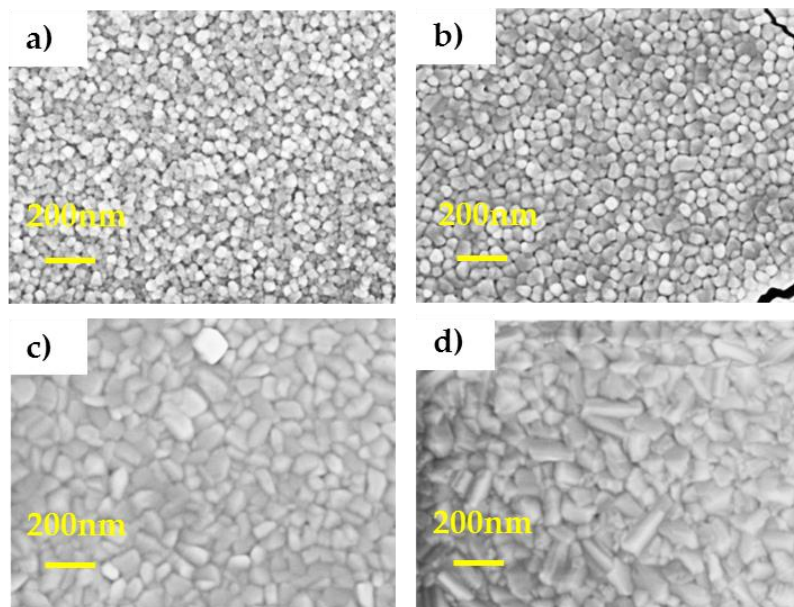


Figure 3.4. Evolution of LSC microstructure deposited at P=70mT with respect to substrate temperature a) 500°C b) 600°C c) 700°C d) 800°C.

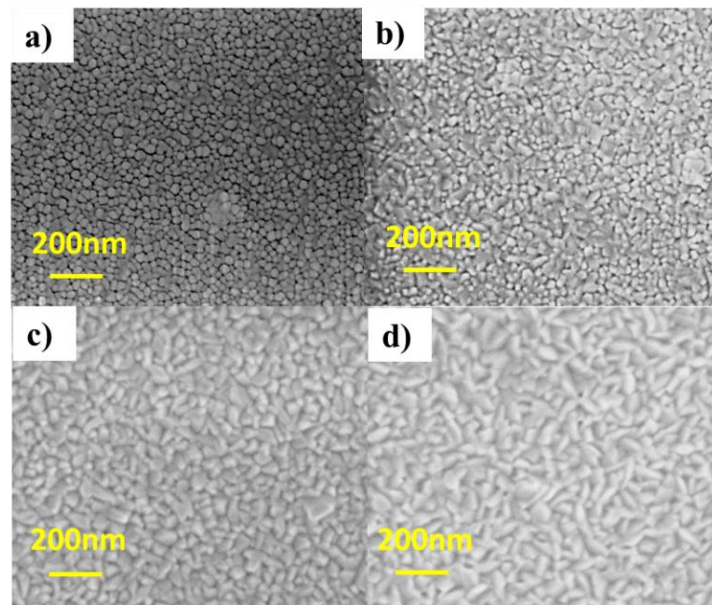


Figure 3.5. Evolution of LSF microstructure deposited at $P=70mT$ with respect to substrate temperature a) $500^{\circ}C$ b) $600^{\circ}C$ c) $700^{\circ}C$ d) $800^{\circ}C$.

SEM image confirms the morphological changes in LSM, LSC, LSF layers deposited at different substrate temperature. Especially two parameters such as film porosity and grain size are affected by the substrate temperature.

The microstructure of LSM, LSC and LSF thin film consists of nanoparticles forming a dense layer at high temperature ($800^{\circ}C$). The grain size of LSM, LSC and LSF at $700^{\circ}C$ and $800^{\circ}C$ are higher than the one observed at $500^{\circ}C$ and $600^{\circ}C$. Generally in the thin film microstructural evolution mechanism, a fast grain growth occurs at high temperature through impingement and coalescence of islands [18]. Therefore, dense and improved grain size observed at $700^{\circ}C$ and $800^{\circ}C$ can be related to high temperature grain growth mechanism.

LSM layer is porous at $500^{\circ}C$, $600^{\circ}C$, $700^{\circ}C$, while both LSC and LSF layer show porosity at $500^{\circ}C$, $600^{\circ}C$ as a result of low energetic surface adatoms involved in the crystallization and grain growth process.

Regarding crack formation, in LSM and LSF layers cracks are observed only in the samples deposited at $800^{\circ}C$ with dense microstructure where as in LSC layers, cracks can be observed in all sets of temperature irrespective of dense and porous microstructures (Figure 3.4a to 3.4d).

Generally, cracks arise in thin film due to two factors which are thermal expansion mismatch with underneath substrate [19] and thin film thickness [20]. Thin films with

dense microstructure release its stress in the form of cracks after certain thickness. This thickness is called as critical thickness [20] that does not have to be confused with the critical length (L_c) used in interdiffusion process explained in section 3.3.2. Therefore, cracks observed in LSM ($TEC_{LSM} \approx 10.08 \times 10^{-6} \text{ K}^{-1}$) [21], LSC ($TEC_{LSC} \approx 21.54 \times 10^{-6} \text{ K}^{-1}$) [21] and LSF ($TEC_{LSF} \approx 13 \times 10^{-6} \text{ K}^{-1}$) [17] layers may be due to the thermal mismatch with Si ($TEC_{Si} \approx 4 \times 10^{-6} \text{ K}^{-1}$) substrate [22, 23, 24].

It is found that 40nm is the critical thickness to grow crack-free dense LSC layers in this deposition conditions (Fig 3.6). In opposite, critical thickness to grow crack-free dense LSM layer is $\approx 250\text{nm}$ (Fig 3.6).

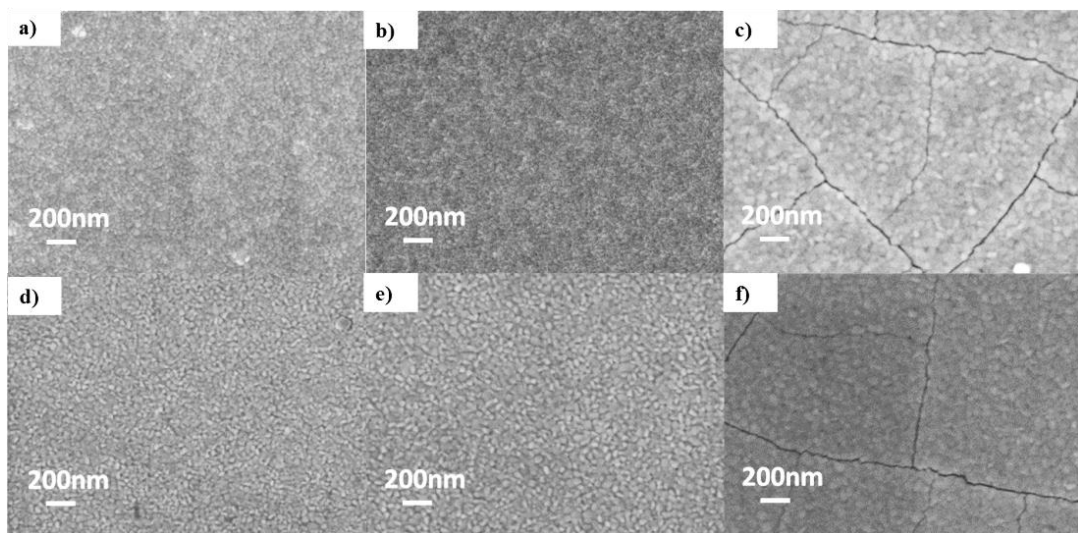


Figure 3.6. Crack-evolution¹ in LSM thin films a) 100nm b) 200 c) 250nm. LSC thin films a) and b) are $<40\text{nm}$ c) 40nm.

XRD investigation revealed that 700°C is the best temperature to process LSM, LSC and LSF layers. It is important to remark that using the same deposition temperature is highly recommended for the parent materials (LSM and LSC) which are involved in the combinatorial deposition for technical reasons (see chapter 5 section 5.4 for the detailed description of combinatorial deposition).

Although the deposition temperature is optimized at 700°C to grow LSM, LSC and LSF polycrystalline layers based on XRD results, the layers are not dense enough for performing functional studies on these layers. In the following section, microstructural

¹ Crack-evolution study was performed in LSM and LSC layers as preliminary analysis for LSMC pseudo-binary thin film system fabrication.

evolution of LSM, LSC and LSF layers are studied over different oxygen pressure in order to optimize the dense microstructure.

3.2.2 Effect of pressure on thin film microstructure

Depositions are performed at three different pressures such as 20mT, 70mT, 200mT, in order to achieve dense and porous LSM, LSC and LSF layers. **Figure 3.7** shows the microstructural evolution of LSM, LSC, LSF layers upon different oxygen pressure which confirms the morphological changes taking place over oxygen pressure.

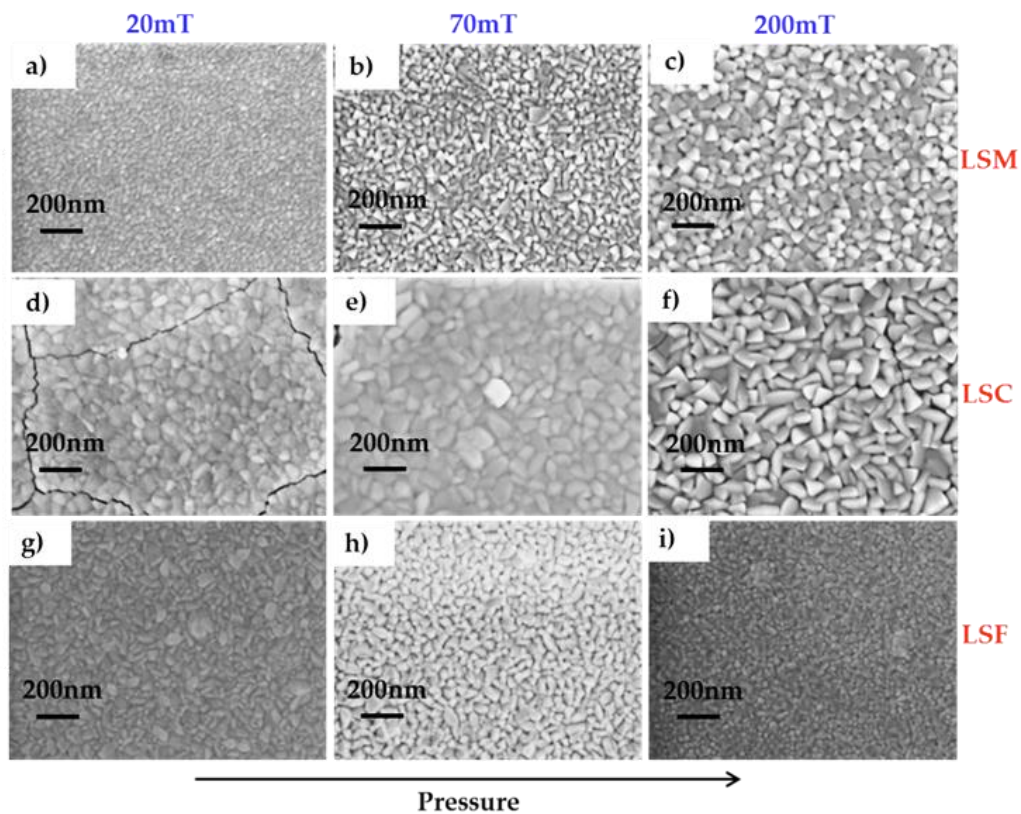


Figure 3.7. Microstructural evolution of LSM thin films with respect to different oxygen Pressure **a)** 20mT **b)** 70mT **c)** 200mT. LSC microstructure evolution under **d)** 20mT **e)** 70mT **f)** 200mT. LSF microstructure evolution under **g)** 20mT **h)** 70mT **i)** 200mT.

At high oxygen pressure ($P = 200mT$), LSM, LSC and LSF layers are porous whereas at low pressure ($P = 20mT$) they are (or seem to be) dense. In particular, changes in the porosity and grain size can be observed over oxygen pressure.

Increasing oxygen pressure confines the plasma expansion that will reduce the mean free path of the particle collisions happen inside the plasma. As a consequence, particles arrive at the substrate surface are low energetic. Then, energy is not sufficient

to involve in the surface diffusion. It will make the particle to stick on the substrate surface where it lands. Hence, porosity and cluster size increases upon pressure [25].

At high pressure, high energetic adatoms involve in surface diffusion, nucleation, crystallization, grain growth process which lead to dense microstructure [26, 27]. Also, this low and high energetic plasma can affect the growth rate of thin films. **Figure 3.8** shows the influence of the oxygen pressure on the growth rate of LSM, LSC and LSF layers.

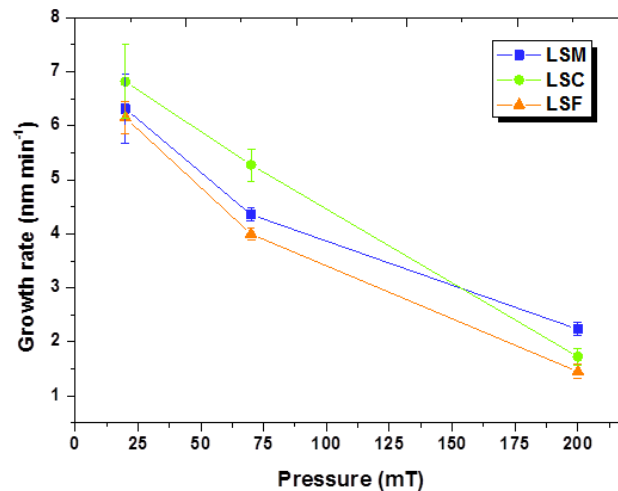


Figure 3.8. Growth rate of LSM, LSC, LSF layers upon pressure. Growth rate is calculated in terms of nm/1000pulses for a fixed laser frequency.

It clearly indicates that the film grows faster at lower pressure than at higher pressure [26, 27, 28]. When the pressure is increased to 10 times from 20mT to 200mT, growth rate increases from 3 to 4 times, which clearly depicts the kinetic energy of plasma play a significant role in determining the growth rate.

3.3 Interdiffusion mechanism

3.3.1 What is interdiffusion/intermixing process?

The general driving force of diffusion is chemical potential gradient. Gradient in temperature, pressure, voltage, stress etc [29, 30] can also setup atomic diffusion in a system from bulk to thin film form.

When two different materials with non-zero atomic diffusion coefficient are kept in contact with each other, ions will start to diffuse at different rates. This diffusion will

induce a local change in chemical composition. This process is called “**intermixing or interdiffusion**” process **Figure 3.9**.

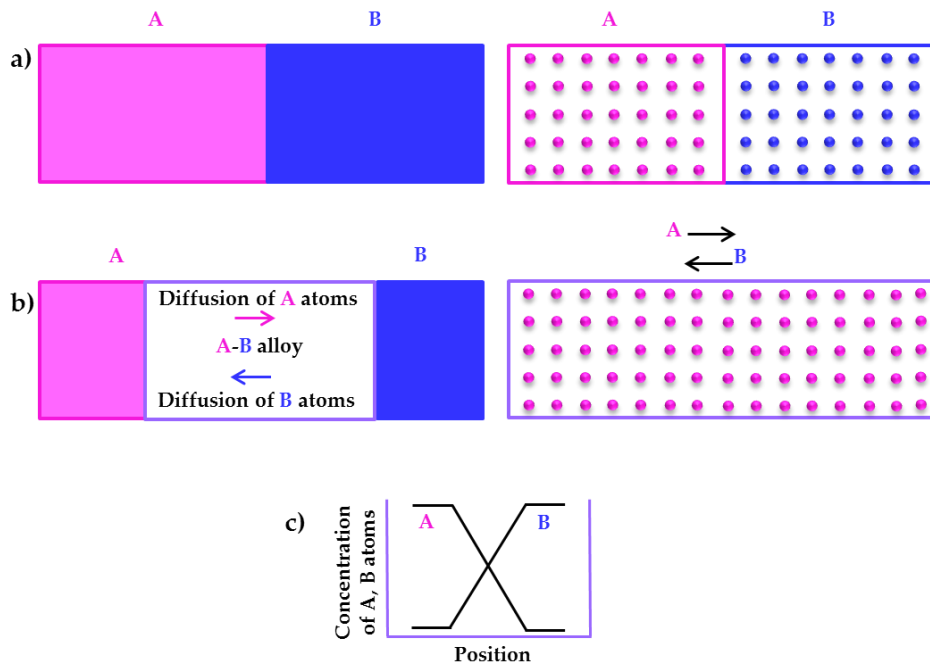


Figure 3.9. illustration of interdiffusion process **a)** A and B are two solid materials kept in contact **b)** interdiffusion of A atoms in B medium and B atoms in A medium **c)** Concentration gradient after interdiffusion at A-B interface.

The resultant product obtained from interdiffusion process might be mixed either in homogeneous or heterogeneous way, which depends upon the diffusion length (thickness) of the interdiffusing media. This thickness is called “**critical length (L_c)**”. Moreover, the diffusion length (thickness) can also alter the time and temperature of intermixing process [31].

3.3.2 Rate-limiting factors of intermixing mechanism

Diffusion and nucleation are the two rate-limiting steps which controls the interdiffusion mechanism across thin films. These rate-limiting step compete each other when the interdiffusion process is taken place between two different solid layers.

Case (i) Diffusion is rate-limiting: For a multilayer system composed of ultra-thin films, the thickness of parent layers below critical length ($l < L_c$) allow the completion of intermixing process between these multilayers before the nucleation step begins to

dominate at the interface. In this case, parent layers are first homogeneously mixed with each other through the occurrence of diffusion process as first step, followed by nucleation or atomic arrangement as a next step which lead to the formation of a new material with single phase. Therefore when the diffusion step is rate-limiting, a pure final product (composition) can be achieved through a completed intermixing process.

Case (ii) Nucleation is rate-limiting: when a multilayer system composed of thicker films, the thickness of parent layers above critical length ($l > L_c$) allow the nucleation step to dominate in the multilayer interface resulting in the precipitation of parasitic phases at interface which hinder the formation of a pure final product (composition). In the end, parent layers are saturated with incomplete intermixing process. Therefore when the nucleation step is rate-limiting the desired final composition cannot be attained due to incomplete intermixing process.

The above limitations explain the importance of critical length L_c , which acts as a deciding factor of the purity of the final product (composition) [31-34].

3.3.3 Methodology to fabricate new composition in thin film form by intermixing process

The possibility of fabricating a new composition from an ultra-thin film multilayer system and its rate-limiting steps has been explained in the previous section.

Generally, a new composition from an ultra-thin film multilayer system can be processed in two different methodologies (**Figure 3.10**) by using the latest deposition techniques [10, 12, 13]. However, the “**formation stage**” of the new product depends on the amorphous or crystalline phase of the multilayers involved.

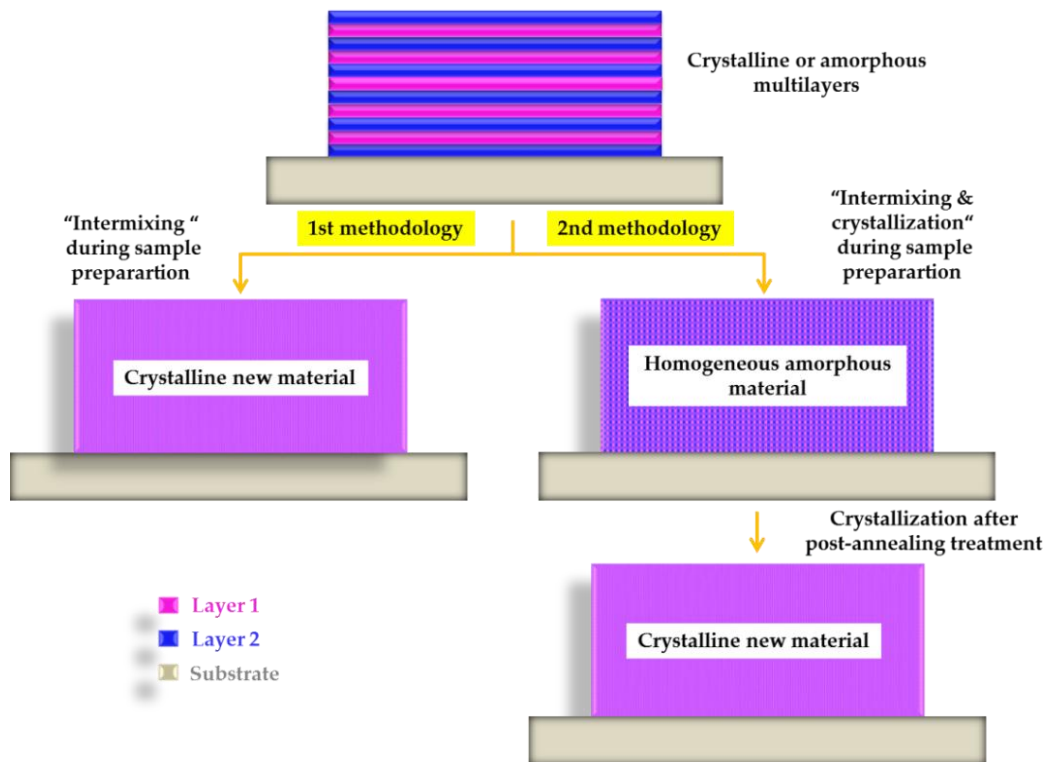


Figure 3.10 Schematic diagram of methodology to fabricate a new composition from ultra-thin film multilayer system.

In the first methodology (**Figure 3.10**), ultra-thin multilayers are directly grown in crystalline form using right deposition conditions, usually imposing high energy to the involved species (eg. high temperature deposition). The advantage of this first methodology is that the desired composition can be directly achieved during material processing or deposition itself through the diffusion step followed by nucleation step.

In the second methodology (**Figure 3.10**), ultra-thin multilayers are directly grown as amorphous layers using low deposition temperatures. This kind of low energy deposition would allow the homogeneous mixing of parent layers. The resultant homogeneously mixed amorphous compound is a reaction intermediate. However, it still needs a post-annealing treatment to make the nucleation step to complete in order to achieve the desired final product.

The first methodology is more efficient than the second one in terms of time and energy consumption. Moreover, second method needs the optimization of post-annealing parameters as an extra step to attain the desired product.

Various thin film processing techniques such as PLD, CVD, MOCVD, ALD, etc [12, 13] equipped with multilayer thin film fabrication facility can be used to fabricate new composition in thin film form. In this thesis, PLD is used as a tool to perform this task.

In a PLD chamber deposition under constant temperature and pressure interdiffusion is normally stimulated by chemical potential between parent layers.

3.3.4 Mn, Co and Fe diffusivity in perovskite-related structures

As explained in the introduction the main goal of **chapter 5** is the fabrication of continuous composition spread (CCS) LSMC system from LSM and LSC multilayers through proper intermixing. Before getting involved in LSMC pseudo-binary system fabrication, it is essential to know the evaluation of the interdiffusion processes of the atoms involved.

The parent compounds such as $\text{La}_{0.8}\text{Sr}_{0.2}\text{MnO}_{3+\delta}$ (LSM), $\text{La}_{0.8}\text{Sr}_{0.2}\text{CoO}_{3-\delta}$ (LSC) composition has the same amount of A-site atomic concentration (La and Sr) which prevents the interdiffusion of La and Sr atoms between LSM and LSC layers. But different chemical potential of B-site atomic concentration can promote interdiffusion of Mn and Co atoms in the B-site of parent layers. To have a theoretical knowledge on the diffusivity of Mn and Co atoms will be highly useful to predict an approximate critical length L_c value, in order to achieve pure LSMC system.

Therefore, self-diffusion and inter-diffusion coefficients of Mn and Co ions including Fe ion in perovskite-related structure has been collected from the literature. The diffusion coefficients found in the literature are determined by different experimental techniques such as tracer annealing, inter-diffusion couple, solid state reaction etc [35-39]. The diffusion coefficients of Mn, Co and Fe ions is given in the following Arrhenius plot.

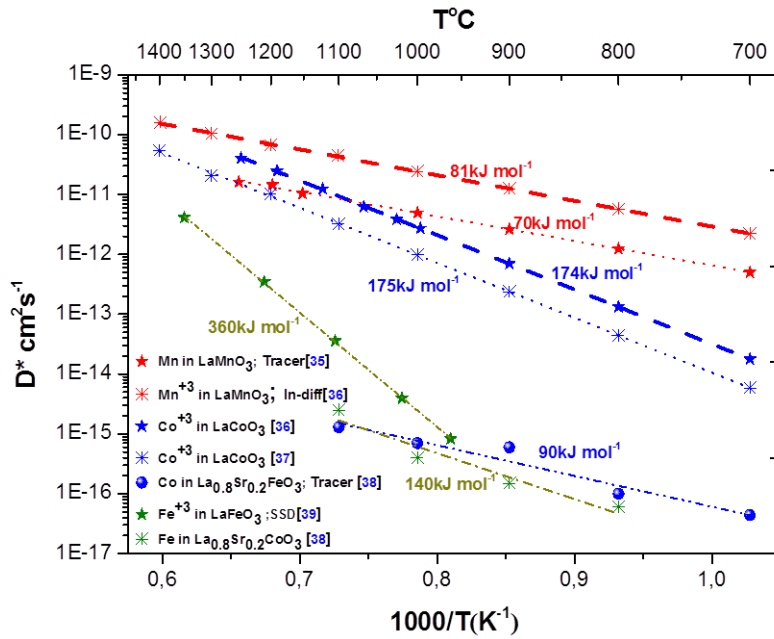


Figure 3.11. Arrhenius plot of Mn, Co, Fe diffusion coefficients vs temperature.

In **Figure 3.11** Mn diffusion in LaMnO_3 (LMO), Co in LaCoO_3 (LCO), Fe in LaFeO_3 (LFO) represents the self-diffusion coefficient of Mn, Co, Fe ions. While Fe diffusion in $\text{La}_{0.8}\text{Sr}_{0.2}\text{CoO}_3$ (LSC), Co diffusion in $\text{La}_{0.8}\text{Sr}_{0.2}\text{FeO}_3$ (LSF) represents inter-diffusion coefficients. The diffusion of an ionic species taken place without any driving force is called as self-diffusion, whereas diffusion of an ionic species in a foreign material is called interdiffusion [29, 38].

Generally, cation diffusion in perovskite-related oxides takes place by vacancy migration mechanism [35-39]. Hence, B-site diffusion is facilitated by B-site vacancies, sometimes also promoted by vacancies in A-site. *De Souza et al.* [40] performed atomic simulations on cation migration in LMO. They observed a significant decrease in Mn migration energy from 8eV to 3.5eV after removing La from its saddle point, due to the absence of electro-static repulsion between migrating Mn and La ion which facilitated B-site diffusion [40].

In **Figure 3.11**, Mn diffusivity in LMO is relatively higher than Co in LCO and Fe in LFO due to larger amount of cation vacancies present in LMO system. Inter-diffusion coefficient of Fe in LSC, Co in LSF is 4 to 5 orders of magnitude lower than Mn in LMO, Co in LCO as a result of diffusion affected by chemical environment.

Dissimilar activation energies such as 81kJmol⁻¹, 70kJmol⁻¹ is observed in Mn self-diffusion coefficient measured by tracer annealing and inter-diffusion couple measurements. This dissimilarity in activation energy is attributed to difference in cation vacancy population influenced by the thermal history of a sample gone through in different experimental techniques [36]. It can be the explanation for dissimilar activation energies observed in the self-diffusion coefficients of Co. However, cation diffusion can also be influenced by various other parameters such as bond distance, pressure etc [36, 41].

3.3.5 Influence of thickness on effective diffusion time (t_{eff}) of Mn, Co and Fe cations

Mn, Co and Fe diffusion coefficients obtained from the literature is used to estimate the effective diffusion time (t_{eff}) of a mobile species. Effective diffusion time (t_{eff}) is the time required for a mobile species to cross its characteristic diffusion length [35, 36].

Characteristic diffusion length is nothing but average length (thickness) a mobile species with its characteristic diffusivity can travel through in certain time. The effective diffusion time is given by the following equation,

$$t_{eff} = \frac{l^2}{2D} \quad (3.1)$$

Where t_{eff} is effective diffusion time, l is film thickness or characteristic diffusion length, D is diffusion coefficient of a mobile species.

The effective diffusion time (t_{eff}) estimated for Mn, Co and Fe ions to travel under different thickness from 1nm to 10nm at 700°C is plotted in **Figure 3.12**. Self-diffusion and inter-diffusion coefficients values taken from the literature (**Figure 3.11**) at 700°C has been used to determine t_{eff} .

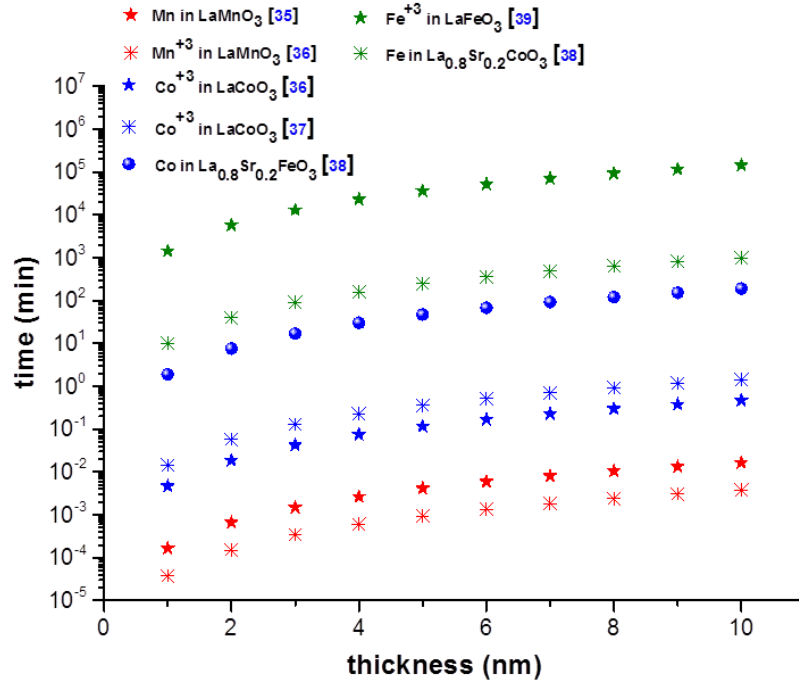


Figure 3.12. Effective diffusion time (t_{eff}) of Mn, Co and Fe cations Vs thickness at 700°C.

In Figure 3.12 the effective diffusion time t_{eff} of Mn is in millisecond range to travel 1nm to 10nm of thickness, while the diffusion time of Co, Fe ions are longer than Mn. The effective diffusion time of Fe in LSC, Co in LSF is longer than Mn in LMO and Co in LCO. In particular, Fe in LFO has the longest diffusion time in all of them. It needs 1 day to 100days to cross a layer with 1nm to 10nm thickness.

In general based on the results obtained in Figure 3.12, the diffusivity of different cations can be arranged as $Mn > Co > Fe$ irrespective of the type of diffusion. Also, the effective diffusion time t_{eff} obtained here for different cation has given a rough value about the critical length range, which can be expected in sub-nm level.

3.4 Validation of interdiffusion mechanism

3.4.1 LSF/LSC multilayer deposition

After optimizing the deposition conditions of parent materials, LSC/LSF multilayer trial deposition is carried out (Figure 3.13) to fabricate $La_{0.8}Sr_{0.2}Co_{0.4}Fe_{0.6}O_{3\pm\delta}$ (LSCF46) thin film with 40% Co and 60% Fe.

The density of LSC is 7.11g/cm³ while LSF is 6.43 g/cm³ and its average area density would be directly proportional to composition. The average area density ρ_a can be

given as $\rho_a = \rho t$. Where ρ is density of the material, t is film thickness. Since the densities of LSC, LSF are almost similar thickness ratio between LSC and LSF layer will directly give Co and Fe concentration.

In order to achieve LSCF film with 40% Co and 60% Fe approximately, LSC and LSF periodic layers are fabricated by controlling LSC with 4nm and LSF with 6nm in each cycle (**Figure 3.13**). It is prepared based on the 1st methodology introduced in **section 3.3.3**.

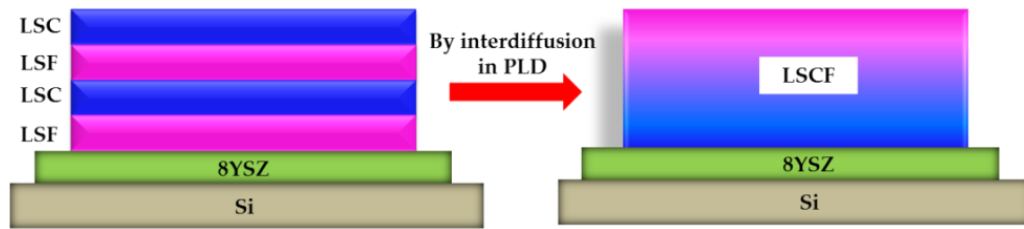


Figure 3.13. Schematic diagram of LSCF phase formation from LSC/LSF ultra-film multilayer in PLD.

These trial depositions are performed to corroborate the influence of critical length (L_c) of parent layers (LSC and LSF) on the purity of final composition LSCF46 achievable through interdiffusion mechanism as discussed in **section 3.3**. The deposition condition optimized in the previous section is applied in these test depositions. The exact depositions conditions are: Temperature $T = 700C$, Pressure $P = 20mT$, Fluency $F = 0.7Jcm^{-2}(LSC)$ and $1.1Jcm^{-2}(LSF)$, target to substrate distance $d = 95mm$, frequency $f = 10Hz$.

Figure 3.14a represents the XRD pattern of the LSCF46 thin film achieved through the interdiffusion between LSC/LSF multilayers, but ended up with a parasitic phase. The impurity phase is indexed as Sr_2FeO_4 and $Sr_3Fe_2O_6$ with tetragonal structure.

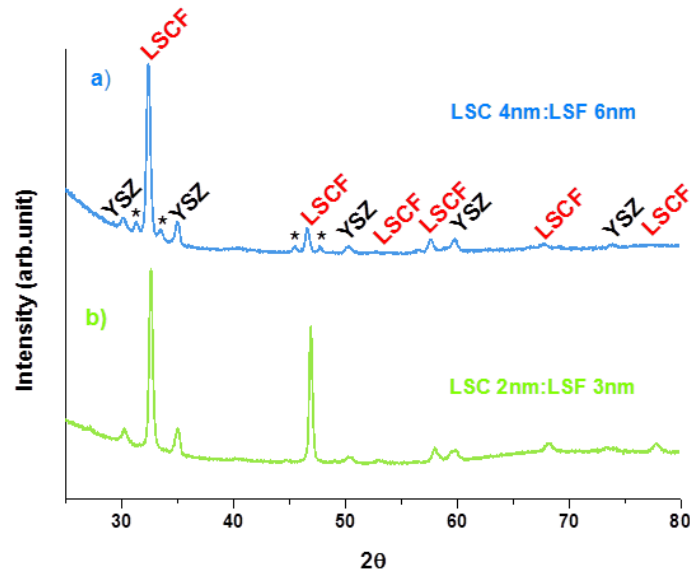


Figure 3.14. XRD pattern of LSC/LSF multilayers with different thickness. *a)* LSC:LSF=4nm:6nm per cycle. Star symbol indicates the parasitic phases such as Sr_2FeO_4 and $\text{Sr}_3\text{Fe}_2\text{O}_6$. *b)* LSC:LSF=2nm:3nm per cycle

A homogeneous mixing between parent material is necessary to attain a final composition without any parasitic phase as explained in **section 3.3.2**. For a homogeneous mixing, the thickness of parent layer should be under or equal to the critical length (L_c). The presence of parasitic phase here exhibits the precipitation of Sr_2FeO_4 and $\text{Sr}_3\text{Fe}_2\text{O}_6$ in LSC/LSF interface resulting from the nucleation-limited intermixing of LSC and LSF multilayers (**case ii** in **section 3.3.2**).

According to effective diffusion time (t_{eff}) predicted for Co, Fe cations in **Figure 3.12**, Fe atom needs 159min to penetrate completely into 4nm thickness of LSC layer, whereas Co atom needs 68min to diffuse into 6nm thickness of LSF layer. The thickness of 4nm LSC, 6nm LSF multilayers may be above critical length L_c hindered the formation of pure LSCF46.

Therefore a second LSC/LSF multilayer test deposition is repeated by reducing LSC/LSF layer thickness two times lower than the first trial deposition. In the second trial, LSC film thickness is maintained as 2nm, LSF as 3nm per cycle. After reducing the thickness, a pure LSCF46 composition is finally achieved through the homogeneous mixing of LSC/LSF multilayers.

Figure 3.14b shows the XRD pattern of pure LSCF46 thin film without any parasitic phase after reducing the thickness. This is due to the thickness of parent layers

(LSC:LSF = 2nm:3nm) may be under critical length L_c in the 2nd trial, might induced homogeneous mixing followed by nucleation step.

3.4.2 LSM/LSC multilayer deposition

Similarly, LSM/LSC multilayer deposition is also carried out to check the compatibility between LSM and LSC layers in attaining the intermediate compositions of LSMC system. Intermediate compositions such as $\text{La}_{0.8}\text{Sr}_{0.2}\text{Mn}_{1-x}\text{Co}_x\text{O}_{3\pm\delta}$ ($x = 0.25, 0.5, 0.75$) are fabricated from the multilayer depositions of LSM and LSC parent materials by controlling the thickness of parent layer under 2nm. The density of LSM is 6.4g/cm^3 and LSM:LSC thickness ratio is maintained as 1.5nm:0.5nm per cycle to fabricate LSMC with $\text{Co} = 0.25$, 1nm:1nm per cycle for $\text{Co} = 0.5$ and 0.5nm:1.5nm per cycle for $\text{Co} = 0.75$.

The XRD pattern acquired from LSMC distinct compositions is given in **Figure 3.15**. which shows that there is good compatibility between LSM and LSC parent layers in the intermediate composition formation LSMC with rich ($x=0.75$) and poor ($x=0.25$) cobalt concentration. Moreover, thickness control of each parent layer under 2nm seems working because there is no secondary phase observed in each LSMC distinct compositions.

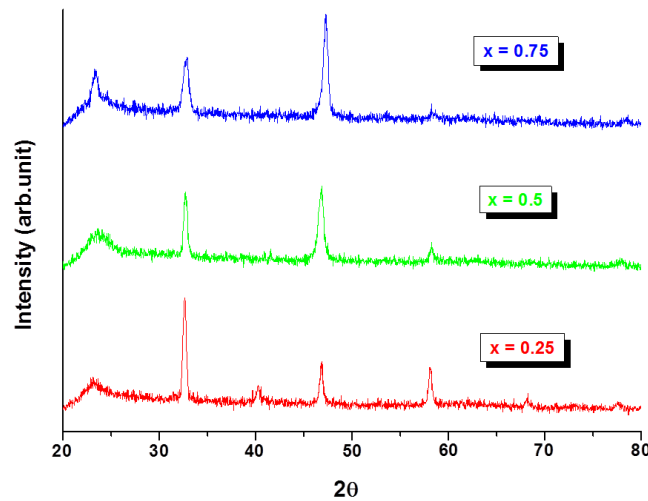


Figure 3.15. XRD pattern of $\text{La}_{0.8}\text{Sr}_{0.2}\text{Mn}_{1-x}\text{Co}_x\text{O}_{3\pm\delta}$ ($x = 0.25, 0.5, 0.75$) distinct compositions obtained from LSM/LSC multilayers.

The above trial deposition validates the significant contribution of critical length L_c on the purity of final product. Also, it validates the 1st methodology introduced in **section 3.3.3** the possibility of attaining a new composition during ultra-thin film

multilayer deposition itself. Hereafter, thickness of parent layer is decided to control below 2nm for combinatorial system fabrication.

3.5 Conclusion

The deposition conditions are optimized in PLD to grow tailored dense, porous, homogeneous and crack-free parent layers. It is found that 700°C is the best common temperature to attain polycrystalline LSM, LSC and LSF layers. 20mT of pressure is an optimum pressure to achieve dense layers while 200mT is preferred for porous layers. The microstructural studies of parent layers are investigated by X-ray diffraction (XRD), Scanning electron microscopy (SEM). Also, interdiffusion mechanism is understood and validated through the experiments on LSC/LSF and LSM/LSC multilayer depositions. It is found that thickness below 2nm to 3nm is an optimum thickness value for growing LSM, LSC and LSF parent layers involved in multilayer deposition in order to achieve desired product from the diffusion-limited homogeneous intermixing.

References

- [1] A. S. Edelstein, R. C. Cammarata, *Nanomaterials: Synthesis, properties and applications*, Taylor and Francis group, New York, USA, 1996.
- [2] P. Dhez, C. Weisbuch, *Physics, fabrication and applications of multilayered structures*, Plenum press, New York, USA, 1988.
- [3] H. E. Cook, J. E. Hilliard, *J. Appl. Phys.*, 1969, 40, 2191.
- [4] L. L. Chang, L. Esaki, W. E. Howard, R. Ludeke, *J. Vac. Sci. Technol.*, 1973, 10, 655.
- [5] J. M. Rondinelli, N. A. Spaldin, *Adv. Mater.*, 2011, 23, 3363.
- [6] K. Chung, C. H. Lee, G. C. Yi, *Science*, 2010, 330, 655.
- [7] C. H. Ahn, K. M. Rabe, J. M. Triscone, *Science*, 303, 488.
- [8] R. Ramesh, N. A. Spaldin, *Nat. Mater.*, 2007, 6, 21.
- [9] M. N. Hyder, S. W. Lee, F. C. Cebeci, D. J. Schmidt, Y. S. Horn, P. T. Hammond, *ACS nano*, 2011, 5, 8552.
- [10] R. Eason, *Pulsed laser deposition of thin films*, John Wiley and sons, New Jersey, USA, 2006.
- [11] M. A. Nicolet, M. Bartur, *J. Vac. Sci. Technol.*, 1981, 19, 786.
- [12] D. G. Schlom, L. Q. Chen, X. Pan, A. Schmehl, M. A. Zurbuchen, *J. Am. Ceram. Soc.*, 2008, 91, 2429.

**III - Interdiffusion mechanism and optimization of LSM,
LSC and LSF deposition by PLD**

- [13] L. W. Martin, Y. H. Chu, R. Ramesh, *Mater. Sci. Eng.*, 2010, 68, 89.
- [14] H. He, Y. Huang, J. Regal, M. Boaro, J. M. Vohs, R. J. Gorte, *J. Am. Ceram. Soc.*, 2004, 87, 331.
- [15] S. P. Simner, J. P. Shelton, M. D. Anderson, J. W. Stevenson, *Solid State Ionics*, 2003, 161, 11.
- [16] K. L. Silva, A. Borger, K. D. Becker, F. Tietz, D. Stover, *Solid State Ionics*, 2011, 192, 552.
- [17] A. Lassman, *Ph.D. Thesis*, University of Connecticut, June, 2011.
- [18] I. Petrov, P. B. Barna, L. Hultman, J. E. Greene, *J. Vac. Sci. Technol.*, 2003, 21, 117.
- [19] F. Tietz, I. A. Raj, M. Zahid, D. Stover, *Solid State Ionics*, 2006, 177, 1753.
- [20] S. M. Zanetti, E. R. Leite, E. Longo, J. A. Varela, *Appl. Organometal. Chem.*, 1999, 13, 373.
- [21] R. V. Wandekar, B. N. Wani, S. R. Bharadwaj, *Solid State Sciences*, 2009, 11, 240.
- [21] Y. Okada, Y. Tokumaru, *J. Appl. Phys.*, 1984, 56, 314.
- [23] S. Giraud, J. Canel, *J. Eur. Ceram. Soc.*, 2008, 28, 77.
- [24] Y. Kimura, T. Kushi, S. Hashimoto, K. Amezawa, T. Kawada, *J. Am. Ceram. Soc.*, 2012, 95, 2608.
- [25] A. Infortuna, A. S. Harvey, L. J. Gauckler, *Adv. Funct. Mater.*, 2008, 18, 127.
- [26] C. Wang, B. L. Cheng, S. Y. Wang, H. B. Lu, Y. L. Zhou, Z. H. Chen, G. Z. Yang, *Thin Solid Films*, 2005, 485, 82.
- [27] P. Plonczak, A. Hutter, M. Sogaard, T. Ryll, J. Martynczuk, P. Hendriksen, L. J. Gauckler, *Adv. Funct. Mater.*, 2011, 21, 2764.
- [28] J. A. Thornton, *Ann. Rev. Mater. Sci.*, 1977, 7, 239.
- [29] P. shewmon, *Diffusion in solids*, McGraw-Hill, New York, USA, 1963.
- [30] P. Heitjans, J. Karger, *Diffusion in condensed matter*, Springer, Heidelberg, Germany, 2005.
- [31] L. Fister, D. C. Johnson, *J. Am. Chem. Soc.*, 1992, 114, 4639.
- [32] M. Noh, J. Thiel, D. C. Johnson, *Science*, 1995, 270, 1181.
- [33] M. Noh, C. D. Johnson, M. D. Hornbostel, J. Thiel, D. C. Johnson, *Chem. Mater.*, 1996, 8, 1625.
- [34] W. Park, L. Fister, D. C. Johnson, J. David Cohen, *J. Appl. Phys.*, 1994, 75, 2294.
- [35] S. Miyoshi, M. Martin, *Phys. Chem. Chem. Phys.*, 2009, 11, 3063.
- [36] M. Palcut, R. Knibbe, K. Wiik, T. Grande, *Solid State Ionics*, 2011, 202, 6.
- [37] A. N. Petrov, L. Y. Rabinovich, V. M. Zhukovskii, A. S. Zhukovskaia, *Dokl. Chem.*, 1987, 292, 18.
- [38] H. Kishimoto, N. Sakai, T. Horita, K. Yamaji, M. Brito, H. Yokokawa, *Solid State Ionics*, 2007, 178, 1317.
- [39] J. B. Smith, T. Norby, *Solid State Ionics*, 2006, 177, 639.
- [40] R. A. De Souza, M. S. Islam, E. Ivers-Tiffée, *J. Mater. Chem.*, 1999, 9, 1621.

- [41] M. Palcut, K. Wiik, T. Grande, *J. Phys. Chem. B.*, 2007, 111, 2299.

Chapter 4

Engineering mixed ionic electronic conduction in nanostructures of $\text{La}_{0.8}\text{Sr}_{0.2}\text{MnO}_{3+\delta}$ through fast grain boundary oxygen diffusivity

Chapter IV

4.1 Chapter outline

The phenomenon of simultaneous conduction of ions and electrons is one that is applied in a wide variety of devices such as batteries [1, 2], fuel cells and electrolyzers [3, 4] and electrochromic displays [5, 6, 7]. Since mixed ionic-electronic conductors (MIECs) are key functional materials in all these solid state devices, novel approaches to improve their ionic/electronic transport properties have attracted increasing attention in recent years [8]. In particular, the search for enhanced ionic conductivity through the design of oxide interfaces has been pursued since *Sata et al.* [9] showed superior anionic conductivity in $\text{CaF}_2/\text{BaF}_2$ heterostructures due to space charge effects. For oxygen ion conductors, another strategy based on the lattice strain generated by multilayering epitaxial films has been proposed to promote an increase in ionic conductivity [10, 11]. However, the implementation of this type of heterostructures still remains a challenge since it is limited to a certain number of substrates and to a lateral architecture. The enhancement of mass and charge transport properties in inherent interfaces, such as grain boundaries (GBs), is therefore clearly advantageous and opens new technological perspectives for GB-dominated materials in advanced devices such as nanoionics-based resistive switching devices [12, 13] or micro-solid oxide fuel cells [14, 15].

While grain boundary diffusion in metals has been widely studied and is reasonably well understood [16], there is a noticeable lack of understanding on this type of ionic diffusion in ceramic materials [17]. In particular, the oxide ion transport along grain boundaries in mixed ionic electronic conductors remains virtually unexplored, primarily due to the limited number of techniques suitable for its direct characterization. However, the fundamental and technological importance of diffusion in this sort of materials requires bridging this knowledge gap, particularly now that a variety of nanostructures can be synthesized and characterized. Because nanomaterials intrinsically contain a high density of grain boundaries, their mass transport properties can be dominated by such grain boundaries [17]. Understanding and controlling this dominant mechanism is obviously interesting for enhancing the electrochemical behavior of catalytic materials but also for avoiding undesirable ionic conductivity that under high dc voltage can cause degradation of electronic components based on thin-

film multilayer technology such as multilayer ceramic capacitors, varistors or oxide transistors [18]. The focus of this work is to analyze the oxygen mass transport properties of $\text{La}_{0.8}\text{Sr}_{0.2}\text{MnO}_{3+\delta}$ (LSM) nanostructures. In bulk form, this compound shows oxygen hyper-stoichiometry with a very low concentration of oxygen vacancies (metal vacancies and electron holes are the predominant defects), making this material a pure electronic conductor [19]. LSM was selected since it is considered a cornerstone material in a wide variety of electrochemical and electronic devices such as solid oxide fuel cells [20] and high-density memories [21], respectively.

4.2 Microstructural Characterization of LSM films

In order to study the dominating transport properties in nanostructured LSM, films with a high density of grain boundaries were prepared by Pulsed Laser Deposition (PLD). PLD is one of the methods of choice for preparing thin films based on complex oxides due to an excellent stoichiometry transfer of the target composition. Moreover, it allows growing fully dense columnar-type nanostructures highly suitable for diffusion studies. We used this technique to grow 100nm $\text{La}_{0.8}\text{Sr}_{0.2}\text{MnO}_{3+\delta}$ /100nm $(\text{ZrO}_2)_{0.92}(\text{Y}_2\text{O}_3)_{0.08}$ (YSZ) heterostructures on (100) silicon substrates passivated with a stress-free combination of amorphous SiO_2 and SiN_x layers. An oxygen partial pressure of 20mT and a substrate temperature of 973 K were employed in the PLD deposition chamber to grow fully dense polycrystalline layers of Ytria-stabilized Zirconia (YSZ) and LSM [22].

The heterostructure was characterized by using X-ray Diffraction (XRD), Scanning and Transmission Electron Microscopy (SEM and TEM), Atomic Force Microscopy (AFM) and Electron Probe X-ray Microanalysis (EPMA).

The XRD patterns all show single phase deposition of polycrystalline YSZ and LSM layers without any noticeable preferential orientation (**Figure 4.1**).

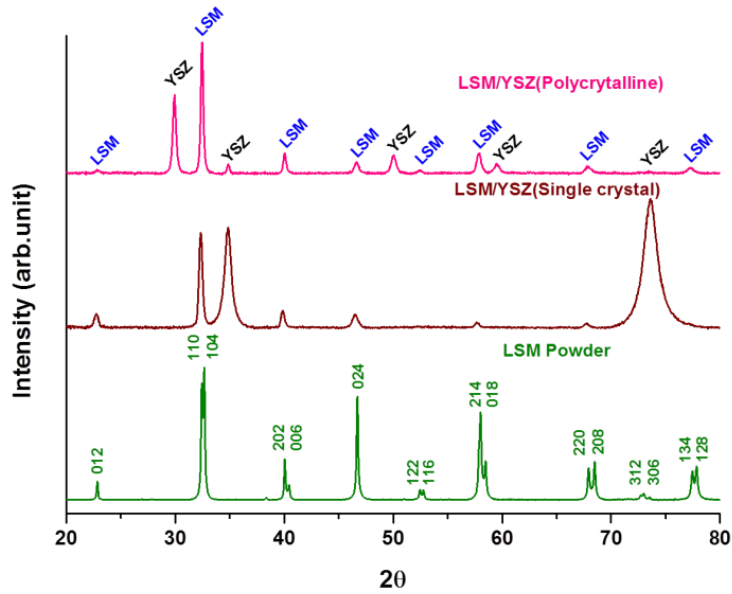


Figure 4.1. Typical XRD diffraction patterns of the LSM deposited on polycrystalline YSZ (employed for IEDP-SIMS experiments) and on YSZ single crystals (employed for EIS experiments).

The patterns in **Figure 4.1** were indexed to a rhombohedral $R3c$ space group with unit cell $a = b = 5.529(2)$, $c = 13.447(3)$ for the LSM/poly-YSZ and $a = b = 5.540(2)$, $c = 13.456(3)$. The diffraction pattern of powder of LSM is included for comparison ($a = b = 5.518(1)$, $c = 13.381(3)$). Crystalline and single phase LSM is observed in both cases. According to the lattice parameters obtained, the deposited films are slightly tensile stressed ($\epsilon < 0.5\%$).

Top view and cross-section SEM pictures (**Figure 4.2a** and **b**) demonstrate the full density of the LSM layers and a columnar-type microstructure with grain sizes in the nanoscale ($d = 16 \pm 7$ nm) and well-defined and vertical grain boundaries with a thickness *ca.* 1nm (**Figure 4.2c**). AFM images of the LSM layer confirm the grain size and yield a surface roughness of $rms = 0.9$ nm. High Resolution TEM (HRTEM) studies reveal the non-homogeneous nature of the LSM columnar grains. Indeed, strain causes distortion at the grain boundaries, which results in the creation of a high density of dislocations in the regions close to the borders (**Figure 4.2d** and **e**).

IV - Engineering mixed ionic electronic conduction in nanostructures of $\text{La}_{0.8}\text{Sr}_{0.2}\text{MnO}_{3+\delta}$ through fast grain boundary oxygen diffusivity

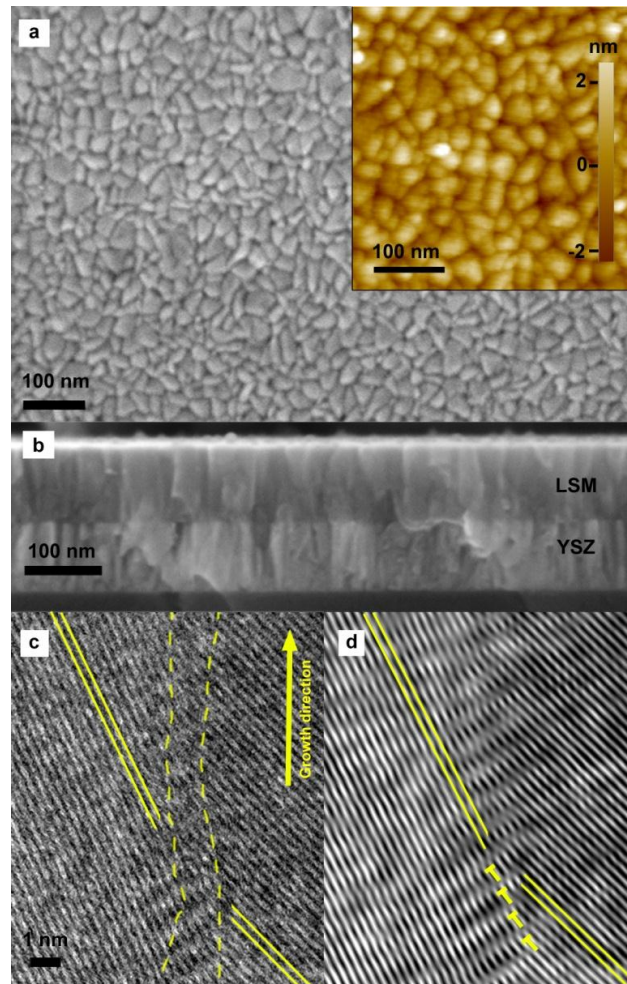


Figure 4.2. *a)* SEM top view image of the LSM dense film deposited by PLD on polycrystalline YSZ. The inset shows an AFM image of the same sample. The color bar refers to the height of the surface. *b)* SEM cross section image of the LSM (100nm) and YSZ (100nm) bilayer deposited by PLD. *c)* and *d)* High resolution TEM and FFT images of the same area and magnification showing a detail of a typical boundary between two LSM grains. Solid lines indicate two families of planes for each grain while the dashed lines represent a guide for the eyes indicating the GB influence region. A high density of dislocations is observed in the GB region, some of them are marked with yellow “T” labels.

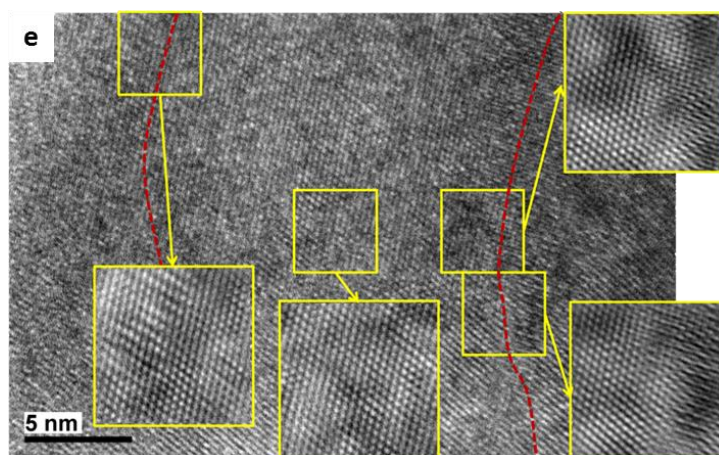


Figure 4.2.e) HRTEM¹ image of three grains of dense LSM (and two grain boundaries represented by red dashed lines). The insets are FFT calculated images corresponding to different regions of the grain interior and grain boundaries. A wave-like contrast caused by lattice strain is clearly observed inside the grain and, more pronounced, close to the borders where likely causes a high dislocation density.

Although the stress is clearly mitigated in the bulk, the grain boundaries are relatively close to each other and that result in a nanodomain texture, with 1-2 nm domains being slightly misoriented from one another.

The stoichiometry of the deposited LSM films was measured by EPMA showing values of 81:19 for the La:Sr ratio.

4.3 Oxygen mass transport study in LSM dense thin films by IEDP-SIMS and EIS techniques

4.3.1 IEDP-SIMS technique

The steps involved in oxygen isotope exchange and the principle and operation of ToF-SIMS is explained elsewhere in **section 2.4.2** in **chapter 2**. The high quality of the multilayer is confirmed by SIMS depth profiling of the different species (**Figure 4.3**).

¹ HRTEM studies were performed by Dr. J. Canales-Vazquez in university of Castilla-la Mancha.

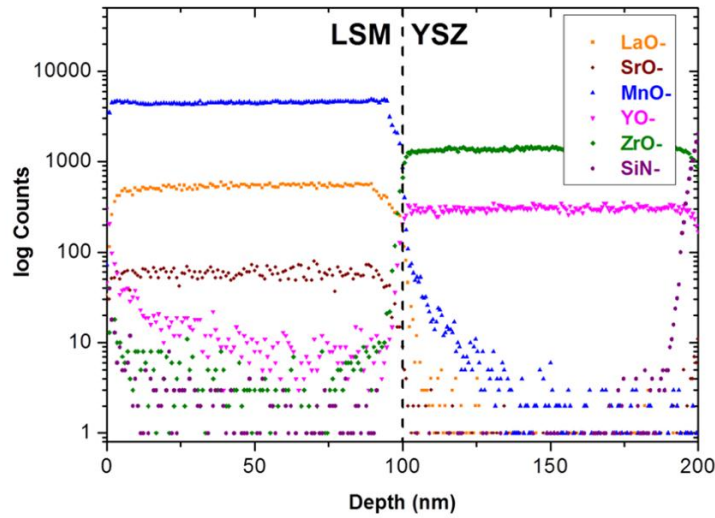


Figure 4.3. Typical SIMS depth profile of the different species contained in the LSM/YSZ bilayer. Sharp interfaces with short interdiffusion close to the LSM/YSZ interlayer can be observed ensuring the high quality of the films.

Sharp interfaces and negligible interdiffusion are observed between the LSM and YSZ layers (**Figure 4.3**). Moreover, this analysis corroborates that dense YSZ layers represent highly efficient diffusion barriers for the silicon coming from the substrate resulting in silicon-free LSM layers.

Although other electrochemical techniques allow measuring mass transport properties, ^{18}O isotope exchange experiments and depth profiling analysis by Secondary Ion Mass Spectroscopy (IEDP-SIMS) is the most direct method to measure oxygen diffusion, in particular when applied to dense mixed ionic electronic conductors in bulk or thin film form [23, 24]. Therefore, to fully understand the oxygen mass transport properties of the prepared heterostructure and calculate the oxygen diffusivity (D^*) and surface exchange coefficients (k^*) of the LSM film, we carried out IEDP-SIMS at different temperatures between 773K and 973K. To avoid oxygen diffusion intake from the backside during the exchange process we employed a silicon wafer substrate, therefore limiting the incorporation of oxygen to the top surface area.

The proper combination of the measured depth profiles of the ^{18}O and ^{16}O ions allowed us to calculate the normalized ^{18}O isotopic fraction (C_x) as a function of the distance to the top surface [23]. High quality data were obtained as illustrated in **Figure 4.4**, which includes a set of isotopic fraction profiles for the whole range of temperature under study. Three regions can be easily distinguished in all profiles

(particularly at low temperatures), namely, a near-surface abrupt decay, a deep-penetrating tail and an unanticipated step at the LSM/YSZ interface (inset in **Figure 4.4**) that results in a higher isotopic concentration in the YSZ layer. This indicates that LSM is not a homogeneous medium since it combines a slow diffusion process limited to a small region close to the surface and a fast diffusion process extended to the YSZ layer.

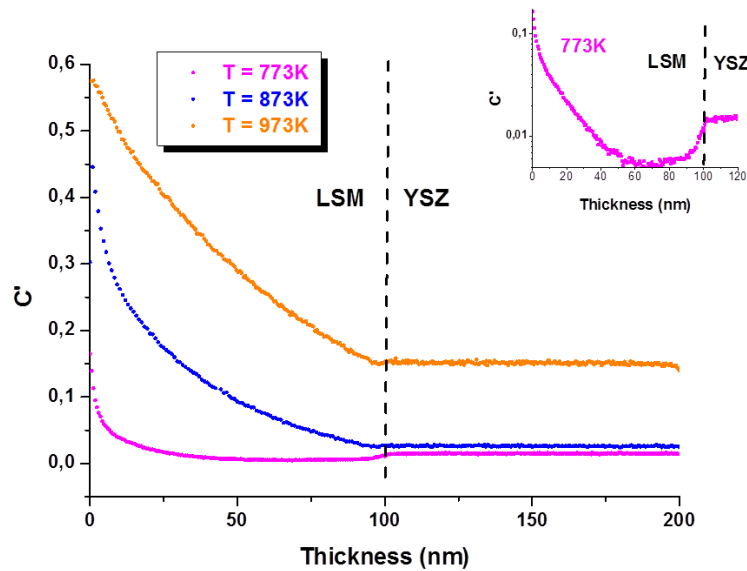


Figure 4.4. Normalized ^{18}O isotope concentration for LSM/YSZ bilayers exchanged at 773, 873 and 973K. Inset shows the enlarged view of ^{18}O concentration profile in LSM layer at 773K.

A higher isotopic concentration in the YSZ layer without accumulation in the LSM layer points toward the existence of narrow fast oxygen diffusion pathways across the LSM film. This is consistent with the columnar-like microstructure obtained by PLD (**Figure 4.2c**) if we consider slow diffusion through the bulk and fast diffusion in the grain boundaries. This model is in agreement with higher oxygen diffusivities for LSM grain boundaries reported by *De Souza et al.* [19].

4.3.2 Finite Element Analysis (FEM) of oxygen diffusion profiles to determine oxygen transport parameters

Since analytical solutions are not available for diffusion in such an inhomogeneous material with finite geometry, the response of an equivalent bilayer was studied by numerical methods using Finite Element Analysis (FEM²) to extract quantitative information of the oxygen transport properties of the bulk and grain boundaries of LSM. Isotope concentration profiles corresponding to the IEDP-SIMS³ experimental

² FEM simulation was performed by Dr. Dolors Pla.

conditions were simulated by FEM for a bilayer consisting of (i) a 100nm thick film exposed to the atmosphere with vertically aligned squared grains of 16nm each side and a typically observed 1nm thick grain boundary [16] (equivalent to the LSM layer) and (ii) a 100nm thick bulk material (corresponding to our YSZ layer). Since YSZ can be considered an oxygen sink in the range of temperatures under study, the oxygen mass transport properties of the LSM layer, i.e. the diffusion and surface exchange coefficients for the bulk (D_b^* and k_b^*) and grain boundaries (D_{gb}^* and k_{gb}^*), were the only parameters to adjust for fitting the experimental and simulated profiles. Previously reported values of the bulk coefficients [19] were employed as a starting point for the adjustment. However, the shape of the simulated profiles was very sensitive to all the involved parameters and it was necessary to slightly modify these bulk coefficients to achieve optimum fittings. Finally, a very good match between experiments and simulations were obtained for the whole range of temperatures (as illustrated in **Figure 4.5a** for T= 823K) yielding a collection of oxygen tracer diffusivities and surface exchange coefficients for bulk and grain boundaries of the nanostructured LSM.

The 3D isotopic concentration maps generated by simulation after fitting the mass transport parameters clearly support the existence of an oxygen diffusion “highway” from the surface to the YSZ through the grain boundaries simply explaining the unexpected step present at the YSZ layer in the IEDP-SIMS³ concentration profiles (see **Figure 4.5b** and **c** for T= 823K).

3

³ IEDP-SIMS measurement was carried out by Dr. Andrea Cavallaro in Imperial College, London.

IV - Engineering mixed ionic electronic conduction in nanostructures of $\text{La}_{0.8}\text{Sr}_{0.2}\text{MnO}_{3+\delta}$ through fast grain boundary oxygen diffusivity

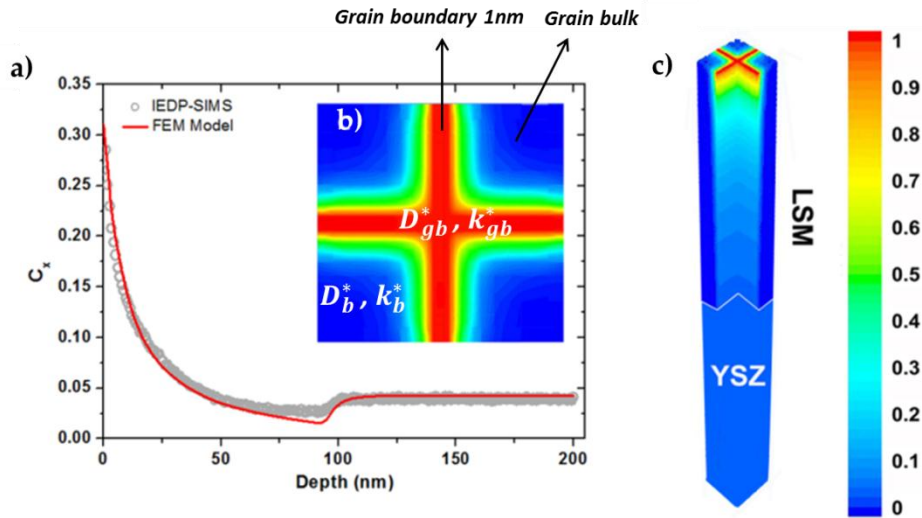
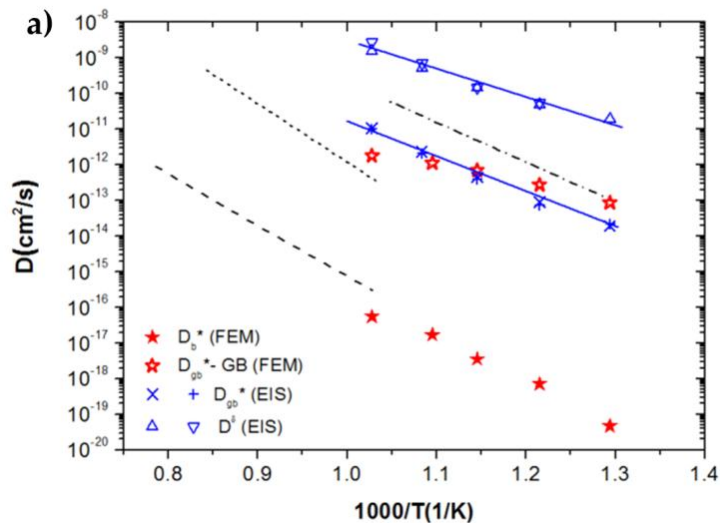


Figure 4.5. a) Normalized ^{18}O isotope concentration and fitted solution to the diffusion equation calculated by FEM for the LSM/YSZ bilayer exchanged at 823 K. b) and c) Top view and cross section of the isotope concentration map for the intersection of four quarters of grain as generated by FEM simulation of the LSM/YSZ bilayer exchanged at 823 K. The image shows a highway for oxygen diffusion along grain boundaries (the scale bar refers to the normalized isotope concentration).

Figure 4.6a and **b** show a representation of the set of oxygen mass transport coefficients obtained by FEM analysis as a function of the reciprocal temperature.



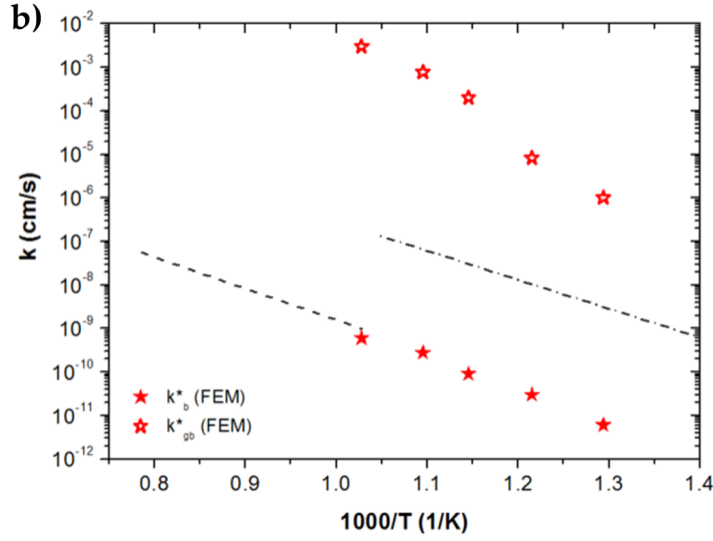


Figure 4.6. a) and b) Arrhenius plot of the oxygen tracer diffusion (D) and surface exchange (k) coefficients of bulk and grain boundary LSM (filled and open stars, respectively) calculated by employing a FEM model to adjust the isotopic concentration profiles measured by IEDP-SIMS. Tracer diffusion coefficients reported in ref [19] for bulk (dashed line) and GB LSM (short dashed line) were included together with bulk values of $\text{La}_{0.8}\text{Sr}_{0.2}\text{CoO}_{3-\delta}$ (dashed dotted line). **a)** Includes GB diffusion coefficients (crosses) and chemical diffusion coefficients (triangles) obtained from EIS measurements for 40 and 180 nm thick dense LSM layers.

The observed straight trends indicate that all the parameters follow an Arrhenius-type behavior. While the values obtained for the bulk coefficients (D_b^* and k_b^*) are consistent with the literature [19] (included in Figure 4.6a and b for comparison), grain boundary properties are orders of magnitude greater. Contrary to the significantly higher activation energy of the GB diffusivity compared to the bulk observed by *De Souza et al.* in micron-sized grain polycrystalline samples [19], the activation enthalpy for D_{gb}^* is smaller than that for D_b^* in our nanostructure. As a consequence, the diffusion through the GBs of the PLD-deposited LSM becomes noticeably higher than that previously published, especially at lower temperatures where an astonishing improvement of up to six orders of magnitude is observed ($T = 773$ K). This accelerated diffusion rate means that, unlike the essentially pure electronic conduction of the bulk, the grain boundaries of LSM possess reasonable oxide ion diffusivity, with values close to those of $\text{La}_{0.8}\text{Sr}_{0.2}\text{CoO}_{3-\delta}$ (see Figure 4.6a).

More interestingly, a superior behavior of the oxygen surface exchange yielded values of k_{gb}^* among the best ones ever reported and within the criteria for good cathodes proposed by Steele ($k^* > 10^{-4} - 10^{-5}$ cm/s) [25] at temperatures as low as $T = 823$ K.

This effective GB oxygen exchange is thought to be enhanced due to the coupling of the oxygen adsorption and dissociation steps, which could occur along the entire LSM surface, with the oxygen incorporation step, mainly occurring in or close to the grain boundaries (with high oxygen vacancy content, see below). The combination of D^* and k^* values places this nanostructure of LSM, with a high density of GBs, among the MIEC materials typically employed as electrodes for SOFCs (see **Figure 4.6b**), making these dense nanostructures of LSM especially interesting for electrochemical applications.

4.3.3 EIS technique

The functionality of these vertically nanostructured thin films was also investigated in conventional two-electrode, supported electrolyte electrochemical cells. Symmetrical cells with 40 and 180nm thick LSM electrodes deposited by PLD on both sides of YSZ single crystal electrolytes were fabricated. PLD deposition conditions were tuned to obtain cells with porous and fully dense (**Figure 4.7a and b**) LSM electrodes to clearly show the transition from a pure electronic to a mixed ionic-electronic conductor.

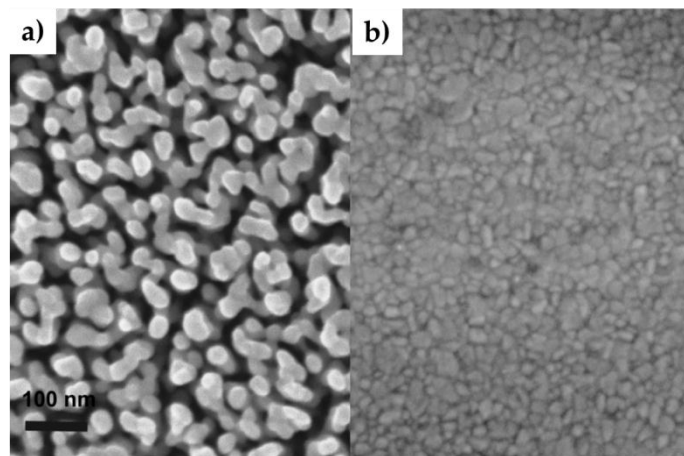


Figure 4.7. a) and b) SEM top view images of porous and dense films of LSM employed for the EIS measurements. The scale bar applies for both images.

It is usually assumed that for porous LSM electrodes with pure electronic conductivity a direct incorporation of oxygen at the triple phase boundary takes placeⁱ (**Figure 4.8**, surface path). However, employing dense electrodes is only possible for materials which operate as MIECs, since the oxygen reduction reaction is limited to the surface and oxide-ion transport to the electrolyte through the electrode is required (**Figure 4.8**, bulk/grain boundary path). The prepared porous and dense LSM/YSZ/LSM symmetrical cells were characterized by using electrochemical impedance spectroscopy

IV - Engineering mixed ionic electronic conduction in nanostructures of $\text{La}_{0.8}\text{Sr}_{0.2}\text{MnO}_{3+\delta}$ through fast grain boundary oxygen diffusivity

(EIS) in the temperature range of 773-973 K and applying ac voltage of 50mV under synthetic air.

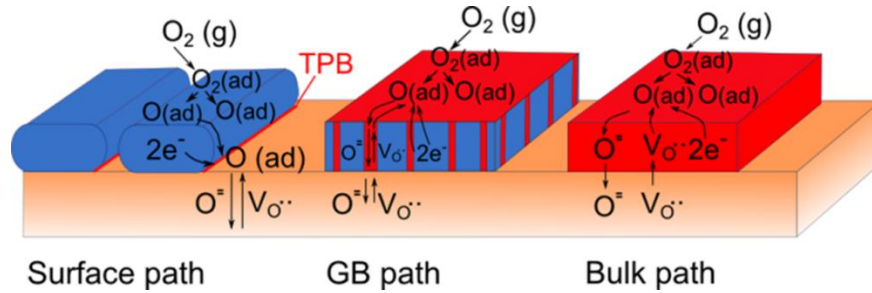


Figure 4.8. Sketches of the three paths of the oxygen reduction and incorporation reactions. The surface path is only available for porous samples while bulk and grain boundary paths are the only option for dense films. The red color indicates the active regions for oxygen adsorption and ionic conduction.

The Nyquist plots in **Figure 4.9** show the contribution of the electrode polarization to the total impedance for porous and dense electrodes of different thickness at 973 K. While porous electrodes yielded lower polarization resistances and a better performance with thickness, dense electrodes present higher resistance with values increasing almost proportionally to the thickness. This clearly indicates that the reactions at the TPB are dominating for the porous samples whereas the oxygen diffusion through the electrode limits the performance of the cells with dense electrodes, i.e. LSM shows a MIEC behavior.

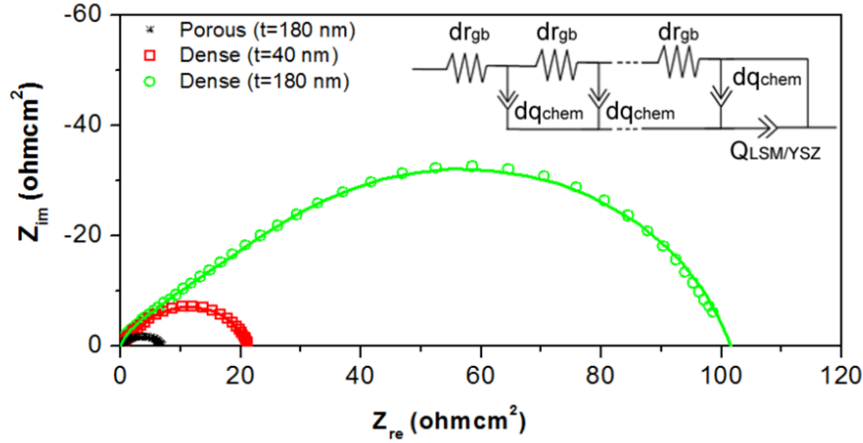


Figure 4.9. Nyquist plot for the electrochemical response of the LSM/YSZ/LSM cells with dense and porous LSM layers with different thickness in air at $T=973$ K. The continuous line presents the fitting of the equivalent circuit sketched in the inset. For clarity, the only contribution shown in the figure is that associated with the electrode polarization (the inductance and series resistance was subtracted by deconvolution).

By adjusting the EIS spectra of the LSM cells with an equivalent circuit recently proposed by *Jamnik et al.* [27] for MIECs (**Figure 4.9**), it was possible to calculate the electrical and chemical diffusion coefficients for the films, D^Q and D^δ , respectively. Moreover, since it is well known that the electrical diffusion coefficient is nearly equal to D^* [28], the tracer diffusion was also easily obtained ($D^Q = D^*/f$, where f is the tracer correlation factor and equal to 0.69[29]). D^* and D^δ obtained from EIS were plotted in **Figure 4.6a**. The excellent agreement between D^* obtained by EIS and the grain boundary diffusion coefficients obtained from the FEM fitting of the IEDP-SIMS experiments, confirms that the electrochemical behavior is clearly dominated by the rapid oxide-ion diffusion along the grain boundaries, i.e. D_{gb}^* . This diffusivity is characterized by an activation energy of $E_{gb}^{D^*} = 1.9(1)$ eV. This value is remarkably below the one reported by *De Souza et al.* [19] for the bulk, $E_b^D = 2.9$ eV, and, more interestingly, for the GBs, $E_{gb}^D = 3.3$ eV. This difference in the activation enthalpy of the GB is clearly associated to the lower degree of order and high dislocation density observed in the shared interface of our columnar grains (see **section 4.2**) [29]. Finally, it is worth mentioning that the chemical diffusion coefficients resulting from EIS are in the same range as the values reported for bulk LSM [30], which indicates that the oxygen stoichiometry changes induced by oxygen diffusivity along GBs take place within the grains.

From the knowledge that the EIS behavior is dominated by the zone of influence of the GBs, the mole fraction of the oxygen vacancies involved in the mass transport can be calculated for the nanostructured LSM thin film ($x_v = D^*/fD^\delta$) [28]. **Figure 4.10** shows the mole fraction (x_v) and concentration of oxygen vacancies (C_v) of the active area as a function of the temperature.

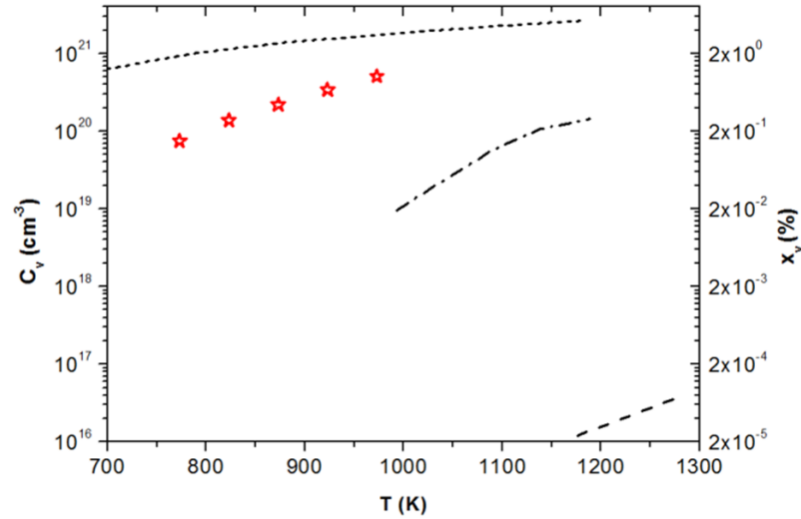


Figure 4.10. Concentration of oxygen vacancies as calculated by EIS measurements for the LSM dense layer. Six order of magnitude of increase is observed with respect to reported bulk LSM [32] (dashed line) and a concentration within the range of the good MIEC LSC family, $\text{La}_{0.9}\text{Sr}_{0.1}\text{CoO}_{3-\delta}$ (dashed dotted line) and $\text{La}_{0.5}\text{Sr}_{0.5}\text{CoO}_{3-\delta}$ (short dashed line) [33].

Contrary to the hyper-stoichiometric bulk LSM with very low concentration of oxygen vacancies [31], GBs of LSM present extremely high vacancy concentration (six orders of magnitude higher) indicating a remarkable oxygen deficiency in these interfaces (with values in the range of excellent MIEC deficient perovskites like the ones of the LSC family [32]). Reverse chemical expansion could be the origin of this vacancy formation since tensile strains, typically present in grain boundaries of slightly tensile stressed thin films [33], could induce oxygen vacancy formation as recently shown by *Jalili et al.* [34]. After vacancy formation, the GB region with high dislocation density (**Figure 4.2d**) would attract these oxygen vacancies defining a preferential fast diffusion pathway along it. Further intensive exploration of the origin of this high vacancy concentration is still required to be able to tailor the GB diffusion properties and therefore reach a fine tunability of the mixed ionic electronic conduction.

4.4 Conclusion

To the best of our knowledge, this is the first time that fast oxide ion diffusivity in grain boundaries has been employed to change the nature of a pure electronic conductor into a MIEC. Our results open the way to the preparation of new families of artificial mixed ionic electronic conductors with tailored properties by engineering nanostructures with an elevated density of highly defective grain boundaries. Controlling the microstructure, grain size and thickness in thin films represents a realistic and simple approach for direct implementation of these nanostructures in high performing devices; therefore, we expect this work to be of particular significance for many technologies that rely on mixed ionic-electronic conductor materials. Besides, we note that fundamental insight into oxide-ionic diffusivity along grain boundaries and oxygen surface exchange of other key technological nanostructured ceramics, particularly those employed in thin film form, deserves a similar intensive exploration by advanced methods.

References

- [1] B. Kang, G. Ceder, *Nature*, 2009, 458, 190.
- [2] J. M. Tarascon, C. Delacourt, A. S. Prakash, M. Morcrette, M. S. Hegde, C. Wurm, C. Masquelier, *Dalton Trans.*, 2004, 2988-2994 (2004)
- [3] J. B. Goodenough, *Nature*, 2000, 404, 821.
- [4] B. C. H. Steele, A. Heinzl, *Nature*, 2001, 414, 345.
- [5] D. T. Gillaspie, R. C. Tenent, A. C. Dillon, *J. Mater. Chem.*, 2010, 20, 9585.
- [6] C. G. Granqvist, *Sol. Energy Mater. Sol. Cells*, 2012, 99 1.
- [7] F. Messerschmitt, M. Kubicek, S. Schweiger, J. M. L. Rupp, *Adv. Funct. Mater.*, 2014, 24, 7448.
- [8] J. Maier, *Nat Mater.*, 2005, 4, 805.
- [9] N. Sata, K. Eberma, K. Eberl, J. Maier, *Nature*, 2000, 408, 946.
- [10] N. Schichtel, C. Korte, D. Hesse, J. Janek, *J. Phys. Chem. Chem. Phys.*, 2009, 1, 3043.
- [11] J. A. Kilner, Ionic conductors: Feel the strain, *Nat. Mater.*, 2008, 7, 838.
- [12] R. Waiser, M. Aono, *Nat Mater.*, 2007, 6, 833.
- [13] J. J. Yang, M. D. Pickett, X. Li, D. A. A. Ohlberg, D. R. Stewart, R. S. Williams, *Nat Nanotechnol.*, 2008, 3, 429.
- [14] M. Tsuchiya, B-K. Lai, S. Ramanathan, *Nat. Nanotechnol.*, 2011, 6, 282.

**IV - Engineering mixed ionic electronic conduction in
nanostructures of $\text{La}_{0.8}\text{Sr}_{0.2}\text{MnO}_{3+\delta}$ through fast grain
boundary oxygen diffusivity**

- [15] I. Garbayo, D. Pla, A. Morata, L. Fonseca, N. Sabate, A. Tarancón, *Energy Environ. Sci.*, 2014, 7, 3617.
 - [16] N. L. Peterson, *Int. Metals Rev.*, 1983, 28, 65.
 - [17] P. Heitjans, S. Indris, *J. Phys.: Condens. Matter.*, 2003, 15, R1257.
 - [18] S. P. Murarka, *Diffusion Barriers in Semiconductor Devices/Circuits*, in: *Diffusion Processes in Advanced Technological Materials*, D. Gupta (Ed.), William Andrew, Inc., Norwich, NY, USA, 2005
 - [19] R. A. De Souza, J. A., Kilner, J. F. Walker, *Mater. Lett.*, 2000, 43, 43.
 - [20] S. P. Jiang, *J. Mater. Sci.*, 2008, 43, 6799.
 - [21] A-M. Haghiri-Gosnet, J-P. Renard, *J. Phys. D: Appl. Phys.*, 2003, 36, R127.
 - [22] A. Infortuna, A. S. Harvey, L. J. Gauckler, *Adv. Funct. Mater.*, 2008, 18, 127.
 - [23] J. A. Kilner, S. J. Skinner, H. H. Brongersma, *J. Solid State Electrochem.*, 2011, 15, 861.
 - [24] M. Burriel, G. Garcia, J. Santiso, J. A. Kilner, J. C. C. Richard, S. J. Skinner, *J. Mater. Chem.*, 2008, 18, 416.
 - [25] B. C. H. Steele, *Mater. Sci. Eng. B*, 1992, 13, 79.
 - [26] J. Fleig, *Ann. Rev. Mater. Res.*, 2003, 33, 361.
 - [27] J. Jamnik, J. Maier, *Phys. Chem. Chem. Phys.*, 2001, 3, 1668.
 - [28] J. Maier, *Solid State Ionics*, 1998, 112, 197.
 - [29] H. Mehrer, *Diffusion in solids: fundamentals, methods, materials, diffusion-controlled processes*, Springer, New York, 2007
 - [30] S. P. S. Badwal, S. P. Jiang, J. Love, J. Nowotny, M. Rekas, E. R. Vance, *Ceram. Int.*, 2001, 27, 431.
 - [31] I. Yasuda, K. Ogasawara, M. Hishinuma, T. Kawada, M. Dokiya, *Solid State Ionics*, 1996, 86-88, 1197.
 - [32] J. Mizusaki, Y. Mima, S. Yamauchi, K. Fueki, *J. Solid State Chem.*, 1989, 80, 102.
 - [33] W. D. Nix, B. M. Clemens, *J. Mater. Res.*, 1999, 14, 3467.
 - [34] H. Jalili, J. W. Han, Y. Kuru, Z. Cai, B. Yildiz, *J. Phys. Chem. Lett.*, 2011, 2, 801.
-

Chapter 5

***Optimization of the combinatorial PLD method
for the study of $\text{La}_{0.8}\text{Sr}_{0.2}\text{Mn}_{1-x}\text{Co}_x\text{O}_{3\pm\delta}$ ($x=0$ to 1)
thin film system***

Chapter V

5.1 Chapter outline

Conventional compositional studies are generally limited by material synthesis procedures and characterization. Much effort has to be devoted for obtaining each material composition and valid characterization methods just for a single composition. Covering a range of compositions consists of a laborious process including trial and error steps, consumption of resources, time and energy.

Therefore a combinatorial approach to material synthesis can be an alternative solution to the traditional methodology [1, 2]. It can accelerate the materials discovery when one wants to correlate functional properties of a multicomponent family. As an example, *Alan et al.* [3] employed a robotic ink-dip printer to prepare a series of 66 compositions of the LSMC family. They followed a discrete combinatorial synthesis (DCS)¹ approach to obtain the LSMC library [4, 5].

Although SOFC materials research is adapted to a modern approach for processing, there is still room for research towards material screening based on a combinatorial approach. A good example of the interest of material screening is on perovskites exhibiting mixed ionic and electronic conducting (MIEC) properties.

In the last two decades much effort has been invested in synthesizing and characterizing new mixed ionic and electronic conducting (MIEC) oxides for low temperature device operation applications such as cathode in SOFCs, oxygen separation membranes, etc [6, 7]. Good oxygen surface exchange and diffusion are the attractive features of MIECs to be implemented as cathodes in SOFCs. Most MIEC exhibits perovskite (ABO_3) structure which support partial aliovalent substitution in A and B-sites to form a multicomponent $\text{A}_{1-x}\text{A}'_x\text{B}_{1-y}\text{B}'_y\text{O}_3$ compound. However, the number of MIEC that displays high catalytic activity towards ORR is less in number [7].

Among them $\text{La}_{0.8}\text{Sr}_{0.2}\text{Mn}_{1-x}\text{Co}_x\text{O}_{3\pm\delta}$ (LSMC) has received much attention for its enhanced oxygen transport properties first revealed by *De Souza et al.* [8, 9] through his ^{18}O isotope exchange depth profiling measurements (IEDP). In this family, Manganese

¹ *DCS approach* is a set of discrete chemical composition is generated from a rapid sequential synthetic technique [4, 5].

V - Optimization of the combinatorial PLD method for the study of the $\text{La}_{0.8}\text{Sr}_{0.2}\text{Mn}_{1-x}\text{Co}_x\text{O}_{3\pm\delta}$ ($x=0$ to 1) thin film system

(Mn) rich members acquire oxygen hyper-stoichiometry while cobalt (Co) rich members have oxygen sub-stoichiometry making it an interesting system to study.

Some studies have been conducted on the influence of Mn replacement by Co (B-site substitution) on the oxygen transport properties of LSMC by various techniques such as Temperature Programmed (TP) measurements [3], Oxygen storage capacity measurements (OSC) [10], Fourier Transform infra-red spectroscopy (FTIR) or X-ray photoelectron spectroscopy (XPS) [11]. In general, an enhancement in oxygen exchange and diffusion properties is observed for Co substitution due to an increment in the oxygen vacancy concentration.

In the above studies LSMC system was mainly synthesized by conventional material processing routes such as reactive grinding [6], glycine nitrate process [11], sol-gel method [12], etc.

In this chapter, continuous composition spread (CCS) [4, 5] approach is followed to fabricate an LSMC pseudo-binary system in thin film form by PLD multilayer deposition, in which thickness and composition are the two parameters that vary spatially. Also, a new methodology is introduced in this chapter to predict thickness and composition distribution maps from the knowledge of the PLD deposition of the parent compound layers.

The combinatorial approach is based on the overlapping of PLD plumes of parent materials and the prediction of thickness and Mn/Co relative concentration from the resulting output. Each step involved in that methodology is detailed in **section 5.2**. Following this methodology, a real CCS combinatorial of the LSMC system is fabricated, with a prior knowledge gained on the prediction of resultant thickness and composition distribution from parent material superposition study. LSMC pseudo-binary system fabrication is explained in **section 5.4**.

The microstructural characterization of combinatorial maps are carried out by various experimental techniques. Structural studies are carried out by XRD and Raman analysis (**section 5.5.1** and **5.5.2**). Sample morphology is studied by AFM (**section 5.5.3**). Thickness distribution is studied by SEM and Raman while composition distribution is studied by EDS, WDS techniques (**section 5.5.4** and **5.5.5**). In **section 5.6** theoretically predicted thickness and composition distribution is compared with experimentally obtained values in order to validate the methodology introduced in this work.

According to the flowchart presented in the introduction (**Figure 1.10 in chapter 1**) the studies such as combinatorial sample fabrication and sample microstructural characterization are covered in the current chapter.

5.2 LSM and LSC thickness map

5.2.1 Large-area LSM and LSC deposition and sample preparation

The deposition conditions to grow dense LSM and LSC thin films have already been optimized in the previous chapter. Following the preliminary optimizations of individual materials in PLD, the LSM and LSC thickness map study is conducted as a subsequent step for performing the LSM and LSC plume superposition optimization.

To generate LSM and LSC thickness plume maps, samples with individual layers of LSM and LSC plumes are deposited on 4-inch Si wafer, with the same deposition conditions optimized for dense microstructures in **chapter 3**. As shown in the **Figure 5.1** for LSM, both LSM and LSC plumes obtained through PLD deposition are elliptical in shape due to the influence of energy distribution in the laser focalization spot [13]. We assumed that the whole plume is symmetrical in shape and has a half-Gaussian thickness distribution including the maximum thickness region called “plume center”.

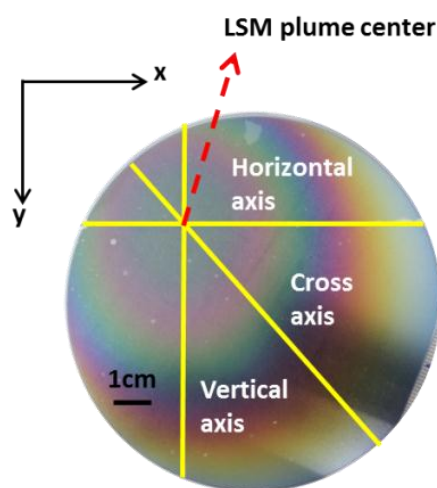


Figure 5.1. LSM plume deposited on 4" silicon wafer. The yellow line represents the axis selected for thickness measurement. The place where the three axes meet each other is the plume center with maximum thickness.

The plume consists of elliptical shaped multicolored concentric rings (**Figure 5.1**) corresponding to a thickness variation or thickness gradient in the LSM layer. Dark

V - Optimization of the combinatorial PLD method for the study of the $\text{La}_{0.8}\text{Sr}_{0.2}\text{Mn}_{1-x}\text{Co}_x\text{O}_{3\pm\delta}$ ($x=0$ to 1) thin film system

green colored central ring is the plume center intentionally located at $\approx 2.5\text{cm}$ in x-y plane (top-left) which has the maximum thickness of 240nm as determined from SEM.

It is possible to generate a whole thickness map by interpolation of experimental points, just with the thickness information along certain axes. Therefore, in the elliptical shaped plume, three axes (yellow lines in **Figure 5.1**) are selected for thickness determination by SEM. The vertical line represents “major or vertical axis” while horizontal line represents “minor or horizontal axis” of the ellipse. One more axis is called “cross axis”, which is an intermediate axis passing through vertical and horizontal lines at 45° .

After precisely choosing and marking the axis lines in LSM and LSC parent depositions, samples were cleaved along these lines by defining trenches in the back side of the Si wafer (**Figure 5.2**) using an automatic dicing saw machine (without damaging the layer deposited on the top of the Si wafer).

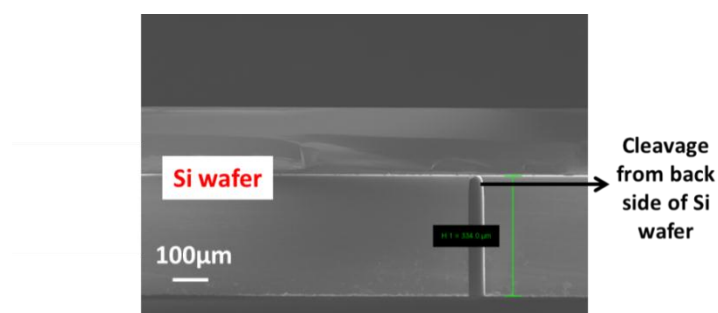


Figure 5.2. SEM cross section image depicts cleaved part in the back side of Si wafer.

5.2.2 Thickness determination by SEM and micro-Raman analysis

After cleavage of the samples, thickness is measured along the horizontal, vertical and cross axis by SEM every 5mm (**Figure 5.3**). Thickness values below 25nm thickness were difficult to precisely determine, therefore thickness measurements were only performed where the thickness was higher than this value (≈ 20 to 25nm).

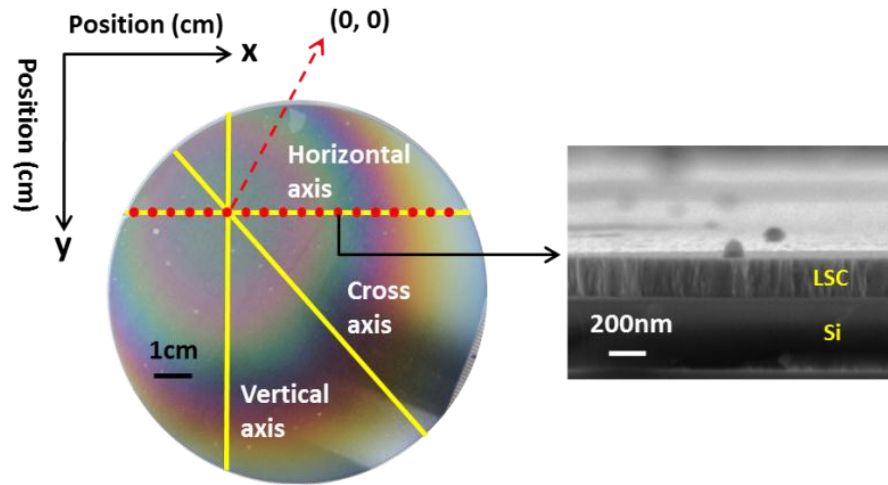


Figure 5.3. Sample with LSM plume deposited on Si wafer. The red dots represent the place where thickness was measured by SEM and μ -Raman along horizontal axis. SEM cross section image of LSC layer located at 5.5cm from the plume center along horizontal axis.

For measuring these ultra-thin layers present at the axis end (wafer edge), where it is not possible to obtain accurate thickness by SEM technique, μ -Raman can be an alternative technique. In addition, with μ -Raman is possible to measure thin film thickness in the nm level without destroying the sample.

Figure 5.4 illustrates the thickness determination by μ -Raman analysis based on Beer's law of attenuation [14]. According to Beer's law, when the laser employed for the Raman modes excitation hits the sample surface, the out coming substrate intensity is attenuated exponentially by any thin film deposited on top of the substrate [14, 15]. The post-attenuation of the substrate's Raman intensity is proportional to the thickness and absorption coefficient of the top layer, which can be written as,

$$\ln[I/I_0] = -2\alpha t \quad (5.1)$$

Where $\ln[I/I_0]$ represents natural logarithmic value of relative intensity of the substrate, I is the substrate intensity with top layer, I_0 is the substrate intensity without top layer, α is the absorption coefficient of the top layer (that can be obtained from the slope of **equation 5.1**) and t is the film thickness. In this work, the top layer is LSM or LSC deposited by PLD and the substrate is Si wafer.

V - Optimization of the combinatorial PLD method for the study of the $\text{La}_{0.8}\text{Sr}_{0.2}\text{Mn}_{1-x}\text{Co}_x\text{O}_{3\pm\delta}$ ($x=0$ to 1) thin film system

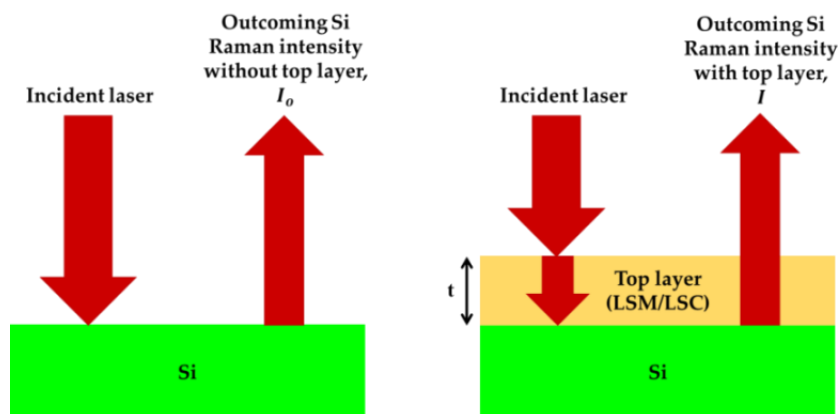
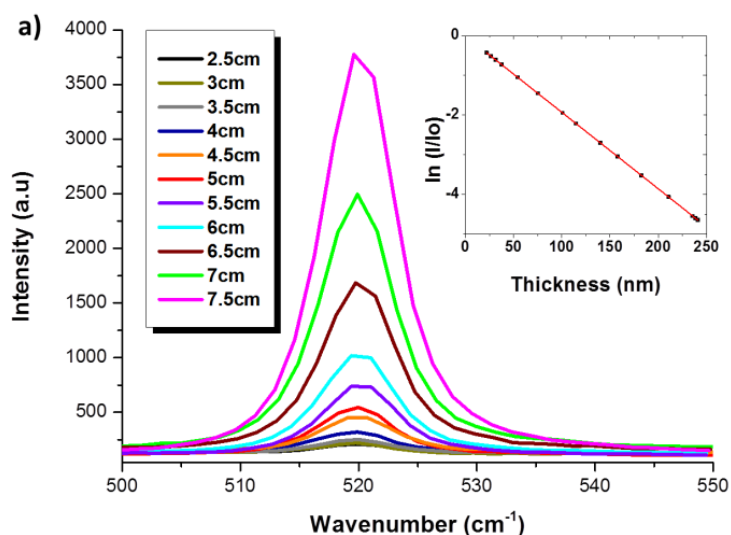


Figure 5.4. Illustration of thickness determination by μ -Raman analysis from the substrate signal attenuation.

The μ -Raman measurement was therefore performed along the aforementioned three axes every 5mm (in the same place where SEM measurements were carried out). Post-processing of Raman spectra were carried out for base-line and peak-shift corrections. A collection of Raman spectra for different points of the LSM and LSC parent depositions is presented in **Figure 5.5a** and **b**.



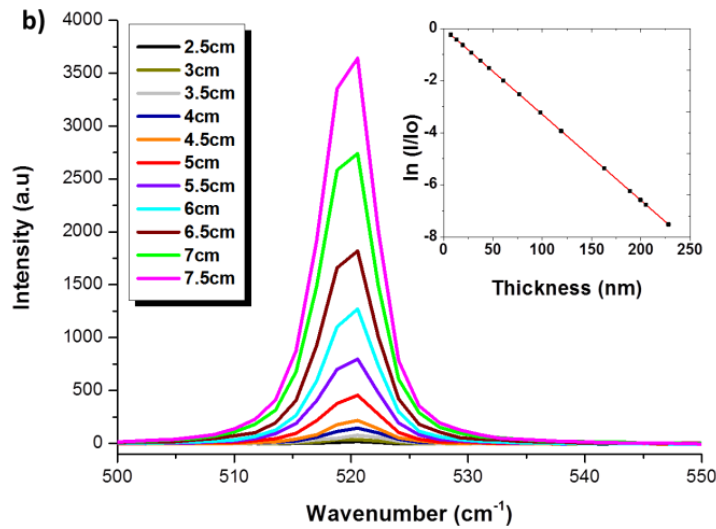


Figure 5.5. The attenuation of the major Si peak intensity due to thickness variation along horizontal axis of **a)** LSM **b)** LSC deposition. Natural logarithm of the relative intensity of Si is plotted against thickness in the inset.

The prominent peak for Si is positioned at 520cm^{-1} . This is the peak used as a reference to determine the LSM and LSC thickness by employing its relative intensity I/I_0 (equation 5.1).

Figure 5.5a and **b** indicates the evolution of the Si peak intensity along horizontal axis of LSM and LSC individual depositions, which clearly depicts the thickness variation of parent layers along the horizontal axis. There are ultra-thin layers at the wafer edges $\approx 7.5\text{cm}$ which emits strong Si signal. This is due to a weak attenuation of the substrate Si signal by ultra-thin parent layers. In opposite, Si intensity coming out from the plume center positioned at 2.5cm is very weak due to a strong attenuation of the Si signal in the thickest region (plume centers) of the sample.

Insets in **Figure 5.5a** and **b** illustrate the relative intensity of Si signal, its attenuation over thickness variation along the horizontal axis of LSM and LSC plumes which obey Beer's law of attenuation. The α value obtained from **equation 5.1** for LSM layer is 0.019nm^{-1} while for LSC it is 0.032nm^{-1} .

5.2.3 LSM and LSC thickness map

Thickness distribution information acquired by SEM (along three axes) was used for the interpolation of this discrete data in order to generate the LSM and LSC thickness maps (**Figure 5.6** and **5.7**).

V - Optimization of the combinatorial PLD method for the study of the $La_{0.8}Sr_{0.2}Mn_{1-x}Co_xO_{3\pm\delta}$ ($x=0$ to 1) thin film system

Thickness was interpolated on the x-y plane using 2D Gaussian functions. Gaussian function was used because of the Gaussian nature of the original thickness distribution of the angular distribution of a plasma as explained in plume expansion dynamics in **section 2.2.1.2 in chapter 2**.

The following equation represents the 2D Gaussian function used for the thickness fitting of the LSM and LSC depositions.

$$Z_{LSM}(x, y) = Z_o + A \exp \left[-\frac{(x - x_c)^2}{2 w_1^2} - \frac{(y - y_c)^2}{2 w_2^2} \right] \quad (5.2)$$

$$Z_{LSC}(x, y) = Z_o + A \exp \left[-\frac{(x - x_c)^2}{2 w_1^2} - \frac{(y - y_c)^2}{2 w_2^2} \right] \quad (5.3)$$

Where Z stands for thickness, $Z_{LSM}(x, y)$, $Z_{LSC}(x, y)$ represents thickness of LSM, LSC layer at a particular point (x, y) in their respective plumes. $Z_o, A, x_c, y_c, w_1, w_2$ are constants. A represents amplitude, x_c, y_c represents position of plume centers, w_1, w_2 represents Full-Width Half Maximum (FWHM) in x and y axis.

Table 5.1: Summary of fitted parameters and error obtained from 2D Gaussian fitting of LSM, LSC thickness.

2D Gaussian function parameters	LSM		LSC	
	Fitted parameters	Error (\pm)	Fitted parameters	Error (\pm)
Z_o	15	2	14	1
A	221	2	201	2
x_c	2.46	0.05	2.49	0.05
w_1	2.90	0.06	2.59	0.06
y_c	2.45	0.07	2.56	0.06
w_2	3.48	0.08	3.11	0.07

V - Optimization of the combinatorial PLD method for the study of the $\text{La}_{0.8}\text{Sr}_{0.2}\text{Mn}_{1-x}\text{Co}_x\text{O}_{3\pm\delta}$ ($x=0$ to 1) thin film system

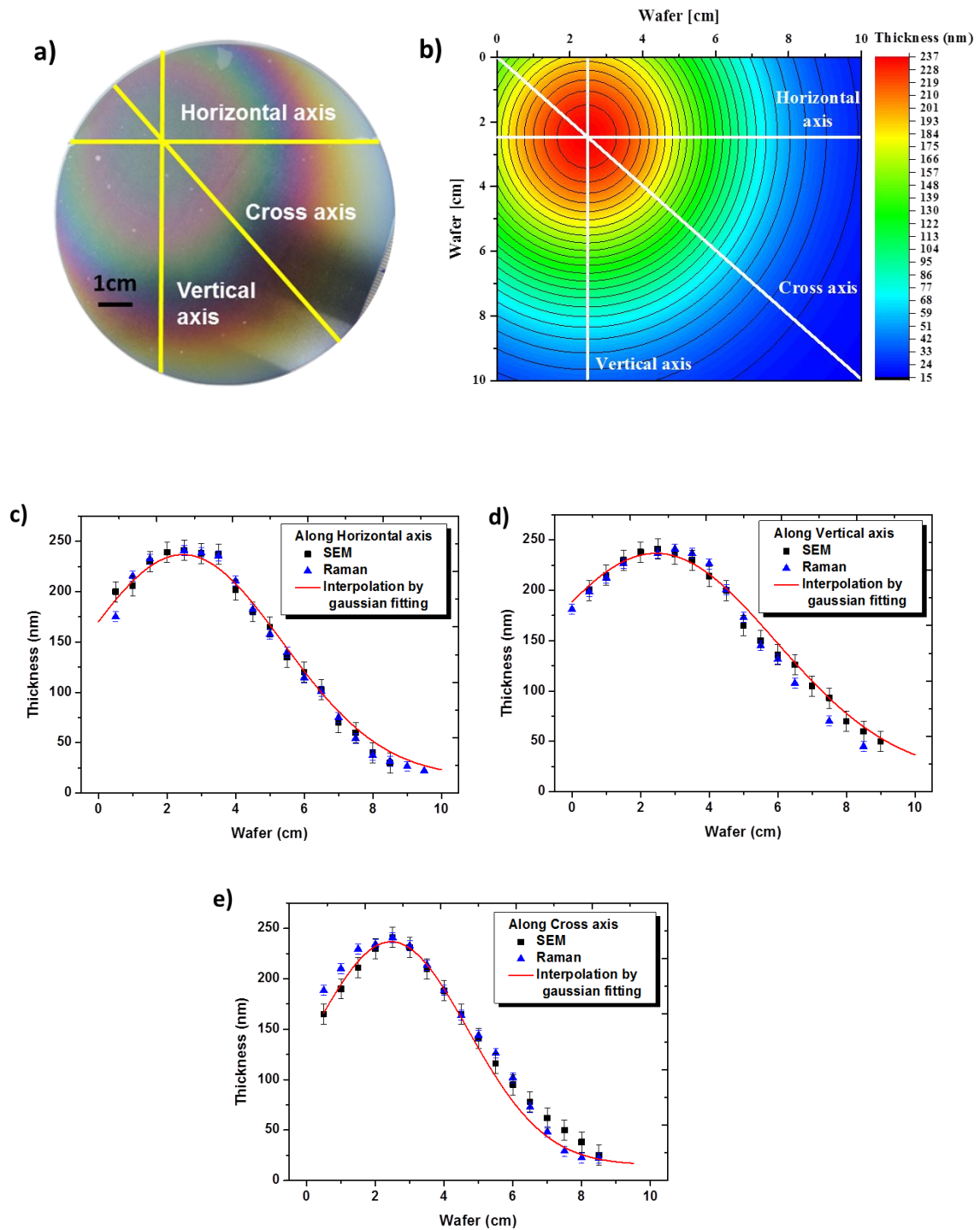


Figure 5.6. Thickness map study in LSM layer a) Sample with LSM plume positioned at the left corner of the Si wafer b) LSM thickness plume map obtained by interpolation using Gaussian function. Color bar represents thickness. c) d) e) Thickness obtained along horizontal, vertical, cross axis by SEM values obtained from μ -Raman is compared with thickness obtained by Gaussian interpolation.

V - Optimization of the combinatorial PLD method for the study of the $\text{La}_{0.8}\text{Sr}_{0.2}\text{Mn}_{1-x}\text{Co}_x\text{O}_{3\pm\delta}$ ($x=0$ to 1) thin film system

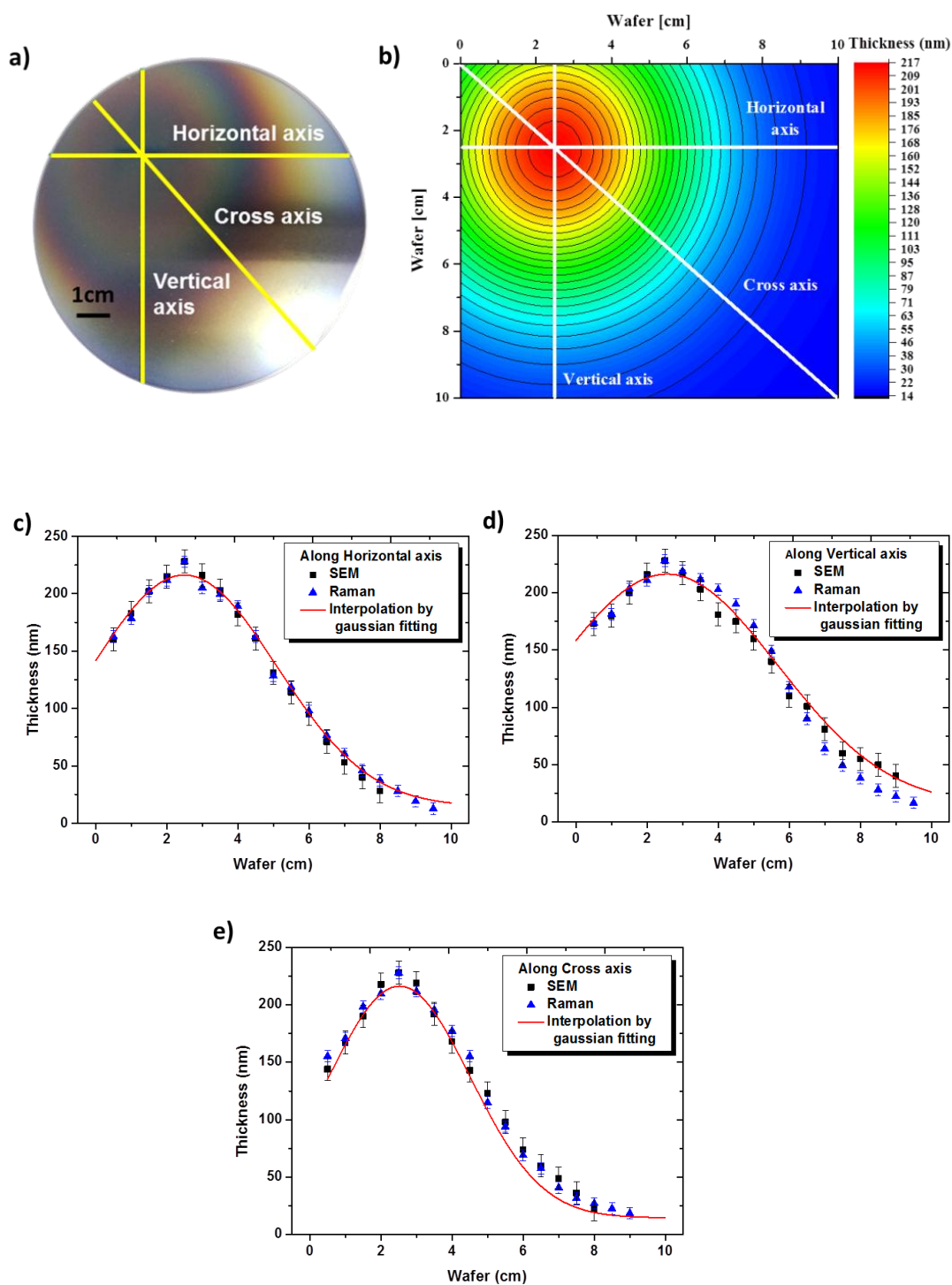


Figure 5.7. Thickness map study in LSC layer **a)** Sample with LSC plume positioned at the left corner of the Si wafer **b)** LSC thickness plume map obtained by interpolation using Gaussian function. Color bar represents thickness. **c) d) e)** Thickness obtained along horizontal, vertical, cross axis by SEM values obtained from μ -Raman is compared with thickness obtained by Gaussian interpolation.

V - Optimization of the combinatorial PLD method for the study of the $\text{La}_{0.8}\text{Sr}_{0.2}\text{Mn}_{1-x}\text{Co}_x\text{O}_{3\pm\delta}$ ($x=0$ to 1) thin film system

The LSM and LSC thickness maps generated by interpolation using **equations 5.2** and **5.3** are plotted in **Figure 5.6b** and **5.7b**. The color bar represents thickness in nm, in which red color indicates maximum thickness i.e. plume center region. These thickness maps resemble their respective samples **Figure 5.6a** (LSM/Si wafer) and **Figure 5.7a** (LSC/Si wafer) in terms of shape and size of the plume.

In **Figure 5.6c, d, e** and **Figure 5.7c, d, e** the thickness measured along horizontal, vertical, and cross axis by experimental techniques such as SEM and μ -Raman (with error bar) are gathered together with the thickness fitted through Gaussian interpolation along the same axes.

The maximum thickness of LSM and LSC at the plume centers estimated from SEM is 240nm and 228nm. In the wafer edges of both plumes, the minimum thickness is always in the range between 1nm to 25nm according to SEM and μ -Raman results.

In general, thickness estimated by SEM is in good agreement with the one obtained by μ -Raman and with the thickness obtained by Gaussian fitting. These results confirm the possibility of attaining a whole thickness map by a non-destructive technique such as Raman and to use an analytical function to define the shape by using a limited number of experimental values. Having an analytical function allowed to combine different materials and plume center position to predict the thickness (composition) map of the resulting layer (see next section).

5.3 Optimization of plume center position from superposition of LSM and LSC layers

The LSM and LSC thickness maps comprise crucial information, as it allows to predict the thickness and composition distribution resulting from the superposition of the two plumes as a function of plume position.

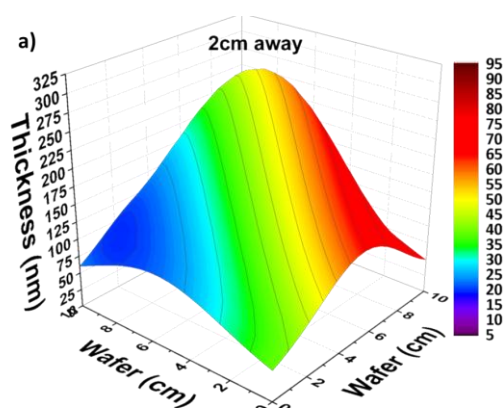
For this, we assume that the overlapping of LSM and LSC plume gives rise to a layer in which the thickness at every point is the sum of the thickness of parent layers separately. Positioning the center of the Gaussian distribution at different distances will generate different thickness profile of the combinatorial layer. Therefore, the resultant thickness will directly give a thickness distribution map. Since the density of LSM and LSC (LSM = 6.4g/cm³; LSC = 7.11g/cm³) are almost similar, the thickness ratio will directly give a compositional map of a combinatorial system.

V - Optimization of the combinatorial PLD method for the study of the $\text{La}_{0.8}\text{Sr}_{0.2}\text{Mn}_{1-x}\text{Co}_x\text{O}_{3\pm\delta}$ ($x=0$ to 1) thin film system

Parent compounds superposition is carried out between LSM and LSC, by varying their plume center positions at different places on the Si wafer. LSM and LSC thickness maps are normalized to 180nm maximum thickness.

LSM and LSC plume centers are kept in a way that their cross axis face each other on x-y plane. This is the axis where almost have the whole range of composition $\text{La}_{0.8}\text{Sr}_{0.2}\text{Mn}_{1-x}\text{Co}_x\text{O}_{3\pm\delta}$ ranges from i.e. $x \approx 0$ to 1 attained from the maximum to the minimum thickness of LSM and from the minimum to the maximum thickness of LSC. This main axis will be called as “**central axis**” for the convenience. The plume center position of each material and the distance between plume centers are considered the parameters to modify to control the compositional map. A first analysis of the final compositional map is obtained by changing the distance between LSM, LSC plume centers in 2cm, 4cm, 6cm, 7cm, 8cm, 9cm.

The resultant thickness and concentration distribution obtained from the double deposition is given as 3D plot in **Figure 5.8a** to **5.8g** where x-y plane represents 4-inch wafer (position in cm). Z-axis represents the resultant thickness obtained at different plume center positions which gives an overview about thickness and concentration distribution of different LSMC possible systems. The color bar in right hand side represents Co percentage relative to Mn. When the distance between LSM and LSC plume centers are varied, there is a change in the resultant thickness and a Co concentration distribution can be observed.



V - Optimization of the combinatorial PLD method for the study of the $\text{La}_{0.8}\text{Sr}_{0.2}\text{Mn}_{1-x}\text{Co}_x\text{O}_{3\pm\delta}$ ($x=0$ to 1) thin film system

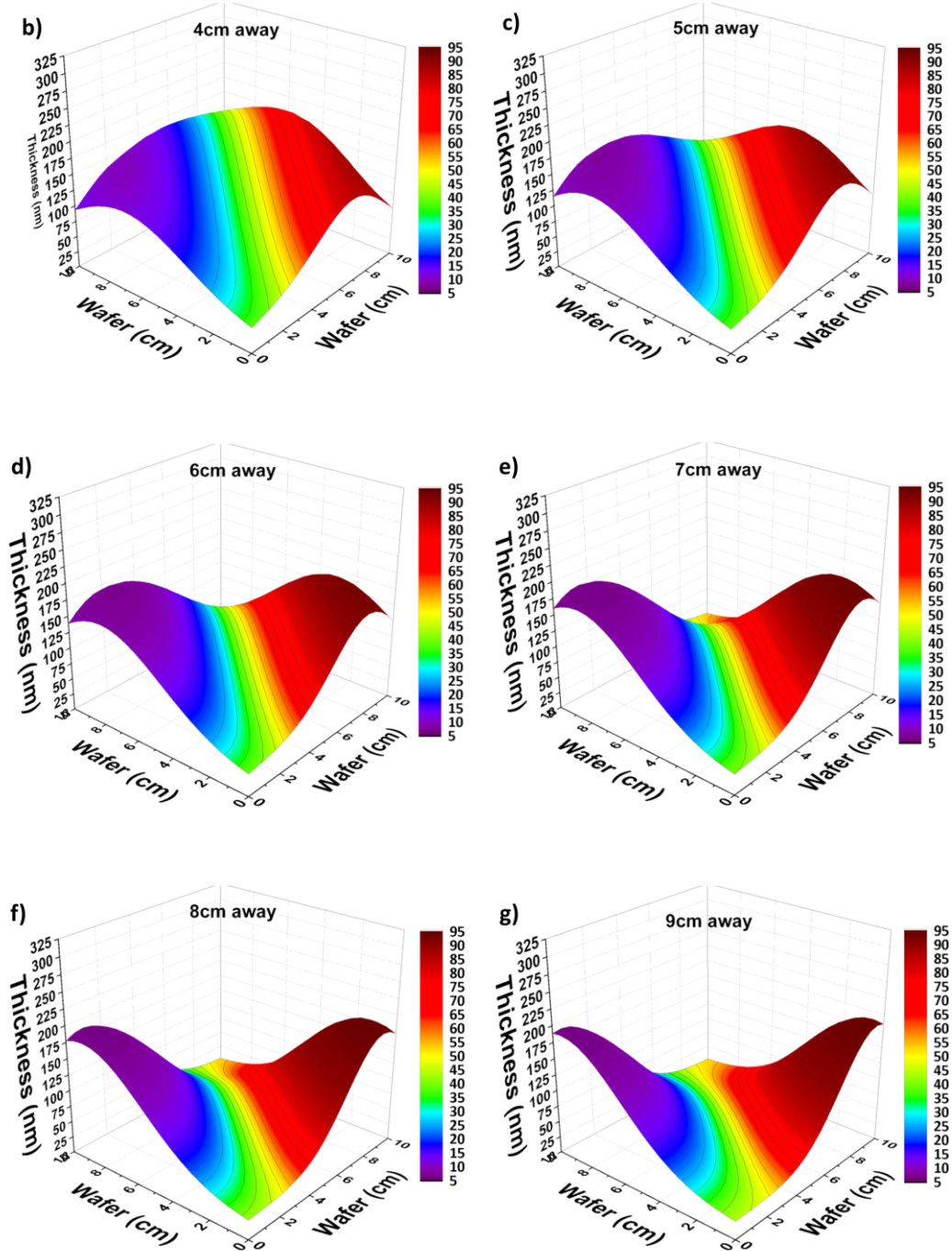


Figure 5.8. Resultant thickness, concentration distribution map when the distance between LSM and LSC plume centers is **a)2cm b)4cm c)5cm d)6cm e)7cm f)8cm g) 9cm**. x-y axis represents position in cm, z-axis represents thickness, color bar represents Co relative concentration to Mn. The thickness maxima at the two ends in longitudinal direction represents LSM (left), LSC (right) plume centers.

V - Optimization of the combinatorial PLD method for the study of the $\text{La}_{0.8}\text{Sr}_{0.2}\text{Mn}_{1-x}\text{Co}_x\text{O}_{3\pm\delta}$ ($x=0$ to 1) thin film system

It is convenient to have a well spread variations in composition in order to have larger areas which can be considered as homogeneous in composition. Therefore, there are two important parameters such as thickness and concentration gradient that have to be carefully considered in the plume position optimization to obtain a sample with reasonable concentration gradient. In the following section the influence of the plume center position on the thickness and Mn/Co distribution is discussed.

5.3.1 Effect of plume center position on thickness and Co concentration distribution

The resultant thickness emerged as a result of different plume center distance is plotted against wafer position in **Figure 5.9**.

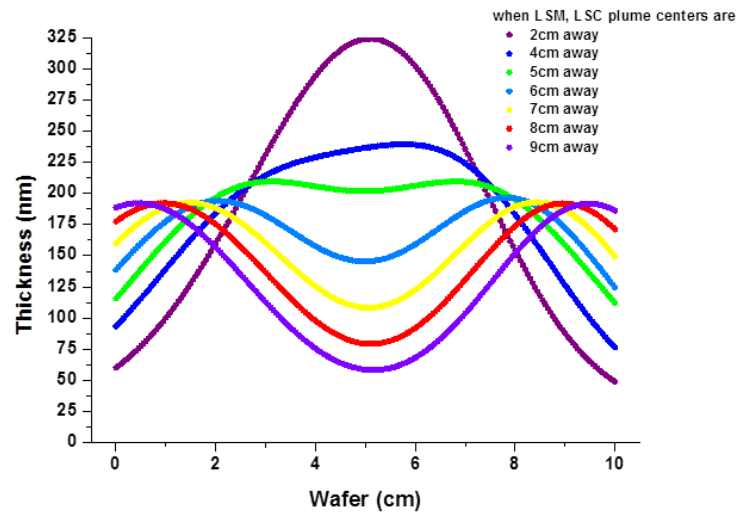


Figure 5.9. Resultant thickness along central axis Vs different plume center position.

It is observed that, moving the plumes farther away from 2cm to 9cm each other causes a dip in thickness which is due to the mixing of thickness present in the gradient and corner region of the Gaussian profile **Figure 5.6** and **Figure 5.7**. In opposite, the dip is vanished when plumes are moved closer each other from 9cm to 2cm, which is due to the mixing of plume center portions mainly.

The resultant thickness given in **Figure 5.9** were obtained by adding the Gaussian functions of two plumes which can be written as,

$$Z_{res}(x, y) = Z_{LSM}(x, y) + Z_{LSC}(x \pm \Delta x, y \pm \Delta y) \quad (5.4)$$

V - Optimization of the combinatorial PLD method for the study of the $La_{0.8}Sr_{0.2}Mn_{1-x}Co_xO_{3\pm\delta}$ ($x=0$ to 1) thin film system

where $Z_{res}(x, y)$ represent resultant thickness at certain point (x, y) in z -direction when the thickness at specific points in LSM plume $Z_{LSM}(x, y)$, LSC plume $Z_{LSC}(x \pm \Delta x, y \pm \Delta y)$ are superimposed each other.

Similarly, Mn/Co relative percentage at certain point can be obtained from the ratio of LSM or LSC layer thickness at particular point to the resultant thickness at that point. The following equation is used to determine Mn/Co relative percentage,

$$Mn\%(x, y) = \frac{Z_{LSM}(x, y)}{Z_{res}(x, y)} \times 100 \quad (5.5)$$

$$Co\%(x, y) = \frac{Z_{LSC}(x \pm \Delta x, y \pm \Delta y)}{Z_{res}(x, y)} \times 100 \quad (5.6)$$

$$ie. Co\%(x, y) = 100 - Mn\%(x, y) \quad (5.7)$$

Where $Mn\%(x, y)$ and $Co\%(x, y)$ represents the relative percentage of Mn and Co content at a certain point (x, y) . $Z_{LSM}(x, y)$ represents LSM thickness Z_{LSM} at (x, y) , $Z_{LSC}(x \pm \Delta x, y \pm \Delta y)$ represents LSC thickness Z_{LSC} at $(x \pm \Delta x, y \pm \Delta y)$, $Z_{res}(x, y)$ represents resultant thickness Z_{res} at (x, y) .

The thickness and composition distribution values obtained along central axis at different plume center distance is compiled in the following table.

V - Optimization of the combinatorial PLD method for the study of the $\text{La}_{0.8}\text{Sr}_{0.2}\text{Mn}_{1-x}\text{Co}_x\text{O}_{3\pm\delta}$ ($x=0$ to 1) thin film system

Table 5.2: Summary of thickness and concentration distribution obtained from plume superposition study

Along central axis									
Distance between LSM and LSC plume centers (cm)	Thickness distribution in			Concentration distribution in				Co % distribution	
				Middle		Edge		Max %	Min %
	Plume centers; average value (nm)	middle (nm)	Edges; average value (nm)	Gradient (% mm ⁻¹)	Span (cm)	Gradient (% mm ⁻¹)	Span (cm)		
2	300	324	55	0.92	6	0.39	4	72.1	27.9
4	219	237	85	1.64	5	0.26	5	87.3	12.7
6	195	145	132	2.17	4	0.09	6	92.6	7.4
7	193	108	155	2.27	4	0.09	6	93.4	6.6
8	192	80	174	2.29	4	0.11	6	93.8	6.3
9	192	59	187	2.17	4	0.17	6	93.9	6.2

The above **table5.2** shows the influence of plume position on the thickness and Co concentration distribution along the central axis.

There is no considerable change observed in the composition gradient per mm. However, composition gradients with the rate of $\approx 1\%$ to 2% mm⁻¹ in the middle whereas 0.1% to 0.4% mm⁻¹ in the edges of central axis with different distribution (span) length.

When the plume centres are closer to each other such as 2cm and 4cm away, Co concentration distribution is limited to $\approx 20\%$ to 80% . Besides that the other plume positions such as 6cm to 9cm away almost fulfils ($\approx 7\%$ to 93%) the expected whole range of Co concentration 1% to 100% .

Although it is possible to fabricate a combinatorial sample with $\approx 7\%$ to 93% Co in certain plume position, the thickness exceeds 100nm in the middle region of central axis when plume centres are 6cm and 7cm away. This thickness can cause thermal mismatch induced cracks in Co rich compositions, which may restrict from achieving crack-free intermediate compositions in LSMC family. It has to be mentioned that the TEC of LSMC system increase as a function of Co content [12]. This represents a significant limitation to take into account.

In **chapter 3** it was found that critical thickness to grow a crack-free LSC layer is 40nm which is a pure Co composition. It is expected that the critical thickness for Co rich ($x > 50\%$) intermediate LSMC compositions supposed to be higher than 40nm thickness as its TEC is relatively smaller than pure LSC.

Therefore, in thickness point of view plume positions such as 8cm and 9cm are attributed as the best positions to achieve crack-free Co rich intermediate compositions. Also, crack-free dense microstructure is an appropriate microstructure required for performing oxygen diffusion studies in LSMC combinatorial system.

5.4 LSMC combinatorial sample preparation in PLD

After performing the parent compounds deposition analysis (**section 5.2**) and the superposition study (**section 5.3**), a CCS LSMC combinatorial sample is prepared based on the favorable plume center position obtained from the parent layer mixing study. The sample is prepared by keeping LSM and LSC plume centers 8cm away.

The sample is fabricated in a PVD-5000 PLD system specially designed for fabricating CCS libraries in wafer level. The novel technical feature of this PLD is a precise and rapid synchronization of target exchange, target movement (rotation and translation), laser ablation and substrate rotation that allows the possibility of fabricating a multilayer system. The specification of PLD is given in detail in **section 2.2.3 in chapter 2**.

As shown in **Figure 5.10**, 4-inch Si wafer is used as a substrate for combinatorial sample fabrication. Firstly, 8YSZ layer of 100nm in thickness is grown on the top of the Si wafer with the following deposition conditions temperature $T = 600^\circ\text{C}$, Pressure $P = 20\text{mT}$, target-substrate distance $d = 9\text{cm}$, frequency $f = 10\text{Hz}$, fluency $F \approx 1.1\text{J}/\text{cm}^2$ (**Table 5.3**). The value of 100nm represents the average thickness of the 8YSZ layer on the whole Si wafer. The main variation in thickness is in the wafer edge with a thickness of the 8YSZ is in between 75 and 90nm. This thickness inhomogeneity in the wafer edge is typical in large area PLD depositions due to uneven laser beam raster movement over a large diameter target [**16, 17**].

V - Optimization of the combinatorial PLD method for the study of the $\text{La}_{0.8}\text{Sr}_{0.2}\text{Mn}_{1-x}\text{Co}_x\text{O}_{3\pm\delta}$ ($x=0$ to 1) thin film system

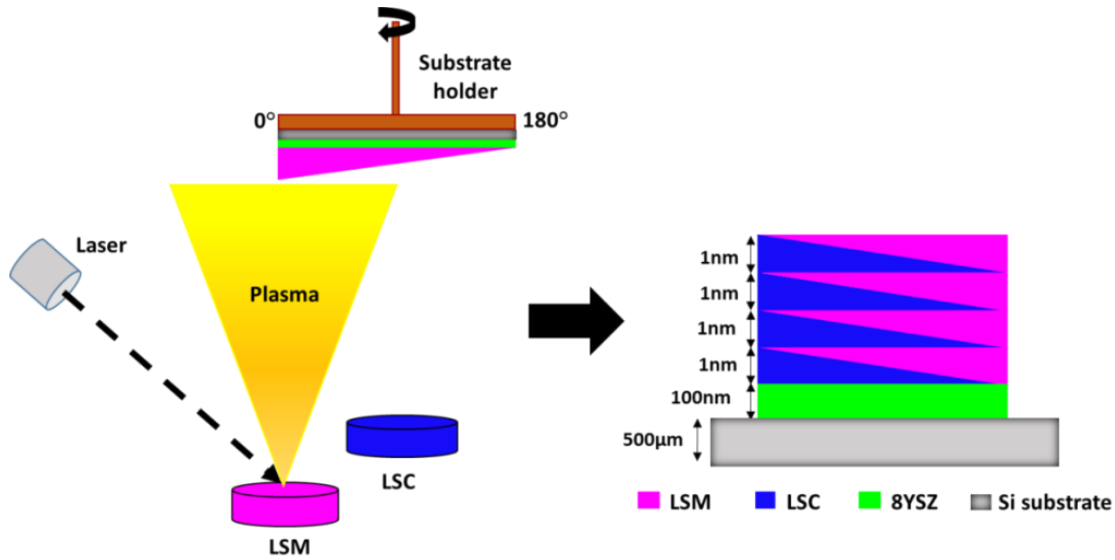


Figure 5.10. Schematic diagram of LSMC combinatorial sample fabrication in PLD and the resultant LSM/LSC multilayer system.

After YSZ deposition, the LSM and LSC dense multi-layers are grown under the following deposition conditions $T = 700^\circ\text{C}$, $P = 20\text{mT}$, $d = 9.5\text{cm}$, $f = 10\text{Hz}$, $F \approx 1.1\text{J}/\text{cm}^2$ (LSM), $0.7\text{J}/\text{cm}^2$ (LSC) already optimized conditions in **chapter 3** to grow a dense LSM and LSC layer. A sequence of alternated LSM and LSC layers is deposited (**Figure 5.10**). The first parent layer of LSM is grown with 95 laser pulses, over which a second layer of LSC is grown with 88 pulses (**Table 5.3**). Each layer attains a thickness of $\sim 1\text{nm}$ with the above number of pulses, which is the maximum thickness at the corresponding plume centers of LSM and LSC. This maximum 1nm plume center thickness starts to decrease from the center due to the LSM and LSC plume positions are fixed at one place during the deposition (**Figure 5.10**).

Table 5.3: Deposition conditions of LSM, LSC, 8YSZ layer is organized in the following table.

Layer	Temperature (°C)	Pressure (mT)	Target to substrate distance (cm)	Energy density (J/cm^2)	Frequency (Hz)	Growth rate (Pulses nm^{-1})	Micro structure
LSM	700	20	9.5	1.1	10	95	Dense
LSC	700	20	9.5	0.7	10	88	Dense
8YSZ	600	20	9	1.1	10	120	Dense

V - Optimization of the combinatorial PLD method for the study of the $\text{La}_{0.8}\text{Sr}_{0.2}\text{Mn}_{1-x}\text{Co}_x\text{O}_{3\pm\delta}$ ($x=0$ to 1) thin film system

The substrate is rotated 180° after every deposition in order to make LSC to deposit opposite to LSM layer.

As-prepared LSMC combinatorial sample is given in **Figure 5.11** in which LSM and LSC plume centers can be clearly seen, located opposite to each other. LSMC thin film system is attained through the interdiffusion of LSM/LSC multilayers during sample preparation itself. A brief introduction to interdiffusion mechanism in ultra-thin film layers is given in **section 3.3 in chapter 3**.

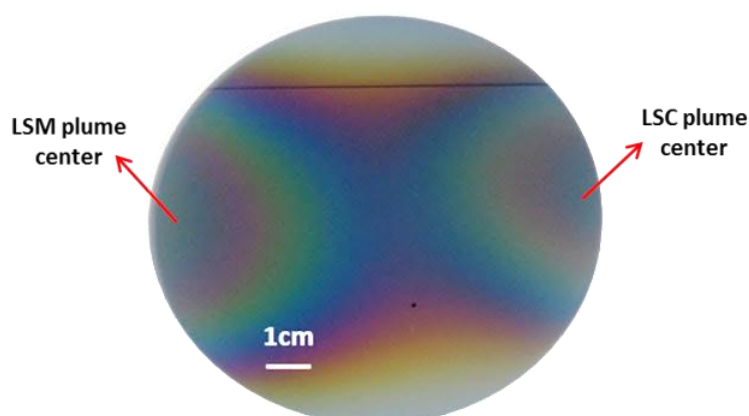


Figure 5.11. As-prepared LSMC pseudo-binary system fabricated in PLD.

Therefore a continuous composition spread LSMC pseudo-binary system is successfully fabricated from the thickness gradients of LSM and LSC multilayers by exposing half-portion of LSM and LSC plumes ablated from corresponding targets.

5.5 Microstructural characterization of combinatorial sample

5.5.1 Structural investigation by X-Ray diffraction (XRD)

Structural investigations in the combinatorial sample are carried out by X-Ray diffraction. For that, the central axis where LSM and LSC plume center meet each other is selected for XRD measurement. As explained earlier, this is the place where the whole $\text{La}_{0.8}\text{Sr}_{0.2}\text{Mn}_{1-x}\text{Co}_x\text{O}_{3\pm\delta}$ ($x \approx 0$ to 1) concentration is distributed. This part is cut into chips of $1 \times 1 \text{cm}^2$ and XRD measurement is performed in these 10 chips and the samples are scanned in offset scanning mode in the region $2\theta = 20^\circ$ to 80° with step size of 0.02° . **Figure 5.12** shows the series of XRD patterns acquired from the diced chips of

V - Optimization of the combinatorial PLD method for the study of the $\text{La}_{0.8}\text{Sr}_{0.2}\text{Mn}_{1-x}\text{Co}_x\text{O}_{3\pm\delta}$ ($x=0$ to 1) thin film system

combinatorial sample which is arranged based on the increment in Co concentration from $x=0.03$ to $x=1$.

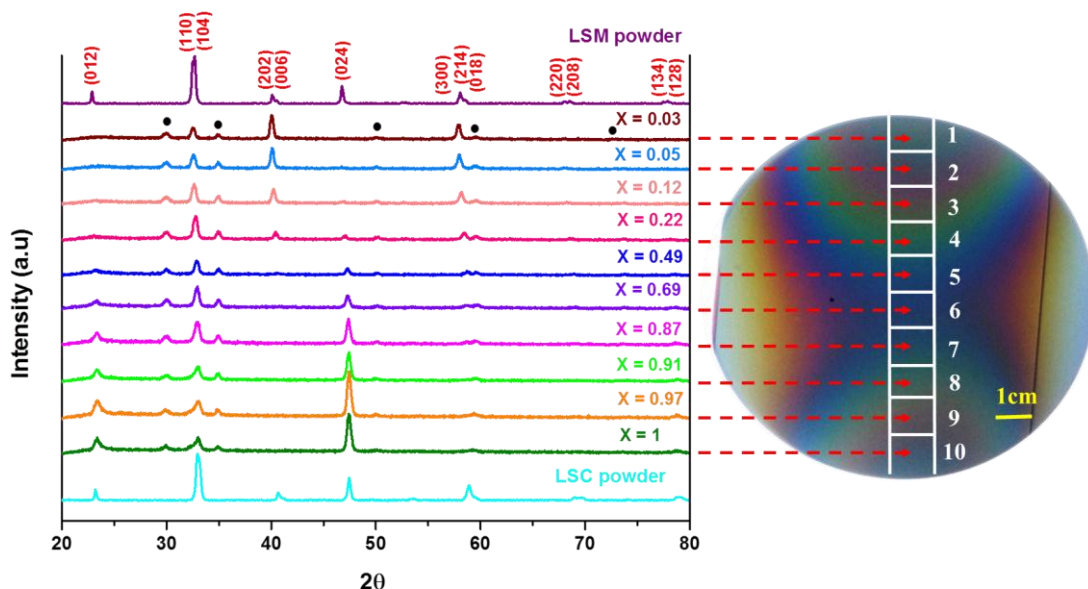


Figure 5.12. XRD pattern of the LSMC system. The arrow marks represent the place where XRD patterns are acquired from each chip in the combinatorial sample.

The XRD pattern (**Figure 5.12**) shows polycrystalline grains with the main diffraction peaks come from (012), (110), (104), (202), (006), (024), (300), (214), (018) reflections. No impurity or parasitic phases are found in the XRD pattern. The film is crystallized in Rhombohedral structure with the $R\bar{3}c$ space group [3, 12, 18, 19].

When the Co concentration is $x=0.03$ (Mn rich side), peak positioned at $\approx 40^\circ$ shows maximum intensity, which goes down and disappears at $x=0.49$. Whereas the intensity of the peaks positioned at 22.8° and 46.7° starts to increase when Co concentration $x=0.69$ and reach maximum when $x=1$. The frequent appearance and disappearance of peaks from LSM to LSC indicates preferential orientation in LSMC system. But XRD measurement was carried out with an offset to avoid peak from the substrate (Si) which might have removed the preferential orientations (peaks) of LSMC system.

When Co concentration increases there is a peak shift towards higher angle 2θ (**Figure 5.13**) which indicates a change in the cell parameter of LSMC crystal structure due to Mn replacement by Co atoms. Le Bail refinement [20] is performed on the combinatorial XRD patterns for a fixed single crystallographic structure Rhombohedral

V - Optimization of the combinatorial PLD method for the study of the $\text{La}_{0.8}\text{Sr}_{0.2}\text{Mn}_{1-x}\text{Co}_x\text{O}_{3\pm\delta}$ ($x=0$ to 1) thin film system

with the $R\bar{3}c$ space group. The refinement is performed to extract various thin film structural information such as cell parameter, volume and reflection intensities (I_{hkl}).

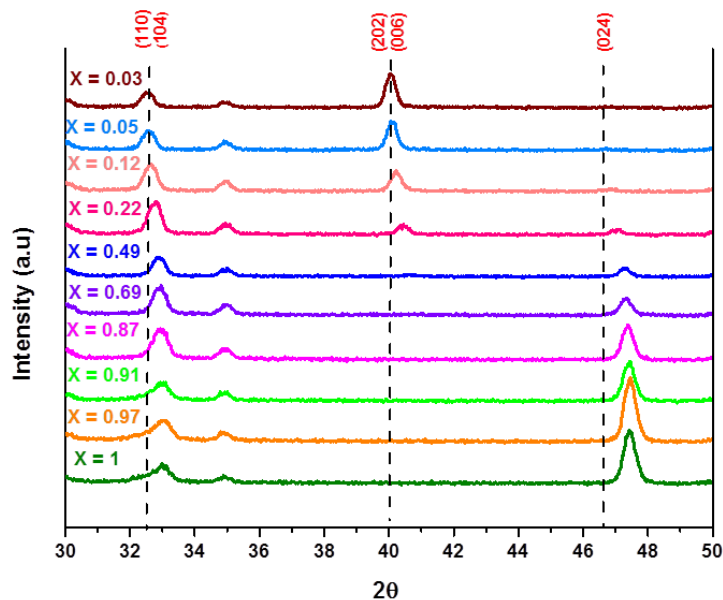
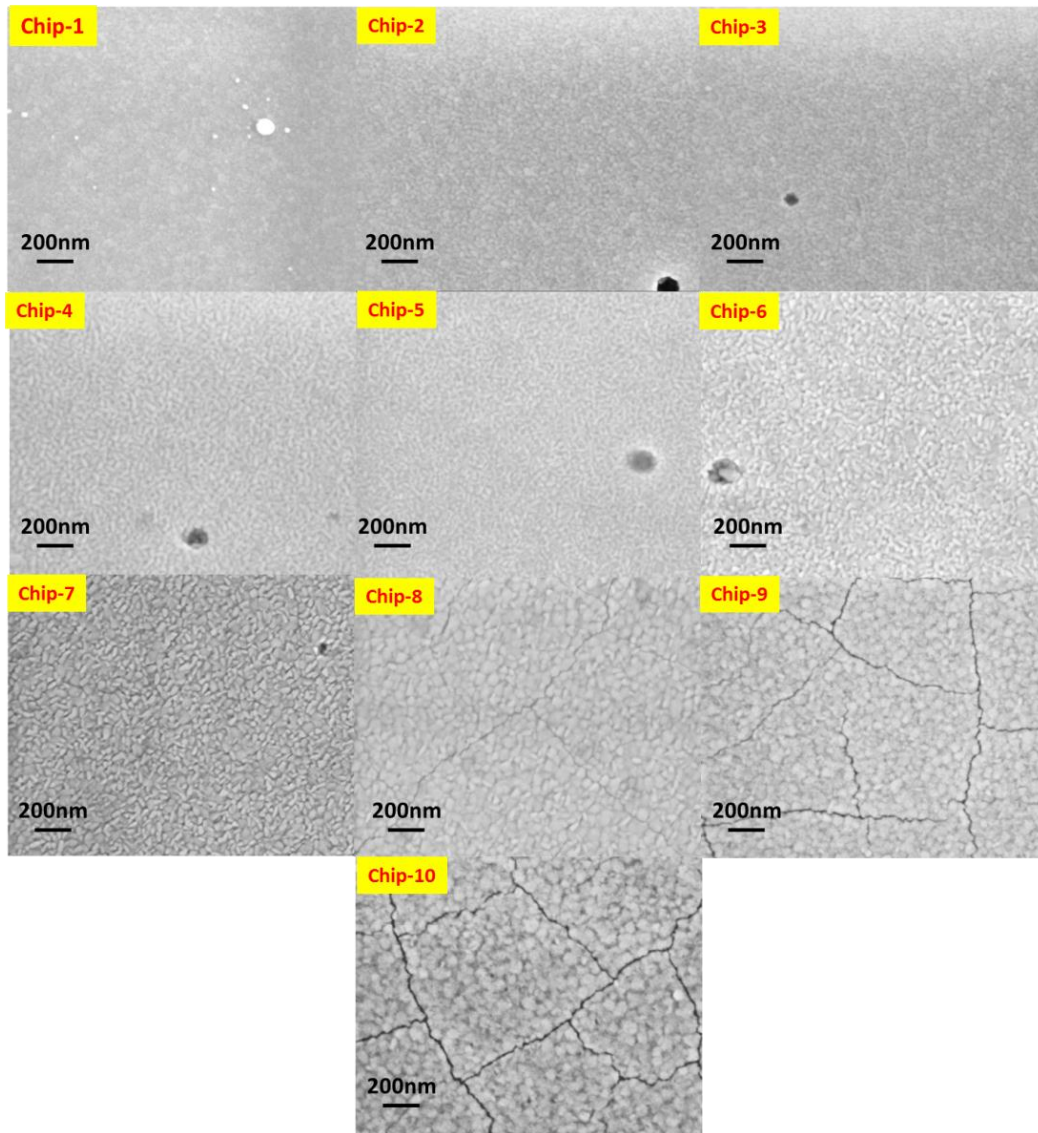


Figure 5.13. XRD pattern of 30° to 50° indicates a peak shift over Co concentration.

Since the chips numbered 8, 9, 10 are cracked, XRD pattern acquired from the chips from 1 to 7 were only used for Le Bail refinement. Crack-formation in LSMC combinatorial system from chip 1 to 10 studied by SEM is given in the following figure (Figure 5.14).

V - Optimization of the combinatorial PLD method for the study of the $\text{La}_{0.8}\text{Sr}_{0.2}\text{Mn}_{1-x}\text{Co}_x\text{O}_{3\pm\delta}$ ($x=0$ to 1) thin film system



*Figure 5.14. SEM top-view images depict crack-formation in the chips of combinatorial sample. The chips numbered 8, 9 and 10 with high Co content ($x \approx 0.9$ to 1) display cracks in their microstructure. As mentioned earlier in **chapter 3**, high thermal mismatch between LSMC system and Si substrate is attributed to be responsible for crack-formation in Co rich compositions.*

The cell parameters obtained by Le Bail refinement including cell volume (V) are plotted against Co concentration in the following figure (**Figure 5.15a** and **5.15b**).

V - Optimization of the combinatorial PLD method for the study of the $\text{La}_{0.8}\text{Sr}_{0.2}\text{Mn}_{1-x}\text{Co}_x\text{O}_{3\pm\delta}$ ($x=0$ to 1) thin film system

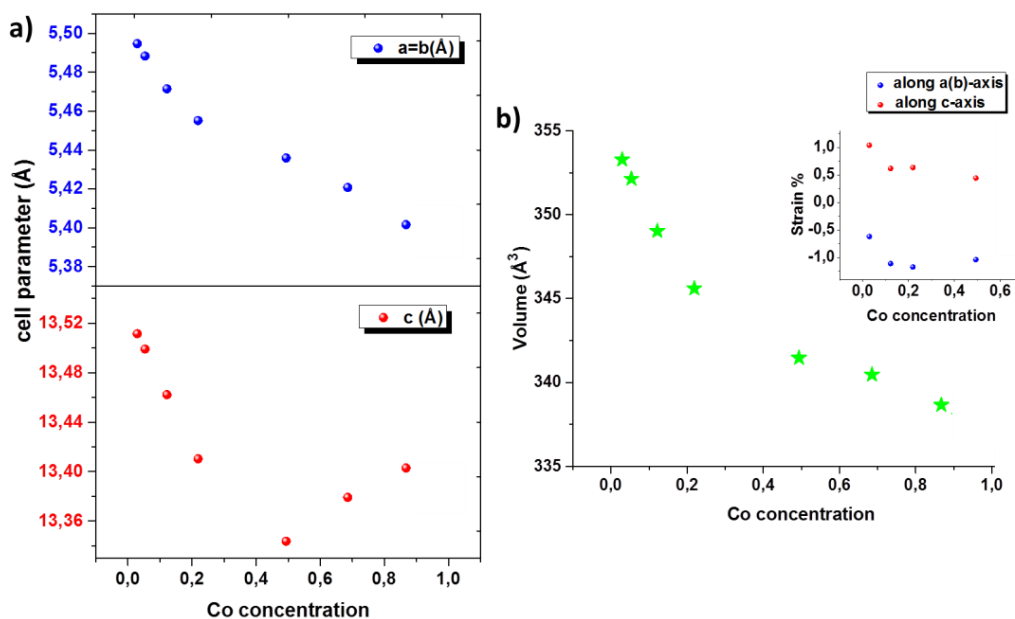


Figure 5.15. a) Cell parameters of Rhombohedrally crystallized LSMC system along a-axis, c-axis obtained by Le Bail refinement is plotted against Co concentration b) Cell volume is plotted against Co concentration. The type of strain in LSMC crystal structure is plotted in the inset, in which c-axis exhibit tensile strain while a-axis exhibit compressive strain.

There is a significant reduction in cell parameter along a(b) axis when Co concentration increases (**Figure 5.15a**). It is reported that lattice parameter decreases with the increment in Co content because Co ions are smaller in size than Mn ions [12, 18, 21]. Opposite to a(b) axis, there is a linear decrease along c-axis until Co content $x=0.49$, later expansion is observed till $x=0.87$.

The anomalous behavior in c-axis cannot be due to phase transition in LSMC system. If it is phase change it will affect the total shape, peak position and number of peaks in Raman spectra [25]. But such kind of changes have not been observed in the Raman study of LSMC system which is given in the upcoming section. Therefore, non-linearity in c-axis may be due to strain induced by substrate.

The deposited film is in compressive strain along a(b)-axis, while in tensile strain along c-axis (inset in **Figure 5.15b**). The strain values are calculated for LSMC system with Co concentration $x \approx 0, 0.1, 0.2$ and 0.5 using the cell parameters given in the literature for the corresponding composition in powder form [12].

V - Optimization of the combinatorial PLD method for the study of the $\text{La}_{0.8}\text{Sr}_{0.2}\text{Mn}_{1-x}\text{Co}_x\text{O}_{3\pm\delta}$ ($x=0$ to 1) thin film system

The structural information obtained from Le Bail refinement is summarized in the following table.

Table 5.4: Summary of cell parameters of LSMC system obtained from Le Bail refinement

Co concentration (x)	Lattice parameter		Volume (\AA^3) (error = ± 0.1 to 0.2\AA^3)	Structure	Space group
	a=b (\AA) (error = $\pm 0.001\text{\AA}$)	c (\AA) (error = $\pm 0.001\text{\AA}$)			
0.03	5.494	13.511	353.3	Rh	$R\bar{3}c$
0.05	5.488	13.499	352.1	Rh	$R\bar{3}c$
0.12	5.471	13.462	349.0	Rh	$R\bar{3}c$
0.22	5.455	13.410	345.6	Rh	$R\bar{3}c$
0.49	5.436	13.344	341.4	Rh	$R\bar{3}c$
0.69	5.421	13.379	340.4	Rh	$R\bar{3}c$
0.87	5.402	13.403	338.7	Rh	$R\bar{3}c$

5.5.2 Structural investigation by Raman analysis

Raman spectroscopy is a powerful and sensitive technique to study the local structure, phase transition, and oxygen disorder of a crystalline system [22]. Mn site replacement by Co in LSMC system definitely cause distortion in $\text{Mn}(\text{Co})\text{O}_6$ octahedra which is expected to produce changes in the phonon modes of LSMC system [23]. Raman measurement is applied here to study the structural distortion induced by Co doping in LSMC system.

Perovskite like manganites (LaMnO_3) and cobaltites (LaCoO_3) are well studied materials by Raman spectroscopy due to its interesting magnetic and electrical properties [21]. Generally $\text{LaMn}_{1-x}\text{Co}_x\text{O}_3$ (LMC) compounds without Sr exhibit in two different crystal structures. When $x < 0.5$ these compounds exhibit in orthorhombic structure with $Pnma$ space group. When $x > 0.5$ it exist in Rhombohedral structure with $R\bar{3}c$ space group [21, 23, 24]. Interestingly, the whole $\text{LaMn}_{1-x}\text{Co}_x\text{O}_3$ system turns to Rhombohedral structure when it is doped with Sr in the A-site.

Figure 5.16 represents Raman mapping acquired at every $\approx 2\text{mm}$ along the central axis of combinatorial sample from Mn rich side to Co rich side. Baseline corrections and Silicon peak position adjustments are made before performing fittings on Raman spectra in order to extract precise peak position and intensity. There are changes can

V - Optimization of the combinatorial PLD method for the study of the $\text{La}_{0.8}\text{Sr}_{0.2}\text{Mn}_{1-x}\text{Co}_x\text{O}_{3\pm\delta}$ ($x=0$ to 1) thin film system

be observed in the peak position, size, and intensity of Raman spectra as a function of Co content.

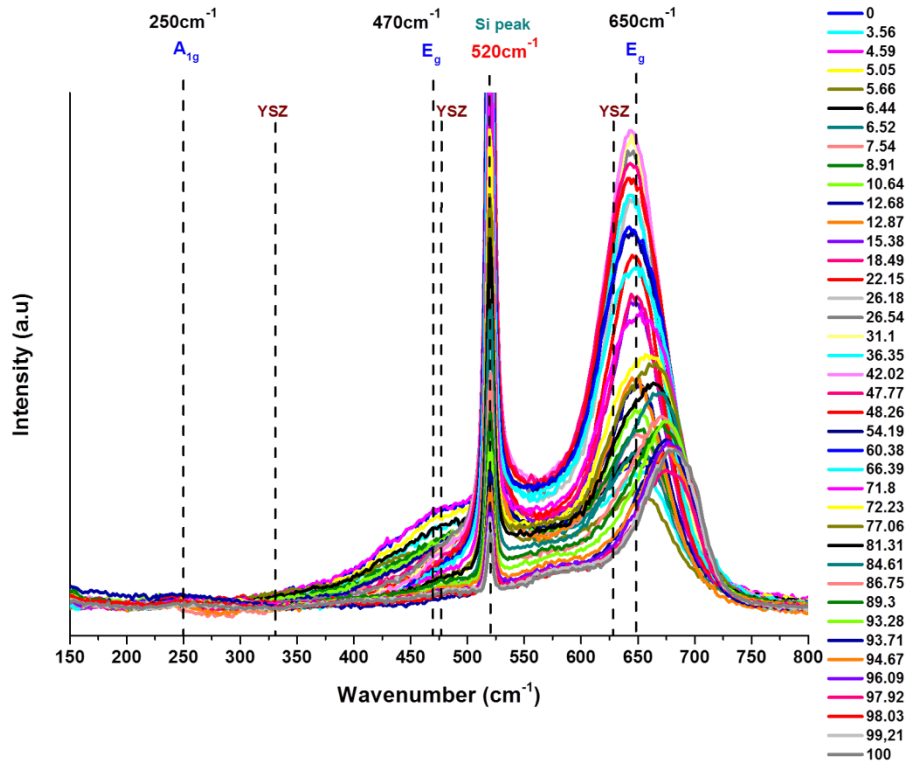


Figure 5.16. Raman mapping performed in LSMC combinatorial system.

5.5.2.1 Phonon modes of LSMC Rhombohedral crystal system

In general, a rhombohedral LSMC crystal system has a total of 20 phonon modes, among them 5 modes ($A_{1g}+4E_g$) are Raman active modes [24, 25]. In the Raman spectra of combinatorial sample there are three main bands positioned between 230-270cm⁻¹, 460-520cm⁻¹ and 640-680cm⁻¹ can be observed [23, 24, 25].

Peak centered between the wavenumber 230-270cm⁻¹ is associated with the rotational vibration of Mn(Co)O₆ octahedra. While peaks corresponding to high frequencies are associated with the internal modes of Mn(Co)O₆ octahedra. The peaks in between 460-520cm⁻¹ belongs to the bending vibration, whereas peaks between 640-680cm⁻¹ represents the stretching vibration of Mn(Co)-O bonds in Mn(Co)O₆ octahedra. In particular, the bands in between 460-520cm⁻¹, 640-680cm⁻¹ are related to Jahn-Teller octahedral distortions (JT-distortion) (Figure 5.17) [23 - 27].

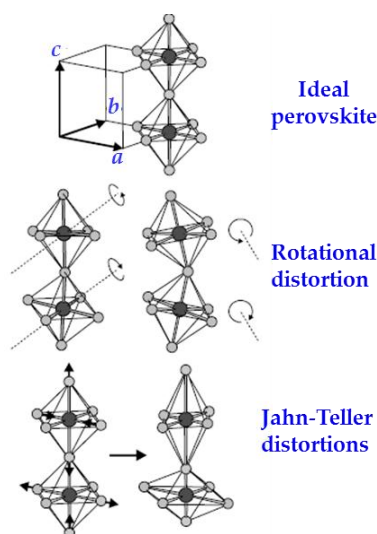


Figure 5.17. Visual representation of Rotational and Jahn-Teller distortion in a perovskite structure taken from ref [29].

5.5.2.2 Effect of Co content on Raman mode peak wavenumber

The peak frequencies of the three main modes in LSMC system between $230\text{-}270\text{cm}^{-1}$, $460\text{-}520\text{cm}^{-1}$ and $640\text{-}680\text{cm}^{-1}$ found from the fitting are plotted as a function of Co content in **Figure 5.18**. All the three modes display a change in the frequencies of their vibration when Co content varies.

In particular, peak comprises JT-distortion (**Figure 5.17**) induced bending and stretching vibrations ($460\text{-}520\text{cm}^{-1}$, $640\text{-}680\text{cm}^{-1}$) of $\text{Mn}(\text{Co})\text{O}_6$ octahedra shows an increase in frequency after Co concentration $x=0.54$. Whereas peaks constitute rotational vibration between $230\text{-}270\text{cm}^{-1}$ increases until $x=0.54$ and then maintain a constant value of frequency from $x=0.6$. Therefore, the above changes in peak position over Co content confirm the presence of octahedral distortion in LSMC structure.

V - Optimization of the combinatorial PLD method for the study of the $\text{La}_{0.8}\text{Sr}_{0.2}\text{Mn}_{1-x}\text{Co}_x\text{O}_{3\pm\delta}$ ($x=0$ to 1) thin film system

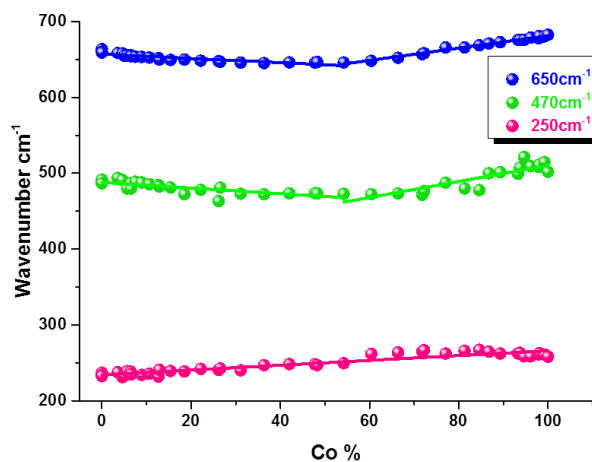


Figure 5.18. The peak frequencies of phonon modes near 250cm^{-1} , 470cm^{-1} , 650cm^{-1} plotted against Co concentration.

5.5.2.3 Effect of Co content on Raman mode peak intensity

The intensity corresponding to phonon modes between $230\text{-}270\text{cm}^{-1}$, $460\text{-}520\text{cm}^{-1}$ and $640\text{-}680\text{cm}^{-1}$ is plotted against Co content in **Figure 5.19**. Generally, the intensity of Raman bands can be affected by two factors such as thickness [14, 15] and local structural distortion [23]. Both factors are directly proportional to Raman intensity.

In **Figure 5.19** intensities corresponding to the phonon modes of LSMC layer are not proportional to its thickness along the central axis when the plume centers are 8cm away (**Figure 5.8f**). Instead they are sensitive to local structural distortion.

V - Optimization of the combinatorial PLD method for the study of the $\text{La}_{0.8}\text{Sr}_{0.2}\text{Mn}_{1-x}\text{Co}_x\text{O}_{3\pm\delta}$ ($x=0$ to 1) thin film system

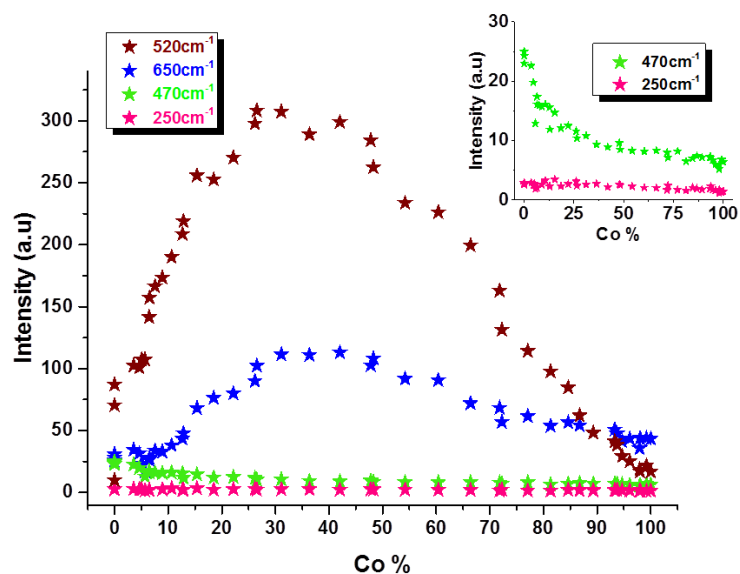


Figure 5.19. The intensities of phonon modes near 250cm^{-1} , 470cm^{-1} , 650cm^{-1} including Si peak intensity 520cm^{-1} plotted against Co concentration. Inset shows the zoom view of the phonon mode intensities 250cm^{-1} , 470cm^{-1} .

The intensity of Raman band near 650cm^{-1} shows a non-linear trend over Co content. Here, distortion due to stretching vibration increases over Co content until $x\approx 0.5$ and then decreases after $x\approx 0.5$ [23]. Whereas the band near 470cm^{-1} shows a decrement in intensity over Co content (inset in **Figure 5.19**) indicates decrement in distortion induced by bending vibration of $\text{Mn}(\text{Co})\text{O}_6$ octahedra [23]. Raman band near 250cm^{-1} involving rotational vibration shows almost an invariant response to Co which depicts either the rotational distortion is minimum or no distortion.

As a conclusion Raman analysis on LSMC combinatorial system confirms the existence of distortion in LSMC system. The Raman analysis has also explained the type of distortion and the effect of Co content on the tendency of distortion.

5.5.3 Morphology study by Atomic Force Microscopy (AFM)

The surface morphology of the LSMC combinatorial sample is studied by Atomic Force Microscopy (AFM). The samples used for XRD are also used for the morphology study by AFM and the measurement is performed in the region where the XRD measurement was performed.

LSMC system on YSZ/Si substrate deposited at 700°C exhibit a dense and smooth surface (**Figure 5.20a** to **5.20j**). The average RMS value of roughness is in the range 1nm

V - Optimization of the combinatorial PLD method for the study of the $\text{La}_{0.8}\text{Sr}_{0.2}\text{Mn}_{1-x}\text{Co}_x\text{O}_{3\pm\delta}$ ($x=0$ to 1) thin film system

to 3nm (error is $\pm 0.5\text{nm}$) which indicates the surface of LSMC system is smooth and flat.

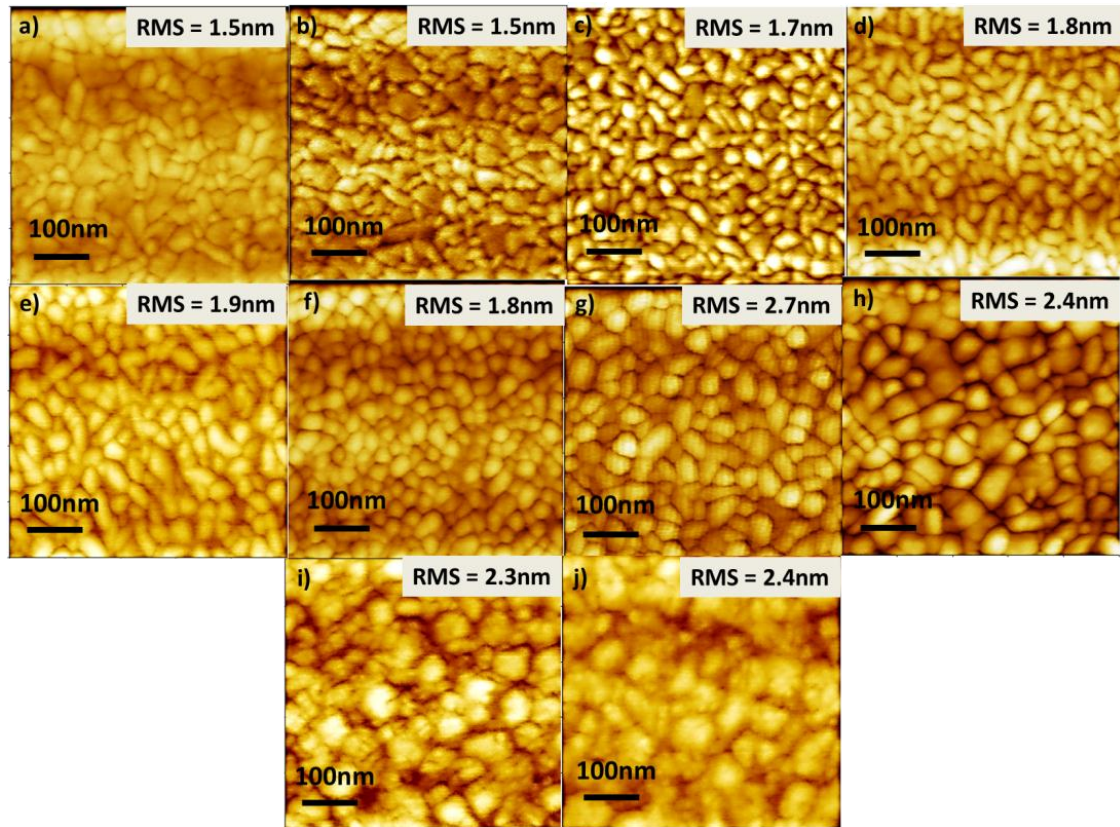


Figure 5.20. Morphology study of LSMC combinatorial sample by AFM along the central axis (from chip 1 to 10 in Figure 5.12)

The grain size values are determined in each chip using SEM and AFM top-view images of LSMC system and the average grain size value estimated from the central point of each chip is given in the following figure (Figure 5.21).

V - Optimization of the combinatorial PLD method for the study of the $\text{La}_{0.8}\text{Sr}_{0.2}\text{Mn}_{1-x}\text{Co}_x\text{O}_{3\pm\delta}$ ($x=0$ to 1) thin film system

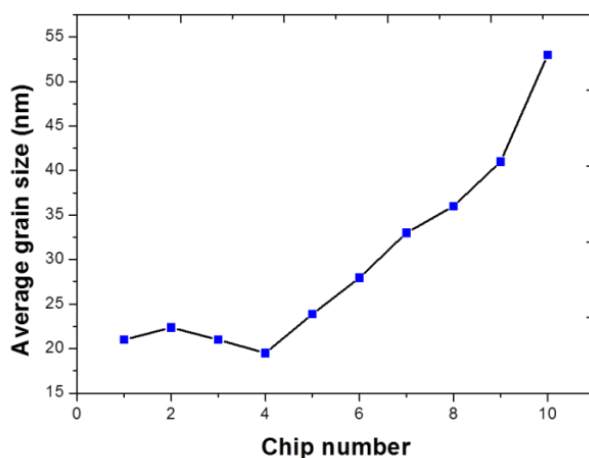


Figure 5.21. Average grain size estimated from AFM, SEM images is plotted against combinatorial samples (chips from 1 to 10).

The above figure illustrates the average grain size values associated with the chips from 1 to 10 (**Figure 5.12**) and the grain size values are in the range 20nm to 55nm. The increment in grain size values can be observed from chip-4 which has $\approx 20\%$ Co (an average value).

The grain size values estimated from AFM and SEM are applied in Finite Element simulation (FEM) in the following **chapter 6** to simulate the oxygen diffusion profiles of LSMC combinatorial samples.

5.5.4 Thickness mapping by Scanning Electron Microscopy (SEM) and comparison with parent layers superposition results

The thickness and composition distribution map in the combinatorial sample are characterized by different experimental techniques. The thickness map along the central axis of combinatorial sample is obtained by SEM.

In **Figure 5.22** the thickness obtained by SEM measurement is compared with parent layer superposition values estimated (**section 5.3**) at 8cm away LSM and LSC plume centers. They are plotted together against the wafer position along central axis.

V - Optimization of the combinatorial PLD method for the study of the $\text{La}_{0.8}\text{Sr}_{0.2}\text{Mn}_{1-x}\text{Co}_x\text{O}_{3\pm\delta}$ ($x=0$ to 1) thin film system

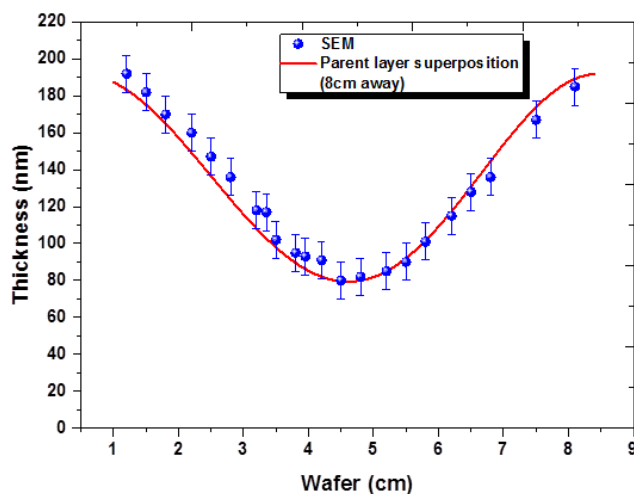


Figure 5.22. Thickness obtained by SEM is compared with plume superposition values plotted against wafer position in cm.

The minimum and maximum thickness values obtained when the plume center distance 8cm away are 80nm and 192nm (**Table 5.2**) that exactly matches with the minimum and maximum thickness values determined by SEM (which are 192nm and 79nm). Also, the thickness progresses in the same way in both method of measurement.

Therefore there is a good agreement in thickness obtained between SEM an experimental technique and superposition prediction method.

5.5.5 Composition mapping by Energy Dispersive Spectroscopy (EDS), Wavelength Dispersive Spectroscopy (WDS) and comparison with superposition results

The composition distribution along the central axis of combinatorial sample is studied by EDS and WDS analysis. In **Figure 5.23a** atomic percentage of A and B-site atoms in LSMC system estimated from WDS technique is plotted against wafer position. In which the atomic percentage of A-site atoms such as La and Sr follows the nominal percentage of 80% for La, 20% for Sr. The atomic percentage of Mn and Co atoms follow Gaussain distribution along the central axis (similar to thickness).

The atomic ratio between La/Sr (A-site), Mn/Co (B-site), La+Sr)/Mn+Co (A/B-site) atoms are also estimated from the atomic concentration of microprobe (WDS) measurement. They are plotted against the position along central axis in **Figure 5.23b**.

V - Optimization of the combinatorial PLD method for the study of the $\text{La}_{0.8}\text{Sr}_{0.2}\text{Mn}_{1-x}\text{Co}_x\text{O}_{3\pm\delta}$ ($x=0$ to 1) thin film system

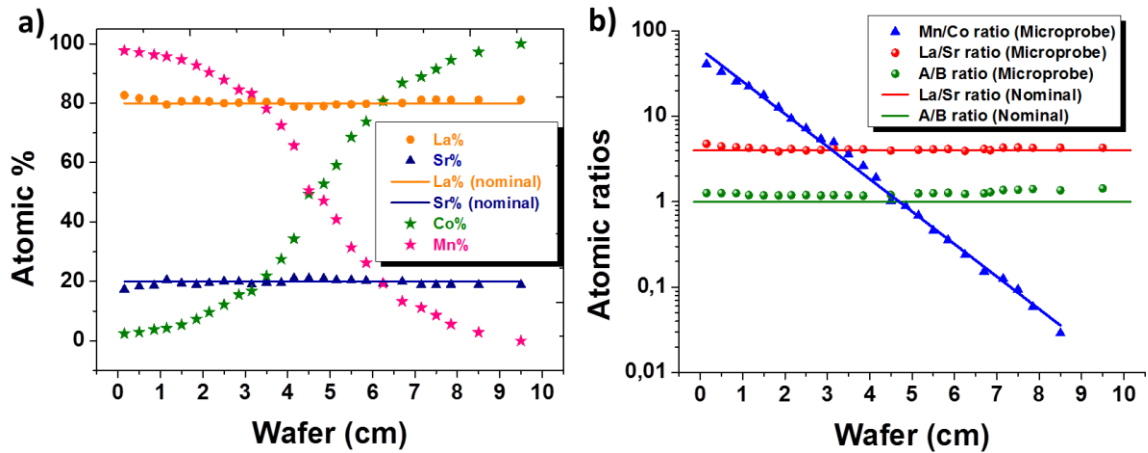


Figure 5.23. Composition mapping along the central axis of combinatorial sample studied by WDS technique a) Atomic percentage of La, Sr, Co, Mn atoms and b) Atomic ratios such as La/Sr, Mn/Co, La+Sr/Mn+Co (A/B) are plotted against wafer position. Straight line represents nominal values.

In **Figure 5.23b** the atomic ratio between A-site atoms such as La/Sr ratio follows the nominal value 4 throughout the central axis. But the ratio between A and B-site atoms ($A/B=(\text{La}+\text{Sr})/(\text{Mn}+\text{Co})$) is ≈ 1.2 an average value estimated from the central axis, which is slightly higher than the theoretical value 1. Hence, it is clear that there is deficiency in the B-site atoms of LSMC system according to WDS measurement which arises from the B-site under-stoichiometric PLD targets due to the frequent laser ablation as already mentioned in **section 2.2.3** in **chapter 2**.

Apart from the discrepancy in B-site, the stoichiometry of A-site atoms are La = 0.8, Sr = 0.19 which is equal to the nominal stoichiometry La is 0.8, Sr is 0.2.

Mn/Co relative concentration estimated from EDS, WDS technique is compared with the relative concentration predicted from plume superposition study using **equations 5.5, 5.6** and **5.7** when the distance between plume centers are 8cm away. They are plotted together against position along central axis in **Figure 5.24**.

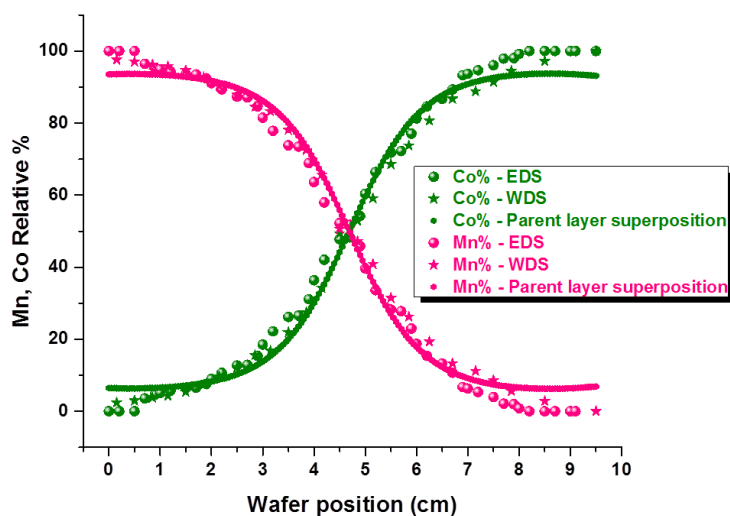


Figure 5.24. Mn/Co relative concentration obtained by EDS, WDS technique is compared with plume superposition values plotted against wafer position.

When the plume centers are 8cm away there was $2.3\% \text{mm}^{-1}$ Mn/Co concentration gradient in the middle and $0.1\% \text{mm}^{-1}$ in the wafer edges (**Table 5.2**). Whereas Mn/Co atomic concentration changes with the rate of $2.0\% \text{mm}^{-1}$ estimated by EDS and $1.97\% \text{mm}^{-1}$ by WDS in the middle region. In the edges it is $0.5\% \text{mm}^{-1}$. Therefore, Mn/Co concentration gradient determined by bulk elemental analysis methods such as EDS and WDS matches with the prediction by superposition.

However, concentration predicted in the wafer edges follows a flat profile ($0.1\% \text{mm}^{-1}$) which is slightly lower than experimental values (**Figure 5.24**). This is probably due to an error (**Table 5.1**) of the best fitting obtained at the edges.

5.6 Validation of plume superposition results with experimental results

The thickness, concentration distribution and gradient estimated from the parent layer superposition at 8cm away plume center and experimental techniques are compared in the following **table 5.4**.

V - Optimization of the combinatorial PLD method for the study of the $\text{La}_{0.8}\text{Sr}_{0.2}\text{Mn}_{1-x}\text{Co}_x\text{O}_{3\pm\delta}$ ($x=0$ to 1) thin film system

Table 5.4: Comparison of thickness and concentration distribution between experimental and parent layer superposition values

Method	Thickness distribution in		Composition gradient in				Co concentration distribution	
	Plume centers; average value (nm)	middle (nm)	Middle		Edge		Max %	Min %
			Gradient (% mm ⁻¹)	Span (cm)	Gradient (% mm ⁻¹)	Span (cm)		
Super position of Parent materials (8cm away)	192	80	2.29	4	0.11	6	93.8	6.3
SEM	192	79						
EDS			2.03	4	0.5	6	0	0
WDS			1.97	4	0.45	6	100	2.4

Table 5.4 confirms that the thickness, concentration distribution and gradient estimated from the parent layer superposition at 8cm away plume center is in good agreement with the values acquired through experimental techniques in the combinatorial sample prepared by keeping LSM and LSC plume centers \approx 8cm away. It validates that the technical methodology introduced in this chapter to predict thickness and composition distribution map is functioning.

5.7 Conclusion

The continuous composition spread LSMC pseudo-binary system was successfully fabricated without any parasitic phase based on the best plume center position predicted from an analytical superposition study. The microstructure of the combinatorial sample was studied by various experimental techniques such as XRD, Raman, AFM, SEM, EDS and WDS. The thickness, Mn/Co distribution and gradient values determined by experimental techniques is consistent with the values predicted from plume superposition when the LSM and LSC plume centers are 8cm away. Therefore the new methodology adopted in this chapter to fabricate CCS based combinatorial system is trustworthy.

References

- [1] K. Rajan, *ACS Comb. Sci.*, 2011, 13, 579.
- [2] R. B. Van Dover, L. F. Schneemeyer, R. M. Fleming, *Nature*, 1998, 392, 162.
- [3] A. Thursfield, J. C. H. Rossiny, S. Fearn, J. A. Kilner, I. S. Metcalfe, *Solid State Ionics*, 2012, 225, 182.
- [4] X. D. Xiang, X. Sun, G. Briceno, Y. Lou, K. Wang, H. Chang, W. G. Wallace-Freedman, S. Chen, P. G. Schultz, *Sci.*, 1995, 268, 1738.
- [5] H. M. Christen, I. Ohkubo, C. M. Rouleau, G. E. Jellison, A. A. Puretzky, D. B. Geohegan, D. H. Lowndes, *Meas. Sci. Technol.*, 2005, 16, 21.
- [6] B. C. H. Steele, *Curr. Opin. Solid St. M.*, 1996, 1, 684.
- [7] J. Sunarso, S. Baumann, J. M. Serra, W. A. Meulenber, S. Liu, Y. S. Lin, J. C. Diniz da Costa, *J. memb. Sci. Technol.*, 2008, 320, 13.
- [8] R. A. De Souza, J. A. Kilner, *Solid State Ionics*, 1998, 106, 175.
- [9] R. A. De Souza, J. A. Kilner, *Solid State Ionics*, 1999, 126, 153.
- [10] S. Royer, H. Alamdari, D. Duprez, S. Kaliaguine, *Appl. Catal. B-Environ.*, 2005, 58, 273.
- [11] K. Ahn, H. Kim, Y. C. Chung, H. R. Kim, J. W. Son, H. W. Lee, J. H. Lee, *Appl. Catal. A-Gen.*, 2010, 387, 203.
- [12] R. V. Wandekar, B. N. Wani, S. R. Bharadwaj, *Solid State Sciences*, 2009, 11, 240.
- [13] P. E. Nica, G. B. Rusu, O. G. Dragos, C. Ursu, *IEEE Transactions on plasma science*, 2014, 42, 2694.
- [14] S. Shivaraman, M.V.S. chandrashekhar, J. J. boeckl, M. G. spencer, *J. Electron. Mater.*, 2009, 38, 725.
- [15] Z. X. Shen, *Raman microscopy in characterization of Si devices* (Publication from National University of Singapore).
- [16] J. A. Greer, *J. Phys. D*, 2014, 47, 1.
- [17] Robert Eason, *Pulsed Laser Deposition of Thin films*, Wiley, NJ, USA, 2007 .
- [18] A. N. Petrov, V. I. Voronin, T. Norby, P. Kofstad, *J. Solid State Chem.*, 1999, 143, 52.
- [19] I. O. Troyanchuk, A. P. Sazonov, H. Szymczak, D. M. Tobbens, H. Gamari-Seale, *J. Exp. Theor. Phys.*, 2004, 99, 363.
- [20] V. K. Peterson, *Powder Diffr.*, 2005, 20, 14.
- [21] C. Autret, J. Hejtmanek, K. Knizek, M. Marysko, Z. Jirak, M. Dlouha, S. Vratislav, *J. Phys. Condens. Matter*, 2005, 17, 1601.
- [22] S. S. R. kumar, *Raman spectroscopy for Nanomaterials characterization*, Springer, Heidelberg, Germany, 2012.
- [23] N. V. Minh, I. Yang, *Vib. Spectrosc.*, 2006, 42, 353.

V - Optimization of the combinatorial PLD method for the study of the $\text{La}_{0.8}\text{Sr}_{0.2}\text{Mn}_{1-x}\text{Co}_x\text{O}_{3\pm\delta}$ ($x=0$ to 1) thin film system

- [24] V. P. Gnezdilov, A. V. Yeremenko, *Low Temp. Phys.*, 2003, 29, 963.
- [25] P. T. Phong, S. J. Jang, B. T. Huy, Y. I. Lee, I. J. Lee, *J. Mater. Sci.*, 2013, 24, 2292.
- [26] M. N. Lliev, M. V. Abrashev, *J. Raman. Spectrosc.*, 2001, 32, 805.
- [27] L. Carron, A. Andres, M. J. Martinez-Lope, M. T. Casais, J. A. Alonso, *Phys. Rev. B*, 2002, 66, 174303.

Chapter 6

*Study of oxygen transport properties of
 $\text{La}_{0.8}\text{Sr}_{0.2}\text{Mn}_{1-x}\text{Co}_x\text{O}_{3\pm\delta}$ ($x=0$ to 1) combinatorial thin
film system by IEDP-SIMS technique*

Chapter VI

6.1 Chapter outline

In the previous chapters, by using the combinatorial PLD deposition technique, LSMC thin film system was fabricated with a continuous variation in Mn and Co concentration. The morphology, composition and phase of LSMC system was characterized by various experimental techniques. The purpose of this chapter is to assess the oxygen transport properties of LSMC system IEDP-SIMS technique.

The oxygen transport properties of oxide ion conductors can be studied by various experimental techniques such as electrical conductivity relaxation (ECR) [1, 2], AC impedance spectroscopy [3], curvature relaxation method [4, 5], gravimetric [6] and manometric [7] methods. In this chapter the functional property is examined by the mapping of LSMC combinatorial thin film system using Isotope exchange depth-profiling technique (IEDP) coupled with Secondary ion mass spectrometry (SIMS) [8, 9, 10]. This is a direct method to determine oxygen kinetic parameters [8] where oxygen mass transport takes place under zero electrochemical driving force and the parameters acquired from such kind of transport are oxygen surface-exchange coefficient (k^*) and oxygen self-diffusion coefficient (D^*).

Since the samples studied here are in thin film form, some of the traditional sample processing steps involved in isotope exchange measurement are not required. As an example, a thin film sample has well-defined smooth surface and morphology which avoid polishing step that can modify the sample surface and alter k^* [9, 10].

The present chapter is about the functional characterization of LSMC thin film combinatorial system is presented in the following way. The crack-study performed in combinatorial system and the details of the samples used for IEDP-SIMS¹ mapping is organized in **section 6.2**. In **section 6.3** Finite Element Method (FEM) simulations are carried out in the ¹⁸O isotope concentration profiles of LSMC thin film system. The oxygen transport coefficients acquired from FEM simulation and the results are discussed in **sections 6.3.1 and 6.3.2**.

¹ IEDP-SIMS measurement on LSMC combinatorial system was carried out by Dr. Monica Burriel in Imperial College, London.

6.2 IEDP-SIMS measurements in combinatorial sample

6.2.1 IEDP-SIMS measurement sample details

The combinatorial sample (4-inch wafer) was diced into chips of $1 \times 1 \text{ cm}^2$ for IEDP-SIMS measurement. The graphical representation of LSMC combinatorial system is given in **Figure 6.1**. Among them, only the chips with crack-free microstructure will be useful for oxygen isotope exchange study because there is a chance of pore diffusion along grain boundaries in cracked layers during oxygen exchange that would alter the obtained profile and lead to wrong conclusions [9, 10].

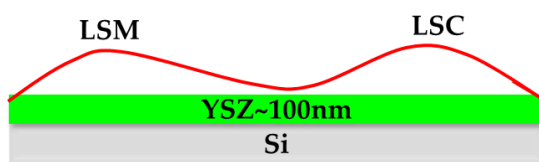


Figure 6.1. Illustration of LSMC binary system deposited on YSZ layer and 4-inch Si wafer. The top layer shows a typical thickness gradient profile obtained from combinatorial deposition in PLD.

In order to avoid that, the chips exhibit gas-tight dense microstructure, chips labelled from 1 to 7 ($x < 0.85$) were used for IEDP-SIMS measurement (**Figure 6.2**). The crack-evolution with thickness study performed in combinatorial chips can be found in **Figure 5.14 in chapter 5**.

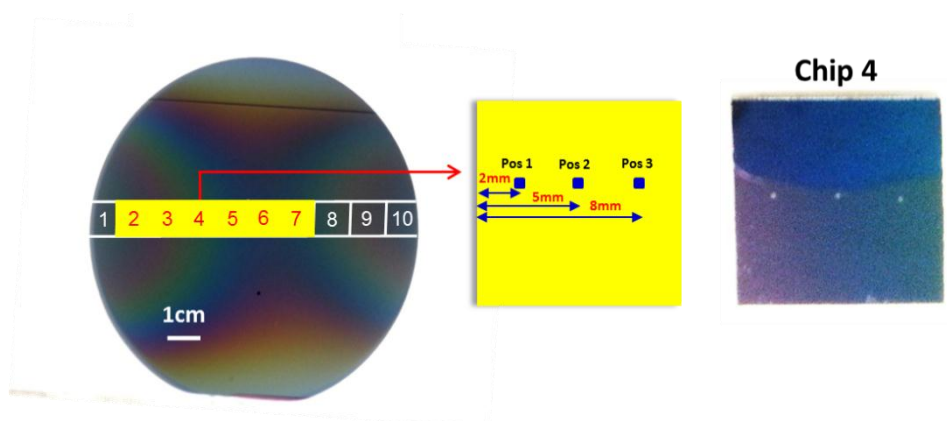


Figure 6.2. Illustration of chips used for IEDP-SIMS measurement and the location of punctual SIMS measurement points in chip-4 belonging to combinatorial sample.

VI - Functional study of $\text{La}_{0.8}\text{Sr}_{0.2}\text{Mn}_{1-x}\text{Co}_x\text{O}_{3\pm\delta}$ ($x=0$ to 1) combinatorial thin film system by IEDP-SIMS technique

In these chips, ^{18}O isotope was exchanged for around 30 minutes under temperatures 600°C , 700°C and 800°C . Each step involved in oxygen isotope exchange process is explained in detail in **section 2.4.2 in chapter 2**.

Following the exchange step, punctual SIMS measurement was performed in 3 to 5 points in every chip at every 1 to 3mm distance approximately. The graphical representation of punctual SIMS measurement points in chip-4 including real image of the same chip is given as an example in **Figure 6.2**.

The samples are sputtered with Bi^+ primary ion beam that created a $200\times 200\mu\text{m}$ crater. Simultaneously, the secondary ion intensities of the milled ions are recorded in the detector based on the time of flight of arrival (ToF) of the secondary ions. As an example, **Figure 6.3** shows an image of a crater taken by SEM in chip-2 at position 8mm (sample code-C2-700-c).

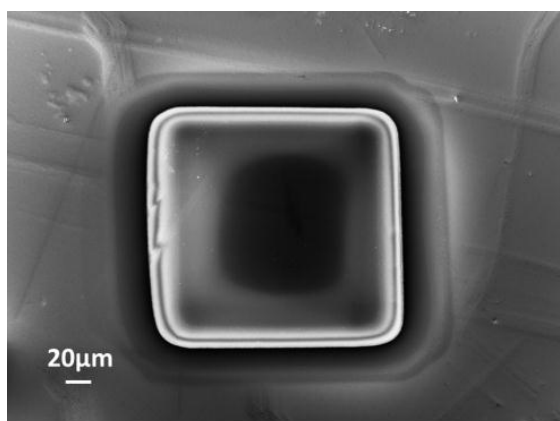


Figure 6.3. SEM image depicts $200\times 200\mu\text{m}$ size crater created during sputtering of sample surface by Bi^+ primary ion beam. The image corresponds to sample code-C2-700-c located in chip-2 at 8mm.

Also, the list of samples used for IEDP-SIMS measurement including ^{18}O -exchange temperature and time is given in the following **Table.6.1**.

VI - Functional study of $\text{La}_{0.8}\text{Sr}_{0.2}\text{Mn}_{1-x}\text{Co}_x\text{O}_{3\pm\delta}$ ($x=0$ to 1) combinatorial thin film system by IEDP-SIMS technique

Table 6.1: List of samples used for IEDP-SIMS measurement.

Chip	Sample code	Temperature (°C)	Exchange time (s)
6	C6-600-a	600	1244
6	C6-600-b	600	1244
6	C6-600-c	600	1244
7	C7-600-a	600	1244
7	C7-600-b	600	1244
7	C7-600-c	600	1244
2	C2-700-a	700	1318
2	C2-700-b	700	1318
2	C2-700-c	700	1318
3	C3-700-a	700	1591
3	C3-700-b	700	1591
3	C3-700-c	700	1591
4	C4-700-a	700	1318
4	C4-700-b	700	1318
4	C4-700-c	700	1318
5	C5-700-a	700	1472
5	C5-700-b	700	1472
5	C5-700-c	700	1472
6	C6-700-a	700	1472
6	C6-700-b	700	1472
6	C6-700-c	700	1472
4	C4-800-a	800	1322
4	C4-800-b	800	1322
4	C4-800-c	800	1322
4	C4-800-d	800	1322
4	C4-800-e	800	1322

6.2.2 ^{18}O concentration profile in LSMC combinatorial system

In order to determine oxygen transport parameters such as oxygen surface exchange coefficient k^* and oxygen diffusion coefficient D^* , ^{18}O concentration profile obtained from IEDP-SIMS measurement has to be analyzed with the normalized value of ^{18}O intensities. For that, ^{18}O oxygen isotope fraction is first calculated from ^{18}O , and ^{16}O secondary ion intensities which can be written as,

$$C(x, t) = \frac{\text{counts}(\text{O}_{18})}{\text{counts}(\text{O}_{16}) + \text{counts}(\text{O}_{18})} \quad (6.1)$$

Then the oxygen isotope fraction can be normalized with the following equation,

$$C' = \frac{C(x, t) - C_1}{C_2 - C_1} \quad (6.2)$$

Where C' is normalized oxygen isotope concentration, $C(x, t)$ is oxygen isotope concentration at certain time and depth in the sample, C_1 is the natural abundance of ^{18}O isotope which is always 0.002 (0.2%), C_2 is ^{18}O gas concentration in isotope enriched

VI - Functional study of $\text{La}_{0.8}\text{Sr}_{0.2}\text{Mn}_{1-x}\text{Co}_x\text{O}_{3\pm\delta}$ ($x=0$ to 1), combinatorial thin film system by IEDP-SIMS technique

surrounding atmosphere which is 0.553 (55.3%) in the oxygen isotope exchange gas used for the combinatorial sample. The above **equation 6.1** is also used to determine the elemental fraction of other secondary ion intensities such as LaO^- , SrO^- , MnO^- , CoO^- , YO^- , ZrO^- , Si.

In **Figure 6.4** the in-depth distribution of ion concentration acquired by IEDP-SIMS in LSMC/8YSZ bilayers (sample-C2-700-c) is given as an example. The secondary ion signals such as LaO^- was used to determine LSMC/8YSZ interface. The drop of LaO^- counts from 90% to 10% was located as LSMC/8YSZ interface position. The sputter-time axis was converted into thickness axis using the thickness of LSMC and 8YSZ layers determined by SEM (see **section 5.5.4** in **chapter 5** for more details about thickness).

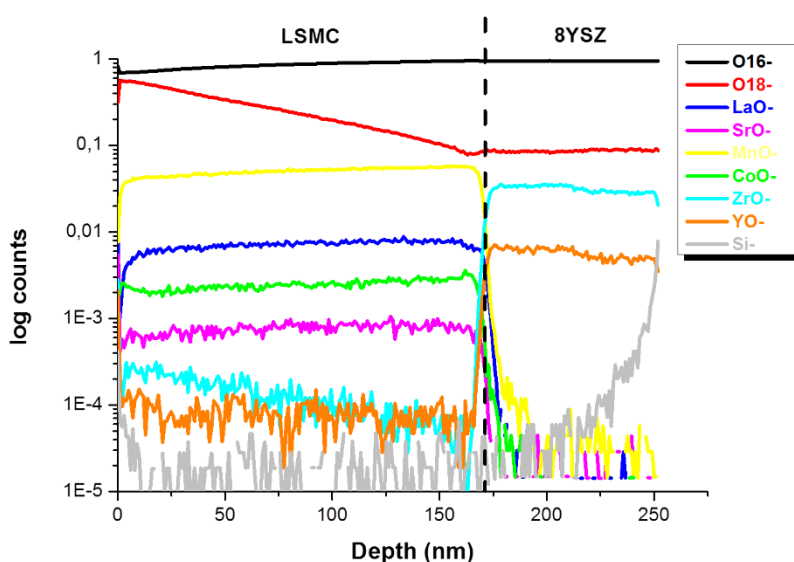


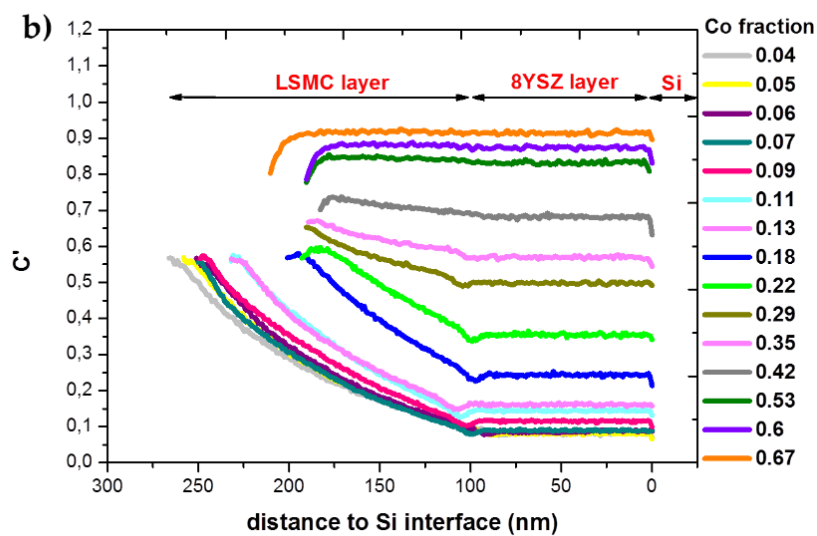
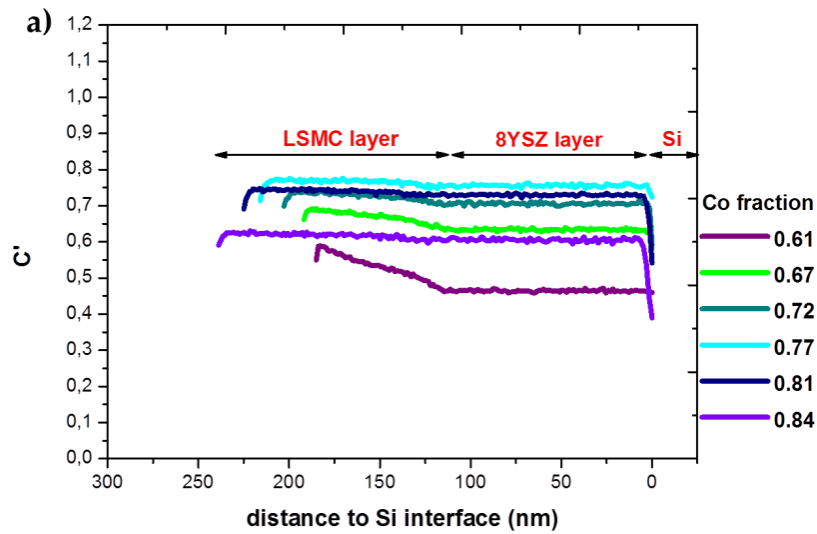
Figure 6.4 Typical SIMS depth profile of the different species contained in the LSMC/YSZ bilayer corresponding to sample C2-700-c. Sharp interfaces with short interdiffusion close to the LSMC/YSZ interlayer can be observed ensuring the high quality of the films.

In **Figure 6.4**, it is noticeable that the intensity of Si in LSMC and 8YSZ layers are in the order of 10^{-5} to 10^{-4} which is close to zero that indicates there is no Si diffusion from the substrate to the deposited top layers. Similarly, intensities of YO^- , ZrO^- in LSMC layer are in the same range, which confirms that the sample C2-700-c used for oxygen exchange is a pure composition unaffected by the diffusion of substrate atoms.

VI - Functional study of $La_{0.8}Sr_{0.2}Mn_{1-x}Co_xO_{3\pm\delta}$ ($x=0$ to 1) combinatorial thin film system by IEDP-SIMS technique

Similarly, the concentration profile of other samples (sample list in **Table.6.1**) were analyzed confirming that any impurity is found in LSMC layer.

The ^{18}O normalized concentration depth profile obtained in LSMC/8YSZ bilayers with varying Co content are organized based on different oxygen exchange temperatures 600°C, 700°C and 800°C which is given in the following figures (**Figure 6.5a, b and c**).



VI - Functional study of $\text{La}_{0.8}\text{Sr}_{0.2}\text{Mn}_{1-x}\text{Co}_x\text{O}_{3\pm\delta}$ ($x=0$ to 1) combinatorial thin film system by IEDP-SIMS technique

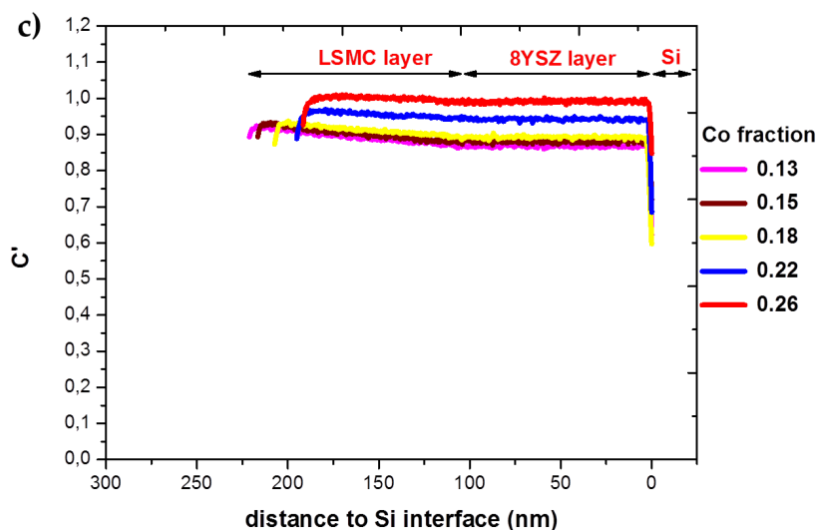


Figure 6.5. ^{18}O normalized concentration depth profile obtained in LSMC/8YSZ bilayers obtained through IEDP-SIMS measurement which is categorized based on different oxygen isotope exchange temperature a) 600°C b) 700°C c) 800°C. x-axis represents distance (thickness) of LSMC/YSZ layer over Si interface.

It can be seen clearly in **Figure 6.5** that the influence of Co content on ^{18}O oxygen isotope concentration which seems highly sensitive to the amount of Co content present in LSMC system. The different length of diffusion profiles corresponding to different thickness of the LSMC system as seen in **section 5.5.4 in chapter 5**.

There was difficulty in achieving ^{18}O concentration profile at high temperature 800°C due to fast oxygen diffusion that produced saturation of ^{18}O isotope in LSMC layer. The sample with Co fraction above 0.26 at 800°C is saturated with ^{18}O isotope, hence SIMS mapping was not performed for higher that concentration of Co.

The total amount of oxygen isotope concentration in LSMC surface and the diffusion concentration inside LSMC layer increase over Co concentration. Also the concentration profile becomes straight with respect to Co. This trend suggests an increment in diffusion coefficient D^* and surface exchange coefficient k^* values over Co percentage in LSMC system that can be expected from oxygen isotope depth profile fittings.

6.3 Determination of oxygen transport parameters of LSMC system by FEM simulation

There are numerous analytical solutions available in the literature to extract D^* and k^* values from the oxygen isotope concentration profile which depends on the particularity of the system studied [12]. In **appendix A**, some commonly used models to study the oxygen transport in oxides are explained. In addition to that, Two-slab model is also introduced to study bilayer systems. (Readers are recommended to go through **appendix A** for more information about Two-slab model).

Initially, oxygen diffusion profiles of LSMC/8YSZ bilayers (**Figure 6.5a, b and c**) are fitted using a Two-slab model. As an example, the fitting obtained in LSMC layer (sample code - C2-700-c) with 6% Co using Two-slab model is given in **Figure 6.6**.

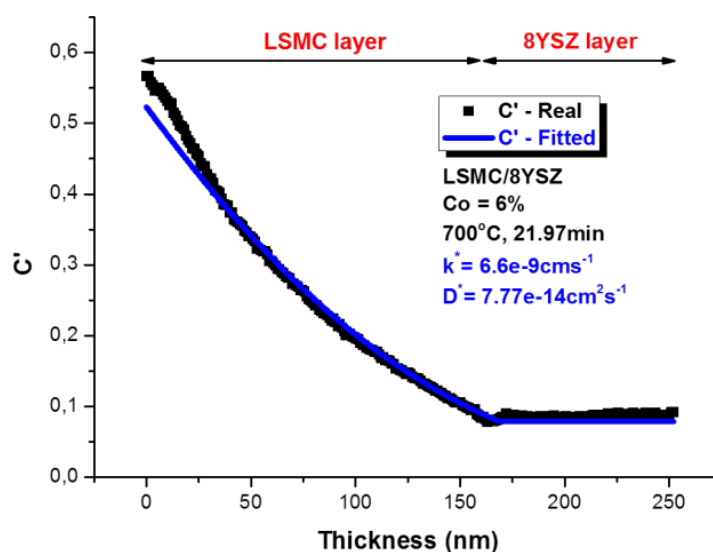


Figure 6.6. Fitting of oxygen isotope diffusion profile using Two-slab model corresponding to LSMC layer with 6% Co (sample code - C2-700-c).

The experimental profile in **Figure 6.6** corresponding to the sample C2-700-c seems to have three regions constitute of a gradual decay in LSMC surface, a deep-penetrating tail inside LSMC layer and a small dip at LSMC/YSZ interface. In addition, there is back-diffusion can always be observed in all oxygen diffusion profiles at gas/LSMC interface (**Figure 6.5a, b and c**).

VI - Functional study of $\text{La}_{0.8}\text{Sr}_{0.2}\text{Mn}_{1-x}\text{Co}_x\text{O}_{3\pm\delta}$ ($x=0$ to 1) combinatorial thin film system by IEDP-SIMS technique

In **Figure 6.6** it is clear that the whole experimental profile cannot be fitted using Two-slab model. The reason can be due to LSMC system may act as a heterogeneous medium with multiple pathways for oxygen transport. The presence of such heterogeneity could be due to columnar-shaped grains obtained by PLD deposition. The associated vertically aligned grain boundaries may act as highway for oxygen transport, compared to the samples prepared with other techniques. These grain boundaries can offer extra diffusion and exchange pathways, with different properties compared to bulk.

Generally, Two-slab model is defined for homogeneous media, with that it is not possible to distinguish D_b^* , D_{gb}^* and k_b^* , k_{gb}^* or more than one D^* and k^* values embedded in an oxygen isotope diffusion profile of particular composition. where D_b^* is oxygen self-diffusion coefficient along bulk, D_{gb}^* is oxygen self-diffusion coefficient along grain boundary. Similarly, k_b^* is oxygen self-exchange coefficient along bulk, k_{gb}^* is oxygen self-exchange coefficient along grain boundary.

Since there is no analytical solution available for a bilayer heterogeneous thin film system with different D^* and k^* values, the oxygen isotope diffusion profiles of LSMC/8YSZ bilayer are studied by numerical solutions using Finite Element method (FEM) to extract the oxygen transport parameters along the bulk and grain boundaries (D_b^* , D_{gb}^* and k_b^* , k_{gb}^*) of the LSMC layer.

The isotope oxygen concentration in LSMC/8YSZ bilayer was simulated by constructing a geometry equivalent to LSMC/8YSZ nanostructure. The geometry consists of a vertically aligned columnar set of grains associated with LSMC and 8YSZ layer in which the top-layer LSMC is exposed to oxygen enriched isotopic atmosphere (55.3% of ^{18}O). In the vertically aligned LSMC/8YSZ nanostructure, a unit cell is taken into account for FEM simulation, consisting of two-half grains in series which is parallel to other two half-grains arranged in series. These grains are separated by 1nm thick grain boundary. The top-view of unit cell is equivalent to the microstructure of a brick-layer model [13]. The thickness and average grain size values estimated by SEM, AFM studies in the previous **chapter-5 (section 5.5.3 and 5.5.4)** was applied in the construction of the sample geometry for FEM simulation.

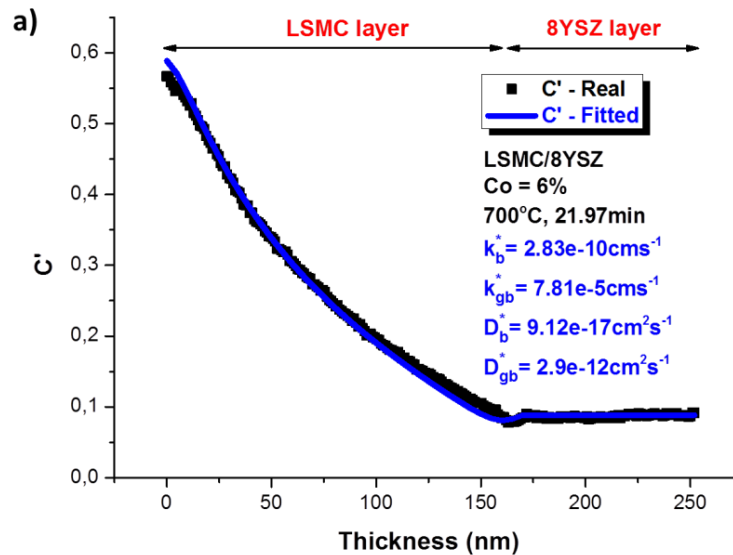
In grain bulk, *De-souza et al.* [14, 15] values of oxygen diffusion and exchange coefficients (D_b^* and k_b^*) are used as reference to simulate the oxygen isotope profiles. In grain boundary, manually adjusted values of diffusion and exchange coefficients

VI - Functional study of $La_{0.8}Sr_{0.2}Mn_{1-x}Co_xO_{3\pm\delta}$ ($x=0$ to 1) combinatorial thin film system by IEDP-SIMS technique

$(D_{gb}^*$ and k_{gb}^*) are used to simulate the experimental profile. It is found that the shape of experimental profile is very sensitive to D_b^* , D_{gb}^* and k_b^* , k_{gb}^* values and they are adjusted till a good fitting was obtained.

As an example, the oxygen isotope profile simulated in LSMC/8YSZ bilayer sample with 6% Co (sample code - C2-700-c) is given in **Figure 6.7** which shows that the simulated profile is in good agreement with the experimental profile and confirms the possibility of fitting the whole experimental profile with FEM simulation that was not possible using a simple Two-slab model.

Also, 3D isotopic concentration distribution in sample C2-700-c (**Figure 6.7b**) reveals that both grain boundary and grain bulk are active for oxygen exchange and diffusion. Although both pathways are active, oxygen isotope concentration inside and surrounding region of grain boundary (top-view image in **Figure 6.7b**) is particularly high compared to the grain bulk region, which confirms that the grain boundary pathway acts as the most desirable preferential pathway for oxygen entry on LSMC surface (exchange process) and oxygen transport (diffusion transport) inside LSMC.



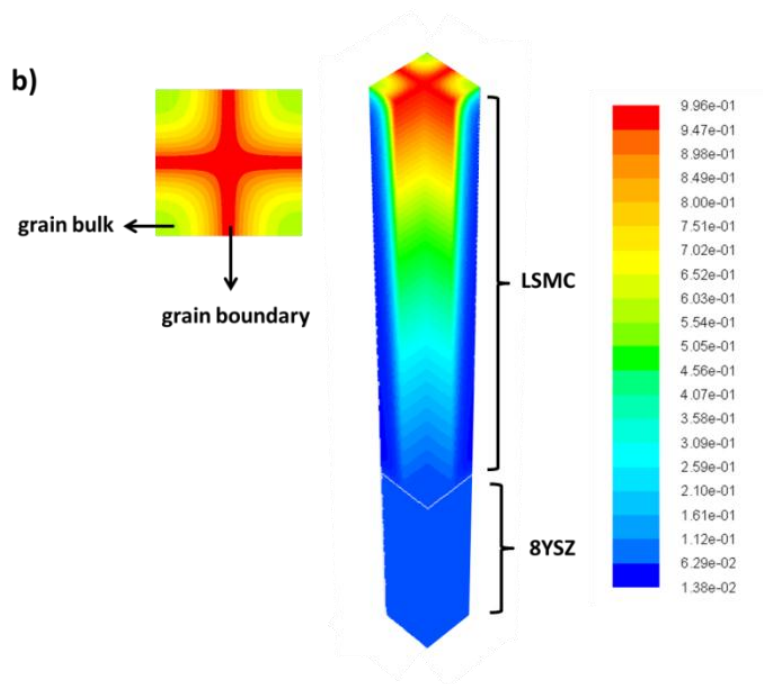


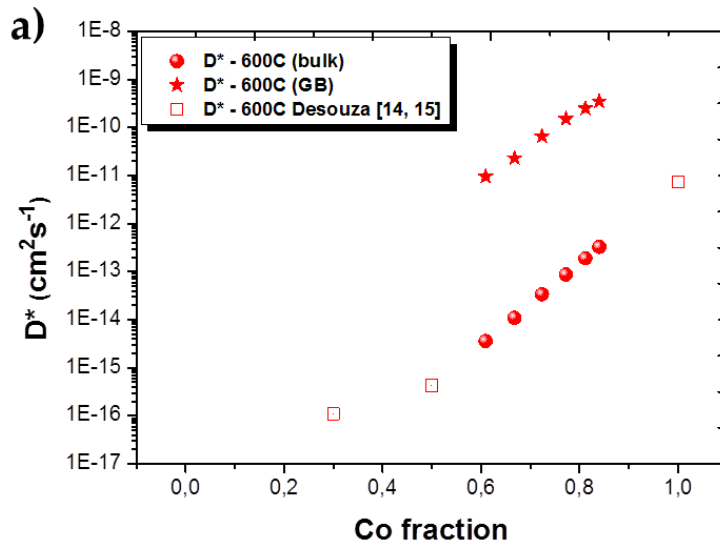
Figure 6.7. a) Oxygen isotope simulated concentration profile is compared with experimental profile corresponding to sample C2-700-c with 6% Co. b) Top-view and cross-section 3D images of oxygen isotope ^{18}O concentration distribution map in LSMC/8YSZ bilayer for the intersection of four quarters of grain generated by FEM simulation belong to the same sample C2-700-c.

In the previous study on pure LSM (**chapter-4**) [16] it was found that the grain bulk pathway was orders of magnitude lower diffusivity than GB as it is known that LSM is a bad oxygen-ion conductor. In the present stud on LSMC thin film combinatorial system, oxygen vacancies may present everywhere in LSMC which is proportional to Co concentration, but the amount of vacancies available in grain boundary should be comparatively higher than grain bulk region. Therefore higher amount of oxygen vacancy concentration is supposed to be responsible for the higher amount of oxygen isotope concentration in the surface and innermost part of grain boundary.

Similarly, an appropriate profile was simulated for various oxygen isotope diffusion experimental profiles acquired in LSMC combinatorial thin film system (**Figure 6.5a, b and c**). A collection of D_b^* , D_{gb}^* and k_b^* , k_{gb}^* values of LSMC combinatorial system acquired from FEM simulation is plotted and the results are discussed in **sections 6.3.1 and 6.3.2**.

6.3.1 Oxygen self-diffusion coefficients D_b^* , D_{gb}^* Vs Co content

In Figure 6.8a, b and c both diffusion coefficients along grain bulk D_b^* and grain boundary D_{gb}^* increase as a function of Co content, as well as with temperature 600°C, 700°C and 800°C. However, the oxygen diffusivity values of D_b^* , D_{gb}^* at 700°C and 800°C remains almost constant until Co content $x \approx 0.2$ and increases after $x \approx 0.2$. A similar trend was also observed by *De Souza et al.* [14, 15] in his oxygen self-diffusion coefficient values on LSMC bulk until $x = 0.2$ fraction of Co substitution. This trend shows that Co substitution (from $x \approx 0.04$ to 0.2) in LSM perovskite structure does not produce any remarkable change in the oxygen diffusivity values of grain boundary and bulk pathways.



VI - Functional study of $\text{La}_{0.8}\text{Sr}_{0.2}\text{Mn}_{1-x}\text{Co}_x\text{O}_{3\pm\delta}$ ($x=0$ to 1)
combinatorial thin film system by IEDP-SIMS technique

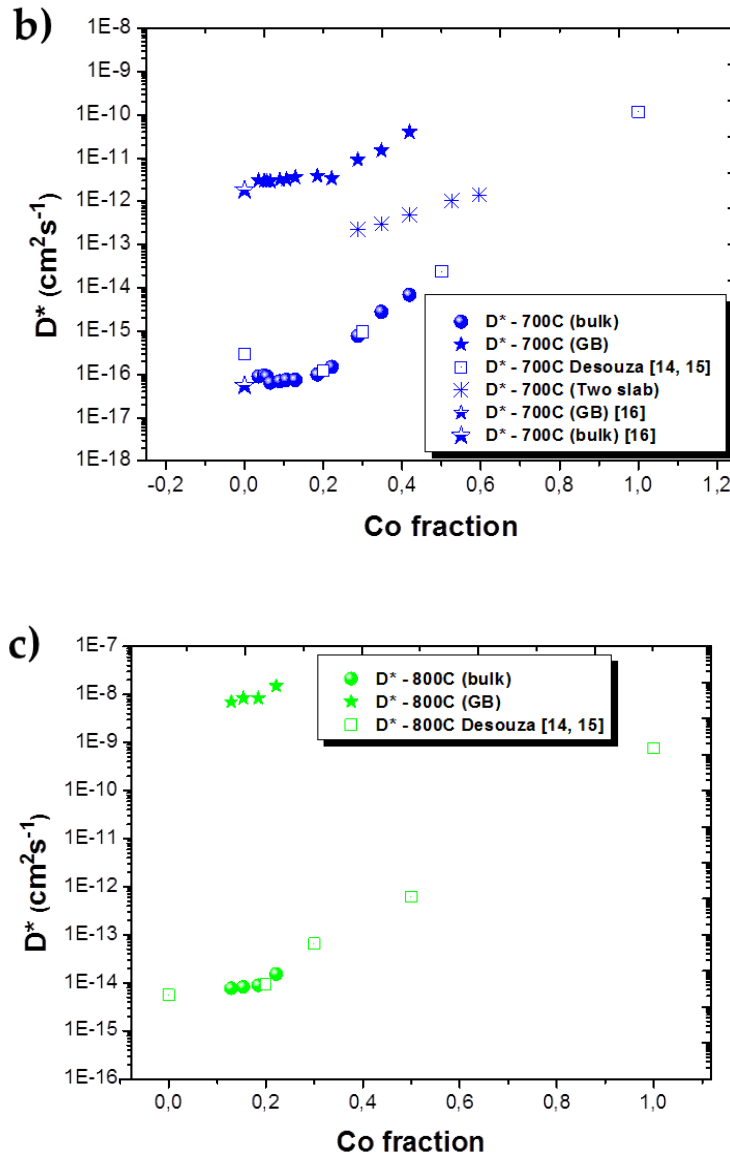


Figure 6.8. Oxygen self-diffusion coefficient along grain bulk D_b^* and grain boundary D_{gb}^* extracted at a) 600°C b) 700°C c) 800°C is plotted against Co content. The values are compared with literature [14, 15, 16].

D^* dependency on Co fraction can be explained by the defect chemistry of parent materials [17-20]. It is well-known that LSM is an oxygen hyper-stoichiometric material system where the metal vacancies, electron and holes are the predominant defects while oxygen vacancy concentration $[\dot{V}_o]$ is very low. In opposite to LSM, LSC is an oxygen sub-stoichiometric material where oxygen vacancies are the major defects including electrons and holes [11, 14, 15, 21]. Typically, Oxygen diffusivity is promoted by the concentration of oxygen vacancies \dot{V}_o [11, 14, 15, 21]. The following equation

**VI - Functional study of $\text{La}_{0.8}\text{Sr}_{0.2}\text{Mn}_{1-x}\text{Co}_x\text{O}_{3\pm\delta}$ ($x=0$ to 1)
combinatorial thin film system by IEDP-SIMS technique**

shows the relation between D^* and oxygen vacancy concentration $[\dot{V}_o]$ which can be given as,

$$D^* = f^* D_v [\dot{V}_o] \quad (6.3)$$

Where f^* is oxygen isotope correlation factor which is 0.69 for perovskites [14, 22], D_v is vacancy diffusion coefficient.

Alan et al. [23] studied oxygen non-stoichiometry (δ) values in LSMC system and it is found that $\delta = 0.006$ when Co content $x = 0$ and $\delta = 0.002$ when $X = 0.1$, measured by TGA at 1040°C in air. Even though TGA measurement is higher than 700°C , almost constant values of D_b^* and D_{gb}^* from $x \approx 0.04$ to 0.2 in **Figure 6.8b** is attributed to there is no considerable change in the oxygen non-stoichiometry values based on *Alan et al.* results. Therefore, increment in D_b^* and values above $x > 0.2$ may due to an increment in the oxygen vacancy concentration $[\dot{V}_o]$ or non-stoichiometric (δ) values in LSMC system over Co content. But D_{gb}^* values are not in the same order of magnitude as D_b^* instead it is 3 to 6 orders greater than D_b^* .

In **Figure 6.8** it is also noticed that as temperature increases, the gap between D_b^* and D_{gb}^* values of particular temperature also increases in order of magnitude. At 600°C D_{gb}^* values are 3 orders of magnitude higher than D_b^* values, at 700°C it is 4 orders of magnitude higher. Similarly, at 800°C D_{gb}^* is approximately 6 orders of magnitude higher than D_b^* .

Based on the knowledge gained in oxide-ion transport in grain boundary region of pure LSM by IEDP-SIMS, impedance and TEM studies [16] strain induced high density of dislocations in grain boundary region can be responsible behind the remarkable enhancement in the diffusivity along the grain boundary D_{gb}^* of LSMC nanostructures. It can be the explanation for increment in D_{gb}^* observed above $x > 0.2$ and the increment in magnitude difference between D_b^* and D_{gb}^* values against temperature. Further, the increase of D_{gb}^* as a function of Co goes in parallel to D_b^* . It is probably due to the effect of Co on the grain boundary is similar to bulk.

The activation energy or enthalpy of oxygen diffusion ΔH_{D^*} is the sum of oxygen migration enthalpy ΔH_m and association enthalpy ΔH_a which can be written as,

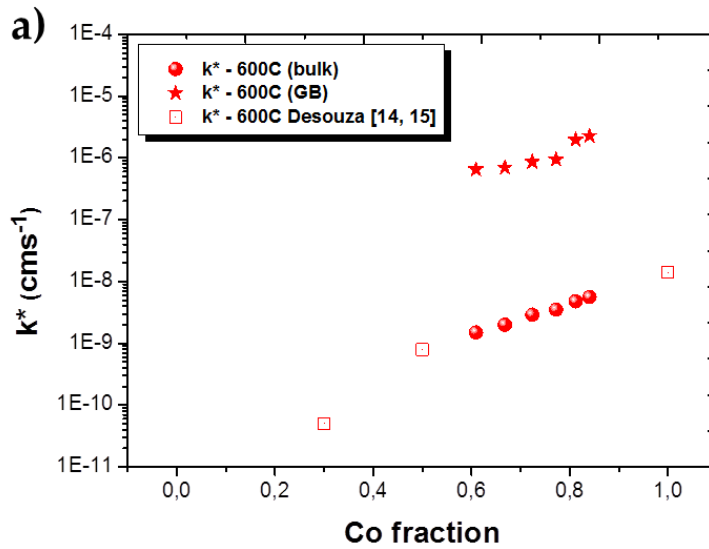
VI - Functional study of $La_{0.8}Sr_{0.2}Mn_{1-x}Co_xO_{3\pm\delta}$ ($x=0$ to 1) combinatorial thin film system by IEDP-SIMS technique

$$\Delta H_{D^*} = \Delta H_m + \Delta H_a \quad (6.4)$$

Association enthalpy is related to the enthalpy associated with formation of complex defects such as oxygen vacancies due to A or B-site substitution, here Mn is replaced by Co. The representation of D_b^* and D_{gb}^* values in the form of arrhenius plot and the estimation of ΔH_{D^*} from arrhenius plot cannot be attained in the present work because LSMC compositions measured at different temperatures are not exactly the same composition and very limited.

6.3.2 Oxygen self-exchange coefficients k_b^* , k_{gb}^* Vs Co content

In Figure 6.9a, b and c it is clear that both oxygen surface coefficient along grain bulk k_b^* and grain boundary k_{gb}^* increases as a function of Co content and temperature, however changes in k_b^* , k_{gb}^* over Co content is relatively smaller than D_b^* , D_{gb}^* values.



VI - Functional study of $\text{La}_{0.8}\text{Sr}_{0.2}\text{Mn}_{1-x}\text{Co}_x\text{O}_{3\pm\delta}$ ($x=0$ to 1)
combinatorial thin film system by IEDP-SIMS technique

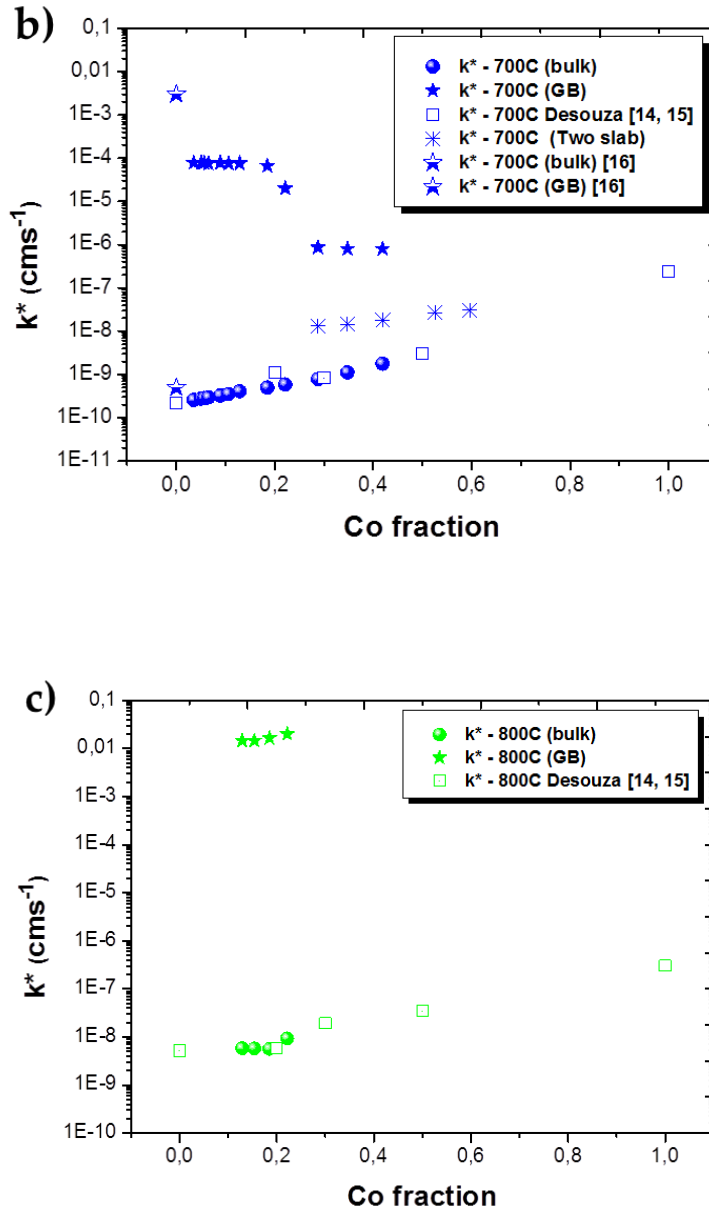


Figure 6.9. Oxygen self-exchange coefficient along grain bulk k_b^* and grain boundary k_{gb}^* extracted at a) 600°C b) 700°C c) 800°C is plotted against Co content. The values are compared with literature values [14, 15, 16].

At 600°C and 800°C both k_b^* and k_{gb}^* (Figure 6.9a and c) increases upon Co content. Although k_b^* increases against Co fraction at 700°C (Figure 6.9b), oxygen exchange along grain boundary k_{gb}^* remains same until Co content $x = 0.18$ and starts to decrease reach minimum at $x = 0.29$. Then k_{gb}^* values remain constant from $x = 0.29$. According to FEM simulation k_{gb}^* decreases after $x = 0.18$ amount of Co concentration. The values

VI - Functional study of $La_{0.8}Sr_{0.2}Mn_{1-x}Co_xO_{3\pm\delta}$ ($x=0$ to 1) combinatorial thin film system by IEDP-SIMS technique

from $x = 0.29$ to 0.42 is two orders of magnitude lower than than the value around $x \approx 0.18$.

Although the k_{gb}^* values are attained by good fitting at 700°C , it is not clear whether the step-down trend in k_{gb}^* after $x = 0.18$ is due to change in LSMC nanostructure that can affect the surface exchange rate with single or multiple exchange coefficients. FEM model has to be modified according to change in nanostructure of the thin film in order to extract accurate oxygen exchange coefficient values. Hence, Two-slab model is used to fit the oxygen diffusion profile with Co concentration $x = 0.29$ to 0.42 in order to find the average value of surface exchange coefficient k^* which is plotted in **Figure 6.9b**.

Similar to D_b^* and D_{gb}^* magnitude gap observed in the last section, the oxygen exchange coefficient gap between k_b^* and k_{gb}^* also increases with respect to temperature. At 600°C , k_{gb}^* values are 3 orders of magnitude higher than k_b^* values, whereas it is 3 to 5 orders of magnitude higher at 700°C . Similarly, at 800°C the value of k_{gb}^* is 7 orders of magnitude higher than k_b^* .

Normally, oxygen surface exchange coefficient k^* describes the rate of oxygen exchange flux between the gas phase and solid electrode. In Kroger-Vink notation, the oxygen exchange equilibrium reaction can be written as,



In the forward side of above equation, oxygen from gas phase is exchanged into solid surface occupies oxygen vacancy \dot{V}_o by generating holes.

Generally, oxygen exchange process constitute of several steps such as gas phase diffusion, adsorption, electronation, dissociation, vacancy migration and incorporation of oxygen ions into the crystal lattice [24-28], which act as rate-limiting steps. The oxygen exchange coefficient values k_b^* and k_{gb}^* attained through tracer exchange measurements is an average value of all these rate-limiting steps [20].

A recent study on oxygen exchange kinetics in LSMC like perovskites by ab-initio calculations states that when there is a high concentration of oxygen vacancies, vacancy mobility on the surface are the key factors of oxygen exchange rate. In a system like LSMC, electrons cannot not influence the surface-exchange rate because LSMC is a very good electronic conductor its conductivity is several orders of magnitude higher than ionic conductivity.

VI - Functional study of $\text{La}_{0.8}\text{Sr}_{0.2}\text{Mn}_{1-x}\text{Co}_x\text{O}_{3\pm\delta}$ ($x=0$ to 1) combinatorial thin film system by IEDP-SIMS technique

Apart from the defects, there are other factors such as cation (Sr in most cases) segregation [30, 31], surface termination (AO, BO₂ type) [28, 23], surface electronic structure that can also affect oxygen exchange rate on the surface. Alan *et al.* [23] found that the dominance of A-site cations on LSMC surface in which surface oxygen species (α -oxygen) are unaffected by Co concentration.

If oxygen exchange along grain boundary and grain bulk of LSMC is influenced by oxygen vacancy concentration [\dot{V}_o], k_b^* , k_{gb}^* should follow the same trend as D_b^* , D_{gb}^* . Instead the relative changes of k_b^* , k_{gb}^* over Co fraction is smaller than D_b^* , D_{gb}^* .

The surface chemistry and type of defects present in surface of LSMC grain bulk and grain boundary is not clear, however grain boundary region acts as a favorable path for oxygen introduction in certain range of compositions in LSMC system. A further examination on the surface state of LSMC is necessary in order find a valid explanation about k_b^* and k_{gb}^* trend in LSMC system.

6.4 Conclusion

The oxygen transport properties of LSMC/8YSZ bilayer combinatorial system was mapped by isotope exchange depth-profiling (IEDP) coupled with punctual SIMS measurement. The oxygen self-diffusion coefficients D_b^* , D_{gb}^* and self-exchange coefficients k_b^* , k_{gb}^* obtained by FEM simulation reveal that grain boundary act as fast diffusion and exchange pathways for oxygen ion transport. However, further investigation on the surface chemistry and structure of LSMC system is required to understand the influence of Co on enhanced k_{gb}^* values and the step down trend in k_{gb}^* values at 700°C.

References

- [1] J. A. Lane, J. A. Kilner, *Solid State Ionics*, 2000, 136, 997.
- [2] X. Chen, S. Wang, Y. L. Yang, L. Smith, N. J. Wu, B. I. Kim, S.S. Perry, A. J. Jacobson, A. Ignatiev, *Solid State Ionics*, 2002, 146, 405.
- [3] M. Kubicek, T. M. Huber, A. Welzl, A. Penn, G. M. Rupp, J. Bernardi, M. S. Pollach, H. Hutter, J. Fleig, *Solid State Ionics*, 2014, 256, 38.
- [4] Q. Yang, J. D. Nicholas, *J. Electro. chem. Soc.*, 2014, 161, F3025.
- [5] Q. Yang, T. E. Burye, R. R. Lunt, J. D. Nicholas, *Solid State Ionics*, 2013, 249, 123.
- [6] M. Rekas, T. Bak, J. Nowotny, C. C. Sorrell, Y. Zhao, K. Fogger, E. R. Vance, *J. Mater. Sci.*, 2000, 11, 691.
- [7] S. P. S. Badwal, S. P. Jiang, J. Love, J. Nowotny, M. Rekas, E. R. Wance, *Solid State Ionics*, 2001, 27, 431.
- [8] J. A. Kilner, S. J. Skinner, H. H. Brongersma, *J. Solid State Electrochem*, 2011, 15, 861.
- [9] E. Fischer, J. L. Hertz, *Solid State Ionics*, 2012, 218, 18.
- [10] R. J. Chater, *Ph.D. Thesis*, University of London, June, 2014.
- [11] R. V. Wandekar, B.N. Wani, S.R. Bharadwaj, *Solid State Sciences*, 2009, 11, 240.
- [12] John Crank, *The Mathematics of Diffusion*, Oxford, UK, 1986.
- [13] H. L. Tuller, *Solid State Sciences*, 2000, 131, 143. (brick layer)
- [14] R. A. De Souza, J. A. Kilner, *Solid State Ionics*, 1998, 106, 175.
- [15] R. A. De Souza, J. A. Kilner, *Solid State Ionics*, 1999, 126, 153.
- [16] A. M. Saranya, D. Pla, A. Morata, A. Cavallaro, J. C. Vázquez, J. A. Kilner, M. Burriel, A. Tarancon, *Adv. Energy Mater.*, 2015, 5, 1500377.
- [17] J. Mizusaki, Y. Mima, S. Yamauchi, K. Fueki, *J. solid state chem.*, 1989, 80, 102.
- [18] S. Carter, A. Selcuk, R. J. Chater, J. Kajda, J.A. Kilner, B.C.H. Steele, *Solid State Ionics*, 1992, 53, 597.
- [19] Y. Ji, J. A. Kilner, M. F. Carolan, *Solid State Ionics*, 2005, 176, 937.
- [20] E. N. Armstrong, K. L. Duncan, E. D. Wachsman, *Phys. Chem. Chem. Phys.*, 2013, 15, 2298.
- [21] S. Kuharungrong, T. Dechakupt, P. Aungkavattana, *Materials Letters*, 2004, 58, 1964.
- [22] M. Kubicek, Z. Cai, W. Ma, B. Yildiz, H. Hutter, J. Fleig, *J. Am. chem. Soc.*, 2013, 7(4), 3276.
- [23] A. Thursfield, J. C. H. Rossiny, S. Fearn, J. A. Kilner, I. S. Metcalfe, *Solid State Ionics*, 2012, 225, 182.
- [24] R. A. De Souza, *Phys. Chem. Chem. Phys.*, 2006, 8, 890.
- [25] W. C. Jung, H. L. Tuller, *Adv. Energy Mater.*, 2011, 1, 1184.

**VI - Functional study of $\text{La}_{0.8}\text{Sr}_{0.2}\text{Mn}_{1-x}\text{Co}_x\text{O}_{3\pm\delta}$ ($x=0$ to 1)
combinatorial thin film system by IEDP-SIMS technique**

- [26] J. Fleig, H. R. Kim, J. Jamnik, J. Maier, *Fuel cells*, 2008, 5, 330.
- [27] G. J. laO, Y. S. Horn, *J. Electrochem. Soc.*, 2009, 156, B816.
- [28] L. Wang, R. Merkle, Y. A. Mastrikov, E. A. Kotomin, J. Maier, *J. Mater. Res.*, 2012, 27, 2000.
- [29] J. A. Kilner, R. A. De Souza, I. C. Fullarton, *Solid State Sciences*, 1996, 86, 703.
- [30] M. Kubicek, A. Limbeck, T. Fromling, H. Hutter, J. Fleig, *J. Electro. chem. Soc.*, **2011**, 158, B727.
- [31] H. Jalili, J. W. Han, Y. Kuru, Z. Cai, B. Yildiz, *J. Phys. Chem. Lett.*, 2011, 2, 801.

7 Conclusion

7. Conclusions

The work developed in this thesis was devoted to investigate the oxygen ion transport in perovskite-related Mixed Ionic and Electronic Conducting (MIEC) oxides of thin film cathodes to correlate the oxygen ion transport with thin film nanostructure consisting of grain bulk and grain boundaries. There are various experimental, technological and theoretical strategies have been adopted to achieve the goal. The most relevant achievements attained in this thesis are listed below,

- In the chapter about **interdiffusion mechanism and parent layer optimization in PLD** - Interdiffusion mechanism is validated through the experiments on LSC/LSF and LSM/LSC multilayer depositions. It was found that thickness below 3nm is an optimum thickness value for growing LSM, LSC and LSF parent layers involved in multilayer deposition to achieve the pure desired product from the diffusion-limited homogeneous intermixing. This result laid a foundation to fabricate LSMC binary system.
- In the work on the **investigation of oxygen ion transport in LSM thin film nanostructure** – LSM an electronic conductor is converted into a good mixed ionic electronic conductor by synthesizing a nanostructure with high density of vertically aligned GBs in PLD with high concentration of strain-induced defects. Further, a remarkable enhancement is observed in the oxide ion mass transport (up to 5 to 6 orders of magnitude) along the grain boundary region of LSM in the temperature range 500-700°C. The result confirms the possibility of tailoring the electrical nature of the whole material by nanoengineering, especially at low temperatures.
- In **LSMC binary thin film system fabrication** - The continuous composition spread (CCS) LSMC Pseudo-binary system is successfully fabricated without any parasitic phase based on the best plume center position predicted from the parent layer superposition study. Hence, the adopted new methodology to predict the thickness and Mn/Co concentration has been proved as trustworthy

Conclusion

to fabricate LSMC binary system. It validates that the same methodology is applicable to fabricate a ternary or quaternary system.

- In the **functionality study of LSMC binary system** - The oxygen transport properties of LSMC/8YSZ bilayer combinatorial system is successfully mapped by isotope exchange depth-profiling (IEDP) coupled with punctual SIMS measurement. The oxygen self-diffusion coefficients D_b^* , D_{gb}^* and self-exchange coefficients k_b^* , k_{gb}^* obtained by FEM simulation reveal that grain boundary act as fast diffusion pathway for oxygen ion transport in LSMC system.
- The oxygen transport coefficients of LSM thin film and LSMC binary system are determined by FEM simulation and two-slab model, first ever two models are introduced in this thesis to fit the oxygen diffusion profiles.

The presented results lead to fundamental insights into oxygen diffusion along GBs (charge transport along interfaces) and to the application of these engineered nanomaterials in new advanced solid state ionics devices such are micro solid oxide fuel cells.

Appendix-A

Introduction to Two-slab model

Appendix-A

A.1 Outline

^{18}O diffusion profile obtained from IEDP-SIMS measurement can be fitted using different models. A model is a solution of the diffusion equation, obtained by fixing boundary conditions and solving the diffusion equation for a particular geometry of a system. In most cases the system is treated as isotropic medium where diffusion coefficient D is constant in all directions [1, 2].

Most of the samples employed for IEDP-SIMS measurement in this thesis are semi-infinite or thin film system composed of oxide bilayers deposited on Si substrate that can be called as “Cathode/Electrolyte/Substrate (CES)” system. There are two kinds of classical models that are commonly applied to fit the ^{18}O diffusion profile which are the models for semi-infinite medium and plane sheet medium [1]. However, each model has its own limitation of application based on the system geometry and boundary conditions that cannot be applicable in the system studied in this thesis.

In this appendix a new model is proposed as an alternative to classical semi-infinite and plane sheet model to determine oxygen diffusion coefficient D^* , oxygen surface exchange coefficient k^* in oxide bilayers deposited on oxygen insulating substrate. The proposed model arises from the “Two-slab model”, a remarkable work of E. Mayer entitled “Heat flow in composite slabs”, [3] suitable to apply in the thin film system (CES) studied in this thesis.

Appendix A is organized in following way. The classical models and its place of validity are explained in **section A.2**. The solution to Two-slab model is given in terms of diffusion equations in **section A.3**. To validate the Two-slab model, IEDP-SIMS profile corresponding to a sample with 4% Co is tested by fitting the experimental profile. The results and validity of two-slab model is discussed in **section A.3.5**.

A.2 Classical models and its validity

A.2.1 Solution to semi-infinite medium

In most cases, traditional semi-infinite solution is used to determine the oxygen-diffusion and surface exchange coefficient (D^* and k^*) values in a medium that can be approximated to have an infinite thickness. When the sample is thicker in comparison

with the diffusion length \sqrt{Dt} of the tracer (^{18}O isotope), then the tracer diffusion profile can be modeled using solution to a semi-infinite medium.

In a semi-infinite medium, isotopic concentration C_x is associated with the concentration value at depth x equal to the background concentration C_{bg} which is 0.002 (natural abundance of ^{18}O).

Regarding boundary condition at gas-solid interface, the rate of transfer of exchanging gas (^{18}O) at gas-solid interface is proportional to the difference between ^{18}O isotopic concentration in the sample surface (C_s) and isotopic concentration in the surrounding atmosphere (C_{gas}) at any time which is equivalent to *surface evaporation boundary condition*. It can be expressed as,

$$-D^* \frac{\partial C(x, t)}{\partial t} = k^* [C_{gas} - C_s] \quad (\text{A.1})$$

Where k^* is constant of proportionality nothing but oxygen surface exchange coefficient.

The solution to Fick's 2nd law of diffusion equation for semi-infinite medium after isotope exchange-anneal time duration t , is given by **crank (page 36, equ.3.35) [1]**,

$$C' = \frac{C(x, t) - C_{bg}}{C_{gas} - C_{bg}} = \text{erfc} \left[\frac{x}{2\sqrt{D^* t}} \right] - \exp[h x + h^2 D^* t] \cdot \text{erfc} \left[\frac{x}{2\sqrt{D^* t}} + h\sqrt{D^* t} \right] \quad (\text{A.2})$$

Where $h = k^*/D^*$. $C(x, t)$ represents tracer concentration within the material as a function of depth x and time t . C_{bg} represents natural abundance of ^{18}O isotope which is always 0.002. C_{gas} represents gas concentration in the surrounding atmosphere. C' or $C(x, t) - C_{bg}/C_{gas} - C_{bg}$ is the normalized tracer concentration. The term $2\sqrt{D^* t}$ is called diffusion length explains the decay of diffusing species concentration as a function of thickness x .

A.2.2 Solution to Plane-sheet model

In thin films, during ^{18}O isotope exchange-annealing, isotopic concentration gradient inside the sample can create a significant amount of isotope concentration at film-substrate interface. This concentration will exceed C_{bg} (0.002) due to the thickness constraint in thin films. In this condition semi-infinite solution cannot be applicable in

thin films. Therefore plane-sheet solution is commonly applied in thin films to fit oxygen diffusion profile.

In a typical plane sheet sample system (**Figure A.1**), ^{18}O diffuses into both sides of thin parallel plane sheet from the gas phase, which can be considered as a symmetrical system. But in a typical thin film sample system, a thin film deposited on oxygen blocking substrate (**Oxide layer/Insulating substrate**) where ^{18}O can diffuse only through the one side of the plane sheet, which is equal to one-half of the diffusion profile obtained in Crank's plane sheet model (**page 60, equ.4.50**) [1].

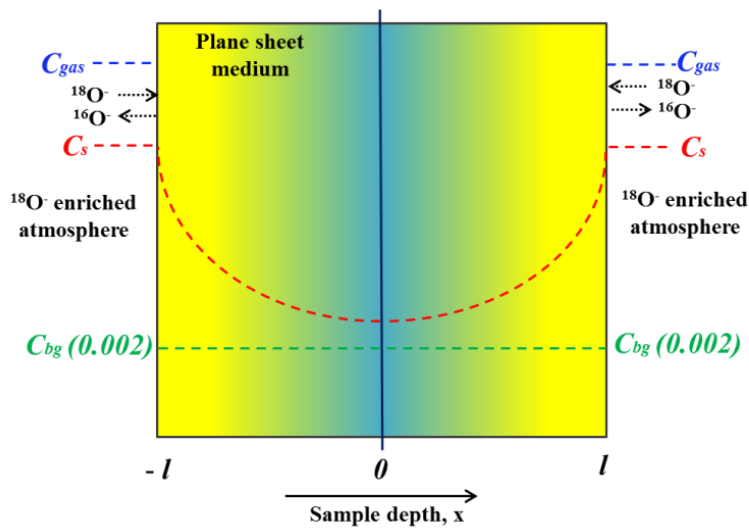


Figure A.1. Illustration of ^{18}O diffusion in a plane sheet medium through both sides of flat surface whose thickness is $-l$ to 0 and l to 0 . C_{gas} is ^{18}O gas concentration in the surrounding atmosphere, C_s is ^{18}O concentration on the sample surface, C_{bg} is the ^{18}O background concentration (0.002).

Similar to semi-infinite solution an Oxide layer/oxygen insulating substrate system has surface evaporation boundary condition at film-air interface ($x = -l$ or $x = l$) which is given as,

$$-D^* \frac{\partial C(x, t)}{\partial t} = k^* [C_{gas} - C_s] \quad (\text{A.3})$$

At film-substrate interface, the substrate acts as an insulator to oxygen where adiabatic or insulating boundary condition (**equation A.10**) can be applied.

Therefore, the solution to Fick's second law of diffusion in a plane sheet medium is given by (**page 60, equ.4.50**) [1],

$$C' = \frac{C(x, t) - C_{bg}}{C_{gas} - C_{bg}} = 1 - \sum_{n=1}^{\infty} \frac{2L \cdot \cos(\beta_n \cdot x/l) \exp(-\beta_n^2 D^* t/l^2)}{(\beta_n^2 + L^2 + L) \cos(\beta_n)} \quad (A.4)$$

where C' or $C(x, t) - C_{bg}/C_{gas} - C_{bg}$ is normalized ^{18}O isotropic concentration, l is film thickness, t is the duration of isotope exchange-annealing. β_n ($n=1, 2, 3, \dots$) are positive roots of transcendental equation,

$$\beta_n \tan \beta_n = L \quad (A.5)$$

Where L is critical length which is a dimensionless parameter,

$$L = \frac{lk^*}{D^*} \quad (A.6)$$

In general the first nine roots of β_n ($n = 1$ to 9) is far enough to determine D^* and k^* values accurately by fitting ^{18}O diffusion profile using Least square minimization routines.

A.3 Two-Slab model

A.3.1 Plane sheet model Vs Two-Slab model

All samples committed to IEDP-SIMS measurement in this work have two oxide ion conducting layers where the first layer is a cathode material (MIEC), second layer is an electrolyte (8YSZ) which are deposited on top of Silicon substrate constitute a “CES system”. Each oxide layer has its own characteristic oxygen diffusion coefficient D^* and surface exchange coefficient k^* values. Therefore, plane sheet solution cannot be applicable in this kind of oxygen ion conducting bilayer system. In the following section, the solution to Two-slab system is given in terms of diffusion problem simply by converting the heat equations to the diffusion equations [3, 4].

A.3.2 Solution to Two-Slab model

Consider a system consisting of two different oxide layers which are oxide layer 1, oxide layer 2 with different oxygen transport D_1^* , D_2^* and exchange properties k_1^* , k_2^* deposited on oxygen blocking substrate. The first layer extends from $-l_1$ to 0 and the second layer is 0 to l_2 .

The system is surrounded by ^{18}O gas enriched atmosphere where the tracer incorporation occurs through the flat-surface of first oxide layer (Figure A.2).

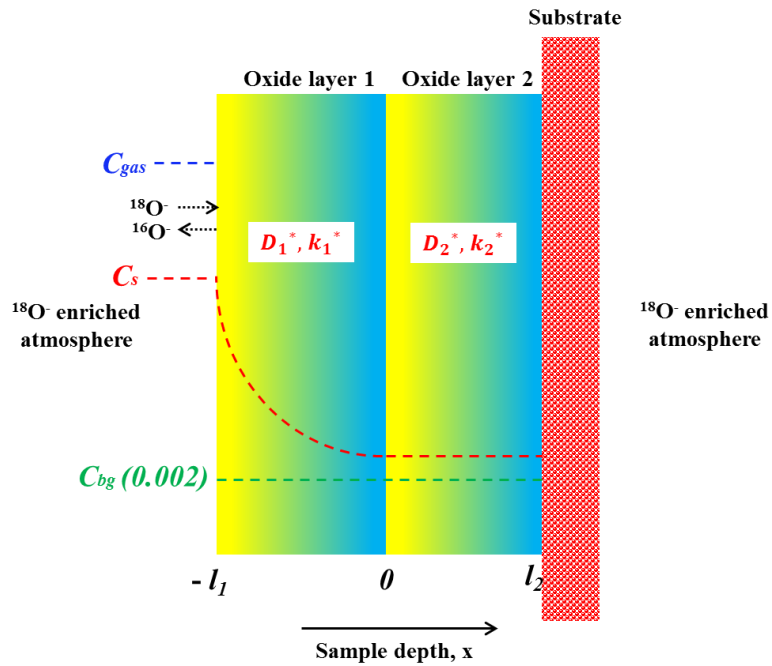


Figure A.2. Illustration of ^{18}O diffusion in cathode/electrolyte/substrate (CES) system of thickness $-l_1$ to 0 and 0 to l_2 . Where C_{gas} is ^{18}O gas concentration in the surrounding atmosphere, C_s is ^{18}O concentration on the surface, C_{bg} is ^{18}O background concentration (0.002).

One-dimensional ^{18}O concentration distribution $C(x, t)$ inside the sample is governed by Fick's second law of diffusion which can be given as,

$$\frac{\partial C(x, t)}{\partial t} = D^* \frac{\partial^2 C(x, t)}{\partial x^2} \quad (\text{A.7})$$

Where D^* represents oxygen self-diffusion coefficient is a constant. D^* for each solid oxide layer is given by,

$$D^* = \begin{cases} D_1^* & -l_1 \leq x \leq 0 \\ D_2^* & 0 \leq x \leq l_2 \end{cases} \quad (\text{A.8})$$

The boundary condition at gas-solid interface ($x = -l_1$) is the surface evaporation boundary condition which can be expressed as,

$$-D_1^* \frac{\partial C(-l_1, t)}{\partial x} = k^* [C_{gas} - C_s(-l_1, t)] \quad (\text{A.9})$$

The solid-insulating interface ($x = l_2$) has vanishing ^{18}O concentration, therefore adiabatic or insulating boundary condition at film-substrate interface is given by,

$$\frac{\partial C(-l_2, t)}{\partial x} = 0 \quad (\text{A.10})$$

^{18}O concentration distribution $C(x, t)$ in the 1st and 2nd layer can be represented by two different functional forms in two regions which is,

$$C(x, t) = F_1(x, t) \quad -l_1 \leq x \leq 0$$

$$C(x, t) = F_2(x, t) \quad 0 \leq x \leq l_2 \quad (\text{A.11})$$

Equation 11 in terms of equation 7 is,

$$D_1^* \frac{\partial^2 F_1(x, t)}{\partial x^2} = \frac{\partial F_1(x, t)}{\partial t} \quad -l_1 \leq x \leq 0$$

$$D_2^* \frac{\partial^2 F_2(x, t)}{\partial x^2} = \frac{\partial F_2(x, t)}{\partial t} \quad 0 \leq x \leq l_2 \quad (\text{A.12})$$

The continuity boundary condition at Oxide layer 1-Oxide layer 2 interface ($x = 0$) is given by,

$$F_1(0, t) = F_2(0, t) \quad (\text{A.13})$$

$$D_1^* \frac{\partial F_1(0, t)}{\partial x} = D_2^* \frac{\partial F_2(0, t)}{\partial x} \quad (\text{A.14})$$

By solving the diffusion **equation A.7** using aforementioned boundary conditions (**equations A.9, A.10, A.14**), the following two kinds of solutions are obtained under two different cases. Readers are suggested to go through reference [3] for detailed solution.

A.3.3 Special case 1: D_1^* , D_2^* are finite

The following general solution **equation A.15** is obtained by assuming oxygen diffusion coefficients of 1st and 2nd layer D_1^* , D_2^* are finite. Therefore, solution to Fick's second law of diffusion equation in a Two-slab medium after isotope ^{18}O exchange-anneal time duration t is given by,

$$C' = \frac{C(x, t) - C_{bg}}{C_{gas} - C_{bg}} = \begin{cases} C_{gas} + \sum_{n=1}^{\infty} A_n \left(\cos \beta_{1n} \frac{x}{l_1} + \mu_{1n} \sin \beta_{1n} \frac{x}{l_1} \right) e^{-\lambda_{1n}^2 t} & -l_1 \leq x \leq 0 \\ C_{gas} + \sum_{n=1}^{\infty} A_n \left(\cos \beta_{2n} \frac{x}{l_2} + \mu_{2n} \sin \beta_{2n} \frac{x}{l_2} \right) e^{-\lambda_{2n}^2 t} & 0 \leq x \leq l_2 \end{cases} \quad (\text{A.15})$$

Where ,

$$A_n = -C_{gas} \frac{N_{mn} + N_{2n}}{D_{1n} + D_{2n}} \quad (\text{A.16})$$

$$\mathbf{D}_{1n} = \frac{l_1}{2\beta_{1n}} [(1 + \mu_{1n}^2)\beta_{1n} + (1 - \mu_{1n}^2)\sin \beta_{1n} \cos \beta_{1n} - 2\mu_{1n} \sin^2 \beta_{1n}] \quad (\text{A.17})$$

$$\mathbf{D}_{2n} = \frac{l_2}{2\beta_{2n}} [(1 + \mu_{2n}^2)\beta_{2n} + (1 - \mu_{2n}^2) \sin \beta_{2n} \cos \beta_{2n} + 2\mu_{2n} \sin^2 \beta_{2n}] \quad (\text{A.18})$$

$$\mathbf{N}_{1n} = \frac{l_1}{\beta_{1n}} [\sin \beta_{1n} + \mu_{1n}(\cos \beta_{1n} - 1)] \quad (\text{A.19})$$

$$\mathbf{N}_{2n} = \frac{l_2}{\beta_{2n}} [\sin \beta_{2n} - \mu_{2n}(\cos \beta_{2n} - 1)] \quad (\text{A.20})$$

Amplitude ratios are given by,

$$\mu_{1n} = \frac{\tan \beta_{2n}}{\sigma} = \frac{\tan \eta \beta_{1n}}{\sigma} = \frac{\tan \left(\frac{\sqrt{D_1^*} l_2}{\sqrt{D_2^*} l_1} \beta_{1n} \right)}{\sigma} \quad (\text{A.21})$$

$$\mu_{2n} = \tan \beta_{2n} = \tan \left(\frac{\sqrt{D_1^*} l_2}{\sqrt{D_2^*} l_1} \beta_{1n} \right) \quad (\text{A.22})$$

Eigen value equation for **equation A.15** is given by,

$$\tan \left[\beta_{mn} + \tan^{-1} \frac{\beta_1}{L_1} \right] = \sigma \cot \eta \beta_{mn} \quad (\text{A.23})$$

where $\beta_{mn} = \beta_{11}, \beta_{12}, \dots, \beta_{1n}$ are the positive roots of eigen value equation.

$$L_1 = \frac{l_1 k^*}{D_1^*}; \quad \sigma = \frac{\sqrt{D_1^*}}{\sqrt{D_2^*}}; \quad \eta = \frac{\sqrt{D_1^*} l_2}{\sqrt{D_2^*} l_1} = \frac{\beta_2}{\beta_1}$$

To determine eigen values, the parameters such as L_1, σ, η need to be computed for different values of D_1^*, D_2^*, k^* values. Eigen values are located at branches of tangent on left of **equation A.23** intersect with branches of cotangent on the right at an infinite set of points as abscissae of intersections.

A.3.4 Special case 2: D_1^* is finite and D_2^* is ∞

When the oxygen diffusion coefficient of 1st oxide layer is lower than the 2nd layer ($D_1^* \ll D_2^*$) or thickness of $l_1 \gg l_2$ where ^{18}O concentration diffuses through

oxide 1/oxide 2 interface (at $x = 0$) with small value of tracer concentration. Consequently ^{18}O concentration throughout the 2nd oxide layer will remain at interface concentration $C(\mathbf{0}, t)$. As a result ^{18}O diffusion profile in the 2nd oxide layer becomes straight due to infinite self-diffusion coefficient $D_2^* = \infty$ of the second layer. Therefore solution to Fick's second law of diffusion equation in such condition after isotope ^{18}O exchange-anneal time duration t is given by,

$$C' = \frac{C(x, t) - C_{bg}}{C_{gas} - C_{bg}} = \begin{cases} C_{gas} + \sum_{n=1}^{\infty} A_n \left(\cos \beta_{1n} \frac{x}{l_1} + \mu_{1n} \sin \beta_{1n} \frac{x}{l_1} \right) e^{-\lambda_n^2 t} & -l_1 \leq x \leq 0 \\ C_{gas} + \sum_{n=1}^{\infty} A_n e^{-\lambda_n^2 t} & 0 \leq x \leq l_2 \end{cases} \quad (\text{A.24})$$

Where,

$$A_n = \frac{\sin \beta_{1n} + \mu_{1n} \cos \beta_{1n}}{[(1 + \mu_{1n}^2) \beta_{1n} + (1 - \mu_{1n}^2) \sin \beta_{1n} \cos \beta_{1n} + 2\mu_{1n} \cos^2 \beta_{1n}]} \quad (\text{A.25})$$

$$\lambda_1 = \frac{\beta_{11} \sqrt{D^*}}{l_1}; \lambda_2 = \frac{\beta_{12} \sqrt{D^*}}{l_1} \quad (\text{A.26})$$

Eigen value equation for **equation A.24** is given by,

$$\tan \left[\beta_{mn} + \tan^{-1} \frac{\beta_{mn}}{L_1} \right] = \frac{1}{\beta_{mn}} \frac{l_1}{l_2} \quad (\text{A.27})$$

where $\beta_{mn} = \beta_{11}, \beta_{12}, \dots, \beta_{1n}$ are the positive roots of eigen value equation.

$$L_1 = \frac{l_1 k^*}{D^*}$$

Eigen values can be determined by computing L_1 for different values of D^* and k^* values.

A.3.5 Validation of Two-slab model by manual fitting and MATLAB fitting routine

The system studied in this thesis are LSMC/8YSZ/Si multilayers in which the straight diffusion profiles are always obtained in 8YSZ layer through the IEDP-SIMS measurements performed at temperatures 600°C, 700°C and 800°C. The straight diffusion profile in 8YSZ layer represents infinite oxygen diffusion coefficient for 8YSZ

($D_2^* = \infty$). Therefore, the diffusion solution **equation A.24** (in **special case 2**) is suitable to apply in our system.

Before programming **equations A.24** to **A.27** in MATLAB, the equations are validated by fitting the experimental profile manually. The experimental data used for testing corresponds to the combinatorial sample LSMC/8YSZ/Si with 4% cobalt (**Figure A.3**) where ^{18}O diffusion profile was obtained at 700°C under 21.97min of ^{18}O exchange-annealing. After validating the equations by manual fitting, the same experimental data is fitted by MATLAB numerical routine using least-square fitting method in order to determine D^* and k^* of LSMC layer.

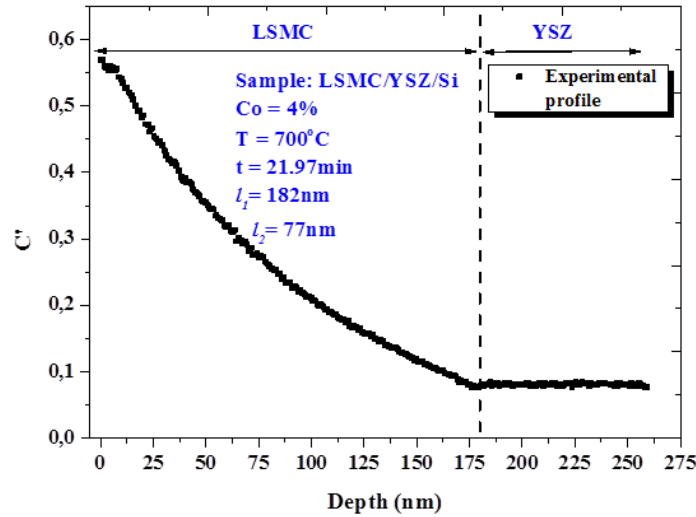


Figure A.3. Experimental isotope diffusion profile obtained in sample LSMC/YSZ/Si with 4% Co. y-axis represents normalized concentration C' which is plotted against thickness (nm) in x-axis.

Further, the fitting requires the calculation of n roots of β_{mn} in the transcendental eigen value equation A.27 which is, $\tan[\beta_{mn} + \tan^{-1} \beta_{1mn}/L_1] = l_1/\beta_{mn}l_2$. These roots can be determined by computing the equation with different combinations of D^* and k^* until the best combination is obtained. Therefore, a complex routine was coded in a way to determine the first two positive roots of $\beta_{mn} = \beta_{11}, \beta_{12}$ which is sufficient to determine D^* and k^* values of LSMC layer accurately [3].

Figure A.4 represents the fitting of experimental profile corresponds to the sample with 4% Co (**Figure A.3**) which is fitted using MATLAB numerical routine. A good fitting is obtained in general, which shows that the Two-slab model is functioning.

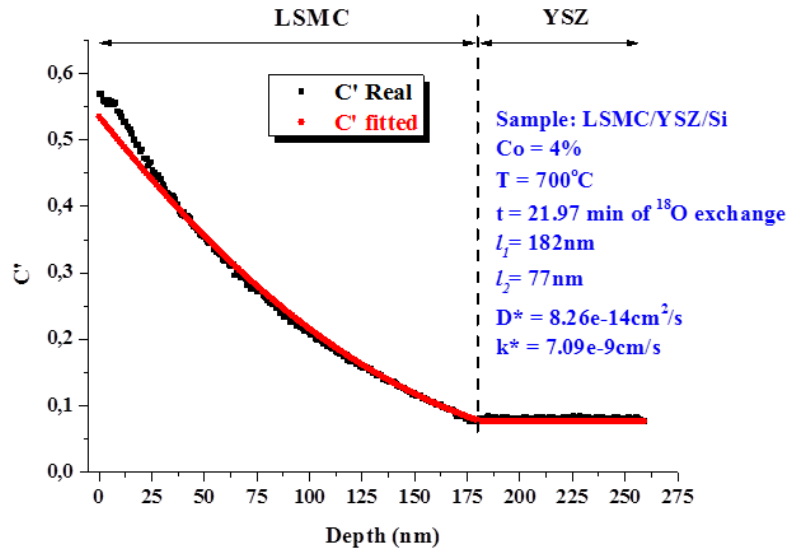


Figure A.4. ^{18}O diffusion profile of LSMC sample with 4% Co is fitted by MATLAB numerical fitting routine using Two-slab solution.

There are two slopes that can be seen in the experimental profile (**Figure A.3**). The first slope is located in the sample surface which spans for around $\approx 30\text{nm}$ and the presence a deep penetrating profile inside the sample until LSMC/YSZ interface is the second slope. The presence of more than one slope confirms that LSMC layer behaves as an inhomogeneous medium. Further, the presence of two slopes in the experimental profile represents two different diffusion pathways in the LSMC layer.

Although Two-slab model can fit the bilayer diffusion profile in **Figure A.4**, it fits only a part of the diffusion profile which is the second slope. In **chapter 4 and 6**, FEM simulation was performed to fit the oxygen diffusion profiles of LSM and LSMC system due to the multiple diffusion pathways in the diffusion profile. In the following section, the place of validity of Two-slab model is explained.

A.3.6 Two-slab model - Place of validity

Two-slab model cannot be applicable in diffusion profile having two or more slopes with slope arise from the fast diffusion pathway like grain boundaries. Even though Two-slab model is inoperative in certain conditions, it can be applied in some special cases which are,

Case (i): When the oxygen diffusion and exchange coefficients along the grain bulk (b) and grain boundary (gb) are the same, that is, $D_b^* = D_{gb}^* = D^*$ and $k_b^* = k_{gb}^* = k^*$. where D_b^* and D_{gb}^* represents oxygen diffusion coefficients along grain bulk and grain

boundary. Similarly, k_b^* and k_{gb}^* represents oxygen exchange coefficients along grain bulk and grain boundary.

Case (ii): Either D_b^* and k_b^* is dominating ie. $D_{gb}^* \approx k_{gb}^* \approx 0$ or D_{gb}^* and k_{gb}^* is dominating ie. $D_b^* \approx k_b^* \approx 0$.

Therefore, D^* and k^* values obtained in **Figure A.4** using Two-slab model represents an average value along grain bulk and grain boundary region. The main drawback of Two-slab model is it cannot differentiate fast and slow diffusion and exchange pathways however an average fitting can be obtained. Readers should choose the model accordingly, after carefully analyzing the oxygen diffusion profiles.

References

- [1] John Crank, *The Mathematics of Diffusion*, Oxford, UK, **1986**.
- [2] Paul Shewmon, *Diffusion in solids*, McGraw-Hill, USA, **1963**.
- [3] E. Mayer, *J. Am. Rocket Soc.*, **1952**, 22, 150.
- [4] H. S. Carslaw, *Mathematical theory of the conduction of heat in solids*, Macmillan and Co., UK, **1921**.

Appendix-B

$\text{La}_{0.8}\text{Sr}_{0.2}\text{MnO}_3$ - $\text{La}_{0.8}\text{Sr}_{0.2}\text{CoO}_3$ - $\text{La}_{0.8}\text{Sr}_{0.2}\text{FeO}_3$

Ternary sample preparation in PLD

Appendix-B

B.1 LSM-LSC-LSF multilayer test deposition

The first LSM/LSC/LSF multilayer trial deposition is performed in PLD. The periodic layers of LSM with 1nm thickness, LSC with 1nm thickness and LSF with 1nm thickness are deposited on a Si chip with 100 thickness 8YSZ layer on top of it. The deposition condition is given in the following **section B.2**.

XRD pattern in **Figure B.1** represents the formation of a single pure composition attained from LSM/LSC/LSF multilayers with thickness ratio 1nm:1nm:1nm.

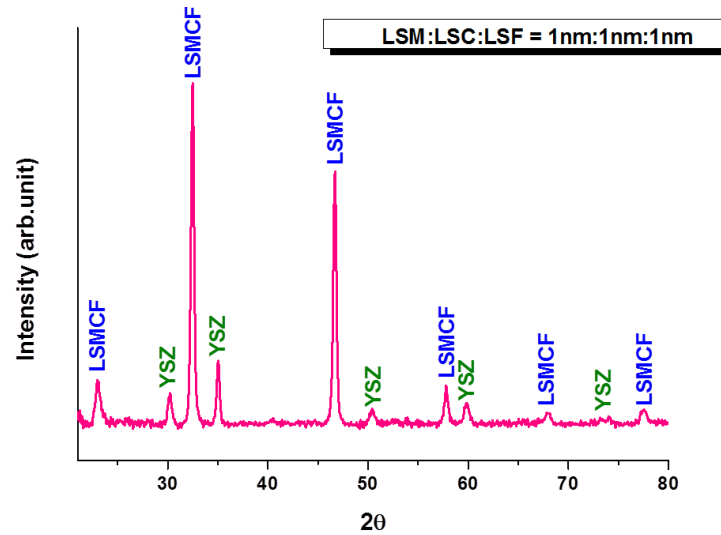


Figure B.1. XRD pattern of LSM/LSC/LSF multilayers with the thickness ratio 1nm:1nm:1nm per cycle.

B.2 LSM-LSC-LSF Ternary sample preparation

After making sure that there is no reaction between LSM, LSC and LSF multilayers in chip level deposition, a ternary trial deposition is performed on a 4-inch Si wafer. Before the ternary deposition, a thin uniform 8YSZ layer is deposited on the Si wafer.

Then a dense LSM, LSC and LSF multilayers are grown under the deposition condition $T = 700^{\circ}\text{C}$, $P = 20\text{mT}$, $d = 9.5\text{cm}$, $f = 10\text{Hz}$, $F \approx 1.1\text{Jcm}^{-2}$ (LSM), 0.7Jcm^{-2} (LSC) and 1.1Jcm^{-2} (LSF). The parent layer LSM is grown with 95 pulses as a first layer. Over that the second layer LSC is grown with 88 pulses and LSF is grown with 98 pulses as a third layer. All the three layers reached a thickness of 1nm with the above pulse rates

and it is repeated for 180cycles. The substrate is rotated to 120° every time before each successive layer deposition.

Finally, LSM-LSC-LSF a Pseudo-ternary thin film sample is successfully fabricated in PLD. The as-prepared sample is given in **Figure B.2** where the presence of LSM, LSC and LSF plumes can be seen at the three different corners of wafer.

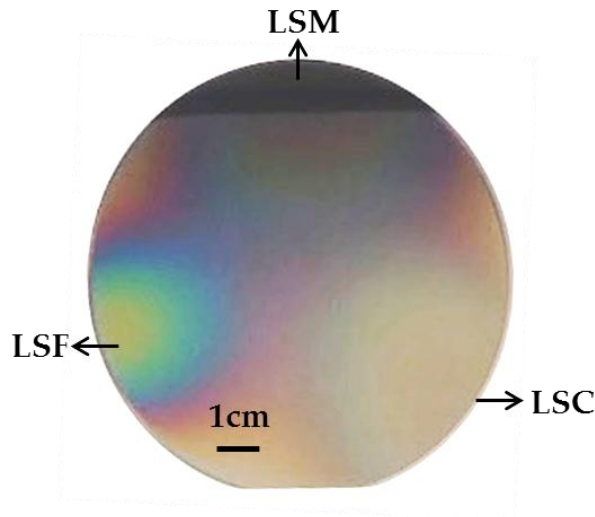


Figure B.2. As-prepared LSMCF Pseudo-ternary system fabricated in PLD.

Because of time constraints the microstructural characterizations such as XRD, SEM, AFM including functional characterization could not be performed. But Mn, Co and Fe distribution in the ternary sample was studied by EDS and the result shows that Mn, Co and Fe atoms exhibit a maximum concentration of $\approx 90\%$ in the plume center region and the concentration starts to decrease if one move away from the plume center.

The concentration and thickness distribution in the ternary sample can be altered and controlled by adjusting the parent layer plume position explained in **section 5.3 in chapter 5**.

Scientific contributions

Publications in international journals (Masters and PhD)

- [A. M. Saranya](#), D. Pla, A. Morata, A. Cavallaro, J. C. Vázquez, J. A. Kilner, M. Burriel, A. Tarancón, "Engineering Mixed Ionic Electronic Conduction in $\text{La}_{0.8}\text{Sr}_{0.2}\text{MnO}_{3+\delta}$ Nanostructures through Fast Grain Boundary Oxygen Diffusivity", *Adv. Energy Mater.*, 2015, 5, 1500377. **Impact factor - 16.146**
- S. Manivannan, [A. M. Saranya](#), B. Renganathan, D. Sastikumar, G. Gobi, K. C. Park, "Single-walled carbon nanotubes wrapped poly-methyl methacrylate fiber optic sensor for ammonia, ethanol and methanol vapors at room temperature", *Sensor Actuat. B – Chem.*, 2012, 171, 634., **Impact factor - 4.286**
- S. Manivannan, L. R. Shobin, [A. M. Saranya](#), B. Renganathan, D. Sastikumar, Kyu Chang Park, "Carbon Nanotubes Coated Fiber Optic Ammonia Gas Sensor" *Proc. SPIE Integrated Optics: Devices, Materials, and Technologies XV*, 2011, 7941, 79410M. **Impact factor - 0.2**

ACADEMIC OUTPUTS (Papers, Proceedings, Contributions)

AUTHORS: A. M. Saranya, D. Pla, A. Morata, A. Cavallaro, J. C. Vázquez, J. A. Kilner, M. Burriel, A. Tarancón

TITLE: Transforming $\text{La}_{0.8}\text{Sr}_{0.2}\text{Mn}_{1-x}\text{Co}_x\text{O}_{3\pm\delta}$ into a good mixed ionic-electronic conductor through nanoengineering: grain boundaries as oxygen diffusion highways

TYPE OF PRESENTATION: Oral

CONGRESS: TO-BE Spring Meeting 2015

MEETING PLACE: Aveiro (Portugal)

YEAR: 2015

AUTHORS: A. M. Saranya, A. Morata, M. Burriel, John A. Kilner, A. Tarancón

TITLE: Engineering Mixed Ionic Electronic Conduction in $\text{La}_{0.8}\text{Sr}_{0.2}\text{MnO}_{3+\delta}$ Nanostructures through Fast Grain Boundary Oxygen Diffusivity

TYPE OF PRESENTATION: Oral

CONGRESS: MRS

MEETING PLACE: Lucerne (Switzerland)

YEAR: 2015

AUTHORS: M. Burriel, R. Schmitt, A. M. Saranya, A. Morata, A. Hornes, S. Schweiger, M. Bourdard, J. L. M. Rupp, A. Tarancón

TITLE: $\text{La}_{0.8}\text{Sr}_{0.2}(\text{Mn},\text{Co})\text{O}_3$ Perovskite Oxides as Resistive Switches: Influence of B-Site Substitution on the Resistive Switching Properties

TYPE OF PRESENTATION: Oral

CONGRESS: MRS

MEETING PLACE: Lucerne (Switzerland)

YEAR: 2015

Scientific contributions

AUTHORS: A. M. Saranya, A. Morata, M. Burriel, S. N. Cook, John A. Kilner, A. Tarancón
TITLE: Combinatorial pulsed laser deposition of $\text{La}_{0.8}\text{Sr}_{0.2}\text{Mn}_x\text{Co}_{1-x}\text{O}_{3\pm\delta}$ for SOFC cathode applications
TYPE OF PRESENTATION: Poster
CONGRESS: 38th International Conference on Advanced Ceramics and Composites
MEETING PLACE: Florida (USA)
YEAR: 2014

AUTHORS: C. Fabrega, A. M. Saranya, A. Morata, A. De Luca, S. Zeeshan, A. Tarancón, F. Udrea, J.R.Morante
TITLE: Perovskite materials for oxygen gas sensors integrated on silicon on insulator membranes
TYPE OF PRESENTATION: Oral
CONGRESS: E-MRS Spring Meeting
MEETING PLACE: Lille (France)
YEAR: 2014

AUTHORS: A. M. Saranya, A. Morata, M. Burriel, John A. Kilner, A. Tarancón
TITLE: SOFC materials search by combinatorial pulsed laser deposition: A case study on $\text{La}_{0.8}\text{Sr}_{0.2}\text{Mn}_{1-x}\text{Co}_x\text{O}_{3\pm\delta}$
TYPE OF PRESENTATION: Poster
CONGRESS: 11th European SOFC Forum 2014
MEETING PLACE: Lucerne (Switzerland)
YEAR: 2014

AUTHORS: M. Burriel, A.M. Saranya, D. Pla, A. Morata, A. Cavallaro, J. A. Kilner, A.Tarancón
TITLE: Combinatorial PLD for mixed conducting oxides: Exploration of entire compositional diagrams in a single experiment
TYPE OF PRESENTATION: Oral
CONGRESS: 2014 MRS Fall Meeting
MEETING PLACE: Boston (USA)
YEAR: 2014

AUTHORS: Iñigo Garbayo, Saranya Arupukottai, Guilhem Dezanneau, Alex Morata, Neus Sabaté, Jose Santiso, Albert Tarancón
TITLE: $\text{Sr}_2\text{Fe}_{1.5}\text{Mo}_{0.5}\text{O}_{6-\delta}$ as symmetrical electrode for micro SOFC
TYPE OF PRESENTATION: Poster
CONGRESS: 10th European SOFC Forum 2012
MEETING PLACE: Lucerne (Switzerland)
YEAR: 2012

Scientific contributions

AUTHORS: *A. Tarancón, A. M. Saranya, A. Morata, J. Santiso, J. A. Kilner*

TITLE: *On the effect of dopant distribution and pure lattice strain in the fast oxygen transport in acceptor doped fluorites*

TYPE OF PRESENTATION: *Oral*

CONGRESS: *E-MRS Spring Meeting and Energy Bilateral Conference MRS-EMRS*

PUBLICATION: *Proceedings of the E-MRS 2011 Spring Meeting, Symposium U, 5 7*

MEETING PLACE: *Nice (France)*

YEAR: *2011*